

University of Nottingham
UK | CHINA | MALAYSIA

^{19}F NMR as a Tool for the Rapid Evaluation of PFAS Removal with Activated Carbon

By

George Earl

Faculty of Engineering

University of Nottingham

A thesis submitted to the University of Nottingham for the degree of Doctor of Engineering

November 2025

Abstract

Activated carbon adsorption is one of the most widely used treatment processes for the removal of per- and polyfluoroalkyl substances (PFAS) from potable water. As countries impose tighter restrictions on their presence in surface and groundwater, efforts must focus on developing more sustainable activated carbon adsorbents to ameliorate the environmental and operational challenges associated with maintaining PFAS-free potable water production. The performance of novel adsorbents in PFAS-removal is traditionally analysed with techniques that require extensive sample preparation times, with the use of liquid chromatography tandem mass spectrometry (LC-MS/MS) being the most common practice. Indeed, LC-MS/MS can reach detection limits of sub-nanogram per litre, but the technique can only quantify PFAS with a corresponding isotopically labelled internal standard, which are expensive and only exist for less than 100 compounds, when over 10,000 PFAS compounds are in existence. Therefore, there is a pressing need to develop a rapid method of PFAS detection and quantification that can complement traditional methods of adsorbent screening. In the present study, a novel method of screening the performances of four commercially available activated carbon adsorbents in removing perfluorobutane sulfonic acid (PFBS), perfluorohexanoic acid (PFHxA), perfluorooctanoic acid (PFOA) and perfluorooctane sulfonic acid (PFOS) from water was developed using ^{19}F NMR spectroscopy. The demonstrated ^{19}F nuclear magnetic resonance (NMR) spectrometric method completely avoids extensive sample preparation, which is a requirement of traditional liquid chromatographic techniques, uses inexpensive standards for quantification, can detect the total-PFAS concentration on the ppm scale and has experimental times that are competitive with traditional techniques.

Combined with their full characterisation data, the four commercial activated carbons were ranked in terms of removal performance using the novel application of the ^{19}F NMR method, with a deep understanding of the prevalent mechanistic features of the adsorptive processes that take place. The adsorption results revealed the overall ranking of adsorbents by performance as CAC-4 > CAC-3 > CAC-2 > CAC-1, with the steam-activated, bituminous coal-derived CAC-4 outranking the two other steam-activated bituminous coal activated carbons and the steam-activated coconut-shell derived activated carbon in removing all four PFAS, due to CAC-4 exhibiting the highest surface area and mesopore volume, in conjunction with presenting the highest concentration of surface oxygen-containing functional groups, which fortify adsorption with favourable hydrophobic interactions and electrostatic interactions, respectively. Moreover, the PFAS removal performance of a wood-based biochar was analysed using the ^{19}F NMR method to explore whether biochar adsorbents could be a viable alternative to activated carbon adsorbents in the treatment PFAS. The results confirmed that the adsorption efficacy of activated carbon is far superior to that of biochar.

Acknowledgments

The author is grateful to Prof. Colin Snape, Dr. Andrew Gill and Dr. Lee Stevens for their encouragement, assistance and constructive criticism.

Grateful thanks are also due to Dr. Wei Lee, Adrian Quinn and Camila Tyler for their technical assistance.

Appreciation goes to Dr. Robin Irons and Dr. Claudia Matz for the successful management of the Centre for Doctoral Training in Resilient Decarbonised Fuel Energy Systems.

Lastly, the author is especially thankful to his parents, sister, brother-in-law, girlfriend and Diego the golden retriever for their unconditional and unwavering support.

Contents

Abstract ii

Acknowledgments iv

List of Figures xii

List of Appendix Figures xv

List of Tables xvii

Chapter 1 General Introduction 2

Chapter 2 Literature Review 9

2.1. PFAS Classification 9

2.1.1. PFAS Properties 11

2.1.2. Presence of PFAS in Water 12

2.1.3. PFAS Toxicity 13

2.2. PFAS Treatment Technologies 14

2.2.1. Membrane Filtration 15

2.2.2. Resins and Polymers 16

2.2.3. Foam Fractionation 19

2.2.4. Phytoremediation 21

2.2.5. Activated Carbon 21

2.2.6. Biochar 24

2.2.7. Clays and Minerals 28

2.3. Degradation technologies 28

2.3.1. Thermal Degradation 29
2.3.2. Electrochemical Oxidation 29
2.3.3. Supercritical Water Oxidation 32
2.3.4. Plasma Treatment 33
2.3.5. Sonochemical Degradation 34
2.3.6. Photodegradation 35
2.3.7. Biological Degradation 36
2.4. Adsorption Mechanisms 37
2.4.1. Physical Adsorption 37
2.4.2. Chemical Adsorption 39
2.5. Preparation of Activated Carbon 40
2.5.1. Granulation 40
2.5.2. Carbonisation/Pyrolysis 41
2.5.3. Physical Activation 42
2.5.4. Chemical Activation 43
2.5.5. Physicochemical Activation 43
2.5.6. Microwave-Assisted Activation 45
2.6. Regeneration of Activated Carbon 46
2.6.1. Thermal Regeneration 46
2.6.2. Chemical Regeneration 47
2.6.3. Steam Regeneration 48

2.6.4. Microwave Regeneration 49
2.6.5. Electrochemical Regeneration 49
2.6.6. Wet Oxidation Regeneration 50
2.6.7. Bio-regeneration 50
2.7. Characterisation of Activated Carbon 51
2.7.1. Morphology 51
Chemical Composition 54
2.7.2. Energy Dispersive X-ray Analysis 54
2.7.3. Elemental Analysis 55
2.7.4. X-ray Photoelectron Spectroscopy 55
2.7.5. Boehm Titrations 56
2.7.6. Infrared Spectroscopy 57
2.7.7. Surface Area, Pore Volume and Pore Size Distribution 58
2.7.8. Adsorption Isotherm Models 61
2.7.9. Freundlich Isotherm 61
2.7.10. Langmuir Isotherm 62
2.7.11. Sips Isotherm 63
2.7.12. Temkin Isotherm 63
2.7.13. Dubinin-Radushkevic Isotherm 64
2.7.14. Redlich-Peterson Isotherm 65
2.7.15. BET Model 65

2.8. PFAS Detection and Quantification 66
2.8.1. Liquid Chromatography Challenges 66
2.8.2. Electrospray Ionisation 67
2.8.3. Tandem Mass Spectrometry 68
2.8.4. High-resolution Mass Spectrometry 69
2.8.5. Total Organic Fluorine Combustion Ion Chromatography 70
2.9. ^{19}F Nuclear Magnetic Resonance Spectroscopy 71
2.9.1. Fundamental Principles of NMR Spectroscopy 71
2.9.2. ^{19}F NMR Spectroscopy Advisements 73
2.9.3. NMR Spectroscopy Applications 74
2.9.4. ^{19}F NMR Spectroscopy Advantages versus ^{1}H NMR Spectroscopy 75
2.9.5. ^{19}F NMR versus other Techniques 76
2.9.6. NMR Limitations 78
2.9.7. ^{19}F NMR Spectra Interpretation 79
2.9.8. PFAS-targeting Adsorbent Testing with ^{19}F NMR 81
Chapter 3 Aims and Objectives 85
3.1. Aims and Objectives 85
3.2. Puragen Activated Carbons: Industrial Partner and Adsorbent Supplier 88
Chapter 4 Experimental 93
4.1. Materials 93
4.2. Activated Carbon Characterisation 97

4.2.1. Proximate Analysis 97
4.2.2. Ultimate Analysis 99
4.2.3. Butane Activity 100
4.2.4. Iodine Number 101
4.2.5. Molasses Number 102
4.2.6. pH Test 103
4.2.7. Point of Zero Charge 103
4.2.8. Boehm Titrations 103
4.2.9. Scanning Electron Microscopy 105
4.2.10. Transmission Electron Microscopy 105
4.2.11. X-ray Photoelectron Spectroscopy 106
4.2.12. BET Surface Area and Pore Analysis 107
4.3. LC-MS/MS Analysis 116
4.4. Quantitative ^{19}F NMR Spectroscopy 119
4.4.1. NMR Parameters 120
4.4.2. NMR Data Processing and Analysis 121
Chapter 5 Characterisation of Activated Carbon Adsorbents 124
5.1. Introduction and Rationale for Comprehensive Adsorbent Characterisation 124
5.2. Textural Properties of Activated Carbons 128
5.3. Morphology of Activated Carbons 141
5.4. Physicochemical Properties of the Activated Carbons 145

5.4.1. Proximate and Ultimate Analyses 145
5.4.2. X-Ray Photoelectron Spectroscopy 148
5.4.3. Boehm Titrations 157
5.4.4. pH and Point of Zero Charge 158
Chapter 6 ^{19}F NMR Method Development for the Rapid Screening of Novel Activated Carbon Adsorbents 162
6.1. Introduction 162
6.2. PFAS Selection 163
6.3. ^{19}F NMR Method Considerations 164
6.4. ^{19}F NMR Parameter Tuning and Optimisation 170
6.5. ^{19}F NMR spectral processing 172
6.6. Method validation with LC-MS/MS 176
6.7. ^{19}F NMR Method Summary 177
Chapter 7 Rapid Screening of PFAS Targeting Activated Carbon Adsorbents using ^{19}F NMR 181
7.1. Evaluation of AC for PFAS adsorption 181
7.1.1. PFAS Adsorption Isotherms Tests 186
7.1.2. PFAS Adsorption Kinetics Tests 205
7.2. Biochar Adsorption Performance 211
7.3. LC-MS/MS analysis 212
Chapter 8 Conclusions and Future Work 216
8.1. Key Conclusions 216

8.2. Future Work 217

References 220

Journal Articles

Earl, G. F.; Stevens, L. A.; Li, W.; Snape, C. E. Analysis of per- and polyfluoroalkyl substances (PFAS) removal with activated carbon using ^{19}F nuclear magnetic resonance spectroscopy. RSC Advances 2026, 16 (7), 5716-5725, 10.1039/D5RA06437F.

List of Figures

Figure 2.1. The proposed degradation pathway for PFOS using SCWO. 33

Figure 2.2. Overview of the hydrothermal carbonisation process. 42

Figure 2.3. Microwave activation process flow diagram (CH-conventional heating, CR-chemical reagents, MW-microwave irradiation and PA-physical activation). 45

Figure 2.5. Schematic of scanning and transmission electron microscopes. 53

Figure 2.6. Illustration of the principle of EDX analysis. 55

Figure 2.7. Schematic of an XPS system and the electron ejection process on which the technique is based around. 56

Figure 2.8. Neutralisation reactions that can take place during the Boehm titrations. 57

Figure 2.9. Mechanism between infrared waves and powder to generate IR spectrum. 58

Figure 2.10. Diagram of how multilayer adsorption and pore filling occurs in porous materials (taken from the Micromeritics website). 59

Figure 2.11. ^{19}F NMR spectrum of PFOA (500 MHz, 298 K, CD3OD), Std = 4,4'-difluorobenzophenone. 80

Figure 4.1. Classification of physisorption isotherms. 113

Figure 5.1. N_2 adsorption isotherms obtained at -196 °C for (a) CAC-1, (b) CAC-2, (c) CAC-3 and (d) CAC-4. (e) Overlayed N_2 adsorption isotherms for all ACs. 133

Figure 5.2. N_2 adsorption isotherm obtained at -196 °C for the biochar. 133

Figure 5.3. Pore size distributions of activated carbons (a) CAC-1, (b) CAC-2, (c) CAC-3 and (d) CAC-4. 137

Figure 5.4. Pore size distributions of biochar. 138

Figure 5.5. SEM images of the four activated carbons; (a) CAC-1, (b) CAC-2, (c) CAC-3 and (d) CAC-4. 142
Figure 5.6. TEM images of the four ACs; (a) CAC-1, (b) CAC-2, (c) CAC-3 and (d) CAC-4. 143
Figure 5.7. The fitted C1s XPS spectra for (a) CAC-1, (b) CAC-2, (c) CAC-3 and (d) CAC-4. 152
Figure 5.8. pH and point of zero charge of the four ACs. 159
Figure 6.1. Lock circuit feedback loop that adjusts the strength of the magnetic field (B_0).[230] 165
Figure 6.2. (A) correct FID shape produced by proper shimming, and (B) Incorrect FID shape produced by improper shimming. 166
Figure 6.3. ^{19}F NMR spectrum of PFOA at 1 mg L^{-1} in 1:1 ratio H_2O:CD_3OD showing the -CF_3 peak at -81.59 ppm (g) with a signal to noise ratio of > 3..... 171
Figure 6.4. NMR spectra exhibiting (a) poor phasing and (b) a poor baseline. 173
Figure 6.5. Minimum integration region required for accurate peak integration (±20 x peak width at half height). 174
Figure 6.6. NMR spectral baseline distortion that occurred in some spectra..... 176
Figure 7.1. Langmuir, Freundlich and Sips adsorption isotherm models for the adsorption of PFOA on (A) CAC-1 and (B) CAC-2. 191
Figure 7.2. Langmuir, Freundlich and Sips adsorption isotherm models for the adsorption of PFOA on (C) CAC-3 and (D) CAC-4..... 192
Figure 7.3. Langmuir, Freundlich and Sips adsorption isotherm models for the adsorption of PFOS on (A) CAC-1 and (B) CAC-2. 193
Figure 7.4. Langmuir, Freundlich and Sips adsorption isotherm models for the adsorption of PFOS on (C) CAC-3 and (D) CAC-4..... 194

Figure 7.5. Langmuir, Freundlich and Sips adsorption isotherm models for the adsorption of PFBS on (A) CAC-1 and (B) CAC-2. 195
Figure 7.6. Langmuir, Freundlich and Sips adsorption isotherm models for the adsorption of PFBS on (C) CAC-3 and (D) CAC-4. 196
Figure 7.7. Langmuir, Freundlich and Sips adsorption isotherm models for the adsorption of PFHxA on (A) CAC-1 and (B) CAC-2. 197
Figure 7.8. Langmuir, Freundlich and Sips adsorption isotherm models for the adsorption of PFHxA on (C) CAC-3 and (D) CAC-4. 198
Figure 7.9. Adsorption capacities and removal efficiencies of (A) PFOA and (B) PFHxA, using the four ACs at varying dose rates. 203
Figure 7.10. Adsorption capacities and removal efficiencies of (C) PFBS and (D) PFOS, using the four ACs at varying dose rates. 204
Figure 7.11. The pseudo-second order adsorption model provides the best fit for the adsorption of (A) PFOA and (B) PFHxA. 209
Figure 7.12. The pseudo-second order adsorption model provides the best fit for the adsorption of (C) PFBS and (D) PFOS..... 210
Figure 7.13. Adsorption capacities and removal efficiencies of Biochar when removing PFBS, PFHxA, PFOA and PFOS. 211
Figure 7.14. Adsorption capacities and removal efficiencies of (A) PFOA and (B) PFHxA, using the four ACs at varying dose rates (LC-MS/MS)..... 213
Figure 7.15. Adsorption capacities and removal efficiencies of (C) PFBS and (D) PFOS, using the four ACs at varying dose rates (LC-MS/MS). 214

List of Appendix Figures

Appendix Figure 1. Stacked NMR spectra obtained for the adsorption isotherms of PFBS with CAC-1 and CAC-2. 237

Appendix Figure 2. Stacked NMR spectra obtained for the adsorption isotherms of PFBS with CAC-3 and CAC-4. 238

Appendix Figure 3. Stacked NMR spectra obtained for the adsorption isotherms of PFHxA with CAC-1 and CAC-2. 239

Appendix Figure 4. Stacked NMR spectra obtained for the adsorption isotherms of PFHxA with CAC-3 and CAC-4. 240

Appendix Figure 5. Stacked NMR spectra obtained for the adsorption isotherms of PFOA with CAC-1 and CAC-2. 241

Appendix Figure 6. Stacked NMR spectra obtained for the adsorption isotherms of PFOA with CAC-3 and CAC-4. 242

Appendix Figure 7. Stacked NMR spectra obtained for the adsorption isotherms of PFOS with CAC-1 and CAC-2. 243

Appendix Figure 8.Stacked NMR spectra obtained for the adsorption isotherms of PFOS with CAC-3 and CAC-4. 244

Appendix Figure 9. Stacked NMR spectra obtained for the adsorption isotherms of PFBS and PFOA with Biochar. 244

Appendix Figure 10. Stacked NMR spectra obtained for the adsorption isotherms of PFHxA and PFOS with Biochar. 244

Appendix Figure 11. Stacked NMR spectra obtained for the adsorption kinetics experiments for PFBS with CAC-1 and CAC-2. 244

Appendix Figure 12. Stacked NMR spectra obtained for the adsorption kinetics experiments for PFBS with CAC-3 and CAC-4. 244
Appendix Figure 13. Stacked NMR spectra obtained for the adsorption kinetics experiments for PFHxA with CAC-1 and CAC-2. 244
Appendix Figure 14. Stacked NMR spectra obtained for the adsorption kinetics experiments for PFHxA with CAC-3 and CAC-4. 244
Appendix Figure 15. Stacked NMR spectra obtained for the adsorption kinetics experiments for PFOA with CAC-1 and CAC-2. 244
Appendix Figure 16. Stacked NMR spectra obtained for the adsorption kinetics experiments for PFOA with CAC-3 and CAC-4. 244
Appendix Figure 17. Stacked NMR spectra obtained for the adsorption kinetics experiments for PFOS with CAC-1 and CAC-2. 244
Appendix Figure 18. Stacked NMR spectra obtained for the adsorption kinetics experiments for PFOS with CAC-1 and CAC-2. 244

List of Tables

Table 2.1. Examples of common types of PFAS compounds. 10

Table 2.2. Recent studies on aqueous PFAS removal with resins and polymeric adsorbents. 19

Table 2.3. Recent studies on aqueous PFAS removal with AC. 23

Table 2.4. Recent studies on aqueous PFAS removal with biochar, mineral and clay adsorbents. 27

Table 2.5. Textural properties of ACs prepared by physical, chemical, physicochemical and microwave-assisted activation. 44

Table 4.1. Details on the activated carbons selected for this project. 95

Table 4.2. The physicochemical properties of the four PFAS analysed in this study (PFOA, PFHxA, PFOS and PFBS)[1]. 97

Table 4.3. Verified physical properties of the Micromeritics silica-alumina standard. 107

Table 4.4. Experimentally determined physical properties of the Micromeritics silica-alumina standard performed on the ASAP 2420 Accelerated Surface Area and Porosimetry System. 108

Table 4.5. LC mobile phase conditions. 118

Table 4.6. LC parameters. 119

Table 4.7. MS parameters. 119

Table 5.1. Surface textural properties of the four ACs. 134

Table 5.2. Butane activity measurements for the four ACs and biochar. 140

Table 5.3. Proximate analysis data for the four activated carbons. 146

Table 5.4. Ultimate analysis data for the four activated carbons. 147

Table 5.5. The chemical groups and corresponding peak labels. 148
Table 5.6. Parameters and line shapes employed for the peak model used in Figure 5.7. 155
Table 5.7. Peak distribution and O:C ratio calculated from the C1s deconvolution. 155
Table 7.1. Non-linear Freundlich, Langmuir and Sips adsorption isotherm constants for PFAS in ultrapure water at 25 °C. 190

List of Abbreviations

AC	Activated carbon
AER	Anion exchange resins
BET	Brunauer–Emmett–Teller
BSE	Backscattered electrons
CAC	Commercial activated carbon
DOSY	Diffusion ordered spectroscopy
EA	Elemental analysis
EDI	Electrospray ionisation
EDX	Energy dispersive X-ray spectroscopy
EO	Electrochemical oxidation
FT-ICR	Fourier transform ion cyclotron resonance
GAC	Granular activated carbon
HFPO-DA	Hexafluoropropylene oxide-dimer acid
HPLC	High-performance liquid chromatography
HRMS	High-resolution mass spectrometry
IR	Infrared
LC-MS	Liquid chromatography - mass spectrometry
LC-MS/MS	Liquid chromatography - tandem mass spectrometry
MIL	Matériaux de l′Institut Lavoisier
MOF	Metal-organic framework
NMR	Nuclear magnetic resonance
NOM	Natural organic matter
PAC	Powdered activated carbon
PEEK	Polyetheretherketone
PFAS	Per- and polyfluoroalkyl substances
PFBS	Perfluorobutane sulfonic acid
PFCA	Perfluoroalkyl carboxylic acid
PFEA	Perfluoroalkyl ether acids
PFHxA	Perfluorohexanoic acid
PFHxS	Perfluorohexane sulfonic acid
PFNA	Perfluorononanoic acid

PFOA	Perfluorooctanoic acid
PFOS	Perfluorooctane sulfonic acid
PFSA	Perfluoroalkyl sulfonic acid
SCWO	Supercritical water oxidation
SE	Secondary electrons
SEM	Scanning electron microscopy
TEM	Transmission electron microscopy
TGA	Thermogravimetric analysis
TOC	Total organic carbon
TOF-CIC	Total organic fluorine combustion ion chromatography
UV	Ultraviolet
WWTP	Wastewater treatment plant
XPS	X-ray photoelectron spectroscopy

Chapter 1 General Introduction

Per- and polyfluoroalkyl substance (PFAS) contamination has emerged as one of the most pressing environmental challenges of the twenty-first century because of their remarkable persistence, global ubiquity and possible risks to human and ecosystem health. PFAS are a vast class of synthetic organofluorine compounds that have been widely used since the 1950s in industry and consumer products including firefighting foams, non-stick cookware, stain-resistant clothing, food packaging and electronics. Their distinct physicochemical properties, particularly the stability of the carbon–fluorine bond, contribute excellent thermal and chemical stability so that they are impermeable to regular degradative processes such as hydrolysis, photolysis and microbial metabolism. As a consequence, PFAS are globally dispersed and persistent contaminants found in surface and groundwaters, soil, sediment, biota and even human blood.

Recent studies have revealed alarming concentrations of PFAS in drinking water sources and remote ecosystems, indicating that they are capable of transporting themselves over long distances and bioaccumulating through food webs. In 2022, the U.S. Geological Survey reported that nearly half of tap water samples collected across the United States had detectable amounts of PFAS, whereas widespread detections have also been reported across Europe, Asia and Oceania.[1] These findings have prompted global interest because exposure to certain PFAS, particularly legacy compounds such as perfluorooctane sulfonate (PFOS) and perfluorooctanoic acid (PFOA), has been linked to a range of adverse health outcomes like immunotoxicity, endocrine disruption, reproductive toxicity and increased risks of certain cancers.[2] As a result, PFOS and PFOA were scheduled under the Stockholm Convention on

Persistent Organic Pollutants in 2009 and 2019, respectively, with many countries enforcing progressively stringent regulations and maximum permissible contaminant levels for potable water.[3]

Despite regulatory success, cleanup of PFAS-contaminated environments is an overwhelming task. The extreme stability of the C–F bond and amphiphilic nature of PFAS molecules render them resistant to the majority of common water treatment techniques such as biological degradation, chemical oxidation and membrane filtration. Advanced oxidation reactions like photocatalysis, electrochemical oxidation and plasma treatment have been promising in the destruction of PFAS but tend to be typically constrained by high operational costs, energy demand and incomplete mineralisation, occasionally resulting in the formation of harmful intermediates. Similarly, ion-exchange resins and reverse osmosis membranes can remove PFAS from water, but these processes merely move impurities from one medium to another, generating secondary waste streams that will need to be disposed of or destroyed.

Among the technologies, adsorption is one of the most practical and effective means of PFAS removal because it is simple, scalable, inexpensive and has the ability to treat large volumes of water. The process uses physical or chemical adsorption between the PFAS molecules and a solid surface with subsequent concentration from the water phase onto the adsorbent surface. The performance of adsorption depends on a variety of parameters such as surface area, porosity, surface chemistry and hydrophobicity of the adsorbent and molecular characteristics of PFAS like chain length and functional group.

Activated carbon (AC) has been the most widely used adsorbent for PFAS removal in industrial and municipal water treatment processes for decades. Its high specific

surface area, adjustable pore structure and high hydrophobicity provide effective adsorption of long-chain PFAS. Granular activated carbon (GAC) filters are ordinarily utilised in drinking water treatment plants, whereas powdered activated carbon (PAC) is usually applied for rapid batch treatment or as a polishing stage following regular treatment processes. However, despite its widespread use, AC also has several limitations that restrict its long-term performance. Its adsorption ability for short-chain PFAS is significantly lower due to weaker hydrophobic interactions and competitive adsorption with natural organic matter (NOM) in environmental waters can also hinder performance. Moreover, thermal regeneration of spent activated carbon is energy-consuming and can lead to partial desorption or degradation of PFAS, which can yield volatile fluorinated by-products. These challenges necessitate the development of substitute or novel adsorbents with higher selectivity, regeneration capacity and environmental sustainability.

Over the last few years, numerous materials have been explored as potential PFAS adsorbents such as ion-exchange resins, alumina, layered double hydroxides, metal-organic frameworks (MOFs) and new carbonaceous materials like biochar and carbon nanotubes. Ion-exchange resins can achieve high removal efficiencies for long- and short-chain PFAS by electrostatic attraction of the positively charged functional groups towards the anionic PFAS head groups. Their sensitivity to fouling and expense as well as the limited capacity for adsorption when there are competing anions present, remain major drawbacks. MOFs have attracted much attention due to the tunability of the pore structure and functionalisation potential, but their elevated synthesis cost and instability of aqueous medium complicates their application in the large scale.

Oxygen-deprived pyrolysed biomass with high carbon content, biochar, has in recent years attracted renewed attention as an environmentally friendly alternative for PFAS

adsorption. Its advantages include low production cost, extensive availability of heterogeneous feedstocks and tuneable physicochemical properties depending on pyrolysis conditions and the activation protocols. The surface of biochar tends to be rich in oxygen-functional groups, such as hydroxyl, carboxyl and carbonyl groups, that facilitate electrostatic, hydrophobic and hydrogen-bonding interactions with PFAS molecules. However, despite their high potential, most biochar-based adsorbents are behind commercial ACs in capacity and selectivity for adsorption, particularly for the short-chain PFAS. In addition, the PFAS sorption mechanisms to biochar remain unclear since surface heterogeneity, pore structure, as well as PFAS–water interaction are complex factors.

Considering these challenges, the development of cost-effective, efficient and sustainable adsorbent materials to address PFAS contamination worldwide is a broad priority. The focus in the future will remain on the optimization of the structure–property features of carbonaceous adsorbents, elucidation of the adsorption mechanism and improvement of the regeneration and reusability. The use of waste-derived or renewable precursors such as lignocellulosic biomass, agricultural residues and polymeric residues is a possible route towards green material synthesis. Besides, surface modification strategies including heteroatom doping, metal impregnation and functional group grafting have the promise to enhance PFAS selectivity and affinity by introducing specific binding sites or altering the polarity on the surface.

An increasingly important aspect of advancing PFAS adsorption research lies in the development of precise analytical tools capable of probing sorption behaviour at the molecular level. Traditionally, PFAS analysis has relied on liquid chromatography coupled with tandem mass spectrometry (LC-MS/MS), which is widely regarded as the benchmark technique for trace-level quantification due to its exceptional sensitivity and

selectivity. LC-MS/MS is capable of achieving sub-ng L^{-1} detection limits and is therefore routinely employed for regulatory monitoring, compliance testing and validation of laboratory studies.

Despite these strengths, LC-MS/MS presents several practical limitations when applied to adsorption screening and mechanistic investigations. Quantification is restricted to PFAS for which isotopically labelled internal standards are available, which are costly and exist for only a limited subset of the thousands of known PFAS compounds. In addition, extensive sample preparation, including solid-phase extraction and matrix clean-up, is typically required, increasing analysis time and analytical complexity. As a targeted technique, LC-MS/MS also provides limited insight into total fluorine content and non-target PFAS species without further high-resolution analysis.

In this context, ^{19}F nuclear magnetic resonance (^{19}F NMR) spectroscopy represents a powerful, non-destructive complementary technique for detecting and quantifying PFAS, owing to the high natural abundance and sensitivity of the fluorine nucleus and the absence of background interference in aqueous systems. While ^{19}F NMR does not achieve the ultra-low detection limits of LC-MS/MS, it enables direct, compound-independent quantification without chromatographic separation or compound-specific internal standards. The technique offers rapid analysis with minimal sample preparation and allows total PFAS concentrations to be quantified at the ppm scale. Furthermore, variations in chemical shift, peak broadening and signal intensity can provide insight into PFAS-adsorbent interactions, making ^{19}F NMR particularly well suited to rapid adsorbent screening and mechanistic studies. Consequently, ^{19}F NMR is not intended to replace LC-MS/MS, but rather to complement it, with LC-MS/MS retained for validation and trace-level quantification where required.

Against this background, the present EngD project aims to contribute to the development of high-performance carbon-based adsorbents for PFAS removal from water treatment systems. The investigation focuses on the screening of AC and biochar adsorbents, with some derived from inexpensive and sustainable precursors, and then extensive characterisation of their chemical and textural properties. Special emphasis is placed on correlating pore structure, surface chemistry and adsorption mechanisms with PFAS adsorption performance under environmentally relevant conditions. With adsorption isotherm and kinetic modelling, this work aims to offer basic understanding into the controlling interactions and mass transfer mechanisms, ultimately leading to the rational design of effective, sustainable adsorbents for large-scale PFAS remediation processes.

Chapter 2 Literature Review

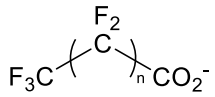
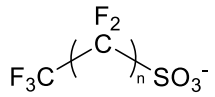
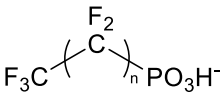
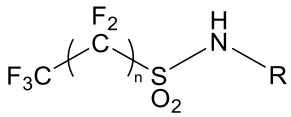
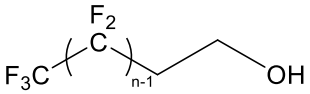
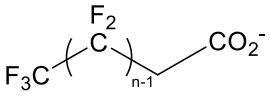
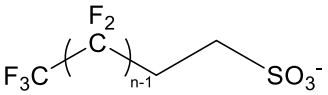
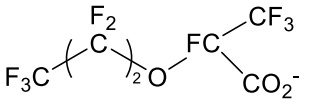
2.1. PFAS Classification

Per- and polyfluoroalkyl substances (PFAS), colloquially known as forever chemicals, are a family of partially or fully fluorinated linear, cyclic or branched synthetic organic compounds. First produced on an industrial scale in the 1940s, there have now been more than 4000 different variants of PFAS manufactured to date, with the majority of them containing a carbon backbone either nearly saturated (polyfluoroalkyl acids) or fully saturated (perfluoroalkyl acids) with fluorine atoms and at least one terminal charged functional group, such as a sulfonic acid or carboxylic acid group[4]. PFAS possess unique chemical properties, being hydrophobic and oleophobic, which has led to their widespread production and application as the active ingredient in various everyday products such as: non-stick pan coatings, firefighting foams, water-resistant clothing and pesticides.[5] Most PFAS can be categorised into two groups: perfluoroalkyl sulfonic acids (PFSAs) and perfluoroalkyl carboxylic acids (PFCAs). These can be further categorised into “long chain compounds” and “short chain compounds”, where long chain compounds cover PFSAs with six or more carbons in the backbone and PFCAs with eight or more carbons. Short chain compounds cover PFSAs with five or fewer carbons and PFCAs with seven or fewer carbons.[6] There is also a group of emerging PFAS, which are per- and polyfluoroalkyl ether acids (PFEAs). PFEAs, or GenX, have been used to replace the stringently regulated legacy PFAS, perfluorooctanoic acid (PFOA) and perfluorooctane sulfonic acid (PFOS).[7] This substitution was driven by regulatory pressure to phase out long-chain PFAS, while maintaining comparable functional performance in industrial applications. The introduction of ether linkages and shorter fluorinated chains in PFEAs was intended to

reduce bioaccumulation and enhance environmental mobility and elimination; however, growing evidence indicates that many PFEAs remain highly persistent in aquatic environments, and their long-term environmental fate and toxicological impacts are not yet fully understood.[8]

Examples of common types of PFAS compounds are presented in Table 2.1.

Table 2.1. Examples of common types of PFAS compounds.

Name	Abbreviation	Structure
Perfluoroalkyl carboxylates	PFCA	
Perfluoroalkyl sulfonates	PFSA	
Perfluoroalkyl phosphonates	PFPA	
Perfluoroalkyl sulphonamides	FASA	
n:2 Fluorotelomer alcohols	n:2 FTOH	
n:2 Fluorotelomer carboxylates	n:2 FTCA	
n:2 Fluorotelomer sulphonamides	n:2 FTSA	
Hexafluoropropylene oxide dimer acid	GenX	

2.1.1. PFAS Properties

The extraordinary physical and chemical properties of PFAS have been a catalyst for their widespread use in industry. However, these same properties have also contributed to their ubiquitous presence in the environment. The carbon–fluorine (C-F) bond is a polar covalent bond and is the strongest single bond in organic chemistry, with a bond energy of approximately 480 kJ mol^{-1} (compared with ~320 kJ mol^{-1} for C-Cl), which is one of the main reasons that PFAS exhibit exceptional chemical and thermal stability.[9] Additionally, the C-F bond is relatively short (~1.4 Å) and fluorine has a van der Waals radius of 1.47 Å, resulting in minimal steric strain along the fluorinated carbon backbone and further enhancing thermal stability. The high electronegativity of fluorine enables the fluorine atoms in PFAS to effectively shield the carbon skeleton from nucleophilic attack, thereby fortifying their chemical stability.

Structurally, PFAS are amphiphilic molecules composed of two chemically distinct regions: a fully or partially fluorinated alkyl chain (the tail) and a polar, ionisable functional head group, most commonly a carboxylic acid (-COOH) or sulfonic acid (-SO_3H). The fluorinated tail is both hydrophobic and lipophobic, behaviour that is largely attributed to the low polarizability of fluorine atoms and the strong C-F bonds, which limit favourable interactions with both water and non-fluorinated organic phases. In contrast, the acidic head group is hydrophilic and readily interacts with water, particularly when deprotonated. Moreover, PFAS exhibit both lipophobic and hydrophobic properties, which are largely attributed to the low polarizability of fluorine atoms.

As a result of this molecular architecture, PFAS behave as surfactants and tend to accumulate at interfaces such as air–water, solid–water and lipid–water boundaries. PFAS solubility has been found to decrease with increasing fluorinated carbon-chain length, whilst lipophilicity increases, as demonstrated by octanol–water partition coefficients (K_ow).[10] The majority of PFAS exhibit low pK_a values (typically 0.5-3.8) and therefore exist predominantly as anionic species at environmentally relevant pH ranges (pH 5.6-8.5), a property that strongly influences their mobility in aquatic environments and their interactions with adsorbent surfaces.

2.1.2. Presence of PFAS in Water

Many types of PFAS are found in aquatic environments, with their presence detected in wastewater, groundwater, stormwater, river water, lake water and drinking water; the latter being the prominent mode of exposure to human beings. In the United Kingdom, current drinking water guidance from the Drinking Water Inspectorate (DWI), which took effect in January 2025, requires water companies to enforce a cumulative limit of 100 nanograms per litre (ng L^{-1}) for 48 different PFAS compounds - a more stringent standard than both the EU (which applies the 100 ng L^{-1} limit to only 20 PFAS) and Scotland.[11] However, this remains guidance rather than legally enforceable statutory legislation, and individual PFAS concentrations up to 100 ng L^{-1} are currently considered acceptable, which is an order of magnitude higher than the 10 ng L^{-1} level that many health and environmental organisations consider 'low risk'.[12] There are thousands of different types of PFAS in circulation (estimates range from 10,000 to 15,000 compounds), and until the January 2025 guidance update, there was no enforceable limit on the total concentration of combined PFAS. In contrast, the USA introduced legally binding limits of 4 ng L^{-1} for both PFOA and PFOS (the most notorious types) in April 2024, whilst the European Union's Drinking Water Directive

mandates a collective 100 ng L^{-1} limit for 20 of the most widely used PFAS, effective from January 2026. In the UK, PFAS contamination has been detected at more than 1,500 sites (based on samples taken between 2003 and 2023), with over 10,000 potential 'problem sites' identified by Environment Agency contractors, and cleanup costs estimated between £31 billion and £121 billion.[13] Due to the phasing out of PFOA, PFOS and other legacy long-chain PFAS, new short-chain and ultra-short-chain PFAS analogues have taken their place in industrial processes, with subsequent migration into the environment. However, there are limited data on their toxicological profiles and environmental fate. Short-chain PFAS are generally not as technically effective as long-chain PFAS in their applications, necessitating the use of larger quantities to achieve comparable performance to the now-restricted long-chain compounds. Importantly, short-chain PFAS have been found to be as environmentally persistent as their long-chain predecessors and can produce recalcitrant transformation products, such as trifluoroacetic acid (TFA), which is itself highly persistent and difficult to remove from water supplies.[14]

2.1.3. PFAS Toxicity

PFAS can induce a range of adverse health effects in humans, where people are typically exposed via oral ingestion. It is probable that PFAS ingestion can cause immunity issues, thyroid disorders, liver disease, reproductive/developmental issues, endocrine disruption and various cancers. PFAS with a carbon chain-length of 6 or greater tend to target and reside in the liver,[15] and current research indicates that the elimination half-life of the two most notable PFAS; PFOA and PFOS, are 3.5 years and 4.8 years, respectively. In 2020, the European Food Safety Authority (EFSA) established a group tolerable weekly intake (TWI) of 4.4 ng kg^{-1} body weight for the sum of PFOA, PFOS, PFHxS and PFNA. This corresponds to a daily equivalent of

approximately 0.63 ng kg^{-1} day^{-1}.[16] By comparison, the former daily limit for PFOA alone was 1500 ng day^{-1}, which equates to approximately 21.4 ng kg^{-1} day^{-1} for a 70 kg adult, more than an order of magnitude higher than the EFSA 2020 group TWI on a body-weight-normalised basis. There are only a handful of PFAS with sufficient health implication data to enable sound decision-making on safe dosage guidance. Moreover, environmental samples usually confirm the presence of a mixture of different PFAS, making it difficult to determine their combined human health risk. With legacy PFAS being phased out and thousands of new PFAS taking their place, it is essential that research is carried out into their safe removal as part of an overall strategy to safeguard drinking water quality.

2.2. PFAS Treatment Technologies

In the United Kingdom, conventional water treatment technologies are not sufficient for PFAS removal/degradation. Owing to the strength of the C-F bond, PFAS are resistant to chlorine disinfection/UV irradiation.[17] Ozone and hydroxyl radicals can be used for PFAS oxidation, but the PFAS are still somewhat resistant and long chain PFAS are often partially degraded into short-chain PFAS[10]. It has been reported that some waste water treatment plants (WWTP) that utilise biological treatment technologies have higher PFAS concentrations in their effluent than in their influent, indicating biotransformation of PFAS precursors taking place during the biological treatment process.[18] However, there are a handful of tertiary treatment technologies/processes which are effective at removing PFAS from water: Adsorption, membrane filtration and anion exchange.[19-21] These technologies do not destroy PFAS but instead funnel the contaminants into a highly concentrated waste stream. Moreover, some PFAS degradation techniques can effectively destroy PFAS from

these pre-concentrated waste streams. Both PFAS removal and degradation technologies are discussed in the following sections.

2.2.1. Membrane Filtration

Membrane filtration processes such as reverse osmosis and nanofiltration utilise high-pressure pumps to efficiently remove short and long-chain PFAS from water streams.[22] In both processes, the water stream is pumped through the pores of the membrane, which are sufficiently small to give rise to a PFAS-free permeate (the rejected solution is called the retentate/concentrate). With membrane filtration, permeate productivity and permeate recovery are prioritised to ensure economical operation.

In membrane filtration, the prime removal mechanism is size exclusion. Removal efficiencies of > 90% can be achieved for short-chain PFAS, but it is easier to remove long-chain PFAS due to their larger size.[22] Reverse osmosis membranes have pore sizes of <1 nm, whereas the pore sizes of nanofiltration membranes are usually in the range of 1 – 10 nm, meaning reverse osmosis removes more PFAS. Interestingly, PFAS concentration build-up at the membrane can develop a large concentration gradient across the membrane, which can cause PFAS to diffuse through; this is called concentration polarisation. Nanofiltration typically has a higher permeate flux so concentration polarisation has a greater effect.[22]

Membrane filtration process efficiency can be affected by the water matrix. Cations present in the water can induce the formation of larger PFAS complexes which can allow for a more PFAS-depleted permeate. Cations may also neutralise the negative head group of the PFAS which, in turn can lower the electrostatic repulsion between the PFAS and the negatively charged membrane which can lead to a greater amount

of PFAS in the permeate. PFAS complex formation can lead to pore-blocking of the membranes, which will decrease the membrane longevity and increase energy use.[23]

2.2.2. Resins and Polymers

Ion exchange treatment utilises anion exchange resins (AERs) to remove PFAS and other organic/inorganic anions from the water. Anion exchange involves the exchange of negatively charged counter ions, such as OH^-, Cl^- and HCO_3^- from the polymeric resin surface to the surrounding aqueous matrix. These single-use resins use ion exchange coupled with hydrophobic interactions to remove the PFAS from the water.[24] AERs have been found to be better at adsorbing PFSAs than PFCAs and typically have a higher adsorption capacity for long-chain PFAS over short-chain PFAS. Moreover, AERs generally perform better than ACs in removing short-chain PFAS due to the former having higher selectivity for PFAS due to a higher concentration of quaternary ammonium groups.[25] At present, manufacturing costs for AERs are higher than those for AC production, and regeneration of the PFAS-laden AERs is more difficult.

Anion Exchange Resins offer effective PFAS removal and are sold as single-use/non-regenerative adsorbents. The resins contain a polystyrene backbone, crosslinked with divinylbenzene, and present complex amino functionality.[26] The amino functionality involves electrostatic interaction with the anionic head group of the PFAS, whilst the divinylbenzene and polystyrene elements of the AER enable hydrophobic interaction with the PFAS tail. The electrostatic interaction process has been confirmed by monitoring the ratio of chloride ion release with PFAS uptake (a ratio close to 1:1 was achieved).[27] It has been reported that AERs can achieve high adsorption capacities towards PFAS and have faster adsorption than ACs do, but are more expensive to

produce commercially, and the PFAS specific AERs cannot be regenerated.[28] A brine solution can be applied to successfully desorb the negatively charged head group of the PFAS from the resin surface however the hydrophobic tail group remains adsorbed. Likewise, an organic solvent, like methanol, can be applied to wash the hydrophobic tail from the resin, but the negatively charged head group will remain adsorbed to the site of ion exchange.[29] Notably, anion exchange offers superior removal of short-chain PFAS compared to AC[30].

Metal organic frameworks (MOFs) are an emerging water treatment technology that utilises adsorption for pollutant removal. MOFs are porous polymers, comprising metal clusters which are coordinated to organic ligands (linkers), producing extended one- two- and three-dimensional structures.[31] The pore sizes and crystal structure of MOF adsorbents are tuneable with modifying additives, which could one day provide a competitive alternative to AC adsorbents, as long as the MOFs are water-stable and inexpensive.[32] However, MOF adsorbent development is in its infancy, and currently, there are presently several disadvantages to their usage at a commercial scale: (i) their synthesis is expensive and complicated, (ii) the majority of MOFs are not stable in water,[33] (iii) there is no standard means of MOF production, (iv) fine powder MOFs limit opportunities for use in waste water treatment plants as they are hard to remove, and (v) MOFs have not received regulatory approval for their use in water treatment plants yet. Despite this, some MOFs exhibiting high specific surface areas, well developed porosity and varied surface functionality have been identified as promising adsorbents for PFAS removal. MIL-based MOFs have been used for PFAS removal due to their thermal/environmental stability as well as their robust structure. Pristine MIL-101-Cr was compared with modified MIL-101-Cr-QDMEN, exhibiting adsorption capacities of 460 mg g^{-1} and 754 mg g^{-1} respectively, for PFOA. The MIL-101QDMEN

was modified to contain quaternary amine groups, which enhanced electrostatic interactions with the PFOA.[34] UiO-67 exhibits a very high adsorption capacity towards PFOA due to pore sizes of 1.2 – 1.6 nm, which are sufficiently large for PFOA to navigate into the pores, as PFOA has a hydrated diameter of 1.2 – 1.5 nm.[35] MOFS MIL-100(Fe), ZIF-8, MIL-54(Al) and HKUST-1 have all been produced on the tonne scale. Although these do not target PFAS, this demonstrates that industrial scale production is credible.[36]

Cross-linked β-cyclodextrin polymers have proved to be promising adsorbents in aqueous PFAS removal.[37] Styrene groups are covalently attached to β-cyclodextrin to form a discrete monomer which can undergo radical polymerisation with styrene and methacrylate comonomers to produce polymers of very high specific surface area. The polymers synthesised with the methacrylate monomer contained a cationic functional group, which enables 100% removal of eight different anionic PFAS molecules. Ateia *et al.*[38] reported the effectiveness of a poly(N-[3-(dimethylamino)propyl] acrylamide methyl chloride quaternary (DMAPAA-Q) hydrogel matrix when removing aqueous PFAS. The DMAPAA-Q polymer exhibited high adsorption kinetics, verified by no change in PFAS concentration between 1 h and 24 h, signalling saturation of the adsorbent. Additionally, the spent DMAPAA-Q was used in batch adsorption tests after 6 regeneration cycles, which confirmed that the adsorptive performance was completely maintained. Various PFAS removing resins and polymers are presented in Table 2.2.

Table 2.2. Recent studies on aqueous PFAS removal with resins and polymeric adsorbents.

PFAS		Resins and Polymers		Q_{max} (mg g^{-1})	Reference
		Type	Surface area $m^2\ g^{-1}$		
PFCA	PFOA	Porous-type AER	N/A	210	[39]
	PFOA	Gel-type AER	N/A	261	[39]
	PFOA	Polyamine AER	381	470	[40]
	PFOA	F-TiO_2@MIL-125	85	70	[41]
PFSA	PFHxS	Strong base AER	N/A	1400	[42]
	PFOS	Polyamine AER	N/A	8000	[43]
	PFOS	MIL-53(Al) MOF	1336	50	[44]
	PFOS	MIL-53(Al)-BPCD MOF	873	200	[44]
GenX	HFPO-DA	Polyamine AER	N/A	1062	[45]
	HFPO-DA	Quaternary ammonium AER	N/A	1010	[45]
	HFPO-DA	MIL-101(Cr)	2478	42	[46]

2.2.3. Foam Fractionation

Foam fractionation takes advantage of the surfactant nature of PFAS via adsorption to air bubbles. The lowering of the surface tension of the 'solution' can enable the formation of bubbles/foam, which contain a very high concentration of PFAS at the air/water interface. Skimming off the foam allows for removing the PFAS-laden foamate and leaves behind a PFAS-exhausted solution. Foam fractionation does not

require intensive pre-treatment or additional chemicals to complete the process.[47] Foam fractionation has its disadvantages in that it is only able to remove compounds which are surface-active, like long-chain PFAS, and so the technique is not useful for short-chain PFAS removal or PFAS that are non-amphiphilic.

Compared to membrane filtration, foam fractionation can obtain better water recoveries because the membrane PFAS-concentrate volumes are greater than the foamate volumes from foam fractionation. Foam fractionation utilises a multistage fractionation process to reduce the total volume, with fractions being <2% of the initial influent volume.[48] The technique benefits from treating a water stream which contains other co-contaminants, as the presence of cations (high ionic strength) will increase the adsorption constants of the PFAS to the air/water interface.[49]

1.2.1. Electrocoagulation

Electrocoagulation is a PFAS removal method that utilises iron and aluminium sacrificial anodes to generate metal ions which can act as coagulants in aqueous media.[50] The metal ions will form metal hydroxides in the water, which will precipitate out, and the PFAS will adsorb to the surfaces of the metal hydroxides. The flocs can then be removed from the water stream via filtration, sedimentation and flotation.[51] Sivagami et al. report that electrochemical approaches related to electrocoagulation have achieved PFAS removal efficiencies ranging from approximately 70 % to over 95 % in controlled laboratory studies, with performance generally higher for longer-chain PFAS and under optimised current densities and electrode configurations (e.g. mixed Fe/Al systems).[51] While these findings demonstrate the potential of electrochemical methods for PFAS remediation, the majority of experimentation has been conducted with synthetic solutions at bench scale, and translation to pilot or field scales remains

limited. Flocculation is the main mechanism of PFAS removal, but it is possible that the formation of hydrogen bubbles at the cathode may enable the adsorption of PFAS to the bubbles.[52]

2.2.4. Phytoremediation

The process of phytoremediation utilises plants to remove PFAS from the water via uptake and effectively bioaccumulating the pollutants. Constructed wetlands containing riparian wetland plants have had success in removing up to 77% and 95% of PFOA and PFOS, respectively from the contaminated water, with species that exhibit fibrous rooting removing the most PFAS.[53] Phytoremediation has a higher affinity for short-chain PFAS removal, which is due to them being more polar and having increased mobility, which promotes faster uptake by the plants.[54] The PFAS-containing plants require harvesting with subsequent incineration at very high temperatures to ensure the PFAS is expunged. The technique poses some risks, such as contamination of food-chains if animals consume the PFAS-containing plant matter. Additionally, phytoremediation is ineffective at sites with significant concentrations of other phytotoxic contaminants, as the plants can die and re-contaminate the water.

2.2.5. Activated Carbon

AC is one of the most popular and extensively used tertiary treatment technologies in water treatment processes across the globe.[55, 56] The adsorptive properties of charcoal when used for gas treatment were first reported by Scheele in 1773. This was followed by Lowitz discovering the decolourisation of solutions by charcoal in 1786.[57] In subsequent years, Lowitz proved charcoal was capable of removing taste and odour from water, but it was Swedish chemist von Ostreijko who developed the first patented chemically and physically ACs.

Activated carbon is a highly porous, carbonaceous material with a well-developed pore volume, pore structure and large internal surface area and can be synthesised from a myriad of carbonaceous precursor materials, such as wood, lignite, coal and coconut shell.[58] The porous network within the AC comprises macro-, meso- and micropores, with the surfaces decorated with a range of different functional groups, allowing this low-cost, versatile material to have multiple real-world applications. Porous materials can be classified into three categories based on different pore sizes: macroporous (>50 nm), mesoporous (2-50 nm) and microporous (<2 nm). Surface functional groups generally contain oxygen, hydrogen, nitrogen and sulphur, all of which are chemically bonded to the carbon structure. Of these groups, it is the oxygen-containing functional groups that are most abundant, with carbon surfaces hosting groups like carboxyl, phenol, carbonyl, lactone, quinone and other groups. The concentration and nature of the surface functional groups can be influenced by the specific chemical and thermal conditions used to produce the ACs, which can be tailored/tuned for specific contaminant removal.

AC is sold commercially in several forms: (i) granular activated carbon (GAC), which has a fine, medium or coarse particle size, a long lifetime and is often used in water treatment processes, (ii) powdered activated carbon (PAC), which can exist as fine- or wide-porous carbon and is often used in the chemical, pharmaceutical and food industries, and (iii) pelletised activated carbon which is used for air purification and solvent recovery due to their great hardness and low pressure losses.

GAC is the most commonly used form of AC when it comes to treating PFAS-contaminated water and is more selective for the removal of long-chain PFAS than short-chain PFAS. PFAS-contaminated water moves down the GAC column and steadily saturates the GAC from the influent inlet to the effluent outlet, which is

subsequently swapped out once fully saturated. Interestingly, the short-chain PFAS concentrations can be higher in the effluent than in the influent due to competitive adsorption with long-chain PFAS and other matter. Dissolved organic matter (DOC) can reduce adsorptive performance of GAC via pore blocking, and once the GAC is fully saturated it needs to be replaced and regenerated physically or chemically.[59] Various types of PFAS targeting ACs are presented in Table 2.3.

Table 2.3. Recent studies on aqueous PFAS removal with AC.

PFAS		Activated Carbon		Q_{max} (mg g^{-1})	Reference
		Type	Surface area $m^2\ g^{-1}$		
PFCA	PFOA	Coconut shell GAC	1191	54	[60]
	PFOA	Silver nanocomposite AC	331	286	[61]
	PFOA	Chitosan GAC	766	149	[62]
	PFOA	Polyamine Functionalised polymer coated AC	194	380	[63]
PFSA	PFOS	Copper modified GAC	512	4.53	[64]
	PFOS	Fluorine doped AC	-	0.99	[65]
	PFOS	Modified AC-H_3PO_4	296	209	[66]
	PFOS	Coffee grounds AC	858	43	[67]
GenX	HFPO-DA	Coconut shell GAC	656	175	[45]
	HFPO-DA	Charcoal GAC	871	114	[68]

2.2.6. Biochar

Biochar is a low-cost adsorbent that can be produced more cheaply and sustainably than AC due to its potential for carbon sequestration and its reduced reliance on chemical activation and fossil-derived feedstocks. Similar to AC production, the biochar pre-cursor material is subjected to pyrolysis, but with no subsequent activation step, producing a biochar with lower carbon content, surface area and porosity compared to AC. However, biochar can be derived from waste materials like crop residues and manure, which provides a solution to challenges presented by the landfill/incineration of contaminated waste, and also opens up a route to valorising these wastes.

The PFAS adsorption performance of biochar is strongly governed by two classes of physicochemical properties: textural properties and surface chemistry. Textural properties, specifically the specific surface area, total pore volume and the distribution of pore sizes in the range that can accommodate PFAS molecules, are positively correlated with adsorption capacity. Higher pyrolysis temperatures (typically 600–900 °C) generally increase SSA and pore volume by driving off volatile matter and increasing the degree of carbonisation and aromatisation, enhancing hydrophobic character and thereby improving uptake of long-chain PFAS such as PFOS and PFOA through hydrophobic interactions. At lower pyrolysis temperatures, electrostatic interactions between polar surface functional groups and the PFAS head group play a comparatively larger role. These two mechanisms are not mutually exclusive and typically act in concert, with the dominant mechanism shifting as a function of pyrolysis conditions and the specific PFAS being removed.

PFAS adsorption by biochar is also highly chain-length dependent. Long-chain PFAS (C8 and above) exhibit markedly stronger adsorption than their short-chain analogues due to greater hydrophobic character and more favourable interactions with the aromatic biochar surface. Sulfonic acid head groups (e.g., PFOS) generally confer slightly stronger adsorption compared to carboxylic acid head groups (e.g., PFOA) of equivalent chain length, reflecting differences in charge density and molecular geometry. The greatest adsorption capacities across a range of agricultural waste biochars have been observed for PFOS (1-6 mg g^{-1}), followed by PFOA (1-3 mg g^{-1}) and PFBS (1-4 mg g^{-1}), with adsorption affinities following the same trend.

Inyang and Dickenson evaluated pinewood (PWC) and hardwood (HWC) biochars — produced at 700 °C by steam activation - for PFOA removal, finding that both achieved K_d values of approximately 49 and 41 L g^{-1} respectively, which were comparable to those of bituminous coal-based GAC. This highlighted the potential of wood-derived biochar as a lower-cost substitute for AC in PFAS-impacted water treatment, provided the feedstock and pyrolysis conditions are carefully controlled to maximise surface area and pore volume.

Krahn *et al.* developed sewage sludge-derived biochars as sustainable sorbents for PFAS-contaminated water and soil.[69] Two sewage sludge biochars (SSBCs) and one wood chip biochar (WCBC) were dry-pyrolyzed at 700 °C and compared in batch sorption experiments using six perfluorinated carboxylic acids (PFCAs), both individually and in mixture, in pure biochar systems and in a biochar–sandy soil matrix. Although the two SSBCs had significantly lower surface areas than the WCBC, one of the SSBCs proved to be an effective sorbent for PFAS, achieving a log K~d~ value of 5.73 ± 0.02 for PFOA at 1 µg L^{-1} - comparable to values previously reported for commercial ACs. This strong sorption performance was attributed to the SSBCs'

relatively high pore volumes in the pore size range that can accommodate PFAS molecules.

Krahn *et al.* also found that sorption was attenuated when multiple PFCAs were present simultaneously (by factors of 6 - 532 relative to single-compound systems) and when biochar was mixed with sandy soil (attenuation factors of 3 - 10), with the two effects combining to attenuate sorption by factors of 8 - 6,581 in the most extreme cases. The attenuation observed in mixed-PFAS systems appears to arise primarily from competition for binding sites amongst structurally similar PFCA congeners, rather than pore clogging or competition from soil organic matter.[70] Springer This is an important practical consideration when translating single-compound laboratory results to multi-contaminant field scenarios, where competitive sorption effects may significantly reduce the effective uptake capacity of the adsorbent.

Despite the promise shown by SSBCs, a key limitation of pristine biochar is that its adsorption capacity for PFAS remains considerably lower than that of well-optimised commercial AC. Several strategies have been explored to overcome this. Functionalization with metal oxides, acid–base treatments and steam activation can significantly enhance SSA, introduce additional adsorption sites and improve mechanical stability. Acid-modified sludge-derived biochar has been shown to achieve theoretical maximum adsorption capacities of 72.17 mg g^{-1} for PFOS and 45.88 mg g^{-1} for PFOA, with the adsorption mechanism comprising electrostatic interaction, hydrogen bonding and hydrophobic interaction.[71] More aggressive modification approaches, such as incorporation of $MgFe_2O_4$ magnetic nanoparticles, can push PFOA and PFOS adsorption capacities into the mg g^{-1} to μg g^{-1} range, though these more complex functionalization routes typically involve greater synthesis cost and

complexity. The performance of representative biochar adsorbents is summarised in Table 2.4.

Table 2.4. Recent studies on aqueous PFAS removal with biochar, mineral and clay adsorbents.

PFAS		Biochar, Clays and Minerals		Q_{max} (mg g^{-1})	Reference
		Type	Surface area m^2 g^{-1}		
PFCA	PFOA	Phosphoric acid biochar	1067	0.4	[72]
	PFOA	Zinc biochar	982	0.3	[72]
	PFOA	Biosolids biochar	11	3.4×10^{-5}	[73]
	PFOA	Nano ceramic clay	N/A	1.18	[74]
	PFOA	Steam-activated pinewood biochar	~500	17.9-31.7	[75]
	PFOA	Sewage sludge biochar	212	Log K_d = 5.73	[69]
	PFOA	Acid-modified sludge biochar	N/A	45.88	[76]
	PFOA	Biosolids biochar	~200	81.57	[77]
PFSA	PFHxS	Sewage sludge biochar	212	3.0×10^{-5}	[73]
	PFOS	Hematite adsorbent	9.9	0.13	[78]
	PFOS	Kaolinite adsorbent	N/A	0.08	[79]
	PFOS	Boehmite adsorbent	300	1.7×10^{-4}	[79]
	PFOS	Corn straw biochar	N/A	169.30	
	PFOS	Acid-modified sludge biochar	N/A	72.17	[76]
	PFOS	Sulfobetaine polymer biochar composite	N/A	634	[80]
GenX	HFPO-DA	Sewage sludge biochar	1183	0.1	[69]
	HFPO-DA	Magnetic modified clay	48	N/A	[81]

2.2.7. Clays and Minerals

Clay minerals and oxidic clays (Si, Al and Fe oxides) have been extensively researched for PFAS removal due to their ubiquity, inexpensive procurement and environmentally safe nature.[82, 83] Clay/mineral adsorbents are not effective for aqueous PFAS removal due to their negative charge if pristine clay/minerals are used. Hence, it is essential for the adsorbents to have their surfaces chemically modified with organic/inorganic chemical agents to improve the variety and concentration of surface functional groups.[84] Gong *et al.*[85] reported that the water soluble, starch-stabilised magnetite nanoparticles adsorbed twice as much PFOA as unmodified magnetite nanoparticles under identical conditions. Magnesium aminoclays are aminopropyl-functionalised magnesium phyllosilicates that are water-dispersible. The amino groups enhance PFAS removal by improving electrostatic interactions. Magnesium amino clays have been used as a stabilisation agent for the synthesis of nano-sized zero-valent iron, which was found to be much more effective at PFAS removal from wastewater than unstable nano-sized zero-valent iron.[86] In other work, soil containing ferrihydrites, desilicated minerals and magnetite has been combined with saw-dust biochar to produce a composite adsorbent material. The composite performed much better than the pristine sawdust biochar in removing aqueous PFOS due to increased surface functional groups which enhances electrostatic interactions, achieving adsorption capacities of 194.6 mg g^{-1} and 178.6 mg g^{-1}, respectively.[87]

2.3. Degradation technologies

PFAS degradation technologies aim to chemically transform or mineralise PFAS rather than remove them by transferring contaminants from the aqueous phase to a secondary solid or concentrate. To date, the majority of PFAS degradation approaches

have been investigated at laboratory scale, typically using PFAS-spiked deionised water under controlled conditions.

2.3.1. Thermal Degradation

The regeneration of PFAS-laden GAC uses high temperature heating (500 – 800 °C) in the presence of steam or an inert atmosphere (N_2 or Ar).[88] Combustion of AERs and GAC is another method of thermally degrading the PFAS in spent GAC and AERs. Both of these methods are used commercially, but what happens to the PFAS during combustion/regeneration is not fully understood. Mineralisation of long-chain PFAS (complete destruction) will occur in the temperature range of 700 – 800 °C, with short-chain PFAS being more easily destroyed.[89] GAC surface area recoveries increase with increasing temperature (80 – 100% when the temperature is >700 °C). As the regeneration yield on a mass basis is never 100% and the GAC may undergo numerous successive regeneration steps, the mixing of regenerated GAC and virgin GAC is usually necessary.

2.3.2. Electrochemical Oxidation

Electrochemical oxidation (EO) is a treatment technique that uses electricity to oxidise PFAS at the anode of an electrochemical cell.[90] The mechanism involves the generation of highly reactive hydroxyl radicals (•OH) and other oxidising species at the electrode surface, which can attack the C-F bonds in PFAS molecules and initiate their degradation. Ideal anodes exhibit a high oxygen overpotential and a weak interaction between the oxidised PFAS and the electrode itself, which prevents fouling and maintains electrode efficiency over extended operation. The high oxygen overpotential is critical as it extends the potential window for water oxidation, allowing the formation of •OH radicals and other reactive oxygen species before oxygen evolution becomes

the dominant reaction. Anodes with a high oxygen overpotential can be made from tin oxide (SnO_2), lead oxide (PbO_2) and boron-doped diamond (BDD). BDD anodes are particularly effective due to their exceptional electrochemical stability, wide potential window, and ability to generate large quantities of hydroxyl radicals, but they are expensive to manufacture due to the complex chemical vapour deposition processes required. Consequently, ceramic alternatives, such as Magnéli phase titanium sub-oxides (Ti_4O_7), which can degrade PFAS effectively whilst offering improved cost-effectiveness and durability, have been the subject of extensive research.

One of the principal advantages of EO is that it can be carried out at ambient temperatures and pressures without requiring the addition of external chemical reagents such as oxidants or catalysts, making it operationally simpler and potentially more sustainable than chemical oxidation methods. EO has demonstrated success in the degradation of PFAS in a variety of challenging water matrices, including groundwater, landfill leachate, aqueous film-forming foam (AFFF) still-bottoms from destructive distillation processes and industrial wastewater.[90-93]

The majority of research to date has been conducted using parallel-plate electrode configurations and perforated electrode flow-through cells, which offer relatively simple geometries and straightforward scale-up potential. However, these conventional electrode designs suffer from limitations in mass transfer efficiency, as PFAS molecules must diffuse from the bulk solution to the electrode surface where oxidation occurs. To address this limitation, recent developments have focused on porous three-dimensional flow-through electrode materials, which offer dramatically increased electrode surface area per unit reactor volume and force convective flow through the porous electrode structure itself, thereby reducing mass transfer resistance.[94] These advanced electrode architectures have shown promising improvements in PFAS

degradation rates and energy efficiency, though challenges remain in terms of electrode fabrication, pressure drop through the porous structure, and long-term stability under continuous operation.

A growing body of research has examined the effectiveness of EO on actual environmental samples rather than synthetic laboratory solutions, revealing important insights into the influence of water matrix components on treatment efficacy. Natural organic-matter, dissolved inorganic ions (particularly chloride, sulphate, and bicarbonate), and pH have all been shown to affect PFAS degradation kinetics and energy requirements. For instance, the presence of chloride ions can lead to the formation of reactive chlorine species that may either enhance PFAS oxidation or compete with PFAS for oxidant species depending on the specific conditions.[95]

Several studies have investigated pre-treatment strategies to concentrate PFAS from dilute environmental samples prior to electrochemical oxidation, which offers multiple benefits: it reduces the total volume requiring treatment (and thus the energy consumption), increases solution conductivity (improving current efficiency), and alleviates mass transfer limitations by increasing the PFAS concentration at the electrode surface.Foam fractionation (FF) has emerged as a particularly promising pre-concentration method that exploits the surfactant properties of PFAS by adsorbing them onto rising air bubbles, allowing PFAS to be harvested as a concentrated foam that can be subjected to electrochemical oxidation.[96] This pilot-scale study combining foam fractionation with electrochemical oxidation has achieved mean total PFAS degradation of 50%, with long-chain PFAS degrading up to 86%. Other pre-concentration methods that have been coupled with EO include ion exchange resins, membrane processes such as nanofiltration and reverse osmosis, and AC adsorption, each with distinct advantages depending on the water matrix characteristics and PFAS

composition.[97] However, challenges remain in optimising the integration of pre-concentration with EO systems, particularly regarding the handling of concentrated PFAS streams and the potential for electrode fouling when treating highly loaded solutions. Further research is needed to develop cost-effective, energy-efficient EO systems that can achieve regulatory compliance for PFAS in diverse water matrices at scales relevant to municipal and industrial water treatment.

2.3.3. Supercritical Water Oxidation

Once water is heated above 374 °C and 22.1 MPa, it enters a supercritical state that exhibits unique physicochemical properties including increased organic solubility and accelerated oxidative reaction kinetics. Supercritical water oxidation (SCWO) exploits these conditions to enable the destruction of highly recalcitrant compounds and has been shown to effectively degrade halogenated organics including PFAS.[98] Li *et al.*[99] developed a continuous-flow SCWO reactor operating between 410 and 650 °C and demonstrated complete destruction of PFOS and PFOA under controlled conditions. For PFOS, degradation is initiated by oxidative cleavage of the C–S bond followed by decarboxylation and sequential $–CF_2$ elimination steps, ultimately achieving complete oxidation. However, despite its demonstrated effectiveness, SCWO has primarily been investigated using PFAS concentrations several orders of magnitude higher than those typically encountered in drinking water or wastewater treatment systems, often in the micromolar range. In addition, the extreme temperature and pressure requirements present significant engineering, energy and materials challenges that currently limit the applicability of SCWO to the treatment of concentrated PFAS waste streams rather than bulk water treatment. As such, SCWO is more realistically positioned as a downstream destruction technology for PFAS-rich residuals generated by separation processes rather than as a primary water treatment solution. The

proposed degradation pathway for PFOS under SCWO conditions is presented in Figure 2.1.

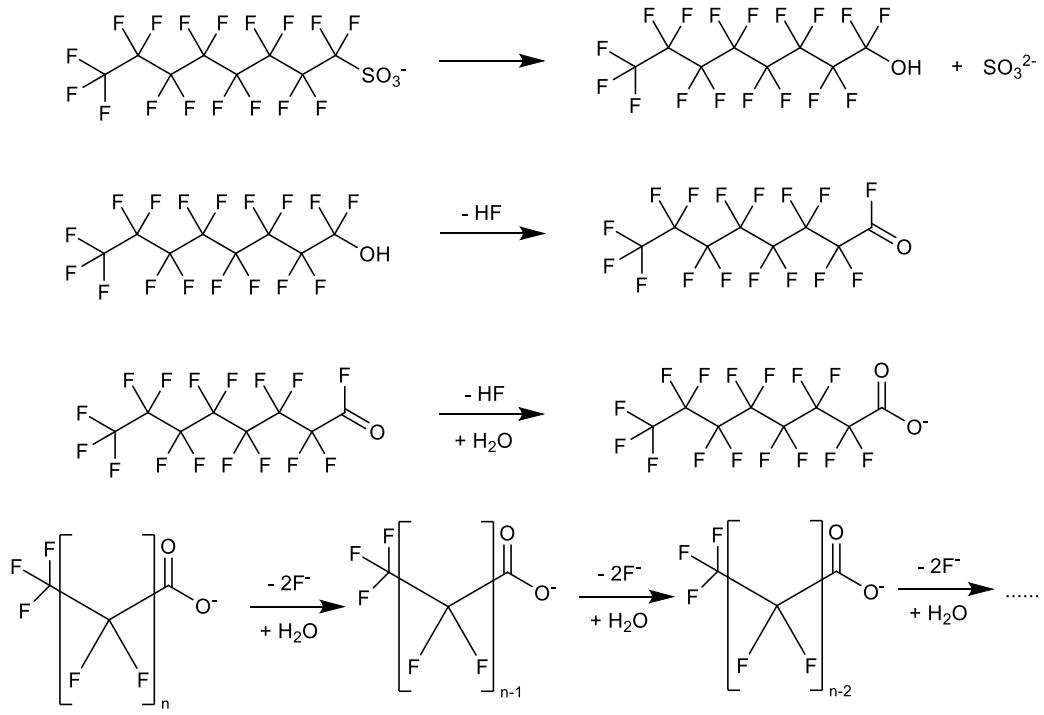


Figure 2.1. The proposed degradation pathway for PFOS using SCWO.

2.3.4. Plasma Treatment

Plasma-based water treatment is a technique that uses electricity to generate an assortment of reactive species (O_2, H_2O_2, OH, O, $H^{\bullet}$, $HO_2^{\bullet}$ H_2, $O_2^{\bullet-}$ and aqueous electrons), which is called plasma.[100] Two electrodes (one high voltage and one grounded within the wastewater stream) enable the formation of plasma via electrical discharge. Argon gas is pumped through the contaminated water which produces bubbles which create a layer of foam on the liquid surface. PFAS has a tendency to concentrate in the foam due to its surfactant-like nature and will increase the contact between the liquid and plasma, effectively exposing the PFAS to the reactive species in the plasma, which will degrade the PFAS.[100] Plasma treatment is unique in that it

can produce reductive species like hydrogen radicals and aqueous electrons without any addition of external reagents. Although some studies have reported near 100% removal of long chain PFAS, some PFAS is converted to the short-chain compound PFBA, which does not readily accumulate at the foam-liquid interface, which means the efficiency of degradation is lower. Nau-Hix *et al.*[101] worked around this issue by adding a cationic surfactant, which enable larger quantities of PFBA to enter the foam for subsequent destruction.

2.3.5. Sonochemical Degradation

Ultrasound is the term given to sound waves which exhibit frequencies which are higher than those that the human ear can detect (>16 kHz) and has shown promise for application in Sonochemical treatment.[102] The ultrasound waves propagate in the contaminated water and cause two processes to occur: compression and rarefaction. The compression of the liquid causes the molecules within to bunch together whilst rarefaction involves negative pressure which pulls the molecules apart. The negative pressure can be so vast that microbubbles are formed, and after successive cycles of rarefaction, they grow to an unstable diameter, which causes them to collapse (cavitation). Cavitation can generate pressures hundreds of times greater than ambient pressure, where vapour pressures (up to 10,000 °C) and bubble interface temperatures can reach 1225 °C.[103] These high temperatures and pressures meet the required conditions to destroy PFAS molecules via pyrolysis and radical oxidation.

Fuller *et al.*[104] demonstrated the use of Sonochemical degradation of the concentrated PFAS in spent brine and still-bottoms of anion exchange resins. Significant mineralisation of the PFOA and PFOS enabled the formation of inorganic fluoride, which is the first report of sonochemical PFAS degradation of ion exchange

regeneration wastes, potentially paving the way for the use of the technological combination in a PFAS capture and destruction treatment train. Unfortunately, the presence of total organic carbon (TOC) can inhibit degradation efficiency, but the addition of chloride, bromide and cationic surfactants can remedy this by stimulation oxidative processes.

2.3.6. Photodegradation

Several treatment techniques utilise ultra-violet radiation to promote PFAS degradation. Photodegradation aims to enable the PFAS to adsorb the photons with a wavelength of <320 nm, which will create a reaction pathway through the formation of electronically excited species and subsequently cause elements of the PFAS to dissociate (photolysis). There are methods of degrading PFAS with photolysis: direct photolysis and indirect photolysis. Direct photolysis ensures photons are absorbed directly by the PFAS molecules, but without the use of a photocatalyst or oxidant, the water is cleaved into hydrogen and hydroxyl radicals. Indirect photolysis uses a combination of UV and a chemical compound, the latter absorbing the UV to form a reactive intermediate, which can then go on to react with the PFAS molecules. Some examples of indirect photolysis are UV/hydrogen peroxide, UV/Ozone and Photo-Fenton. In either case, the cleaved C-F bond will generate F^- ions in water, which can then react with aqueous Ca^{2+} ions, forming the inorganic salt CaF_2, which is environmentally safe. Jing *et al.*[105] demonstrated catalyst-free photolysis of PFOA, achieving 61.7% degradation to short-chain PFCAs and fluoride ions. More recently, Xin *et al.* utilised direct photolysis on 19 different PFAS and found that using far-UVC 222 nm enabled >80% decay of some parent compounds and up to 31% defluorination in 4 h.[106]

Indirect photolysis uses photocatalysts or oxidants/chemical mediators such as hydrogen peroxide, ozone and persulfate. Persulfate induced oxidation shows the most promise for PFAS decomposition as UV irradiation of the persulphate ion ($S_2O_8^{2-}$) gives two sulphate radicals ($SO_4^{\bullet-}$) which can go on to attack the PFAS. Hori *et al.* employed persulphate/UV treatment for PFOA photochemical dissociation and achieved 100% mineralisation within 4 h using 245 nm UV light.[107] Heterogeneous catalysts such as semiconductors and nano-composite based materials can also be used for PFAS degradation. Nano TiO_2 and modified TiO_2 have been used in titanate nanotubes (TNT), which work as photocatalysts when irradiated with UV.[108] Up to 85% of PFOA was removed at the lowest pH tested, enabling the formation of TNT-PFOA complexes. In both cases of photolysis, long-chain PFAS are degraded into short-chain PFAS, but the presence of the latter still poses a threat to human health.

2.3.7. Biological Degradation

Biological degradation utilises the metabolism of microorganisms to degrade PFAS. Microbes and their enzymes can transform and/or defluorinate organic compounds using their metabolic processes, using the substrates for energy. Microorganisms that use recalcitrant chemicals for sustenance are rare, but some can degrade PFAS via co-metabolism where other substrates are available for growth.[109] Polyfluoroalkyl substances are more easily biodegraded than perfluoroalkyl substances, as the non-fluorinated sites provide a point of weakness for the microorganisms to attack. Huang *et al.* studied the autotroph *Acidimicrobium* sp. A6, which is capable of degrading greater than 60% of PFOS and PFOA over a period of 100 days, leaving fluoride in WWTP sludge.[110] The reductive defluorination of PFOA/PFOS requires great quantities of Fe (III), which is used as an electron acceptor. This led to a further study where the reaction was conducted in a microbial electrolysis cell where the electrodes

act as electron acceptors instead, enabling a 77% reduction in PFOA.[111] There is a long way to go before biological degradation becomes commercially viable since there are so few known microorganisms capable of degrading PFAS, and there is a paucity of knowledge of known PFAS degrading enzymes, as well as their metabolic pathways. Understanding which PFAS are most easily biodegraded by which enzymes could help guide the industry in which PFAS would be most safe to use. Additionally, bioremediation experiments have been conducted under prime laboratory conditions with tailored nutrients, co-factors and co-substrates; this environment is very different from the conditions present at a WWTP or contaminated site. Moreover, most research has focused on legacy PFAS, such as PFOA and PFOS. These PFAS are banned in the UK and many other countries (although they are still present in the environment), and new Gen X and short-chain PFAS are taking their place in industrial processes, with some new types being more resistant to biodegradation than their C8 predecessors.[112]

2.4. Adsorption Mechanisms

PFAS exhibit both hydrophobic and hydrophilic properties. In water, most PFAS have a net negative charge attributed to the excess charges of the oxygen-containing functional head group (-COOH or -SOOH) as well as the electronegative fluorine atoms populating the carbon chain/tail. It is the head groups that contribute to the hydrophilicity and electronegativity the most, whilst the C-F chain is the greatest contributor to hydrophobicity.[113] Most PFAS have low pKa values, meaning they will exist as anionic species when in most wastewater. Some PFAS with higher pK_a values may have a neutral charge in wastewater with a much lower pH.[114] These properties will influence the potential adsorptive mechanisms that can take place.

2.4.1. Physical Adsorption

Electrostatic Interaction

PFAS usually exist as anionic species in water that is being treated to be potable, as the WWTP needs to maintain the pH between 6 – 8 to optimise the performance of the coagulation and flocculation stages of the treatment process.[115] When an adsorbent is deployed in the water with a net positive charge, electrostatic attraction will be between the anionic PFAS head group and the positive surface functional groups. pH will significantly influence the strength of the attractive interaction by changing the adsorbent surface charge, which will indirectly alter the adsorption capacity of the adsorbent. The most common functional groups present upon the surface of the adsorbent are phenols, carboxylic acids, alcohols and amines; all these groups can interact with PFAS electrostatically and are capable of being protonated under low pH conditions, in turn increasing the rate of PFAS uptake. As solution pH rises, the surface functional groups can become deprotonated, leading to a lower net positive surface charge and, therefore, weaker attraction between adsorbent and adsorbate (potentially even repulsion if pH is high enough to enable the formation of negative surface functional groups). One research group reported that adsorbed PFAS on kaolinite clay produced a negative charge, effectively 'shielding' the adsorbent from PFAS in the bulk solution and lowering the adsorption capacity.[116]

Upon the addition of divalent cations, such as Mg^{2+} and Ca^{2+}, the adsorption capacities can be improved. This is because the metal cations can induce a cation-bridging effect with the phenol and carboxylic acid surface functional groups, which will make the net surface charge more positive and enable PFAS molecules to adsorb more easily.[117] In contrast, it has been reported that increasing the ionic strength of the bulk solution can cause electrical double layer compression of the adsorbents, which can cause a slight inhibition of PFAS adsorption.[118]

Hydrophobic Interaction

Long-chain, non-polar molecules, like some PFAS, are hydrophobic and will tend to attract molecules of a similar nature. Polar molecules tend to be repelled by hydrophobic molecules, whereas the non-polar chain of PFAS can interact with the hydrophobic surfaces of adsorbents, like AC. In industry, it is favourable to have an AC that has a net positive charge in water to take advantage of the electrostatic attraction between the PFAS anions and the positively charged functional groups. However, it is possible to use a negatively charged AC for PFAS adsorption as the hydrophobic interaction has a greater influence on adsorption than the electrostatic repulsion.[119, 120] Long-chain PFAS, such as PFOA and PFOS, can aggregate and form multilayer structures (micelles and hemi-micelles) if the critical micelle concentration is exceeded; this can potentially enhance PFAS adsorption. Additionally, as long-chain PFAS begin to gather on the adsorbent surfaces, multilayer structures may form as the concentration at the surface is far greater than that of the bulk solution.[121, 122] It has been reported that the modelled adsorption capacities of some adsorbents have been lower than the experimental values, suggesting multilayer structure formation on the surfaces.[123] For short-chain PFAS, electrostatic interaction appears to be the dominant adsorptive mechanism due to the molecules being less hydrophobic.[124]

2.4.2. Chemical Adsorption

Anion Exchange Mechanisms

AERs comprise resin beads made from neutral co-polymers that contain positively charged exchange sites. The AER also includes a neutral hydrophobic backbone and divinylbenzene crosslinks.[29] The carbon-fluorine tail of a PFAS molecule will adsorb

to the backbone/crosslinks of the AER via hydrophobic interactions, and then the negatively charged functional group of the PFAS (-COO^- or -SO_3^-) will be attracted to the positively charged ion exchange site. In the process, negatively charged counter ions such as OH^-, Cl^- and HCO_3^- are exchanged and released into the water.

2.5. Preparation of Activated Carbon

2.5.1. Granulation

The biomass feedstock precursor to GAC must undergo a granulation process before it is carbonised. The biomass is reduced to fine particles, which are subsequently squeezed in a press at high pressures, producing high density granules. The granulation process improves the structure and mechanical strength increasing the precursor feedstock's density. The granules require harsher conditions for activation due to these enhanced properties. The high pressures used in the granulation process produce heat from the friction of the molecules, which can then go on to soften the lignin, resulting in resin formation that can act as a binder on the surface of each granule.[125] Biomass with a lignin content of >20% (dry basis) can be converted into granules without a binder at pressures >150 MPa. The ideal moisture content for biomass should be in the range of 10 – 20% for optimal conditions for hydrogen bond formation; too low and the granules disintegrate, too high and the strength and durability are negatively impacted.

For low density biomass, addition of a binder is required to enable the powdered particles to form granules which are subsequently carbonised. Binders, like coal tar pitch, molasses and citric acid, can greatly improve the strength, porous structure and longevity by filling void spaces and forming bridges between particles that strengthen upon drying. Organic binders can produce more numerous meso- and macropores in

the GAC during the activation process due to calcination at high temperatures. Inorganic binders in GAC, such as bentonite and silicate, can cause corrosion, emissions and deposit formations.[126]

2.5.2. Carbonisation/Pyrolysis

Carbonisation or pyrolysis are the terms used to describe the thermal decomposition of carbonaceous materials when heated in an inert atmosphere. The carbonisation process involves condensation, dehydrogenation, hydrogen transfer and isomerisation reaction, engendering high fixed carbon content in the resulting char. Pyrolysis processes can be classified into three categories: (i) slow pyrolysis (slow heating rates for extended periods of time <300 °C), (ii) moderate pyrolysis (temperatures of 300 – 500 °C), and (iii) fast pyrolysis (high heating rate with temperatures >500 °C). The resulting structure/physicochemical properties of the char are heavily influenced by the chosen pyrolysis method, with higher temperatures causing a greater release of volatiles, thus increasing total pore volume.[127, 128] Generally, as the pyrolysis temperature increases, the char yield decreases due to secondary cracking of the char residues, although this produces a higher quality precursor for subsequent activation.[129] There is a myriad of feedstocks available for carbonisation, with the most popular being highly carbonaceous in nature. Some examples include: wood, lignite, anthracite, petroleum residues, bituminous coal, peat and coconut shell.

Another method of biochar production is through hydrothermal carbonisation, which is a thermo-chemical conversion technique. Biomass is heated with water in a pressure vessel at 180 - 250 °C/1 MPa, which causes the fractionation of the feedstock. The conditions are prime for efficient hydrolysis and dehydration of the biomass, with the

product presenting a high concentration of oxygen-containing functional groups. Often, the biochar (hydrochar) will be chemically activated following hydrothermal carbonisation.[130] The formation of hydrochar is outlined in Figure 2.2.

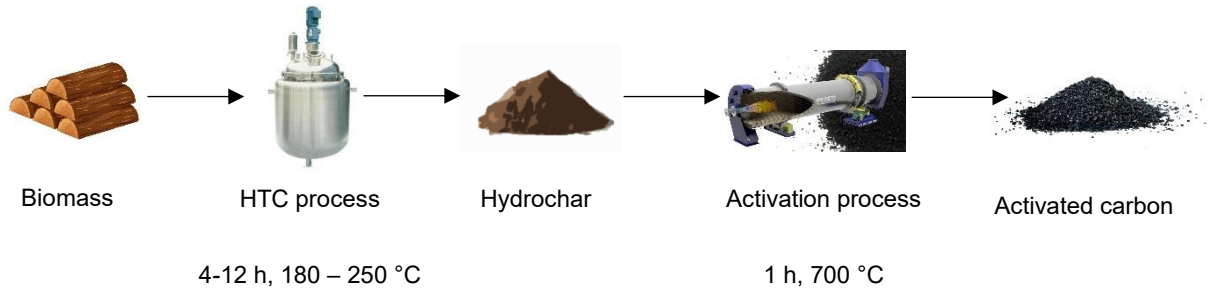


Figure 2.2. Overview of the hydrothermal carbonisation process.

2.5.3. Physical Activation

Following carbonisation of the carbonaceous precursor, the char is then heated at temperatures in the range of 700 – 1000 °C in the presence of an activating agent; either CO_2 or steam. CO_2 is the favoured physical activating agent due to its lower reactivity at higher temperatures, enabling greater control over the process. Additionally, CO_2 activation favours the formation of micropores, which is advantageous in that the micropore volumes are much larger than those produced in char that is activated with steam. Steam favours micropore widening, which engenders the formation of more meso- and macropores.[131] For both CO_2 and steam, it is their respective partial pressure and activation conditions that will determine the development and degree of microporosity in the AC product. Physical activation can also be conducted in a single-step approach, where carbonisation and activation occur simultaneously by heating at 600 – 800 °C in an inert atmosphere and then changing the gas to the activating agent. The single-step process means there is no cooling period between carbonisation and activation, so less energy is required, resulting in

fewer emissions. Some examples of ACs prepared via physical activation are presented in Table 2.5.

2.5.4. Chemical Activation

The precursor material is first impregnated with an activating agent, typically these are H_2SO_4, $ZnCl_2$, H_3PO_4, KOH and NaOH, which is then carbonised at moderate temperatures (~ 550 °C).[132] The resulting AC is washed to eliminate traces of the activator so it can be used for successive chemical activation cycles. Chemical activation requires lower temperatures than physical activation due to the reactive impregnated activating agent, which also enables greater development of the pore structure. However, physical activation is more commonly practised due to the expense and pollution effects associated with the chemical activation agents, as well as the corrosive nature of the chemical activating agents which can damage equipment.

2.5.5. Physicochemical Activation

The physicochemical activation of carbon is a combination of both physical and chemical activation processes, which can be categorised into two separate methods: (i) chemical treatment preceding carbonisation (pre-carbonisation), and (ii) chemical treatment following carbonisation (post-carbonisation). The first stage of pre-carbonisation is very similar to chemical activation in that the precursor material is impregnated with chemical activation agents and is subsequently thermally treated with an oxidising gas (CO_2 or steam), much like the physical activation stage. It has been reported that higher specific surface areas are observed in ACs that have been physicochemically activated using the pre-carbonisation method due to the absence of the dehydrating agent in the thermal activation step, which can cause pore blocking

in post-carbonised carbons.[133] Physicochemical activation is utilised when the chemical activation agent cannot be easily removed in the later acid/base washing steps; remaining chemicals can block pores, which lowers adsorption capacities.[134]

Table 2.5. Textural properties of ACs prepared by physical, chemical, physicochemical and microwave-assisted activation.

Activation method	Type of activated carbon	S_{BET} $m^2\ g^{-1}$	Pore size distribution			D (nm)	Ref
			V_{micro} ($cm^3\ g^{-1}$)	V_{meso} ($cm^3\ g^{-1}$)	V_{Total} ($cm^3\ g^{-1}$)		
Physical	Barley straw	789	0.32	-	0.35	1.78	135
	Date stones	635	0.71	-	-	-	136
	Macadamia	844	0.39	0.09	0.49	2.30	137
	Coal pitch	2487	0.86	-	-	-	138
Chemical	$ZnCl_2$ spruce	1000	0.50	0.08	0.58	-	132
	H_3PO_4 spruce	700	0.45	0.03	0.48	-	132
	$ZnCl_2$ fir	1071	0.50	0.05	0.56	-	139
	$ZnCl_2$ Macadamia	1718	0.72	-	-	-	140
Physicochemical	NaOH Borassus palm	795	-	-	0.48	2.73	141
	NaOH Physic nut	1873	-	-	1.31	2.80	142
	KOH pine	2216	0.90	-	1.11	-	143
Microwave-assisted	Peanut shell	370	-	-	0.21	2.60	144
	Bamboo	1432	0.50	0.19	0.67	-	145
	Coconut shell	2288	1.01	0.29	0.53	-	146
	Palm stone	194.3	89.5	-	0.14	-	147

2.5.6. Microwave-Assisted Activation

In recent years, microwave-assisted activation has become a viable alternative to conventional activation techniques. Microwave irradiation is capable of molecular level heating in the precursor, allowing for fast, selective, volumetric and uniform heating. The carbonisation and activation steps can be achieved simultaneously in the same reactor, or the process can be combined with other procedures, such as carbonisation by microwave irradiation with subsequent physical activation. The physical properties of AC are influenced by the type of feedstock, pyrolysis temperature, radiation power, additives and holding time; all of these parameters can be easily controlled with microwave assisted activation, which helps in process optimisation.[148] It has been reported that some microwave-assisted ACs have

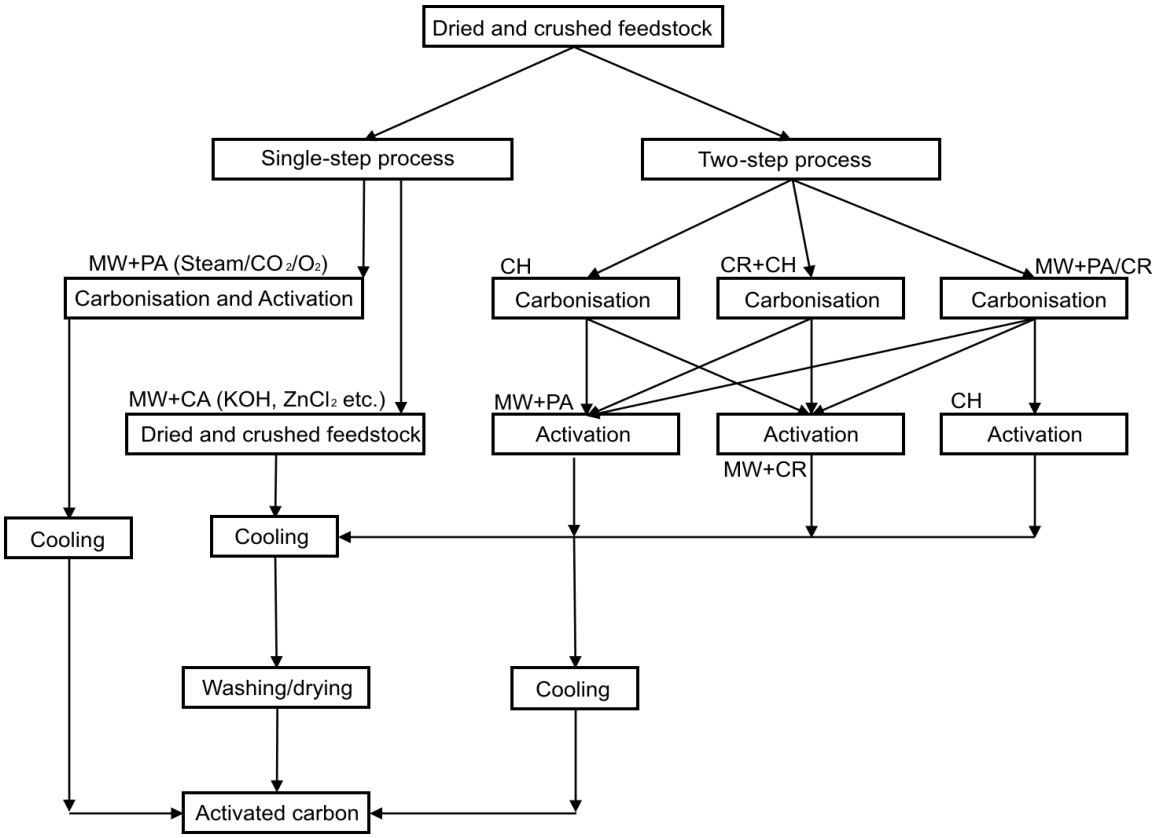


Figure 2.3. Microwave activation process flow diagram (CH-conventional heating, CR-chemical reagents, MW-microwave irradiation and PA-physical activation).

reached specific surface areas of 2500 – 3000 m^2 g^{-1}. The microwave activation process is outlined in **Error! Reference source not found.** (adapted from Ao *et al*.[148]).

2.6. Regeneration of Activated Carbon

Historically, spent/exhausted AC from water treatment processes was disposed of via landfill or incineration, but these destinations are not environmentally friendly and bring the possibility of re-releasing the adsorbed pollutant back into the environment. Typically, PAC is not regenerated due to heavy losses in carbon associated with the few regenerative techniques that are suitable, but GAC and pelletised AC can be regenerated via several methods. During regeneration or reactivation, thermal/chemical processes desorb the pollutants, leaving a functional adsorbent once again. Several conventional and advanced reactivation techniques are described in the following sections.

2.6.1. Thermal Regeneration

Thermal regeneration consists of heating spent GAC in a multi-hearth furnace or rotary kiln, where the adsorbed pollutants are volatilised and destroyed, and the AC is restored to a reusable quality.[88] The reactivation conditions and feed throughput specifications are tailored to the physical properties of the loaded adsorbate within the spent AC. Typical temperatures for thermal reactivation are between 700 – 900 ºC, and the process is carried out in a low oxygen atmosphere. Adsorbates, like PFAS, that are removed but not destroyed by the high temperatures are piped to an abatement system which contains a thermal oxidiser (afterburner), acid gas scrubber and a baghouse to eliminate the emission of particulate matter. Interestingly, there seems to be a dichotomy between the structure of the PFAS and the effectiveness of its removal versus the reactivation of the spent AC. Long-chain PFAS seem to be

more easily adsorbed onto AC than their short-chain analogues, but it is the short chain PFAS that are more favourably removed during thermal regeneration.[149, 150] Likewise, PFAS with the same carbon chain length but with different terminal functional groups behave similarly. PFSAs are more easily adsorbed, but it is the PFCAs that are more easily removed during thermal regeneration.[30, 151] It was found that PFCAs undergo considerable decomposition at temperatures as low as 175 ºC whilst PFSAs required temperatures >475 ºC to decompose. Decomposition temperatures are higher for PFSAs due to the presence of two additional C-F bonds, and the sulfonic acid group makes the molecule more hydrophobic, so there is greater partitioning on the AC surface. Due to the increased regulation of long-chain PFAS, specifically PFOA and PFOS, short-chain PFAS have seen more industrial use, which means that water treatment companies will be adsorbing a greater number of short-chain PFAS, which will be easier to remove via thermal regeneration.

Baghirzade *et al.*[88] reported a loss of 1 - 80% of the BET surface area of GAC upon regeneration of 15 coal-derived ACs, with losses decreasing with increased temperature, with the 207A Waterlink AC's BET surface area decreasing from 850 to 200 m^2 g^{-1} after just one regeneration cycle. Regeneration yield on an adsorption capacity basis has been reported to be as high as 132.8%, which is attributed to pores becoming unblocked and the formation of brand new pores, as reported by Wibowo *et al*.[152]

2.6.2. Chemical Regeneration

Chemical regeneration uses organic solvents or inorganic chemicals to restore the AC. Organic solvents such as acetone, ethanol, methanol, acetic acid and formic acid have been used for the chemical regeneration process, and inorganic chemicals like sodium

hydroxide have also been used.[59, 153, 154] The chemical reagents are used to desorb or decompose bound adsorbates. The efficacy of chemical regeneration depends on the interaction between the chemical reagent and the adsorbate; for PFAS, methanol is an effective chemical for desorption. Unlike thermal regeneration, chemical regeneration typically causes no carbon attrition whilst also restoring adsorption capacities.[155] After contaminant removal, the chemical reagent itself must be removed from the AC to produce the regenerated product, which is costly and adds an extra step to the regeneration process compared to physical regeneration. Larasati *et al.*[156] summarised that the use of more than one type of chemical regenerant can actually increase regeneration efficiencies, with mixtures of methanol/ethyl acetate and sodium hydroxide/methanol engendering AC regeneration efficiencies of 100% and 97%, respectively.

2.6.3. Steam Regeneration

For decades, steam regeneration has been used for the reactivation of AC and has been proven to be an economical and effective technique.[157, 158] The steam swiftly heats the AC bed enabling rapid desorption of contaminants which are removed by the steam itself. During steam regeneration, the AC is thermally decomposed and then subsequently oxidised by the steam. The adsorbate is then vaporised, thermally decomposed and oxidatively decomposed by the steam. Ying *et al.* developed a highly efficient superheated steam regenerative method which used 500 °C steam to re-produce AC with a much cleaner surface than AC regenerated with chemical activation methods (the NaOH used in chemical regeneration is corrosive and can cause the AC surface to collapse)[159]. Additionally, Ledesma *et al.* employed steam regeneration using 200 °C steam and an oxygen partial pressure of 12 bar to reactivated p-nitrophenol saturated AC which produced a regeneration efficiency of 87%.[160]

2.6.4. Microwave Regeneration

Since carbonaceous materials can absorb microwave radiation well, the technique is suitable for regeneration spent AC. Identical spent carbons have been thermally regenerated and heated by microwaves, and it has been found that the rapid heating from microwave radiation promoted accelerated regeneration compared to that achieved via conventional heating.[161, 162] Ania *et al.*[163] reported that microwave heating appears to preserve the integrity of the porous structure compared to that resulting from thermal regeneration, and, in one case, an increase in the specific surface area of an AC was observed, with the S_{BET} increasing from 257 to 386 m^2/g. Gagliano *et al.*[164] reported regeneration efficiencies of >90% for GAC laden with PFOA and PFOS, and the GAC was still effective even after a fifth microwave heating cycle.

2.6.5. Electrochemical Regeneration

AC regeneration by electrochemical oxidation has been studied and has shown promising results, reaching regeneration efficiencies as high as 95%.[165] The technique involves the cracking of adsorbed contaminants whilst maintaining the structural integrity of the AC. Electrochemical regeneration uses mechanisms like electro-sorption, electro-reduction and electro-oxidation to restore the spent AC[166-168]. With no chemical addition or harsh temperature requirement, an applied electric field removes the polar contaminants from the AC and either oxidises or reduces them upon electrodes. Recently, a proof-of-concept study conducted by Ersan *et al.*[169] looking into the electrochemical regeneration of PFAS-laden AC demonstrated that ~ 60% of the initial capacity of the spent AC could be restored after the first regenerative cycle (S_{BET} reduced to 678 $m^2\ g^{-1}$ from 1039 $m^2\ g^{-1}$) and three successive cycles provided similar results.

2.6.6. Wet Oxidation Regeneration

Wet oxidation involves the suspension of the spent AC in an aqueous solution which is subsequently heated to between 100 – 200 ºC, and 10-50 bar of oxygen is pumped through the mixture.[170] The moderate conditions enable the desorption of bound contaminants, which are then replaced by water, and the gaseous oxygen then oxidises the contaminants in the bulk solution. Oxidation of the contaminants shifts the equilibrium to the right thus more contaminants are desorbed and oxidised. Wet oxidation generally causes a gradual decrease in adsorption capacity after successive regenerative cycles due to oxidation of the AC itself.[171] Additionally, wet oxidation is not used commercially for the regeneration of PFAS-laden ACs since the temperatures required to destroy PFAS (> 850 °C) are far greater than the operational temperatures of wet oxidation. The wet oxidation regenerative process is far more suitable for ACs used for treating dye contaminated water, since dye molecules do not usually contain C-F bonds and are therefore more easily degraded[170].

2.6.7. Bio-regeneration

Bio-regeneration utilises colonies of microbes to regenerate the adsorption capacity and surface area of spent carbon.[172] The technique can only be used when the adsorbate is both organic and easily desorbed. Bio-regeneration can be achieved by offline system mixing of AC and bacteria or it can be carried out during the course of biological treatments where biological AC is used. Offline bio-regeneration involves a closed batch system containing acclimated bacteria, dissolved oxygen and nutrients, where the contaminants can be desorbed from the spent AC and be biodegraded. Offline bio-regeneration is preferable to simultaneous bio-regeneration because the latter presents operational difficulties and limitations with providing sufficient dissolved

oxygen and nutrients. Ameh *et al.*[173] employed bio-regeneration on AC used for the remediation of hydrocarbon contaminated soil, where the surface area was largely unchanged (738 down to 730 $m^2 g^{-1}$). Thus far, bio-regeneration of spent PFAS-laden AC has not been reported, which is due to the extreme stability of PFAS, as it is already known that they are not broken down in the environment.

2.7. Characterisation of Activated Carbon

ACs are highly complex materials which cannot be characterised by structural formulae or chemical analysis. Each AC will have unique physical and chemical properties which are directly influenced by the type of feedstock, methods of pre-treatment and the temperatures used in the activation stage. Fortunately, several standard methods of characterisation exist to assist in deconvoluting the surface chemistry, surface area and surface morphology of ACs, thus enabling the assessment and comparison of new adsorbents.

2.7.1. Morphology

Analysis of the external surfaces of AC provides insight into the degree of porosity of the adsorbent's exterior. Typically, the outer pores are larger than the pores at the centre of the AC, with the outer pores normally being meso- or macropores, depending on the source material. The external pores play an important role in adsorption in that they facilitate the transportation of contaminants into the large network of micropores further inside the adsorbent. Scanning electron microscopy (SEM) is a reliable technique for accurate surface investigations. SEM can provide enormous magnifications and achieve excellent resolutions, reaching 2,000,000 x and 1.5 nm, respectively. The SEM version of electron microscopy utilises an electron beam to scan the surface of the AC, providing an electron micrograph at the micro and sub-

micro scale. The beam of electrons is produced by an electron gun/electron source at the top of the instrument (Figure 2.4). The beam follows a vertical downward path through the microscope which is held within a vacuum to avoid collisions with gaseous molecules. To focus the electron beam, it passes through a series of electromagnetic fields and lenses before striking the sample. Once the beam hits the sample, X-rays, back-scattered electrons and secondary electrons are ejected from the sample surface, which are all subsequently detected and provide different information which assist in the characterisation. Detection of the secondary electrons (SE) allow for the imaging of the morphology/topography, the backscattered electrons (BSE) enable the diversity of the surface elemental composition to be known and the X-ray detection allows for elemental composition to be known. The information content provided by SEM includes: the topography (surface features), composition (the elements and relative compositions the material is comprised of), morphology (the size and shape of the material surface) and the crystallographic information (the ordered arrangement of atoms within the material). Although SEM can only provide images of the external surface of AC, the information content is highly relevant for elucidating why some ACs perform better than others in PFAS removal. ACs with both high meso- and microporosity will be better at removing PFAS from wastewater than ACs with just low mesoporosity and high microporosity. It is proposed that PFAS bind in mesopores as well as the micropores, and the mesopores mitigate pore blocking of the micropores by natural organic matter (NOM).[19] The SEM images can assist in verifying the presence of mesopores on the external surface.

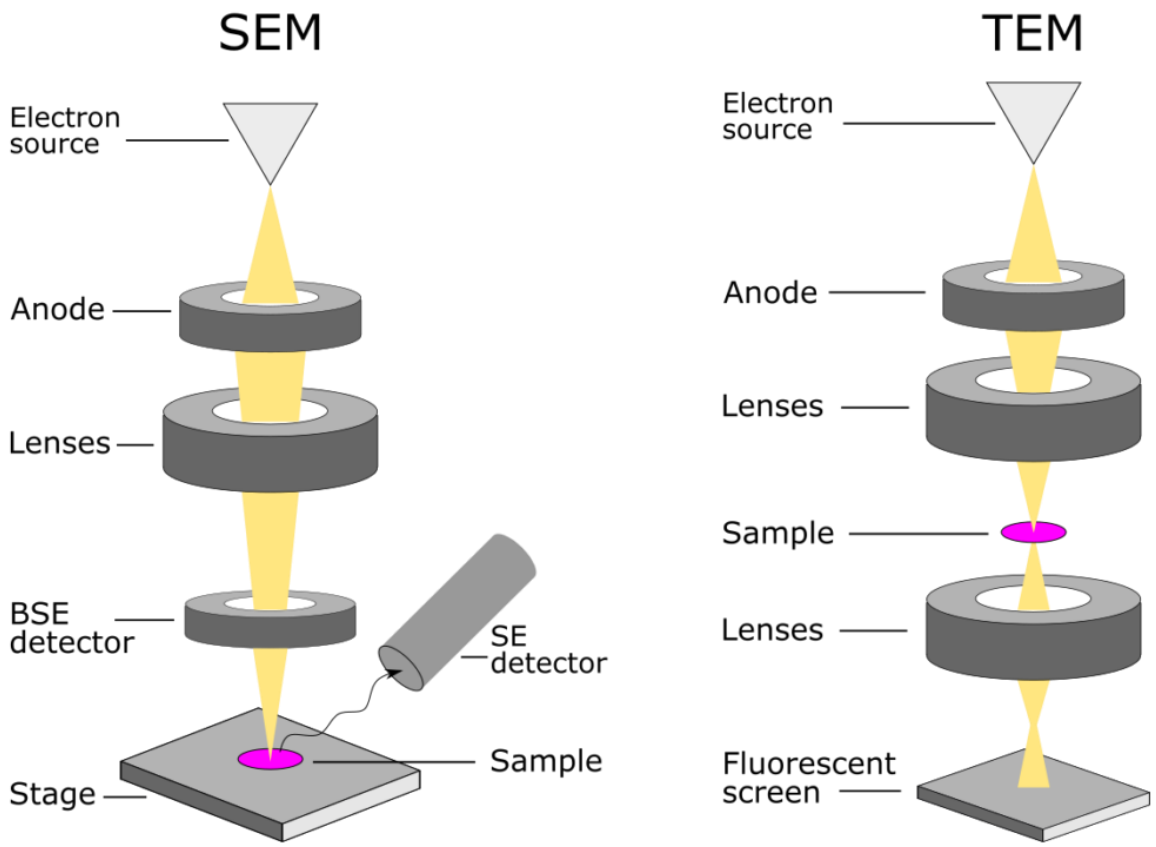


Figure 2.4. Schematic of scanning and transmission electron microscopes.

Transmission electron microscopy (TEM) is another powerful electron microscopy technique that can assist in probing the morphology of AC. TEM is different to SEM in that it uses transmitted electrons that pass through the sample to generate an image, which can give information on the inner structure and crystal structure. A TEM is comprised of three parts: (1) an electron source/electron gun that produces an electron beam and is linked with the condenser system which enables the focusing of the beam onto the sample, (2) an objective lens, adjustable specimen stage and intermediate/projector lenses which assist in focusing the beam of electrons onto the sample, and (3) the image recording system which converts the electron image into a visual image of the sample (Figure 2.4). There are two ways in which the electrons

interact with the sample: (1) elastic scattering (BSE are ejected) and (2) inelastic scattering (SE are created). BSEs emanate from the electron beam and are incidentally scattered by the specimen atoms, whereas SEs are directly produced by the specimen. A vacuum is maintained within the TEM to avoid electron collisions with air molecules. TEM can achieve much higher magnification than a light microscope because the wavelength of an electron is much smaller than the wavelength of a photon. TEM has a far greater spatial resolution than SEM, with recent developments in aberration corrected TEMs achieving resolutions of less than 50 pm. TEM analysis of AC is useful for verifying the disordered crystal structure, revealing the pore development after heat treatments and even imaging the atomic structure of AC.[174]

Chemical Composition

2.7.2. Energy Dispersive X-ray Analysis

Energy Dispersed X-ray (EDX) spectroscopy is an analytical technique that assists in clarifying the elemental composition of a substance based on the information provided by the X-ray emission induced by electron/X-ray irradiation.[175] The technique is viable due to the understanding that each individual element has a unique atomic structure, which will engender a unique set of peaks in the electro-magnetic spectrum. The incident beam of electrons/X-rays is focused on the sample and has the potential to excite an inner shell electron, which will eject it from the atom. A higher energy, outer shell electron will fill the vacant hole in the inner shell, and the energy difference between the two shells can be released as a detectable X-ray of a specific energy corresponding to the atom it was derived from. SEM-EDX can be a useful tool for qualitatively determining the C, O and S content of AC (Figure 2.5).[176]

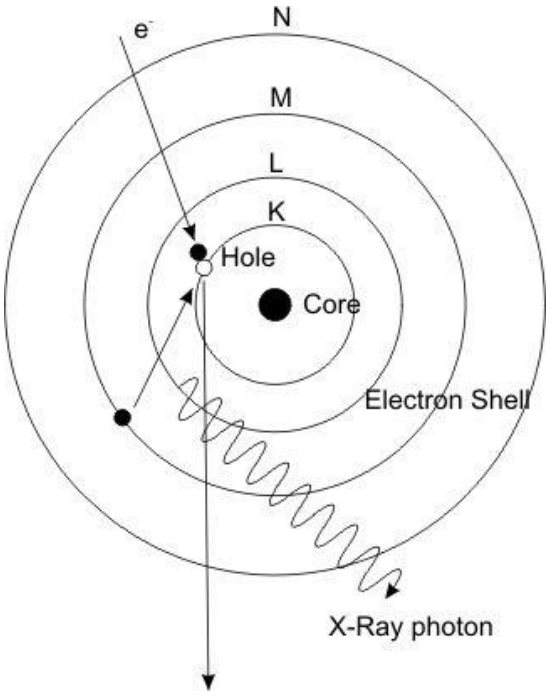


Figure 2.5. Illustration of the principle of EDX analysis.

2.7.3. Elemental Analysis

Elemental analysis (EA) or CHNS elemental analysis is a technique that can be used to determine the C, H, N and S content (weight percentage) of AC. The method involves the high temperature combustion of the sample within the column containing the oxidising-reducing catalytic bed, with the combustion products passing over a thermoconductivity detector, which are subsequently quantified. The information content provides insight into how different feedstocks and activation conditions can influence the chemical composition of ACs.[177]

2.7.4. X-ray Photoelectron Spectroscopy

X-ray photoelectron spectroscopy (XPS) is a quantitative surface sensitive technique which utilises the photoelectric effect to identify elements present in a sample and information on their chemical states.[178, 179] XPS is highly useful as it can also reveal what the surface elements are bonded to. X-ray irradiation of a sample causes the

ejection of photoelectrons from the surface. The kinetic energy and number of the photoelectrons are subsequently detected, and the binding energies are calculated to reveal the elemental composition/chemical states of the species upon the sample surface (Figure 2.7). AC surfaces have a high density of various oxygen-containing functional groups, and the determination of the relative concentration of each group is useful for understanding the adsorptive mechanisms involved in PFAS removal as well as how different activation conditions influence the chemical compositions of the AC surfaces.

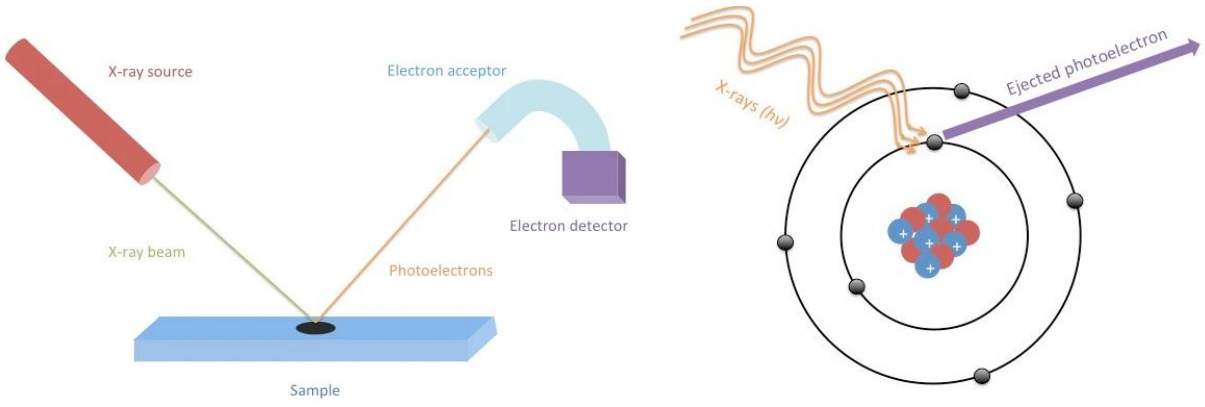


Figure 2.6. Schematic of an XPS system and the electron ejection process on which the technique is based around.

2.7.5. Boehm Titrations

The Boehm titration has been used as a method of quantitatively identifying acidic oxygen-containing functional groups on ACs since the 1960s.[180] The procedure works on the basis that bases of differing strengths can neutralise each oxygen functional group. NaOH is the strongest base used in the process, and it is assumed that it can neutralise all Brønsted acids, which are carboxylic acids, lactones and phenols.

Na_2CO_3 is used to neutralise carboxylic acids and lactonic groups, whilst $NaHCO_3$ is used to neutralise just the carboxylic acids. The difference in the base uptake can be used to calculate/quantify the types of oxygen-containing functional groups on the AC surface and is a complementary technique to other methods of revealing the surface chemistry, such as XPS.[181] The reaction schemes outline the neutralisation reactions that occur on the AC surface upon addition of each reaction base (Figure 2.7).

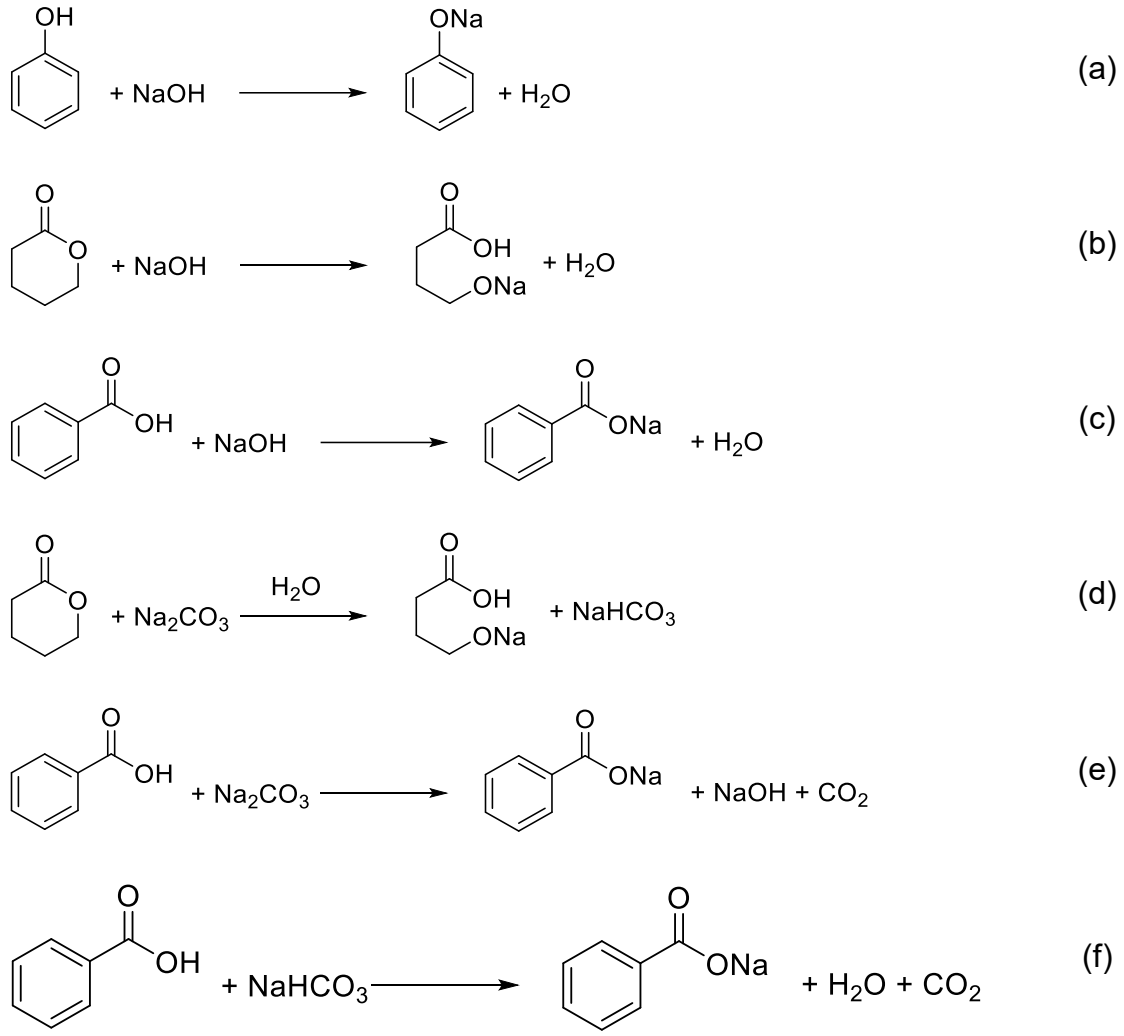


Figure 2.7. Neutralisation reactions that can take place during the Boehm titrations.

2.7.6. Infrared Spectroscopy

Diffuse Reflectance Infrared Fourier Transform Spectroscopy (DRIFTS) is an effective technique for the chemical analysis of the surfaces of powders and finely divided

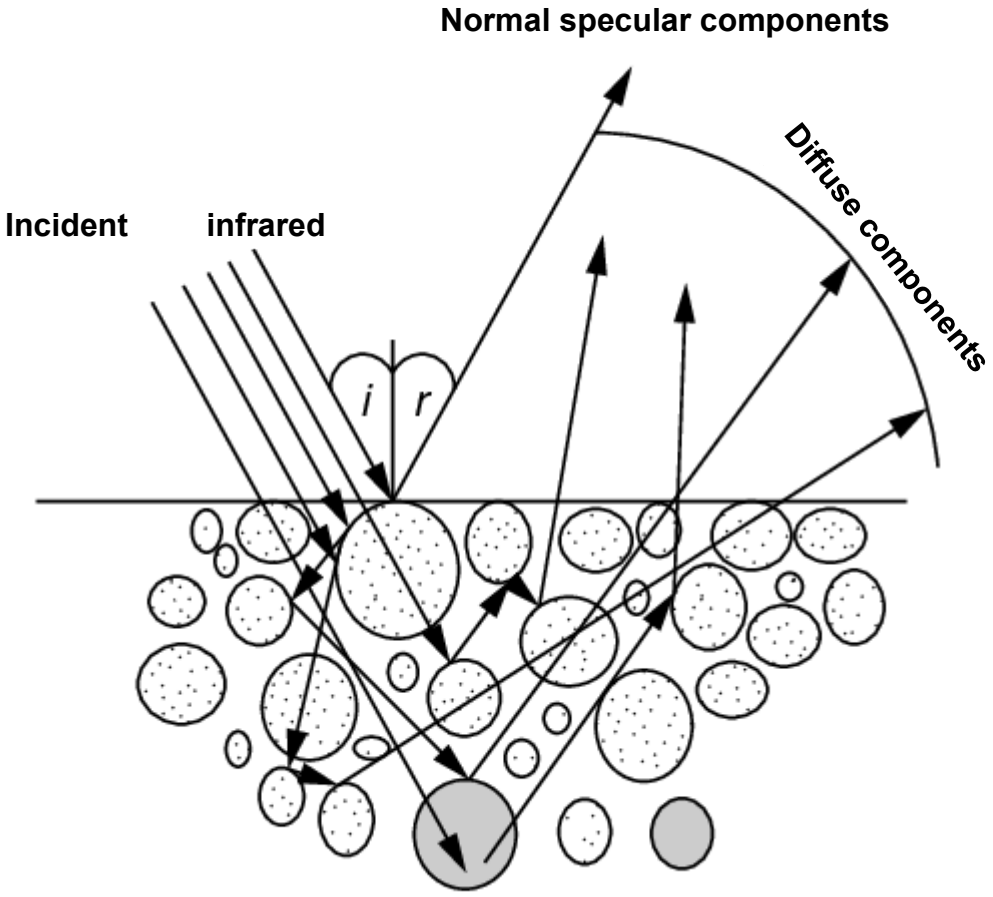


Figure 2.8. Mechanism between infrared waves and powder to generate IR spectrum.

materials like AC. The powdered sample is pressed onto a reflective surface, and infrared light is focused on the sample. The diffusely reflected light is then collected/reflected by a paraboloid, which focuses the beam onto a detector (Figure 2.9, adapted from Amaroli *et al.*[182]). DRIFTS is a qualitative technique which can confirm the presence of the oxygen-containing functional groups upon the surfaces of the AC.[183, 184]

2.7.7. Surface Area, Pore Volume and Pore Size Distribution

Brunauer-Emmett-Teller (BET) surface area analysis utilises controlled gas adsorption to generate a multi-point measurement of the ACs BET surface area (m^2/g).[185] An inert gas, such as CO_2 or N_2, is continuously pumped over the AC at 0 °C and – 196 °C, respectively, and the inert gas molecules adsorb to the surfaces via weak Van der Waals interactions (physisorption), thus forming a monolayer.

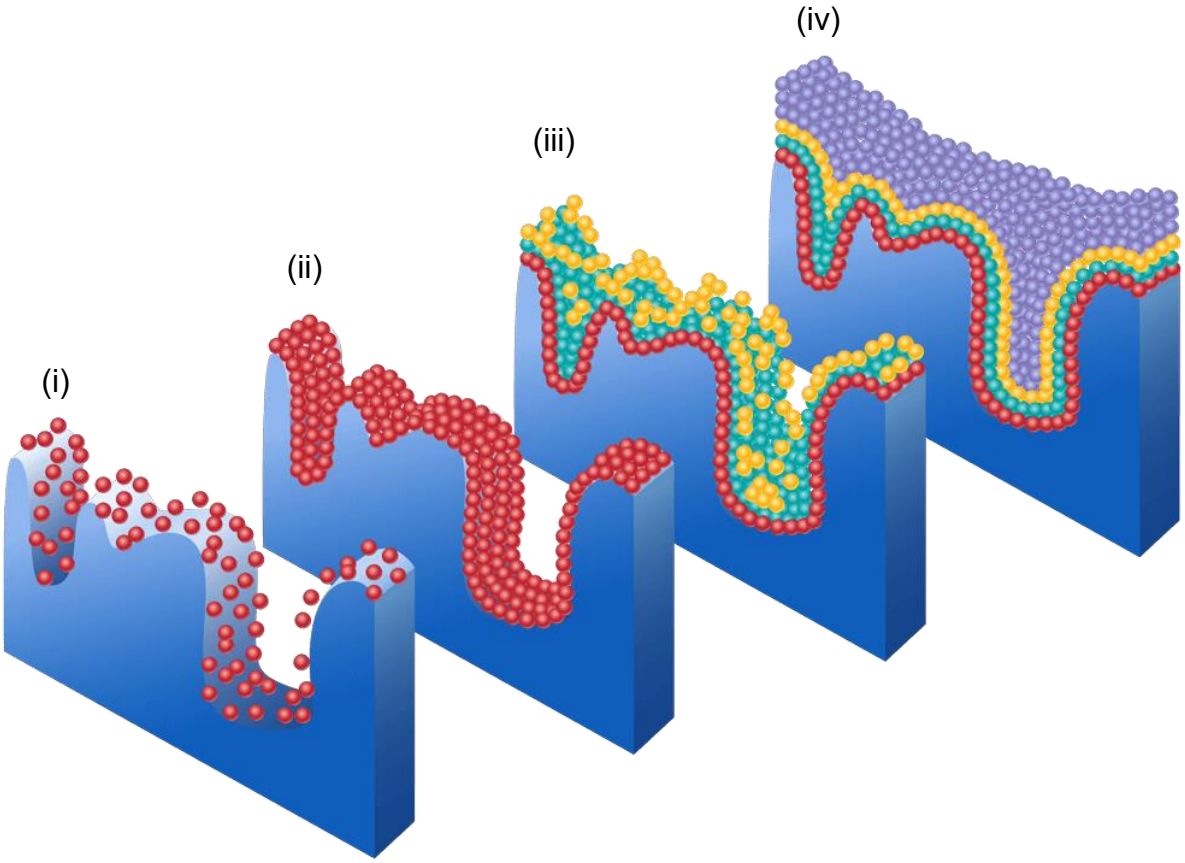


Figure 2.9. Diagram of how multilayer adsorption and pore filling occurs in porous materials (taken from the Micromeritics website).

The diagram in Figure 2.10 (taken from the Micromeritics website) depicts the four stages that occur during physisorption as the gas pressure is increased from i - iv: (i) adsorption occurs at isolated adsorption sites, (ii) a monolayer of gas molecules forms

over the surface of the adsorbent and micropore filling occurs (the surface area can be calculated), (iii) multilayer adsorption occurs, and (iv) total pore filling/condensation in the pores (pore size, volume and distribution can be calculated). The rate of adsorption and formation of the monolayer can be used to calculate the BET surface area of the AC using the BET equation (Equation (2.1)).

$$\frac{\frac{P}{P0}}{n\left(1-\frac{P}{P0}\right)} = \frac{1}{n_m C} + \frac{C-1}{n_m C}\left(\frac{P}{P_0}\right) \qquad (2.1)$$

Where at a specific relative pressure (P/P_0):

n is the quantity of adsorbate adsorbed to the sample, n_m is the monolayer capacity and C is the BET C-value. Once isotherm curves are obtained, expressed as pressure vs. quantity adsorbed, several different theories/models can be used to determine the pore size distribution of the AC, including Density Functional Theory (DFT), Non-linear Density Functional Theory (NLDFT), MP-Method, Horvath-Kawazoe calculations and Dubinin Plots.[186] Generally, N_2 is sufficient as the adsorptive for the analysis of adsorbents with only micropores and mesopores. However, N_2 has difficulty in entering adsorbents containing ultramicropores (< 0.7 nm) due to the large molecular size and slower diffusion kinetics.[187] A work around involves conducting a CO_2 isotherm (273 K) which favours the diffusion of CO_2 into the narrow pores. The CO_2 and N_2 adsorption data can be combined and more accurate surface area, pore volume and pore size distribution data may be obtained.

2.7.8. Adsorption Isotherm Models

Adsorption isotherm models assist in providing mechanistic information about adsorptive processes, which helps in evaluating the performance of adsorbents and adsorbent systems as the models provide information on maximum adsorption capacities. Isotherm refers to the relationship between the liquid-phase equilibrium adsorbate concentrations and the solid-phase equilibrium adsorption amount at a constant temperature. There are many types of adsorption isotherm models; the most relevant to this work are the Freundlich, Langmuir and BET isotherm models, which are discussed in the following sections:

2.7.9. Freundlich Isotherm

The Freundlich adsorption isotherm model represents the empirical relationship between the concentration of solute adsorbed onto the surface of a solid adsorbate and the concentration of solute in the liquid phase.[188] The Freundlich isotherm can also be applied to the quantity of gas adsorbed onto the surface of a solid surface and the pressure of the gas. The linear form and non-linear form of the Freundlich model is given by Equations (2.2) and (2.3), respectively:

$$q_e = K_F C_e^{\frac{1}{n}} \tag{2.2}$$

$$\ln(q_e) = \ln(K_F) + \frac{1}{n} ln(C_e) \tag{2.3}$$

Where q_e is the amount of adsorbed solute at equilibrium in mg/g, C_e is the amount of solute in the liquid phase at equilibrium, K_F is the Freundlich equilibrium constant, and n is an empirical constant which refers to intensity of sorption. When $0 < \frac{1}{n} < 1$,

adsorption is deemed favourable, when $\frac{1}{n}$ > 1, adsorption is deemed unfavourable and when $\frac{1}{n}$ = 1, adsorption is considered irreversible. The Freundlich model is classed as an empirical model with no physical meaning but can be used for multilayer adsorption on heterogeneous sites and assumes exponential decay in the energy distribution of adsorbed sites.

2.7.10. Langmuir Isotherm

The Langmuir isotherm model is used to explain adsorption when it is assumed that the adsorbate behaves like an ideal gas.[189] The model is empirical and suggests adsorption and desorption are reversible processes and was originally developed for gas-solid interactions. Four assumptions are considered when using the Langmuir model: (i) monolayer adsorption, (ii) constant adsorption energy, (iii) homogenous sites, and (iv) zero lateral interaction between adsorbed molecules. The linear and non-linear Langmuir isotherms are given in Equations (2.4) and (2.5), respectively:

$$q_e = \frac{q_o K_L C_e}{1 + K_L C_e} \tag{2.4}$$

$$\frac{C_e}{q_e} = \frac{1}{K_L q_o} + \frac{C_e}{q_o} \tag{2.5}$$

Where q_o is the maximum amount of adsorbate adsorbed to the solid surface (mg/g) and K_L is the Langmuir constant in L/mg. Plotting $\frac{C_e}{q_e}$ versus C_e will produce a straight line where the slope is $\frac{1}{q_o}$ and the intercept is $\frac{1}{K_L q_o}$.

2.7.11. Sips Isotherm

The Sips isotherm model combines features of both the Langmuir and Freundlich equations.[190] It contains three key features: (1) At low adsorbate concentrations, the Sips model reduces to the Freundlich isotherm, (2) at high adsorbate concentrations, the Sips model approaches the Langmuir isotherm, and (3) if the heterogeneity factor, n, is equal to 1, the Sips equation reduces to the Langmuir isotherm (homogeneous surface) and if n is less than 1, the surface is heterogeneous. The Sips equation avoids the limitation of the Freundlich equation, which doesn't predict a saturation point, and is useful for fitting experimental adsorption data across both low and high concentration ranges. The linear and non-linear forms of the Sips equation are given in Equations (2.6) and (2.7), respectively:

$$\ln \frac{q_e}{q_m - q_e} = n ln C_e + ln K_s \tag{2.6}$$

$$q_e = \frac{q_m (K_s C_e^n)}{1 + (K_s C_e^n)} \tag{2.7}$$

Where q_e is the amount of adsorbed solute at equilibrium in mg/g, C_e is the amount of solute in the liquid phase at equilibrium, K_S is the Sips equilibrium constant (L/mg), q_m is the maximum adsorption capacity (mg/g) and n is the heterogeneity factor.

2.7.12. Temkin Isotherm

The Temkin model assumes explicit adsorbent-adsorbate interactions, which the Langmuir and Freundlich model do not factor in.[191] The Temkin model also assumes that the heat of adsorption decreases linearly with increasing surface coverage (because adsorbate–adsorbate repulsion increases as the surface fills). In contrast,

Langmuir assumes the heat of adsorption is constant, and Freundlich assumes it decreases exponentially. The linear Temkin equation is given by equation (2.8):

$$q_e = \frac{RT}{b_T} \ln(K_T C_e) \quad (2.8)$$

Where q_e is the amount of adsorbed solute at equilibrium in mg/g, C_e is the amount of solute in the liquid phase at equilibrium, K_T is the Temkin equilibrium constant (L/mg), b_T is the Temkin constant related to the heat of adsorption (J/mol) and R is the is the universal gas constant (8.314 J/molK).

2.7.13. Dubinin-Radushkevic Isotherm

The Dubinin-Radushkevic model assumes that the porosity of the adsorbent is related to the adsorption curve.[192] This model is useful in identifying the nature of the adsorption taking place, which is physisorption or chemisorption, and to determine the energy of adsorption. Additionally, the model does not assume a homogeneous adsorbent surface. The linear form of the Dubinin-Radushkevic model is given by equation (2.9):

$$\ln(q_e) = \ln q_m - \beta \varepsilon^2 \quad (2.9)$$

Where q_e is the amount of adsorbed solute at equilibrium in mg/g, q_m is the theoretical maximum adsorption capacity (mg/g), β is the Dubinin-Radushkevic constant, which related to the mean free energy of adsorption (mol^2/J^2) and ε is the Polanyi potential in J/mol, which is defined in equation (2.10):

$$\varepsilon = RT \ln\left(1 + \frac{1}{C_e}\right) \quad (2.10)$$

Where R is the universal gas constant (8.314 J/molK), T is absolute temperature (K), and C_e is the equilibrium concentration (mg/L).

2.7.14. Redlich-Peterson Isotherm

The Redlich–Peterson isotherm model is a three-parameter hybrid between the Langmuir and Freundlich models.[193] Like the Sips isotherm, it aims to overcome the limitations of the two-parameter models and provide flexibility for fitting experimental adsorption data across a wide concentration range. The Linear form of the Redlich–Peterson model is given by equation (2.11):

$$\ln\left(\frac{\mathrm{K_R C_e}}{q_e} - 1\right) = g ln C_e + ln a_R \qquad (2.11)$$

Where q_e is the amount of adsorbed solute at equilibrium in mg/g, C_e is the equilibrium adsorbate concentration (mg/L), K_R is the Redlich-Peterson constant in (L/g), a_R is the Redlich-Peterson constant $(L/mg)^g$ and g is the dimensionless exponent.

2.7.15. BET Model

The BET model was created to explain the physical adsorption of gas molecules and multilayer formation on the surface of solid adsorbents.[194] It is a theoretical model and is useful for the calculation of pore size distribution and specific surface areas of porous adsorbents. Assumptions of the BET model are: (1) adsorption is multilayer and homogenous, (2) the adsorption energy for the first layer is not the same for the proceeding layers, and (3) the rate of adsorption is equal to the rate of desorption for each layer. The BET equation is given in equation (2.12):

$$\frac{1}{\mathrm{v}\left(\frac{\mathrm{p_0}}{p} - 1\right)} = \frac{1}{v_m C} + C - \frac{1}{v_m C} \cdot \frac{p}{p_0} \qquad (2.12)$$

Where v is the volume of gas adsorbed at equilibrium pressure p, v_m is the monolayer adsorbed gas quantity (used to calculate surface area), p is the equilibrium pressure

of adsorbate gas, p_0 is the saturation pressure of the adsorbate gas and C is the BET constant, related to the energy of adsorption.

2.8. PFAS Detection and Quantification

The technique regarded as the 'gold standard' for the detection and quantification of PFAS is mass spectrometry.[195-198] There are a range of mass spectrometry methods, including EPA 537.1 and 533, which provide high selectivity and sensitivity.[199] There are many liquid chromatographic (LC) techniques which can be combined with mass spectrometry to achieve great separation and quantification of PFAS, but the focus of this section is on LC with electrospray ionisation coupled with tandem mass spectrometry.

2.8.1. Liquid Chromatography Challenges

Analysis of PFAS from water samples with liquid chromatography requires additional considerations when compared with the analyses of non-fluorinated compounds. For example, agricultural contaminants can be successfully separated using a reverse-phase column, but for PFAS, further measures are necessary to optimise separation whilst limiting the analysis time. The main challenge is that PFAS exists in a vast array of standard laboratory equipment, which can interfere with the chromatographic results, prompting the need for a secondary/isolator column. The addition of a secondary/isolator column to the LC apparatus (between the pump and the autosampler) assists in identifying which PFAS are from the water samples and which PFAS originate from the LC machinery by delaying the elution of the latter, thus enabling analyte peaks to appear first. It is also important to ensure that any LC parts that are made with polytetrafluoroethylene (PTFE) are swapped with parts made from polyetheretherketone (PEEK) (specifically the tubing, vials and caps) that connect as

the former has a tendency to leach fluorinated compounds into the mobile phase of the LC system. Moreover, when conducting reverse-phase separations, a very high aqueous to organic ratio must be used so there is retention of short-chain PFCAs on the column, which happen to be more polar than long-chain PFCAs.

2.8.2. Electrospray Ionisation

Electrospray ionisation (ESI) is a technique that enables the generation of ions which can be detected by a mass spectrometer; a high voltage is applied to the liquid-phase analyte and is atomised, producing an aerosol.[200] There are two modes in which ESI may operate, which are positive and negative modes. The positive mode causes a proton from the solvent to be donated to the analyte, producing ions with the form $[M + H]^-$. The negative mode causes a proton to be removed from the analyte, which generally produces ions with the form $[M – H]^-$. The most commonly used types of PFAS are acidic in nature, which means that the ESI negative mode is most appropriate as the PFAS are negatively charged under standard conditions for LC analysis. PFAS exhibit surfactant-like properties, which means there are reduced intermolecular forces between individual PFAS molecules. These properties facilitate the creation of gas-phase analytes because the surfactant speeds up the charged solvent droplets, further subdividing them into sufficiently small droplets where the solvent can evaporate.[200] Additionally, PFAS tend to appear at the solvent-air interface of the droplets and so the increased concentration at the surface means there is a higher likelihood of charged PFAS being ejected from the droplets much closer to the start of the source. Neutral PFAS, such as those containing a hydroxyl or sulphonamide functional group, are more easily protonated than their acidic counterparts and can be analysed using ESI in positive mode.[201] Further adaptations of standard LC procedures to optimise ESI conditions for PFAS analysis include

correct positioning of the ESI probe, lowering the capillary voltage and using mobile phase additives like ammonium bicarbonate.[202]

2.8.3. Tandem Mass Spectrometry

Tandem mass spectrometry is a technique that is commonly used in the quantification of PFAS in environmental samples. Both long and short chain PFAS are ionised and converted to the gas phase which then enables facile reception by the tandem mass spectrometer, which is capable of high selectivity and sensitivity for PFAS, even at ppt levels. In tandem mass spectrometry, multiple reaction monitoring (MRM) is used to enable higher sensitivity for specific PFAS in more complex environmental samples (this process utilises fragmentation of a precursor ion and the detection of the daughter ion).

Liquid-chromatography tandem mass spectrometry (LC-MS/MS) usually has limits of detection (LOD) of 1 – 10 ng L^{-1} for PFAS,[203] but technological advancements have allowed for LODs to be lowered further and for higher throughputs to be achieved, as methods have been developed where samples can be directly injected into the LC-MS/MS, avoiding a lengthy pre-concentration step. One study has even reported an LOD of 4 ppq for PFOA and 20 ppq for PFOS.[204] Achieving this level of LOD required rigorous discipline in avoiding PFAS contamination of the instrumentation; the laboratory and equipment within were entirely PFAS-free, and all solvents were extensively filtered with HPLC columns before use with the analytes to remove as much background PFAS as possible.

Despite LC-MS/MS being a highly sensitive and selective analytical technique for the detection of PFAS, there are a handful of drawbacks associated with its use. Firstly, there are various chemical reactions that are used industrially to produce PFAS, as

well as various molecular transformations that can occur in the environment, leading to structural variability. Over 9000 poly/per-fluorinated substances have been identified, but only ~750 have been identified with LC-MS/MS.[205] The paucity of identified PFAS via LC-MS/MS is down to poor ionisation of some molecules, varying recoveries during solid phase extraction,[206] a lack of isotopically pure reference standards (a necessity in PFAS quantification with this technique) and some neutral PFAS and newer Gen X PFAS, such as hexafluoropropylene oxide dimer acids (HSPO-DA), which can break down in the LC-MS/MS source.[207] Secondly, the start-up capital required to purchase LC-MS/MS instrumentation is considerable, not to mention the high maintenance and operational costs, as well as the need for highly trained technicians for its operation.

2.8.4. High-resolution Mass Spectrometry

Recent advances in high-resolution mass spectrometry (HRMS) have created opportunities for non-targeted PFAS analysis. HRMS can achieve higher resolution and higher mass accuracy measurements than LC-MS/MS, with some instruments able to measure exact masses, which means PFAS with a similar mass can be detected and differentiated from others, which is not the case with tandem mass spectrometry. There are three HRMS variants: time-of-flight MS (TOFMS), orbitrap MS, and Fourier transform ion cyclotron resonance (FT-ICR) mass spectrometry. HRMS can help with the identification of unknown PFAS which would not be detected in tandem mass spectrometry methods due to a lack of knowledge of fragmentation patterns or that their isotopically labelled standards are not available. To do this, HRMS can compare retention times and matching masses with PFAS databases, as well as utilising Kendrick mass defect analysis to reveal the occurrence of PFAS and their transformation products.

Most multipass and spiral TOF instruments are capable of reaching resolving powers of around 50,000.[208] Orbitrap MS instrumentation employs a highly specialised ion trap which enables resolving powers to reach over 1,000,000, depending on whether trapping time is sufficient for the differentiation of ions which are similar in mass. FT-ICR mass spectrometry may achieve resolving powers in excess of 10,000,000 owing to the introduction of dynamically harmonised FT ICR cells.[209] When it comes to PFAS detection/quantification, there are a handful of limitations associated with HRMS. Confirmation of the presence of specific PFAS requires accurate retention times, masses, and fragmentation times to be known, as well as the use of isotopically labelled PFAS standards (currently available for under 100 compounds). Additionally, HRMS cannot reach the low limits of detection that tandem mass spectrometry instrumentation can reach (1 ng L^{-1} compared to 100 ng L^{-1}) if sufficient trapping times are not utilised. Solid phase extraction may need to be used with HRMS methods, which present issues with inefficiencies in the extraction of fluorinated compounds. When using non-targeted workflows in HRMS, poor ionisation efficiencies could lead to some PFAS not being identified due to the ions not having the requisite intensity to overcome the thresholds for identification. Lastly, in-source fragmentation is another issue which can limit the identification of specific PFAS, particularly PFAS containing ether groups.[210]

2.8.5. Total Organic Fluorine Combustion Ion Chromatography

Total organic fluorine combustion ion chromatography (TOF-CIC) is a technique capable of quantifying the total concentration of fluorine in a sample. PFAS samples are combusted at high temperatures using a combination of oxygen, water vapour and argon. The high temperatures allow for the breaking of the high-strength C-F bonds of the PFAS, which generates F^- and reacts with the water vapour to produce hydrogen

fluoride gas. An absorption solution/bubbler collects the hydrogen fluoride, which is subsequently injected into an ion chromatograph for detection and quantification.[211, 212] TOF-CIC is often used to complement MS/MS and HRMS techniques since it indicates the total fluorine concentration in the samples and can reveal whether the methods missed out on detecting some PFAS.[213] Unfortunately, TOF-CIC data can be affected by a range of different inputs that can result in high background, such as inorganic fluoride in the PFAS samples, the chromatograph itself and salts with indistinguishable elution times. These issues are difficult to avoid, but inorganic fluoride may be separated from organic fluorine by extraction before analysis.

2.9. ^{19}F Nuclear Magnetic Resonance Spectroscopy

Nuclear magnetic resonance (NMR) spectroscopy is a sophisticated analytical technique that takes advantage of the electromagnetic radiation stemming from the re-orientation of atomic nuclei that exhibit non-zero nuclear spins when subjected to an external magnetic field. The fine-tuning of the instrumental parameters can result in the elucidation of structural and quantitative information for a vast range of chemical species. ^{1}H and ^{13}C NMR spectroscopy are frequently used in the laboratory, but it is the ^{19}F nuclei that show the most promise for PFAS detection and quantification with this advanced instrumentation.

2.9.1. Fundamental Principles of NMR Spectroscopy

Some nuclei exist in specific nuclear spin states when they are subjected to an external magnetic field and it is the role of the NMR to detect these transitions exclusive to the particular nuclei being observed, as well as the chemical environment of the nuclei. NMR spectroscopy can only be used on nuclei whose spin (I) is not equal to 0 (nuclei with I = 0 will not provide an NMR spectrum). Nuclei that exhibit spin I ≠ 0 are

associated with a magnetic moment μ ≠ 0, which enables the NMR to be employed for those specific nuclei. In nearly all cases, isotopes with an even number of neutrons and protons will have a magnetic moment equal to zero, which is not usable.

^{1}H and ^{19}F nuclei have spin I = ½, and when an external magnetic field is applied (B), both nuclei present two spin states of + ½ and – ½. The difference in energy between these states can be calculated with Equation (2.13) at specific external magnetic fields.

$$\Delta E = \frac{\mu \cdot B_x}{I} \qquad (2.13)$$

Where ΔE is the change in energy, B is the external magnetic field, μ is the magnetic moment of the nuclei, and I is the spin of the nuclei. Extremely strong magnet fields must be used in the NMR instrumentation to ensure there is sufficient separation between the two spin states so that the change in energy can be measured accurately. Specific nuclei can only absorb electromagnetic radiation at highly specific frequencies, which means NMR spectroscopy can differentiate between various isotopes and elements. Electrons that surround an elemental nucleus can alter the magnetic field present there (magnetic shielding), meaning the frequency that is absorbed by the nucleus is not always the same. Usually, the greater the shielding, the greater the reduction in the magnetic field. This enables one to distinguish between nuclei in different chemical environments as their associated peaks will appear at different chemical shifts, thus giving structural information about the molecule being analysed.

The frequency at which nuclei will precess on its axis is called the Larmor frequency. If the radio frequency (RF) pulse, or excitation pulse, is equal to that of the Larmor frequency, the associated energy will transition from the radio wave to the nuclei, resulting in a change of spin state. When the excitation pulse is no longer active, the

nuclei will steadily relax to their original states (equilibrium). As the nuclei relax, a signal is induced which can be detected by a radio frequency coil which can then amplify it with a radio frequency receiver. The decay can be Fourier Transformed to produce a spectrum with peaks associated with specific chemical environments and peak intensities directly proportional to the concentration of certain chemical species. In order to conduct reliable quantitative NMR experiments, the time it takes for the nuclei to relax back to their equilibrium position must be known. Thereafter, analyte peaks can be directly compared with internal standard peaks to calculate the molecular concentrations.

2.9.2. ^{19}F NMR Spectroscopy Advisements

Several prerequisites must be successfully met in order to obtain valid quantitative results in ^{19}F NMR spectroscopy. The prime factors to consider for quantitative NMR are whether the pulse widths are optimal, and ensuring that all nuclei have relaxed back to equilibrium following the RF pulse. In most cases of quantitative NMR, the pulse width will be 90 °; this ensures that maximum single intensity is reached because a 90 ° pulse width will transfer the most energy and will allow for the highest number of nuclei to transition to a higher energy spin state. Moreover, making sure the nuclei fully relax post RF pulse is vital, as subsequent RF pulses on nuclei that are partially excited can be even more exciting. The longitudinal relaxation time (T_1) is the delay constant for the recovery of the z component of the nuclear spin magnetisation towards its thermal equilibrium; it is the longest relaxation time in ^{19}F NMR.

Lengthy values for T_1 are typical for fluorinated compounds like PFAS, with some PFAS having T_1 values of up to 40 seconds owing to the paramagnetic electrons of the p-orbitals of the F nuclei. The recommended relaxation delay for quantitative NMR

is 5x the value for T_1, which would mean that some PFAS would have a relaxation delay of over 3 min. Considering some quantitative NMR experiments may need over 1000 scans to meet the signal-to-noise ratio requirements, this relaxation delay is not viable. Fortunately, the addition of a paramagnetic relaxation agent to the NMR sample can remedy this issue by reducing relaxation time. Chromium (III) acetylacetonate, or $Cr(acac)_3$, is a paramagnetic compound that is often used in NMR spectroscopy as a relaxation agent due to its paramagnetic properties and its solubility in non-polar organic solvents. It is worth noting that the concentration of $Cr(acac)_3$ in the NMR sample has to be sufficient to significantly reduce the value for T_1, but not so high that it results in line broadening. A concentration of 4 mg mL^{-1} of $Cr(acac)_3$ has been found to be the 'sweet spot' for reducing T_1 whilst not increasing line broadening excessively.

To obtain concentration data from NMR spectra, an internal standard containing the target nuclei must be added to the NMR sample, and its concentration must be accurately known. The peak corresponding to the internal standard can be used as a reference for every single peak in the sample so long as the number of nuclei associated with each peak is known. The concentration of a particular analyte can be calculated with Equation (2.14):

$$C_x = \frac{I_x}{I_{std}} \cdot \frac{N_{std}}{N_x} \cdot C_{std} \qquad (2.14)$$

Where I is the integral area, N is the number of nuclei and C is the concentration of the compound of interest (x) and internal standard (std).

2.9.3. NMR Spectroscopy Applications

NMR spectroscopy is most commonly used for reaction kinetics monitoring, structure elucidation, purity testing and synthetic confirmation within the field of organic chemistry. However, NMR spectroscopy has a good range of applications in environmental science, such as the analysis of humic substances (recalcitrant organic decomposition compounds), the observation of chemical interactions between contaminants and naturally occurring substances, the detection of contaminants in complex matrices and the characterisation of effluent contents.[214-216] Moreover, NMR spectroscopy can even be used to monitor metabolic processes in live organisms due to its non-destructive nature.[217, 218] There are not a lot of naturally occurring fluorinated compounds, and fluorine is not considered an essential mineral element to sustain human life, so it makes sense that the majority of NMR experiments on environmental samples/living organisms have been conducted with ^{1}H and ^{13}C NMR, not ^{19}F NMR. However, the global PFAS contamination problem is still ever-present, and so there have been more publications on PFAS-related investigations using ^{19}F NMR spectroscopy.[219-221]

2.9.4. ^{19}F NMR Spectroscopy Advantages versus ^{1}H NMR Spectroscopy

The ^{1}H and ^{19}F resonance frequencies are highly similar, which is advantageous because it means ^{19}F NMR spectra can be obtained from an NMR probe designed for ^{1}H NMR, although it is recommended to use an NMR probe designed explicitly for ^{19}F NMR as the instrumentation will be fluorine-free and the tuneable parts of the probe will be better suited to fluorinated compound analyses.[222] ^{1}H NMR probes are often manufactured from fluorocarbon polymers, which can produce a very large baseline and distort signals in the spectra. Additionally, the ^{19}F isotope has a sensitivity to NMR detection that is 83% that of the ^{1}H isotope, thus enabling similar lengths of time for experiments and facile quantification.

^{19}F NMR has a far greater resolution than that of ^{1}H NMR, with a chemical shift window of more than 300 ppm for 1D spectra. This window is 20 times larger than the window for ^{1}H NMR, which enables greater differentiation between peaks in more complex matrices with many fluorinated compounds. The greater distance between peaks in the more expansive spectral window means one can push for great apodisation, further increasing sensitivity.

Lastly, fluorine will produce identical splitting patterns in ^{19}F NMR to protons in ^{1}H NMR, which enables facile identification of fluorinated compounds during analyses. F nuclei split by neighbouring ^{19}F nuclei will provide J-coupling values of 5 – 10 Hz. Heteronuclear splitting may also occur between ^{19}F and ^{1}H nuclei due to their similar characteristics in NMR experiments, but ^{19}F - ^{1}H splitting will give rise to J-coupling values of 40 – 60 Hz, which are easily distinguishable from the ^{19}F – ^{19}F splitting. As a precaution, ^{1}H decoupled NMR experiments can be conducted to avoid these spectral features.

2.9.5. ^{19}F NMR versus other Techniques

^{19}F NMR presents several advantages over other analytical techniques. Firstly, life on Earth seldom produces fluorinated carbon compounds due to the difficulty in synthesising the C-F bond. If it is made, its potential biological functions can also be provided by other functional groups that are far more amenable to biochemistry.[223] This is advantageous for ^{19}F NMR as background contamination will be almost zero due to the great paucity of ^{19}F nuclei in environmental samples. Moreover, ^{19}F NMR does not suffer from instrumental PFAS contamination to the same extent as mass spectrographic techniques since it does not use PFAS-containing components like PTFE tubing, bottle coatings and LC solvents. This also means secondary isolator

columns and non-PFAS tubing associated with LC-MS/MS are unnecessary, reducing experimental time and expenditure.

With mass spectrometry, one must consider matrix effects when it comes to analyses of more complex samples. Matrices containing large organic molecules, salts and even the solvent components can influence the ionisation of the PFAS, which can be detrimental to the method's accuracy, precision and sensitivity. Internal standard addition or matrix matching can be used to combat this, but these are necessary steps that prolong experimental time. Quantitative ^{19}F NMR does require the addition of an inexpensive internal standard, but the internal standard of choice can be used for all PFAS types so long as there are no analyte peak overlaps with the internal standard peak. MS methods require very expensive isotopically labelled PFAS standards to be used and the vast majority of PFAS do not have a corresponding isotopically labelled standard readily available. Although NMR experiments do not need to take matrix effects into consideration, the NMR sample must be homogeneous and be free from paramagnetic substances/high salt concentrations to ensure there isn’t excessive line broadening and incorrect shimming processes.

Although mass spectrometry can identify individual PFAS types, it can only identify a fraction of the total PFAS. ^{19}F NMR can identify structural information of PFAS in less-complex samples, but this is not possible where there are many PFAS variants present and where peaks may overlap. However, ^{19}F NMR is capable of calculating total PFAS concentration, which is arguably more useful in some instances, such as at WWTPs, where ideally there would be absolutely no PFAS in the treated water so non-targeted analyses are more appropriate. LC-MS/MS outperforms NMR in detection limits, where it is better suited to detecting trace levels of PFAS.

2.9.6. NMR Limitations

A common limitation associated with NMR analysis is its low sensitivity compared with other techniques, such as tandem mass spectrometry. In order to obtain useable spectra for quantification in an acceptable experimental timeframe, analytes must be in concentrations in the order of μM (ppm), whereas tandem mass spectrometry can detect trace quantities of contaminants several orders of magnitude lower (ppt). The low sensitivity of the NMR instrument is due to the tiny difference in population between excited and ground states. The low sensitivity can be mitigated slightly by using more expensive NMR instrumentation that can generate a much stronger magnetic field, which can increase the energy difference between the two spin states of the nuclei (in 2025, a 1 GHz NMR spectrometer will cost > £12,000,000).

The introduction of cryogenic probes in NMR in the 21st century can be compared to the implementation of faster computer processing units when it comes to increasing the sensitivity of the NMR instrument. Every component of the receiver path of an NMR spectrometer is a source of noise, with the thermal noise produced by the receiver circuitry heavily impacting the final spectrum. The probe coil and signal preamplifier are cooled with a stream of helium gas that has been cooled to a temperature of ~ 20 K, thus cooling the components and significantly reducing the thermal noise generated by the instrument. As a result, the signal to noise ratio is improved fourfold relative to a room temperature probe, allowing for experiments to be completed in 1/16 of the time or samples to have ¼ of the concentration.[224]

Increasing the number of transients (scans) is another useful method of increasing the signal to noise ratio. By increasing the transients, the signals in the final spectrum are increased. However, the signal to noise improvement from increasing transients is

directly proportional to the square root of the number of transients, so there is a threshold where it is no longer worth increasing the sensitivity further (by increasing the quantity of transients) as the length of time per experiment will become impractical.

Another method for improving the signal to noise ratio in NMR is to reduce the relaxation delay of the nuclei (T_1). As mentioned in a previous section, the addition of a paramagnetic relaxation agent like $Cr(acac)_3$ can divert the energy from the excited spin states to itself via interaction with unpaired electrons and direct polar interactions, thus reducing the relaxation time for the nuclei of interest. A sample containing a relaxation agent could complete more transients than a sample without in the same period, increasing the signal to noise. $Cr(acac)_3$ is even more useful in ^{19}F NMR than in ^{1}H NMR since the compound contains no F atoms, so the relaxation agent will not produce peaks on the spectra which could potentially overlap with peaks of interest. One drawback from the addition of relaxation agents is the increase in line broadening, which can lead to loss of spectral detail due to the nuclei relaxing too quickly. However, the agent can be dosed at an optimal concentration to suppress this.

2.9.7. ^{19}F NMR Spectra Interpretation

Elucidating structures in ^{19}F NMR spectra is not quite as straight forward as ^{1}H NMR, but with the correct knowledge of the nuances, there should be no issues. Firstly, F nuclei of the PFAS can be split by both neighbouring F and H nuclei, although a lot of PFAS do not contain any H nuclei so this isn't so much of a problem. Secondly, the filled p-orbitals of the fluorine nuclei will impact the chemical shifts due to the shielding they provide, for example, the terminal $-CF_3$ group signal of PFAS will be shifted much further downfield (higher ppm) than the $-CF_2$ groups as the $-CF_3$ group is not as shielded as the other groups. The $-CF_2$ group adjacent to the functional group will be

the second most de-shielded group and the other -CF_2 groups between the terminal -CF_3 and the -CF_2 adjacent to the functional group are the most shielded, so are pushed up-field (lower ppm). Thirdly, the degree of exposure of each F nuclei to the applied magnetic field can influence the position of the chemical shifts. The ^{19}F NMR spectrum of PFOA can be observed in Figure 2.10.

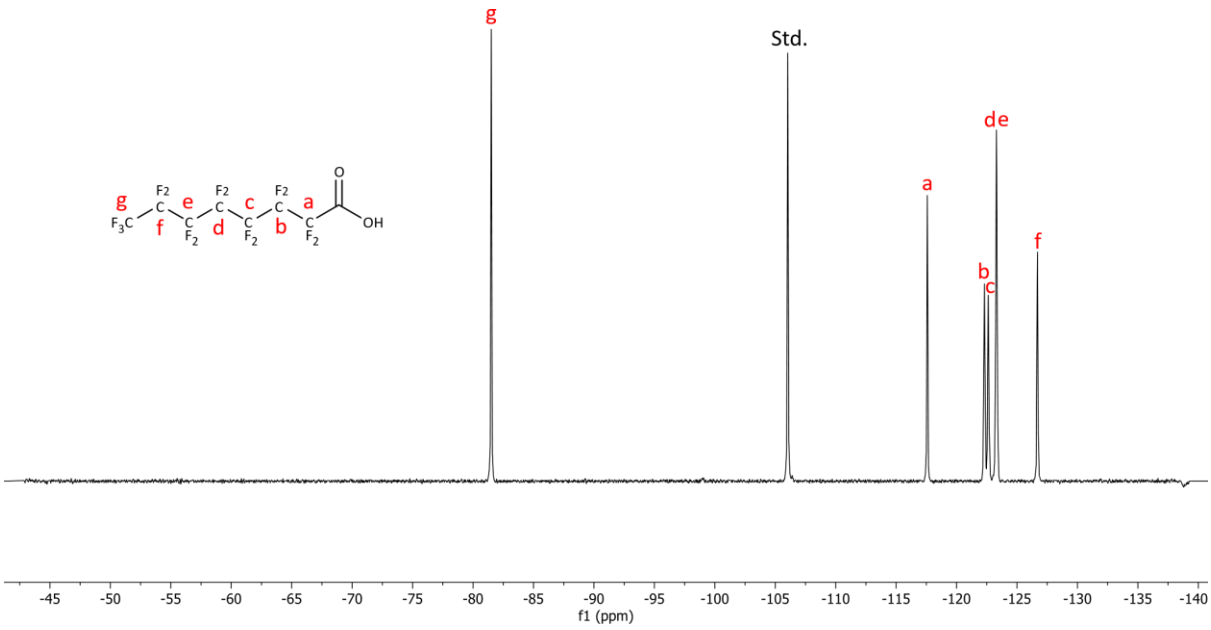


Figure 2.10. ^{19}F NMR spectrum of PFOA (500 MHz, 298 K, CD3OD), Std = 4,4'-difluorobenzophenone.

Deuterated solvent choice and its associated dielectric constant can also play a role in influencing the chemical shifts of the F nuclei, but it is not clear why there is such variation in the chemical shifts when comparing repeat experiments.[225] It has been recommended that an internal standard be added to all ^{19}F NMR experiments (not just quantitative NMR) and compared with published calibrated chemical shift reference tables to ensure the ^{19}F NMR spectra are substantially calibrated.

Spectral overlap is another complexity that can interfere with the quantity of information that can be gleaned from the ^{19}F NMR spectra. Fortunately, ^{19}F NMR has

an exceptionally large spectral window, larger than all other spin active nuclei spectral windows, and so spectral overlap is not that significant. The terminal -CF_3 of any PFAS is the most shielded and therefore has a ppm much further downfield than the rest of the alkyl -CF_2- groups, and therefore doesn't suffer from any overlap. As the -CF_3 peak intensity is used as the basis for quantification, any overlap with any other peaks attributed to the non -CF_3 groups won't make a difference to the accuracy of the quantification data. However, in a more complex sample containing multiple types of PFAS, there will be similar chemical and electronic environments associated with the -CF_2- groups, and so identifying structural information (chain lengths) of various PFAS will be much more difficult/impossible. The use of diffusion ordered spectroscopy (DOSY NMR) is one method of working around spectral overlap that would pose a problem in standard NMR experiments. DOSY NMR employs a magnetic field of various strengths which individual nuclei uniquely interact with. Smaller molecules move much faster across the magnetic field gradient than larger ones, resulting in noticeable differences in the signal intensities throughout the array DOSY NMR spectra. Unfortunately, experimental times are greatly increased compared to standard NMR experiments since an array of NMR spectra will be obtained for each sample, which would not be suitable for a laboratory wanting to regularly differentiate PFAS in many samples.

2.9.8. PFAS-targeting Adsorbent Testing with ^{19}F NMR

PFAS removing adsorbents are widespread, but the assessment of their effectiveness is typically carried out using LC-MS methods. There are only a few examples of researchers using ^{19}F NMR to assess the PFAS removal performance of adsorbents. Lewis *et al.*[226] used ^{19}F NMR to determine whether positively charged carbon dots (PEI-CDs) were capable of adsorbing PFOA from solution. This work monitored the

peak intensities of PFOA after treatment with several different doses of PEI-CD to verify optimal conditions for adsorption. Additionally, they investigated the detail in the peak splitting, and identified that the presence of the broad peaks indicates that PFOA is slowly interchanging between free and CD-associated states, thus confirming the adsorbent was doing its job in PFAS adsorption.

The screening of new PFAS-removing swellable organically modified silica adsorbents was demonstrated by Miglio *et al.* where an optimised quantitative ^{19}F NMR method was employed.[227] The ^{19}F magic angle spinning (MAS) NMR results yielded information about the variety of conformations and configurations in which the PFOA was adsorbed to the silica, which was highlighted by the broad peaks derived from the chemical shift dispersions from the different configurations. Additionally, the presence of shoulders and signal splitting of the -CF_3 peak for all the PFAS tested suggests the potential localisation of the PFAS in a particular region of the silica's pores. Lastly, the research found good agreement between ^{19}F NMR and HPLC quantification data, demonstrating the effectiveness of the ^{19}F NMR method. However, this study did not utilise a relaxation agent in their ^{19}F NMR samples, which could have shortened the experimental time as their relaxation delay was 10 seconds long.

Additional studies have utilised ^{19}F NMR to probe the molecular interactions between PFAS and new adsorbents. Tan *et al.* developed a cationic fluorinated polymer sorbent which was employed for the removal of PFOA.[228] The spectra of PFOA alone and PFOA with 3 different polymeric sorbents were taken, and it was found that the cationic fluorinated polymer caused the -CF_3 peak to have the largest change in chemical shift and peak width relative to the PFOA-only solution, suggesting the PFOA had the strongest interaction with this sorbent.

Despite the compelling research presented in these publications, research groups tend to only use ^{19}F NMR for probing the molecular interactions between the PFAS and adsorbents. The paucity of publications reporting quantitative data using ^{19}F NMR can probably be attributed to the lower sensitivity of the technique, but this does not mean the technique should be completely overlooked in this field.

Chapter 3 Aims and Objectives

3.1. Aims and Objectives

The predominant goal of this project is to demonstrate how ^{19}F NMR spectroscopy can be employed as an efficient tool for the screening of novel PFAS-removing adsorbents. Specifically, how ^{19}F NMR spectroscopy may be used to gather kinetics, isothermal and total-PFAS concentration information which can assist the development of new AC adsorbents which will be used in UK potable water treatment plants. Moreover, the project wanted to verify whether the ^{19}F NMR screening method could outperform traditional LC-MS/MS techniques in terms of expense and experimental time.

In this project, the specific objectives were:

1) To evaluate whether ^{19}F NMR is suitable for the screening of PFAS-removing AC adsorbents.

2) To assess and rank the removal effectiveness of four ACs targeting four representative PFAS.

3) To compare whether ^{19}F NMR is a more efficient quantitative screening method than traditional LC-MS/MS techniques.

4) To determine whether biochar adsorbents have potential for competing with AC adsorbents in PFAS treatment.

To address the objectives outlined above a structured experimental programme was designed encompassing adsorbent characterisation adsorption performance testing and analytical method development. The experiments described in Chapter 4 were selected to generate complementary datasets that together enable robust evaluation of PFAS removal performance and interpretation of the underlying adsorption mechanisms.

Full physicochemical characterisation of the carbon adsorbents was necessary to ensure that differences in PFAS removal behaviour could be interpreted on a mechanistic basis rather than treated as purely empirical outcomes. ACs are inherently heterogeneous materials and their adsorption performance is governed by a combination of pore structure surface chemistry and physical properties which can vary substantially even among carbons derived from the same precursor material. Without comprehensive characterisation it would not be possible to determine whether observed differences in adsorption capacity and kinetics arise from variations in porosity surface functionality or bulk material properties.

Textural characterisation was required to quantify surface area pore volume and pore size distribution which directly influence PFAS accessibility diffusion and adsorption affinity. Given the range of PFAS molecular sizes and functional groups examined in this study, understanding the relative contributions of micropores mesopores and macropores was essential for interpreting differences in uptake behaviour between adsorbents. Surface chemical characterisation was similarly necessary to assess the presence and distribution of oxygen-containing functional groups which influence electrostatic interactions hydrophobic interactions and hydrogen bonding with PFAS molecules.

Batch adsorption experiments including equilibrium isotherms and kinetic tests were conducted to quantify PFAS removal capacity and uptake rates under controlled conditions. Isotherm experiments enable comparison of adsorption affinity and maximum capacity across different adsorbents while kinetic experiments provide insight into mass transfer limitations and adsorption rates which are critical parameters for water treatment applications.

Analytical quantification was performed primarily using ^{19}F NMR spectroscopy, which enabled rapid measurement of PFAS concentrations with minimal sample preparation. This approach generated the majority of the quantitative adsorption data reported in this thesis and was central to achieving the screening and comparative objectives of the study. LC-MS/MS was employed in a more limited capacity, principally to validate selected results and to benchmark the ^{19}F NMR methodology against a conventional targeted analytical technique. As such, LC-MS/MS data were used to support and corroborate NMR-derived findings rather than to generate extensive standalone datasets.

Finally, adsorption experiments using biochar were included to evaluate the potential of lower-cost biomass-derived adsorbents as alternatives to commercial ACs. Assessing biochar and AC under identical experimental conditions enables a direct comparison of performance and highlights the limitations and opportunities associated with biochar materials in PFAS treatment.

Together these experimental approaches form an integrated framework that supports the objectives of this project and ensures that conclusions regarding adsorbent performance and analytical methodology are grounded in measurable material characteristics and comparative evidence rather than inferred production histories.

3.2. Puragen Activated Carbons: Industrial Partner and Adsorbent Supplier

This research project was conducted in collaboration with Puragen Activated Carbons (formerly CPL Activated Carbons, part of CPL Industries), a leading international manufacturer and supplier of purification solutions based on AC filtration technology. The company, which rebranded from CPL Activated Carbons to Puragen in October 2024, is part of Invica Group, a privately owned international industrial and engineering group. The businesses forming Puragen were all established over 30 years ago and brought together under Invica Group since 2019.

Puragen's core business model is fundamentally distinct from conventional AC suppliers in that the company operates one of the most advanced closed-loop carbon reactivation networks in Europe SSRN. Rather than primarily manufacturing virgin ACs for commercial sale, Puragen specialises in the thermal reactivation of spent ACs, restoring their adsorption capacity through controlled high-temperature processing. The company's state-of-the-art reactivation facility in Immingham, north-east Lincolnshire, features three separate reactivation lines: CR1 for 'green' spent carbons from drinking water and food-grade applications (providing per-customer batch reactivation with full traceability), CR2 for 'amber' spent carbons from industrial and environmental applications (pooled reactivation across multiple customers), and CR3 for high-sulphur spent carbons from biogas and biomethane production ACS Publications, a breakthrough technology for which Puragen won the Lorenzo Cagnoni Award for Green Innovation ACS Publications. This reactivation-centric business model enables customers to reduce carbon disposal costs and lower CO_2 emissions by up to 90% compared to virgin carbon use and disposal, contributing to a circular economy approach in water and air treatment applications.

Whilst Puragen does not manufacture commercial-scale virgin ACs for routine supply, the company maintains extensive engineering, manufacturing and R&D capabilities including award-winning chemists, materials scientists and engineers who use leading lab facilities and analytics. These capabilities include a pilot-scale AC production facility where the company develops and tests novel adsorbent materials for research and development purposes. For this doctoral research project, Puragen provided access to their pilot plant and commercial carbon library, which contained over twenty experimental AC samples produced under varying activation conditions, feedstock materials and process parameters. These pilot-scale carbons were manufactured specifically for research and characterisation purposes rather than for commercial distribution, allowing Puragen's technical team to explore the relationships between production conditions and resulting adsorbent properties without the constraints of large-scale commercial production requirements.

From this initial library of experimental pilot plant carbons, a preliminary evaluation and down-selection process was undertaken in consultation with Puragen's technical staff. The pilot plant carbons were assessed for their suitability as test adsorbents, with particular attention paid to ensuring that the selected materials would be representative of commercially relevant ACs whilst exhibiting sufficient diversity in their physical and chemical properties to enable meaningful comparative evaluation. However, following initial characterisation and consideration of the research objectives, it was determined that the most scientifically valuable and practically relevant approach would be to evaluate commercially available ACs that are already in widespread use for water treatment applications, rather than experimental pilot plant materials. This strategic decision ensured that the PFAS adsorption data generated in this study would be directly applicable to real-world water treatment scenarios and

would provide performance benchmarks that could be immediately useful to water utilities and treatment system designers.

Consequently, four commercial ACs were selected for comprehensive characterisation and PFAS adsorption testing. The selection criteria prioritised carbons that spanned a range of precursor materials and activation methods whilst representing products that are readily available at commercial scale. Three of these carbons (designated CAC-1, CAC-3, and CAC-4) were coal-derived ACs that had undergone physical activation via steam, representing the most common class of commercial ACs used in water treatment applications. These three coal-based carbons were sourced from different manufacturers and exhibited different morphologies, surface areas, and pore size distributions despite sharing the same precursor material class and activation method, reflecting variations in raw material properties and production conditions employed by different suppliers. The fourth carbon (CAC-2) was a biomass-derived AC (specifically coconut shell-derived), also physically activated with steam, providing an opportunity to evaluate how precursor material type influences PFAS removal performance when compared against the coal-based alternatives.

The decision to focus on steam-ACs rather than chemically-activated carbons was deliberate, as physical activation is the predominant method used for water treatment applications due to the lower risk of residual activating agents remaining in the carbon structure. Steam activation produces carbons with well-developed micropore networks and relatively clean surfaces compared to chemical activation with phosphoric acid, zinc chloride, or potassium hydroxide, making them more suitable for potable water applications where leaching of chemical impurities is a concern. Furthermore, Puragen's reactivation processes are optimised for physically-activated carbons, as these materials can be thermally reactivated with greater reliability and consistency

compared to chemically-activated carbons, which may undergo irreversible structural changes during reactivation. By selecting commercial carbons that are compatible with Puragen's reactivation infrastructure, this research directly addresses questions relevant to their business operations and the broader water treatment industry.

Throughout the research project, Puragen provided ongoing technical support through their in-house quality control and R&D facilities, including consultation on appropriate experimental protocols for adsorption testing, advice on the interpretation of results within the broader context of commercial AC performance, and access to their extensive knowledge base regarding the behaviour of these materials in real water treatment systems. This collaboration ensured that the experimental programme remained aligned with practical water treatment applications whilst exploring fundamental aspects of PFAS-AC interactions that could inform future adsorbent development, optimisation strategies, and reactivation protocols for PFAS-laden spent carbons.

Chapter 4 Experimental

4.1. Materials

Four commercially available ACs (CAC) were selected for analysis in consultation with CPL Activated Carbons (Table 4.1). CAC-1, CAC-3 and CAC-4 were obtained from steam activation of bituminous coal, whilst Coconut Fines (CAC-2) was obtained from steam activation of coconut shell. As-received GACs were dried at 100 °C for 24 h and stored in an airtight container until use. For experiments that required the AC to be in in powdered form, a ball mill was used to pulverise the GAC which was subsequently sieved to between 50 – 150 µm.

The four ACs selected for this study were chosen to enable a systematic comparison of commercially relevant adsorbents with differing precursor materials and activation histories while maintaining practical relevance to real-world water treatment applications. Three of the ACs were derived from bituminous coal and one was derived from coconut shell. This selection was intended to allow direct comparison between coal-based carbons prepared via different industrial routes and a biomass-derived carbon that is widely used in potable water treatment.

The three bituminous coal ACs were selected because coal-derived carbons remain the dominant class of adsorbents employed in large-scale PFAS treatment systems. Although these carbons share a common precursor material, they were produced using different industrial activation and processing approaches which is reflected in differences in their textural properties surface chemistry and adsorption performance. Evaluating these carbons in parallel allows the influence of manufacturing variability

within a single precursor class to be assessed without confounding effects arising from fundamentally different feedstocks.

The coconut shell AC was included to provide a direct comparison between coal-derived and biomass-derived carbons. Coconut shell carbons are typically characterised by higher microporosity and lower ash content and are frequently marketed as sustainable alternatives to coal-based ACs. Inclusion of this material therefore enabled assessment of whether differences in precursor origin translate into measurable differences in PFAS adsorption behaviour under identical experimental conditions.

It is important to note that the ACs used in this study were commercially sourced materials rather than laboratory-prepared carbons. CPL Activated Carbons operates primarily as a reactivation and regeneration facility and does not manufacture virgin ACs from raw precursor materials. As a result, the precise activation conditions used during the original production of the carbons including activation temperature residence time and activating agents are not available. While this limits the ability to directly link adsorption performance to specific activation parameters it reflects the reality of working with industrial adsorbents used in full-scale water treatment systems. Consequently, the study focuses on comparative performance and structure-property relationships derived from experimentally measured physicochemical characteristics rather than assumed production histories.

Table 4.1. Details on the activated carbons selected for this project.

	CAC-1	CAC-2	CAC-3	CAC-4
Base material	Bituminous coal	Coconut shell	Bituminous coal	Bituminous coal
Iodine number (mg g^{-1})	896	772	959	1046
Butane activity (%)	61.15	51.61	58.82	63.51
Molasses number (mg g^{-1})	337	471	507	856
Density (g cm^{-3})	0.654	0.625	0.606	0.367
Moisture (as received) (%)	4.65	6.77	13.9	5.36

The parameters reported in Table 4.1 provide an initial indication of the pore structure and physical characteristics of the ACs prior to detailed characterisation. The iodine number is a widely used proxy for micropore content and is typically associated with pores smaller than approximately 2 nm. Higher iodine numbers generally indicate a greater extent of microporosity and are often correlated with increased adsorption capacity for small molecular species.

Carbon tetrachloride activity is commonly used to assess the capacity of AC for adsorbing low molecular weight non-polar organic compounds and is influenced by both micropore and small mesopore volume. As a vapour-phase adsorption metric it provides complementary information to the iodine number and offers insight into the accessibility of the pore network for relatively small hydrophobic molecules.

The molasses number is an indicator of mesopore and macropore development and reflects the ability of AC to adsorb larger organic molecules. Higher molasses numbers are typically associated with a more open pore structure and greater contribution from wider pores which can facilitate mass transfer and reduce diffusion limitations during adsorption. Together the iodine number, butane activity and molasses number provide

a qualitative overview of the pore size distribution across micro- meso- and macropore regimes.

Bulk density describes the mass of AC per unit volume including interparticle voids and is an important practical parameter for water treatment applications. Density influences bed packing hydraulic performance and contact time in fixed-bed systems and therefore has direct implications for the design and operation of adsorption columns.

PFOA (CAS No. 335-67-1, ≥ 96% purity), PFHxA (CAS No. 307-24-4, ≥ 96% purity) and PFBS (CAS No. 375-73-5, ≥ 97%), deuterated methanol (CD_3OD) (CAS No. 811-98-3, 99.8 atom % D), LC/MS grade H_2O (CAS No. 7731-18-5), 4,4'-difluorobenzophenone (CAS No. 345-92-6, purity ≥ 99%), Hexafluorobenzene (CAS No. 392-56-3, purity ≥ 99.5%), Chromium(III) acetylacetonate (CAS No. 21679-31-2, purity ≥ 97%) and $CDCl_3$ (CAS No. 865-49-6, 99.8 atom % D) were acquired from Sigma Aldrich, Gillingham, UK. PFOS (CAS No. 2795-39-3) was acquired from New Material Co. Ltd., China. Sodium chloride (CAS No. 7647-14-5), sodium hydrogen carbonate (CAS 144-55-8), sodium carbonate (497-19-8), sodium hydroxide (1310-73-2) and potassium hydrogen phthalate (877-24-7) were purchased from Fisher Scientific UK Ltd., Loughborough, UK.

PFOA, PFHxA, PFOS and PFBS were selected for this project as they represent four of the most ubiquitous subclasses of PFAS, these are long-chain PFCAs, short-chain PFCAs, long-chain PFSAs and short-chain PFSAs. The physicochemical properties of the selected PFAS are presented in Table 4.2.

Table 4.2. The physicochemical properties of the four PFAS analysed in this study (PFOA, PFHxA, PFOS and PFBS)[1].

Compound name (CAS No.)	Formula	MW (g mol^{-1})	Log K_{OW}	Solubility in water (mg L^{-1})	Vapour pressure (mm Hg at 25 °C)	pKa	Boiling point (°C)	Melting point (°C)	Density (g cm^{-3} at 25 °C)
Perfluorooctanoic acid (PFOA) (335-67-1)	$C_7F_{15}COOH$	414.07	4.8	2290	3.16 x 10^{-2}	-0.5 – 4.2	192	54.3	1.8
Perfluorohexanoic acid (PFHxA) (307-24-4)	$C_6F_{11}COOH$	314.05	2.85	1.57 x 10^4	1.49	-0.16	157	12.2	1.7
Perfluorooctane sulfonic acid (PFOS) (2795-39-3)	$C_8F_{17}SO_3H$	500.13	4.49	3.2 x 10^{-3}	2.0 x 10^{-3}	< 1.0	249	~400	1.8
Perfluorobutane sulfonic acid (PFBS) (375-73-5)	$C_4F_9SO_3H$	300.10	1.82	510	2.7 x 10^{-3}	-3.31	211	-93.9	1.8

4.2. Activated Carbon Characterisation

4.2.1. Proximate Analysis

Proximate analysis was carried out in accordance with International Standard Organisation ISO 17246:2024 and a total of 5 repeats were conducted for each sample to confirm precision. The experiments were conducted using a thermogravimetric analyser (TGA, Q500, TA Instruments) and three different temperatures were used to

calculate the relative compositions of moisture (110 °C), volatile matter (900 °C) and ash contents (815 °C).

The powdered AC (~20 mg) was placed into a platinum crucible with empty and full masses recorded by the instrument. The sample was heated to 110 °C in a nitrogen atmosphere, ramping up by 20 °C min^{-1}, and remained isothermal for 30 min. The change in mass during this stage can be attributed to the evaporation of moisture from the AC sample and can be calculated with Equation (4.1).

$$Moisture\ (\%) = \frac{M_{initial} - M_{final}}{M_{initial}} \cdot 100 \qquad (4.1)$$

Where $M_{initial}$ and M_{final} are the initial mass and final mass, respectively.

The sample is then heated to 900 °C in the nitrogen atmosphere, ramping up by 20 °C min^{-1}, and remained isothermal for 7 min to ensure total combustion of the volatile matter. The change in mass during this stage of the experiment can be attributed to the evaporation of volatile matter from the AC sample and can be calculated with Equation (4.2)

$$Volatile\ matter\ (\%) = \frac{M_{initial} - M_{final}}{M_{initial}} \cdot 100 \qquad (4.2)$$

Where $M_{initial}$ and M_{final} are the initial mass and final mass, respectively.

Finally, the AC sample is cooled to 815 °C at a rate of 50 °C min^{-1}, the gas is switched to oxygen and sample remains isothermal for 15 min to ensure total combustion of the

carbon. The change in mass during this stage can be attributed to the combustion of the fixed carbon and can be used to calculate the ash content with Equation (4.3).

$$Ash\ content\ (\%) = \frac{M_{initial} - M_{final}}{M_{initial}} \cdot 100 \qquad (4.3)$$

Where $M_{initial}$ and M_{final} are the initial mass and final mass, respectively.

The fixed carbon content can be calculated by difference using Equation (4.4).

$$Fixed\ carbon\ \ (\%) = 100 - Volatile\ (\%)\ - Ash\ \ (\%) \qquad (4.4)$$

All samples had 5 repeat proximate analysis experiments performed.

4.2.2. Ultimate Analysis

Ultimate analyses were performed with a LECO CHNS628 series elemental analyser and a total of 5 repeats were conducted for each sample to confirm precision. The samples of AC (~75 mg) were placed into a ceramic crucible and combusted in the elemental analyser. The elemental analyser will detect the gases produced/released from the combusted AC and calculate the relative compositions of carbon, nitrogen, hydrogen and oxygen (by difference).

Sulphur content analysis was performed with a Leco 628 Series Sulphur Add-On Module, and a total of 5 repeats were conducted for each sample to confirm precision. To a ceramic combustion boat, powdered AC (0.1 g) was added and placed into the furnace with pure oxygen regulated at 1350 °C. The sulphur within the sample is released and reacts with the oxygen to form sulphur dioxide. The sample gases are

mechanically swept through the combustion tubes in stages to ensure the sample gases remain in the high-temperature zones for a sufficiently long enough time to ensure complete maximal oxidation. The combustion gases are then channelled through an anhydrone tube to remove moisture and then over a sulphur infrared detection cell to determine the sulphur content. Each AC sample was analysed in triplicate.

4.2.3. Butane Activity

Carbon tetrachloride (CTC) activity is the universally accepted method of determining the degree of activation/quality of ACs. A modified method was used which is based on ASTM D3467-04. Since CTC is an ozone depleting substance, butane was used as a substitute. A total of 3 repeats were conducted for each sample to confirm precision

A GAC sample of a representative mass was added to a dual inlet sintered test tube which enables the through-flow of gas whilst keeping the sample contained. Butane gas was passed through the AC sample at a flow rate of 250 cm^3 min^{-1} at 25 °C for 25 minutes to ensure a saturation point was reached and the mass of the butane-laden AC was recorded. The CTC activity was calculated with Equation (4.5).

$$Butane\ activity\ (\%) = \frac{M_{saturated} - M_{initial}}{M_{initial}} \cdot 100 \cdot 2.55 \qquad (4.5)$$

Where $M_{saturated}$ is the mass of the sample after saturation and $M_{initial}$ us the initial mass of the sample.

4.2.4. Iodine Number

The iodine number experiments were performed in accordance with the ASTM D4607 method. First, iodine solution (0.1 N, 25 mL) was normalised by titrating against sodium thiosulphate solution (0.1 N) in the presence of starch solution (1 g L^{-1}, 2mL). The volume of sodium thiosulphate solution was recorded and the iodine solution normality was determined with Equation (4.6).

$$N_2 = \frac{N_1 \cdot I_N}{S} \tag{4.6}$$

Where N_1 is the sodium thiosulphate normality, N_2 is the iodine normality, I_N is the volume of iodine solution and S is the volume of sodium thiosulphate (L).

AC of known mass was milled to a particle size > 74 μM and added to 5 % hydrochloric acid solution (10 mL) until the AC was moistened. The mixture was then boiled for 30 s and left to cool to room temperature. To the mixture, iodine solution (0.1 N, 100 mL) was added and was vigorously shaken. The mixture was filtered and a fraction of the filtrate (50 mL) was added to a starch solution (1 g L^{-1}, 2mL). The filtrate-starch mixture was subsequently titrated against sodium thiosulphate (0.1 N) and the volume required to reach equivalence point was recorded. Each experiment was carried out in triplicate. The iodine number was calculated with Equations (4.7) – (4.10).

$$A = 126.9 \cdot N_2 \tag{4.7}$$

$$B = 126.9 \cdot N_1 \quad (4.8)$$

$$Dilution\ factor = V_I + \left(\frac{V_{HCl}}{V_{Filtrate}}\right) \quad (4.9)$$

$$Iodine\ number\ (mg\ g^{-1}) = \frac{A - (Dilution\ factor) \cdot B \cdot V_{Na_2S_2O_3}}{m_{AC}} \quad (4.10)$$

4.2.5. Molasses Number

The molasses number analyses were determined with the use of a Shimadzu UV-1280 UV-Vis spectrophotometer and the Beer-Lamber Law presented in Equation (4.11).

$$A = \varepsilon \cdot c \cdot l \quad (4.11)$$

Where A is the absorbance, ε is the molar absorptivity coefficient (L mol^{-1} cm^{-1}), c is the concentration (M) and l is the path length (cm).

Powdered AC (0.5 g) was added to molasses solution (10 g L^{-1}, 50 mL) and shaken on a Heathrow Digital Orbital Shaker at 180 rpm for 120 min to ensure equilibrium adsorption has been achieved. The mixture was filtered using a syringe filter (1.2 μm) and analysed using the UV-Vis spectrophotometer. The molasses number was calculated with Equation (4.12).

$$N = \frac{[C_{Initial}] - [C_{Final}]}{m_{AC}} \cdot 0.05 \quad (4.12)$$

Where N is the molasses number (mg g^{-1}), [$C_{initial}$] is the solution concentration before treatment (M), [CAC-2_{inal}] is the concentration after treatment (M) and m_{AC} is the mass of AC (g). Molasses number experiments were carried out in triplicate.

4.2.6. pH Test

The pH of the ACs was conducted using an adapted version of the ASTM D3838 method.

To boiling distilled water (100 mL), AC (10 g) was added and the mixture was heated at reflux for 15 min. Then, the mixture was immediately filtered with glass fibre filter paper (1.2 µm) and the filtrate was allowed to cool to 50 ± 5 °C and the pH was measured a Mettler Toledo FiveEasy Plus pH meter FP20.

4.2.7. Point of Zero Charge

The point of zero charge (pH_{PZC}) is the pH at which the net electrical charge across the AC surface is equal to zero. To ten solutions of sodium chloride (0.01 M, 50 mL), either HCl (0.1 M) or NaOH (0.1 M) was added dropwise so the pH ranged was from 2 – 11. To each solution, powdered AC (0.2 g) was added and the mixtures were shaken on a Fisherbrand™ Digital Orbital Shaker at 150 rpm for 24 h. The final pH values of each mixture were recorded with a Mettler Toledo FiveEasy Plus pH meter FP20 and a plot of $pH_{initial}$ versus pH_{final} was plotted and the point at which $pH_{initial}$ and pH_{final} had the same value was regarded as the pH_{PZC}. A total of 3 repeats were conducted for each sample to confirm precision.

4.2.8. Boehm Titrations

Boehm titrations were performed in accordance with an adapted standardised procedure based on the original Boehm method, which were conducted to determine

the concentrations of acidic oxygen-containing functional groups on the AC surafces.[181] Powdered AC (1.5 g) was added to 50 mL of one of the three reaction bases which had cooled after being heated to 80 °C for 30 min to expel any aqueous CO_2: $NaHCO_3$ (0.05 M), Na_2CO_3 (0.05 M) and NaOH (0.05 M). The mixtures were agitated on a Fisherbrand™ Digital Orbital Shaker at 150 rpm for 24 h. Then, the mixtures were filtered and 10 mL aliquots were taken from each. The aliquots of NaOH and $NaHCO_3$ were acidified by HCl (0.05 M, 20 mL) and the aliquot of Na_2CO_3 was acidified with HCl (0.05 M, 30 mL), since the latter is a diprotic base. The acidified solutions were then back titrated with NaOH (0.05 M) and the volume required to reach a pH of 7 was recorded with a Mettler Toledo FiveEasy Plus pH meter FP20.

The NaOH solution was standardised with potassium hydrogen phthalate (KHP) to ensure the correct NaOH concentration was being used in the Boehm calculations since NaOH is hygroscopic and NaOH solutions may be less concentrated assumed. KHP (0.2 g) was added to distilled water (50 mL) to produce a KHP solution (0.2 M). Then, the KHP solution (0.2 M) was titrated against NaOH (0.05) with the addition of 2 drops of phenolphthalein to determine the end point. The normalised NaOH solution (0.05) was then used as the titrant to normalise the HCl (0.05 M) by titrating until a pH of 7 was achieved. Each experiment was performed in triplicate and the amounts of acidic oxygen functional groups on the ACs can be calculated with Equations (4.13) and (4.14).

$$[HCl]V_{HCl} = [NaOH] \cdot V_{NaOH} + (\frac{n_{HCl}}{n_B}[B]V_B - n_{CSF}) \cdot \frac{V_a}{V_b} \qquad (4.13)$$

$$n_{CSF} = \frac{n_{HCl}}{n_B} \cdot [B] \cdot V_B - ([HCl] \cdot V_{HCl} - [NaOH] \cdot V_{NaOH}) \cdot \frac{V_B}{V_a} \quad (4.14)$$

Where [B] and V_B are the concentration and volume of the reaction base added to the ACs, n_{CSF} is the moles of carbon surface functionalities, V_a is the aliquot volume, [HCl] and V_{HCl} are the concentration and volume of HCl added to the aliquots of the filtered reaction bases.

4.2.9. Scanning Electron Microscopy

Scanning electron microscopy (SEM) was performed with a Zeiss Crossbeam 550 FIB-SEM. Dry samples of the AC were attached to an SEM stub using conductive carbon cement. Samples were fractured and cut with a scalpel to view the internal structure and subsequently coated with ~ 11 nm of iridium at 10 mA for 60 s. Images were acquired at set magnifications and the imaging conditions remained constant. The magnification of SEM is not great enough to reveal meso- or micropores, but it will show the macroporosity which does play a part in PFAS adsorption.

4.2.10. Transmission Electron Microscopy

Bright-field transmission electron microscopy (TEM) was performed at 200 kV on a JEOL 2100F TEM with a Gatan Model 1095 K3-IS direct electron detection camera (point resolution 0.23 nm). Samples were deposited on holey carbon on copper 200 mesh TEM grids (Agar Scientific) by bringing the dry sample into contact with the grid. TEM is a relevant tool to reveal the profile of the polyaromatic layers which forms the framework of the ACs.

4.2.11. X-ray Photoelectron Spectroscopy

The X-ray photoemission spectra of the ACs were evaluated using a Thermo Fisher Scientific K-Alpha X-ray photoelectron spectrometer (XPS) to study the extent of the presence of surface oxygen-containing functional groups that may partake in adsorptive processes. XPS is a surface-sensitive analytical technique that probes the outermost 5-10 nm of the material, providing information on elemental composition and chemical bonding states. A total of 5 repeats were conducted for each sample to confirm precision. Monochromatic X-ray radiation of 1486.6 eV (Al Kα) was used to irradiate each AC sample. All spectra were recorded using a pass energy of 20 eV and the analysis area (spot size) was approximately 400 μm in diameter.

To determine the various oxygen-containing functional groups present on the AC surfaces, high-resolution scans of the C1s region were collected for each sample using 0.1 eV step sizes. The C1s spectrum corresponds to the binding energy region of core-level electrons (1s orbital) in carbon atoms, typically centred around 284-285 eV. This region is particularly informative for ACs because carbon atoms bonded to different functional groups exhibit characteristic shifts in their binding energies due to variations in the local chemical environment. Specifically, carbon atoms in pure graphitic or aliphatic C-C/C-H bonds appear at ~284.8 eV, whilst carbon atoms bonded to oxygen in functional groups such as hydroxyl (C-OH), carbonyl (C=O), and carboxyl (O-C=O) appear at progressively higher binding energies (~286.0 eV, ~287.5 eV, and ~289.0 eV, respectively). By deconvoluting the C1s spectrum into its constituent peaks, each corresponding to a different carbon-oxygen bonding environment, it is possible to semi-quantitatively determine the relative abundance of different oxygen-containing functional groups on the AC surface. This information is crucial for understanding how surface chemistry influences PFAS adsorption, as hydroxyl and carboxyl groups can

engage in hydrogen bonding with the polar head groups of PFAS molecules (the sulfonic acid group in PFOS and PFBS, or the carboxylic acid group in PFOA and PFHxA), whilst the overall oxygen content affects the hydrophilicity and surface charge characteristics of the adsorbent.

The XPS spectra were deconvoluted using CasaXPS software, employing a Shirley-type background subtraction to account for inelastically scattered electrons, and fitting each component peak with mixed Gaussian-Lorentzian line shapes, apart from the C-C primary peak, which was fitted with a Doniach-Sunjic-Shirley line shape. The relative peak areas, after correction for atomic sensitivity factors, were used to calculate the atomic percentage of each carbon-oxygen species, providing quantitative insight into the surface functional group distribution across the four ACs.

4.2.12. BET Surface Area and Pore Analysis

BET Instrumentation Validation

The Brunauer–Emmett–Teller (BET) surface area and pore analysis was performed on a Micromeritics ASAP 2420 Accelerated Surface Area and Porosimetry System. Due to usage limits, the instrument could not be used for repeat analyses of the samples, so a demonstration of the instrumental precision was performed on a Silica-Alumina standard provided by Micromeritics. The verified physical properties of the silica-alumina standard are presented in Table 4.3.

Table 4.3. Verified physical properties of the Micromeritics silica-alumina standard.

BET Surface Area (m^2/g)	Total Pore Volume (cm^3/g)
226 ± 6	0.68 ± 0.08

Six repeat analyses of the BET surface area and the total pore volume of the silica-alumina standard are presented in Table 4.4. The experimentally determined values are all within the limits of the verified sample values, confirming experimental precision for future experiments on the ACs.

Table 4.4. Experimentally determined physical properties of the Micromeritics silica-alumina standard performed on the ASAP 2420 Accelerated Surface Area and Porosimetry System.

BET Surface Area (m^2/g)	Total Pore Volume (cm^3/g)
226	0.662
229	0.663
229	0.664
229	0.663
229	0.665
230	0.665
STD = 1.25	STD = 1.11×10^{-3}

BET Pore Analysis Method

The GACs were left in their granular forms because the porosity and surface area data needed to be representative of the form used in real-world applications. An empty stoppered specialised round-bottomed sample tube had its mass recorded and then to it, GAC (0.15 g) was added and the mass was recorded again. The GAC-filled sample tube was then degassed under vacuum for 15 hours at 393 K and the mass recorded once again. The mass should be slightly less than before due to loss of moisture and volatiles. For nitrogen adsorption isotherms, the samples were analysed

whilst submerged in liquid nitrogen (77 K). To a specialised polymer coated dewar, liquid nitrogen (77 K) was added and the temperature was allowed to equilibrate. The sample tubes were fitted with an isothermal jacket and screwed onto the pore analyser for analysis. Experimental times ranged from 48 – 72 hours depending on how porous the sample was (a more porous sample would have a greater experimental duration).

Once the nitrogen adsorption isotherm was complete, the same samples could be used for obtaining a CO_2 adsorption isotherm at 273 K. The samples were degassed under vacuum for 15 hours at 393 K and had their final masses were recorded. To the dewar, water and crushed ice were added and the temperature was allowed to equilibrate. The sample tubes were screwed into the pore analyser and the experiment commenced. Experimental times lasted for ~24 hours. CO_2 adsorption isotherms were performed because N_2 cannot diffuse into ultra-micropores (< 7 nm) very well at cryogenic temperatures, whereas CO_2 can diffuse in very fast. However, nitrogen is the best choice for micropore and mesopore analysis as CO_2 adsorption isotherms may not be meaningful on an absolute basis as the interactions of CO_2-CO_2 molecules are very strong. Both CO_2 and N_2 adsorption isotherms were used to determine pore size distribution using density functional theory (DFT) using the Micromeritics MicroActive Reporting Software. Only one sample of each AC could be analysed on the BET analyser due to a backlog of researchers requiring instrument usage.

BET Analysis

The BET surface area ($m^2\ g^{-1}$) analysis is a relevant surface area determining technique for solid and porous materials. The BET surface area equation is presented in Equation (4.15).

$$\frac{\frac{P}{P0}}{n\left(1-\frac{P}{P0}\right)} = \frac{1}{n_m C} + \frac{C-1}{n_m C}\left(\frac{P}{P_0}\right) \qquad (4.15)$$

Where at a specific relative pressure (P/P_0):

n is the quantity of adsorbate adsorbed to the sample, n_m is the monolayer capacity and C is the BET C-value.

BET theory assumes that individual gas molecules physically adsorb in layers that can stack infinitely, there is no interaction between separate adsorbed layers and the Langmuir theory can be applied to each individual layer.

To determine a meaningful value for the BET surface area, several criteria had to be met:

1. The BET C-value had to be > 0.
2. The Rouquerol transform $n(1-p/p^o)$ must increase in the selected relative pressure range.
3. The monolayer capacity pressure should be within the selected pressure range
4. The correlation coefficient should be > 0.999.
5. The calculated value should not differ by more than 10% of the same value.

The maximum of the Rouquerol plot and four points below were selected to calculate the BET surface area ($m^2\ g^{-1}$).

Pore Size Distribution

Non-Linear Density functional theory (NLDFT) is a mathematical tool that can determine an approximate solution to the Schrödinger equation for a multi-bodied

system. The MicroActive software enables the NLDFT model to be applied to adsorption isotherms. The pore size distribution and total pore volume ($cm^3\ g^{-1}$) was calculated by combining the 273 K CO_2 and 77 K N_2 density functional theory (slit pores) data and recording the pore size distribution from the cumulative pore volume ($cm^3\ g^{-1}$) versus pore width (nm) plot. The slit pore NLDFT model was used as it is widely accepted as the most suitable method of describing pores in micro- and mesoporous materials, like the ACs in this study.[229]

Average Pore Diameter

The average pore diameter (nm) was calculated with Equation (4.16).

$$Average\ pore\ diameter = \frac{4 \cdot V_{Total}}{S_{BET}} \cdot 1000 \qquad (4.16)$$

Where the average pore diameter is measured in nm, V_{Total} is the total pore volume ($cm^3\ g^{-1}$) and S_{BET} is the BET surface area ($m^2\ g^{-1}$).

Classification of Nitrogen Adsorption Isotherms

Eight physical adsorption isotherms have been classified by IUPAC which are useful for qualitatively understanding the pore size distribution of adsorbents (Figure 4.1, adapted from Donohue *et al.*).[230, 231] Different pore structures and the type of adsorption interactions can influence the shape of the adsorption isotherm curve. Typically, ACs produce either a Type I or Type IV isotherm shape. Type I isotherms are classed as 'reversible' and the isotherm is characteristic of adsorbents which exhibit a high degree of microporosity. The Type I curve is concave to the p/p^0 axis and the steep uptake at low values of p/p^0 is indicative of augmented adsorbate-adsorbent interactions within very narrow micropores. Type I(b) has a less steep

concave curve due to the corresponding adsorbent having a range of wider micropores/narrow mesopores. Type IV isotherms come to light due to an adsorbent presenting high mesoporosity. The ‘knee’ of the Type IV isotherm, which can also be located at the ‘B’ marking of the Type II isotherm in Figure 1, indicates the completion of a monolayer in the mesopores which is then followed by a more gradual increase in amount adsorbed due pore condensation, which is when the gas condenses into a liquid-like state in the pores at a pressure less than the saturation pressure of the bulk liquid. In the Type IV(a) isotherm, a hysteresis loop is present due to capillary condensation which traps the adsorbate in ink pot shaped pores. Type IV(b) isotherms do not present a hysteresis loop as the pores tend to be conically shaped that are closed at the tapered end.

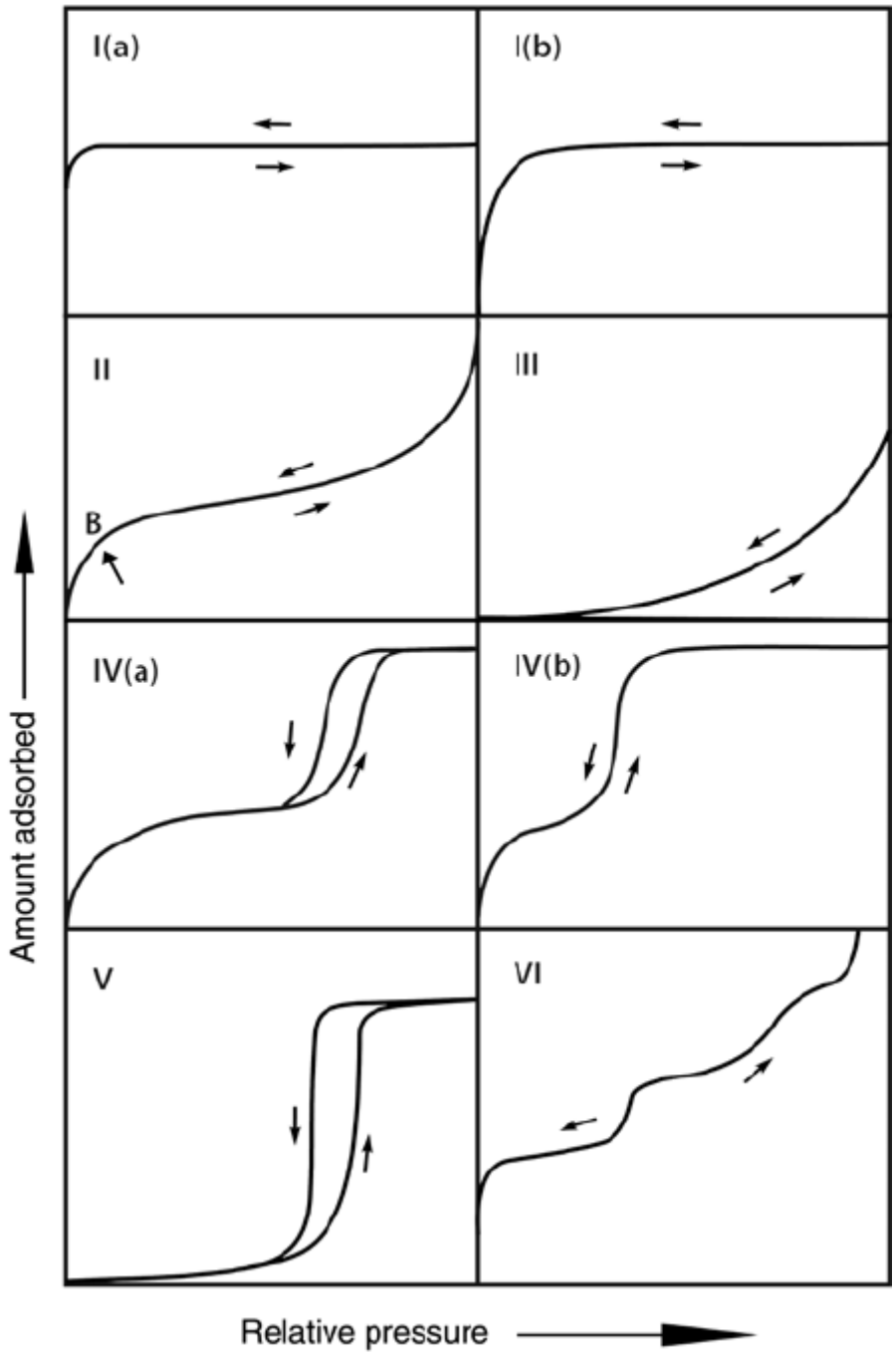


Figure 4.1. Classification of physisorption isotherms.

PFAS Batch Adsorption Experiments

All PFAS adsorption experiments were performed in 250 mL high-density polyethylene (HDPE) bottles to mitigate against PFAS adsorbing to the bottle walls, which is far

more likely when using glass containers, and to protect the samples against the introduction of PFAS contamination. Stock solutions of PFAS were prepared using ultrapure distilled water prepared in an Arium® Pro Ultrapure Lab Water System.

The NMR solvent was modified for this study. To deuterated methanol, 4,4'difluorobenzophenone was added to make a final concentration of 241.5 μM. Then, to standard spiked deuterated methanol, chromium(III) acetylacetonate was added (8 mg L^{-1}), which served as the relaxation agent.

Batch Adsorption Isotherms

Isotherm experiments were performed using 241.5 μM PFAS-spiked ultrapure distilled water containing PFOA, PFHxA, PFOS and PFBS and the four ACs. This molar concentration was selected to ensure direct comparability across PFAS with different molecular weights. The experimental programme was initially designed using PFOA at a mass concentration of 100 mg L^{-1}, which corresponds to a molar concentration of 241.5 μM. To maintain a consistent molecular basis across all adsorption systems, the remaining PFAS were therefore prepared at the same molar concentration rather than the same mass concentration. This approach ensures that each system contains an equivalent number of PFAS molecules and allows differences in adsorption behaviour to be attributed to molecular structure, functional group chemistry and chain length rather than differences in initial solute loading.

Powdered AC was dosed at 40, 80, 160, 320 and 640 mg L^{-1}, with the corresponding masses added to 200 mL of the PFAS solutions (241.5 μM). To homogenise the samples, the flasks were shaken vigorously and then agitated on a Fisherbrand™ Digital Orbital Shaker at 150 rpm for 48 h at 20 °C. From each sample, 5 mL of solution

was separated from the powdered AC using a 0.45 μm Fisherbrand™ PES syringe filter, with the first 3 mL of filtrate discarded to mitigate PFAS adsorption to the syringe filter. Subsequently, 0.3 mL of the filtrate was combined with 0.3 mL of standard-spiked deuterated methanol in an NMR tube for quantitative analysis. A blank sample was run alongside each experiment.

Batch Kinetics Tests

The adsorption kinetics of PFAS-spiked (241.5 μM) ultrapure distilled water (PFOA, PFHxA, PFOS and PFBS) were investigated on the four ACs. Powdered AC was dosed at 640 mg L^{-1} and added to the PFAS solutions (241.5 μM, 200 mL). To homogenise the samples, the flasks were shaken vigorously and then agitated on a Fisherbrand™ Digital Orbital Shaker at 150 rpm for 3 hours at 20 °C. At 15, 30, 60, 90, 120 and 180 min, each sample had 5 mL separated from the powdered AC using a 0.45 μm Fisherbrand™ PES syringe filter, with the first 3 mL of filtrate discarded to mitigate PFAS adsorption to the syringe filter. Then 0.3 mL of the filtrate was combined with the standard spiked deuterated methanol (0.3 mL) in an NMR tube for quantitative analysis. A blank sample was run alongside each experiment.

The kinetics of adsorption were investigated using two kinetics models: the pseudo-first-order and pseudo-second-order models. The expression for the pseudo-first-order model is presented in Equation (4.18):

$$\ln(\mathrm{q_e} - q_t) = \ln(q_e) - K_1 t \qquad (4.18)$$

The expression for the pseudo-second-order model is presented in Equation (4.19):

$$\frac{\mathrm{t}}{\mathrm{q_t}} = \frac{1}{K_2 q_e^2} + \frac{t}{q_e} \quad (4.19)$$

Where q_t (mg g^{-1}) is the quantity of PFAS adsorbed, t is time (min) and q_e (mg g^{-1}) is the amount of PFAS adsorbed at equilibrium. K_1 (min^{-1}) is the pseudo-first-order rate constant and K_2 [mg $(g \cdot min)^{-1}$] is the pseudo-second-order rate constant.

4.3. LC-MS/MS Analysis

Liquid chromatography tandem mass spectrometry (LC-MS/MS) was employed as a targeted analytical technique to validate selected adsorption results obtained by ^{19}F NMR and to benchmark NMR-derived concentrations against a conventional trace-level method. LC-MS/MS was not used to generate the primary adsorption datasets for this study but rather to provide confirmatory measurements for a limited subset of samples.

Isotherm experiments were performed using 2.42 nM PFAS-spiked ultrapure distilled water containing PFOA, PFHxA, PFOS and PFBS and the four ACs. Each experiment was analysed in triplicate to confirm analytical precision. Powdered AC was dosed at 2.5, 5, 10 and 15 mg L^{-1}, with the corresponding masses added to 200 mL of the PFAS solutions (2.42 nM). To homogenise the samples, the flasks were shaken vigorously and then agitated on a Fisherbrand™ Digital Orbital Shaker at 150 rpm for 48 h at 20 °C.

Following equilibration, 25 mL of solution was separated from the powdered AC using a 0.45 µm Fisherbrand™ PES syringe filter, with the first 1 mL of filtrate discarded to mitigate PFAS adsorption to the syringe filter. The resulting filtrate was transferred to HDPE sample tubes and stored at temperatures between 0 °C and 6 °C prior to analysis.

Quantification of PFAS was performed using LC-MS/MS following a method developed based on ASTM D8421-22. Chromatographic separation was achieved using an Agilent 1290 Infinity high-performance liquid chromatography system, with detection carried out using an Agilent 6460 triple quadrupole mass spectrometer operated with electrospray ionisation in negative ion mode and multiple reaction monitoring. Data acquisition and processing were performed using Agilent MassHunter software.

Calibration stock solution A was prepared from a mixed target and surrogate PFAS standard (Wellington Laboratories PFC-C-CS5). A volume of 200 µL of the standard mix was added to a 100 mL volumetric flask and diluted with 50% methanol to produce a 2000 ng L^{-1} stock solution. Working calibration standards in the range of 0 to 1000 ng L^{-1} were prepared by serial dilution with 50% methanol. Calibration curves were generated using a weighted 1/X regression to account for the wide concentration range. Quantification was performed using compound-specific calibration curves, with isotopically labelled internal standards used where available to correct for ionisation efficiency and instrumental variability. As LC-MS/MS is inherently a targeted technique, only PFAS compounds for which suitable standards were available were included in the analysis.

Samples were analysed at the Analytical Instrumentation Laboratory at Puragen and transported under refrigerated conditions between 0 °C and 6 °C. For analysis, 500 µL of methanol was added to a 1.5 mL vial, followed by 40 µL of mass-labelled internal standard and 500 µL of sample. The mixture was vortexed for 15 s prior to direct injection into the HPLC-MS/MS system. No reusable glassware or containers were used to minimise the risk of PFAS contamination.

During the course of this project, the LC-MS/MS system exhibited persistent background PFAS contamination, a recognised challenge in PFAS analysis arising from fluoropolymer components within analytical instrumentation, tubing and laboratory consumables. Elevated and variable background signals were observed across multiple PFAS channels, which limited achievable sensitivity and reproducibility, particularly at low concentrations. Despite extensive mitigation strategies, including the use of PFAS-free solvents and consumables and rigorous blank monitoring, residual system contamination could not be fully eliminated within the timeframe of the project. As a result, LC-MS/MS analysis was necessarily restricted to a limited subset of samples and was used primarily for confirmatory purposes rather than for the generation of comprehensive adsorption isotherms or kinetic datasets. Consequently, LC-MS/MS data were used selectively to corroborate trends observed by ^{19}F NMR. The LC Conditions and LC parameters MS parameters are presented in Table 4.5,

Table 4.6 and Table 4.7, respectively.

Table 4.5. LC mobile phase conditions.

Time (min)	**Mobile Phase A %** (5 mM ammonium acetate in water)	**Mobile phase B %** (HPLC grade methanol)
0.00	95	5
1.00	95	5
1.50	55	45
7.00	2	98
8.00	2	98
8.10	95	5
12.00	95	5

Table 4.6. LC parameters.

Parameter	
Analytical Column	Thermo Scientific Accucore™ C18 (2.6 µm, 3 x 50 mm)
Delay Column	Thermo Scientific Accucore™ C18 (2.6 µm, 3 x 50 mm)
Mobile Phase A	5 mM ammonium acetate in water
Mobile Phase B	LC/MS grade methanol
Flow Rate	0.8 mL/min
Column Oven Temperature	30 °C
Autosampler Temperature	15 °C
Injection Volume	50 µL
Needle Wash 1	1:1:1 MeOH:ACN:Isopropanol

Table 4.7. MS parameters.

Parameter	
ESI Voltage (Negative)	-2500 V
Source Temperature	350 °C
Carrier Gas	Nitrogen
Ollision Gas	Argon
Collision Gas Pressure	1.5 mTorr
Detection Mode	Time Managed MRM

4.4. Quantitative ^{19}F NMR Spectroscopy

Quantitative ^{19}F nuclear magnetic resonance spectroscopy was employed as the primary analytical technique for determining PFAS concentrations throughout this study. The method was selected due to the high natural abundance and sensitivity of the fluorine nucleus, the absence of fluorine background in aqueous matrices and the ability to quantify fluorinated compounds directly without chromatographic separation or compound-specific response factors. These attributes make ^{19}F NMR particularly well suited to high-throughput screening and comparative adsorption studies involving multiple PFAS species.

All quantitative measurements were performed using an internal standard approach to ensure consistency and accuracy across experiments. Signal integration was used to determine PFAS concentrations based on the relative area of fluorine resonances

with respect to the internal standard, enabling compound-independent quantification and direct comparison between samples.

4.4.1. NMR Parameters

^{19}F NMR spectra were acquired on a Bruker 500 MHz spectrometer equipped with a broad-band tuneable liquid-nitrogen cooled cryoprobe and a room temperature TXI probe. The use of a cryogenically cooled probe significantly enhanced signal-to-noise ratios, enabling reliable quantification of PFAS at low micromolar and nanomolar concentrations while maintaining reasonable acquisition times.

All spectra were recorded at 298 K to ensure consistent chemical shift behaviour and minimise temperature-dependent variability in relaxation and signal intensity. The spectral width was set from −145 to −30 ppm to capture the full range of fluorine resonances associated with the PFAS investigated in this study while avoiding unnecessary acquisition of noise outside the region of interest.

An acquisition time of 2.8 s was selected to provide sufficient digital resolution for accurate peak integration, while a relaxation delay of 2 s was used to allow adequate longitudinal relaxation between scans. A 90° pulse width of 14 μs was employed to ensure uniform excitation of all fluorine nuclei and to support quantitative integration. A total of 1024 transients were collected for each sample, resulting in an experimental time of approximately 1.5 h per spectrum**.** These parameters were chosen to balance sensitivity, quantitative accuracy and practical time constraints.

Due to limited allocated experimental time on the NMR instrument at the University of Nottingham, it was not feasible to acquire triplicate spectra for every sample. Instead, quantitative precision was assessed by repeatedly acquiring spectra from the blank sample from each experimental set, with each blank sample re-analysed three times

under identical conditions. This approach confirmed reproducibility of signal integration and demonstrated that single acquisitions were sufficient to provide reliable quantitative data for comparative adsorption analysis.

4.4.2. NMR Data Processing and Analysis

All ^{19}F NMR spectra were processed using MestreNova™ software following a consistent and standardised workflow. Raw free induction decays were subjected to phase correction and baseline correction using the Whittaker–Smoother algorithm to remove baseline distortions and ensure accurate peak integration. Apodisation was not applied to avoid artificial alteration of peak areas that could compromise quantitative accuracy.

Fluorine resonances corresponding to individual PFAS were identified based on their characteristic chemical shifts and integrated manually to ensure consistent treatment across all samples. Chemical shift referencing was performed relative to the internal standard peak, which appeared at −106 ppm, corresponding to $CFCl_3$ at 0 ppm. This referencing approach ensured consistent alignment of spectra across experimental runs and eliminated variability arising from instrumental drift.

Quantification was performed by comparing the integrated area of each PFAS resonance to that of the internal standard, accounting for the known concentration and number of fluorine atoms contributing to each signal. This internal standard normalisation enabled robust quantification across samples and experimental conditions and formed the basis for all NMR-derived concentration data reported in this thesis.

Overall, the quantitative ^{19}F NMR methodology described above proved to be a robust and reliable approach for the screening and quantification of PFAS adsorption across the range of materials and experimental conditions investigated in this study. The method enabled consistent, compound-independent quantification with sufficient sensitivity and reproducibility to support comparative adsorption analysis and structure–property interpretation. Further detail on the development, optimisation and validation of this quantitative ^{19}F NMR method, including assessment of detection limits, precision and comparison with LC-MS/MS, is presented in Chapter 6.

Chapter 5 Characterisation of Activated Carbon Adsorbents

5.1. Introduction and Rationale for Comprehensive Adsorbent Characterisation

The performance of ACs in removing PFAS from aqueous solutions is governed by a combination of physical and chemical properties that collectively determine adsorption capacity, selectivity and kinetics. To understand why certain ACs outperform others in PFAS removal, and to elucidate the fundamental mechanisms by which PFAS molecules interact with AC surfaces, it is essential to conduct a thorough and systematic characterisation of the adsorbent materials prior to adsorption testing. Without such characterisation, observed differences in PFAS removal performance would remain empirical observations disconnected from underlying mechanistic understanding, limiting the ability to rationally design improved adsorbents or predict performance under varying operational conditions.

The objective of this chapter is to present a comprehensive physical and chemical characterisation of the four commercial ACs (CAC-1, CAC-2, CAC-3 and CAC-4) that were selected for PFAS adsorption evaluation (with some limited characterisation of the biochar sample). The characterisation process was designed to quantify the key material properties known to influence adsorption processes in general, and PFAS adsorption specifically, based on the mechanistic understanding developed in the literature review presented in Chapter 2. These properties fall into two broad categories: textural properties, which describe the physical structure of the adsorbent including surface area, pore volume, pore size distribution, and particle morphology;

and surface chemical properties, which describe the elemental composition and functional group chemistry at the adsorbent surface.

The textural properties of ACs are of paramount importance in PFAS adsorption because they determine the accessibility of adsorption sites and the extent of surface area available for interaction with PFAS molecules. PFAS compounds, particularly long-chain perfluoroalkyl acids such as PFOA (with a molecular length of approximately 1.5 nm) and PFOS (approximately 1.8 nm), are relatively large molecules that require appropriately sized pores for effective adsorption. Micropores (pores with widths less than 2 nm) can provide high-energy adsorption sites due to the overlapping attractive forces from opposite pore walls, but may exclude larger PFAS molecules entirely if pore dimensions are too restrictive. Mesopores (pores between 2 and 50 nm) can accommodate PFAS molecules more readily but may provide lower binding energies due to reduced pore wall overlap. The optimal pore size distribution for PFAS adsorption therefore represents a balance between maximising accessible surface area in pores that can physically accommodate PFAS molecules, whilst retaining sufficient micropore volume to provide high-energy binding sites for strong adsorption. Understanding the pore structure of each AC is thus essential for interpreting adsorption performance data.

The surface chemical properties of ACs are equally important because they govern the nature and strength of adsorbate-adsorbent interactions beyond simple physical adsorption. PFAS molecules possess both a hydrophobic perfluorinated tail and a hydrophilic ionic head group (sulfonic acid in the case of PFOS and PFBS, or carboxylic acid in the case of PFOA and PFHxA), making them amphiphilic compounds capable of engaging in multiple types of interactions with the adsorbent surface. The hydrophobic fluorocarbon tail can interact favourably with the graphitic,

hydrophobic regions of the AC surface through van der Waals forces and hydrophobic effects, whilst the charged head group can participate in electrostatic interactions with charged surface functional groups on the carbon, or in hydrogen bonding with polar functional groups such as carboxyl, hydroxyl, or carbonyl groups. The surface chemistry of ACs, characterised by the oxygen-to-carbon ratio, the distribution of oxygen-containing functional groups, and the surface charge as a function of pH, therefore plays a critical role in determining both the magnitude and selectivity of PFAS adsorption.

To quantify these textural and chemical properties, a suite of complementary analytical techniques was employed, each providing specific and non-redundant information about the adsorbent characteristics. Nitrogen adsorption porosimetry at -196°C was used to determine surface area, total pore volume, and pore size distributions via analysis of the adsorption-desorption isotherms according to BET (Brunauer-Emmett-Teller) theory. Scanning electron microscopy (SEM) and transmission electron microscopy (TEM) were employed to visualise particle morphology and internal pore structure at the micro- and nanoscale, respectively. X-ray photoelectron spectroscopy (XPS) provided quantitative surface elemental composition and chemical state information for the outermost 5-10 nm of the adsorbent surface, with particular focus on the carbon and oxygen spectra to identify oxygen-containing functional groups. Boehm titration was conducted to quantify the concentrations of acidic (carboxyl, lactone, phenolic) and basic surface functional groups. Finally, point of zero charge (PZC) measurements were performed to determine the pH at which the AC surface exhibits zero net charge, which is useful for understanding electrostatic interactions between PFAS anions and the adsorbent surface under the experimental pH conditions.

The characterisation data presented in this chapter serve multiple purposes. Firstly, they provide essential baseline information about the ACs that will enable structure-performance correlations to be drawn when adsorption results are presented in Chapter 7. For example, differences in PFAS adsorption capacity between CAC-1 and CAC-4 can be rationalised by comparing their respective surface areas, pore size distributions, and oxygen functional group concentrations. Secondly, the characterisation data allow for mechanistic interpretation of adsorption behaviour. For instance, if one AC shows preferential adsorption of PFOS over PFBS, comparison of the pore size distributions can reveal whether this selectivity arises from size-exclusion effects in micropores. Thirdly, the comprehensive characterisation ensures that any anomalous or unexpected adsorption behaviour can be investigated by examining whether unusual adsorbent properties might be responsible. Finally, the characterisation data provide the necessary information to compare the ACs here with those reported in the literature, enabling the results of this study to be contextualised within the broader body of PFAS adsorption research.

It should be noted that all characterisation measurements were conducted on the ACs min their as-received state prior to any contact with PFAS solutions. This approach ensures that the characterisation data reflect the intrinsic properties of the virgin adsorbents, unperturbed by the presence of adsorbed PFAS molecules. For the biochar sample, the same characterisation protocol was followed to enable direct comparison with the ACs and to assess whether biochar could serve as a viable alternative adsorbent to commercial ACs for PFAS removal applications. The results presented in this chapter represent the foundation upon which all subsequent adsorption performance evaluations and mechanistic interpretations are built.

5.2. Textural Properties of Activated Carbons

The nitrogen (N_2) adsorption isotherms for the four ACs, CAC-1, CAC-2, CAC-3 and CAC-4, are presented in Figure 5.1. Figure 5.1(a)–(d) show isotherms characterised by a steep initial uptake of N_2 at relative pressures (P/P_0) below 0.1, indicating a high degree of micro- and ultra-microporosity across all ACs. This rapid uptake reflects strong adsorbate–adsorbent interactions within narrow pores and is characteristic of micropore filling. Among the four materials, CAC-4 exhibits the highest overall N_2 adsorption capacity, reaching 12.25 mmol g^{-1}, suggesting a more developed pore network.

The isotherms for CAC-1, CAC-2 and CAC-3 are notably similar and closely resemble Type I isotherms, which are typically associated with predominantly microporous materials. This behaviour is evidenced by the development of a plateau at approximately $P/P_0 \approx 0.2$, indicating that the majority of accessible micropores have been filled. However, the presence of distinct hysteresis loops, which are not expected for ideal Type I isotherms, suggests that these materials also possess a secondary mesoporous component and therefore exhibit mixed Type I and Type IV behaviour. The hysteresis observed arises from capillary condensation within mesopores, particularly those with ink-bottle or inkpot geometries, where pore necks restrict desorption relative to adsorption. As a result, a greater quantity of N_2 is retained during desorption than is adsorbed at the same relative pressure during the adsorption branch.

Capillary condensation occurs when a condensable fluid transitions into a liquid-like phase within confined pore spaces at pressures below the bulk saturation pressure, driven by the curvature of the liquid–vapour meniscus. In porous carbons, this phenomenon is most commonly associated with mesopores in the range of

approximately 2 to 50 nm and is reflected experimentally by the presence of hysteresis loops in gas adsorption isotherms. The onset and extent of capillary condensation therefore provide valuable insight into mesopore availability, pore connectivity and pore geometry, all of which influence mass transport and adsorption capacity.

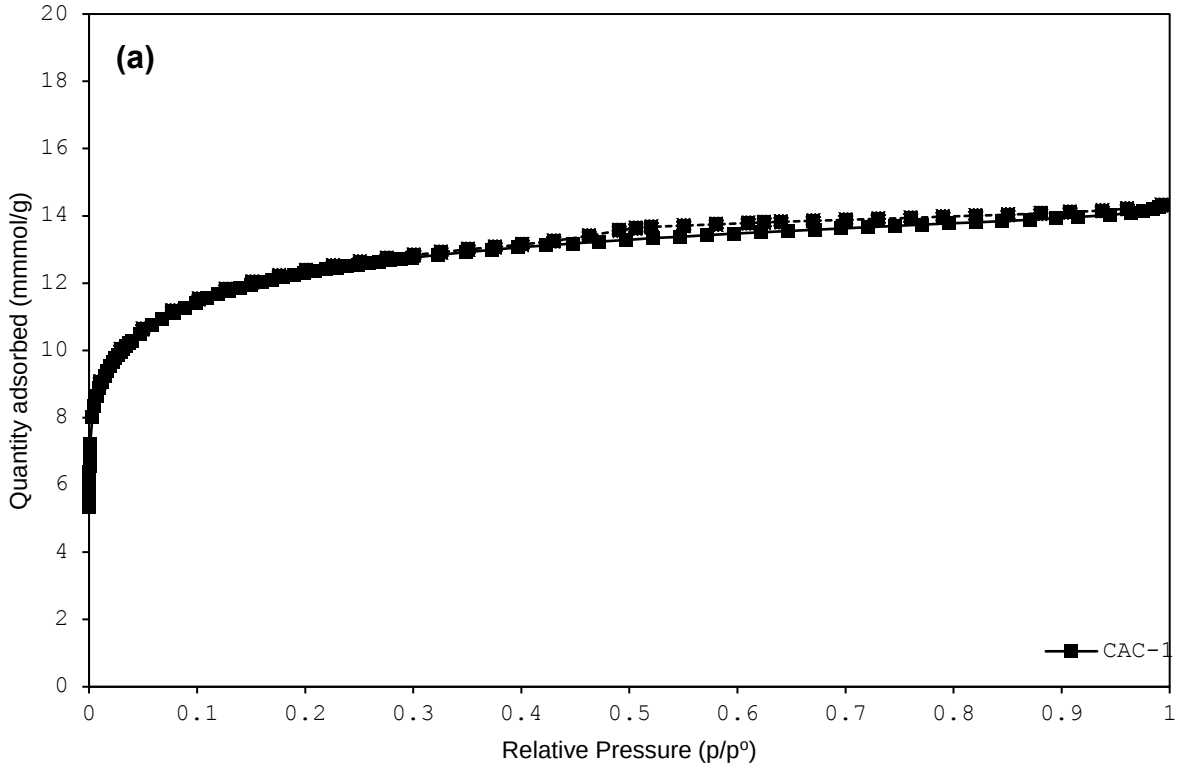
The N_2 adsorption isotherm for CAC-4, shown in Figure 5.1(d), also displays a steep uptake at low relative pressures, confirming significant micro- and ultra-microporosity. However, in contrast to the other ACs, CAC-4 demonstrates stronger resemblance to a Type IV(a) isotherm, characterised by a continuously increasing slope and a pronounced hysteresis loop over a broader relative pressure range. This behaviour indicates a higher degree of mesoporosity and a greater contribution from capillary condensation. The nature of the hysteresis loop suggests the presence of inkpot-shaped mesopores, which are particularly effective at retaining condensed adsorbate phases and contribute to the higher overall adsorption capacity observed for this material.

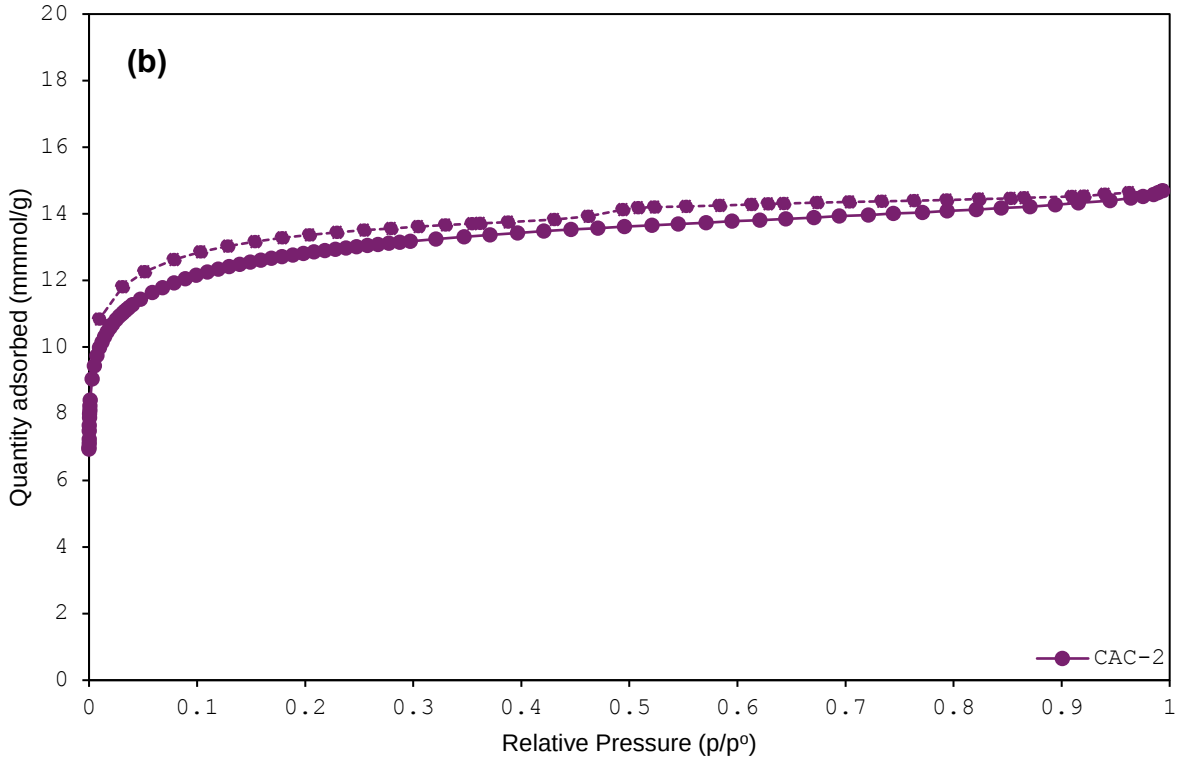
Figure 5.1(e) overlays the isotherms of all four ACs for direct comparison. CAC-4 consistently exhibits the highest N_2 adsorption capacity across the full pressure range, followed by CAC-3, CAC-2 and CAC-1. The hysteresis loops observed for all samples are consistent with Type H4 behaviour, which is typically associated with narrow, slit-like mesopores commonly found in ACs. These mesopores play a critical role in enabling capillary condensation and facilitating pore filling beyond monolayer adsorption, particularly at higher relative pressures.

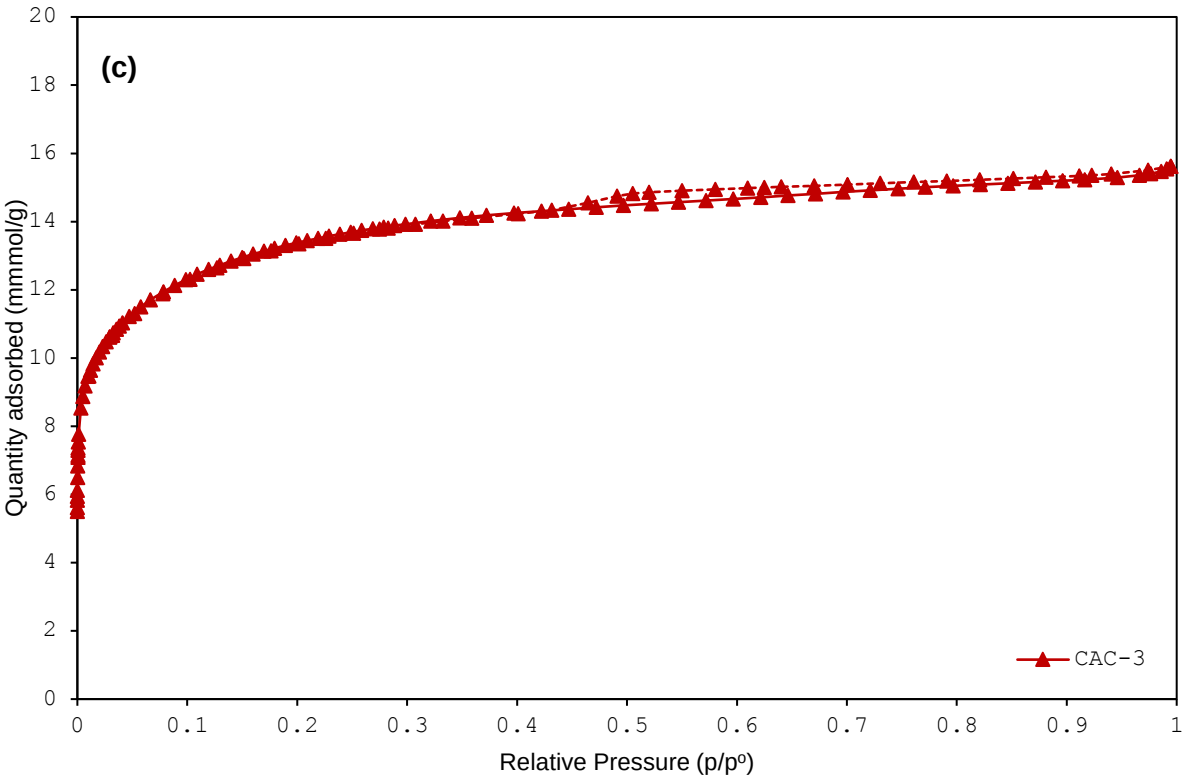
In the context of PFAS adsorption, the presence of mesopores capable of supporting capillary condensation is highly relevant. While micropores provide high-affinity adsorption sites at low concentrations, mesopores can accommodate larger volumes of PFAS-containing solution through pore filling mechanisms. Given the amphiphilic

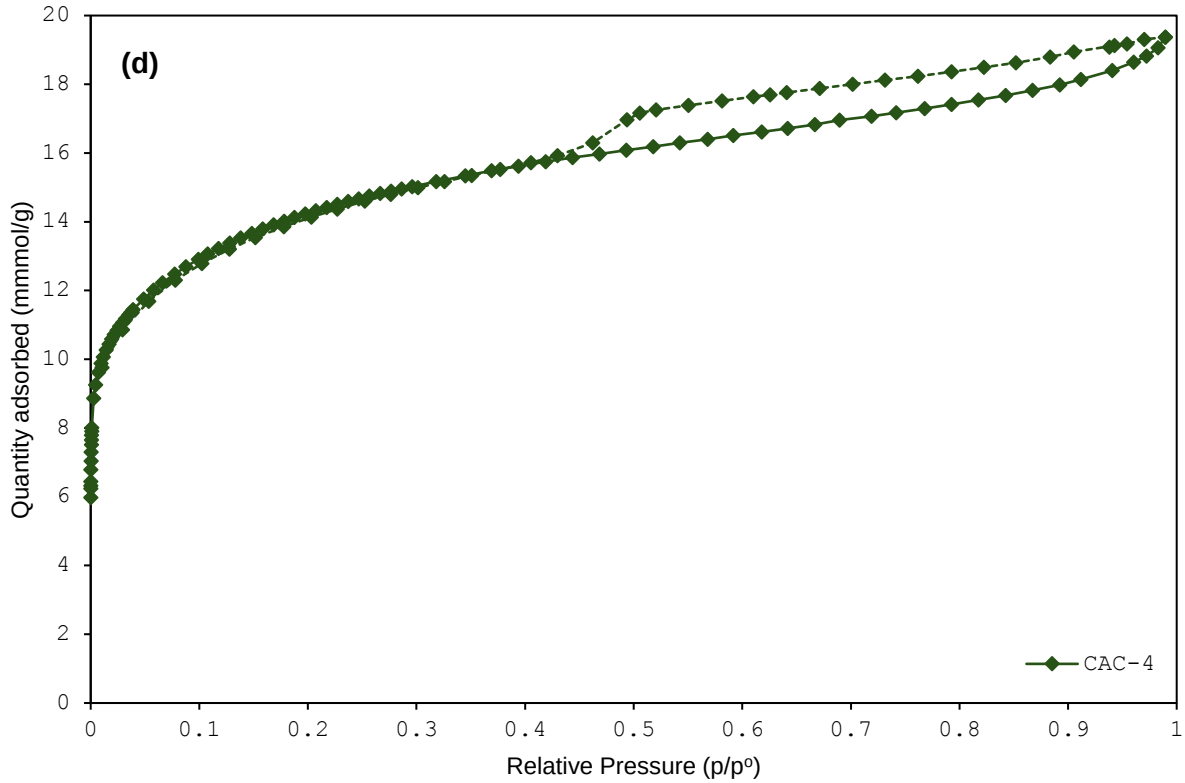
nature of PFAS molecules, capillary condensation within mesopores may lead to cooperative adsorption and enhanced retention, particularly at higher aqueous concentrations. ACs exhibiting a balanced pore structure, combining micropores for strong initial adsorption and mesopores for capillary condensation, are therefore expected to perform more effectively across a wide concentration range.

The N_2 adsorption isotherm for the biochar is presented in Figure 5.2, with the corresponding pore size distribution shown in Figure 5.4. In contrast to the ACs, the quantity of N_2 adsorbed by the biochar is approximately an order of magnitude lower. The BET surface area was determined to be 102.6 $m^2 g^{-1}$, which is also an order of magnitude lower than that of all ACs as summarised in Table 5.1. These significantly reduced values can be attributed to the absence of an activation step following pyrolysis, meaning that many pores remain closed or poorly developed. As a result, the biochar exhibits limited microporosity and negligible mesoporosity, restricting both surface-driven adsorption and capillary condensation mechanisms. This fundamental difference in pore structure provides important context for interpreting the comparatively lower PFAS adsorption performance of the biochar discussed in subsequent sections.


(a)
Quantity adsorbed (mmmol/g)
Relative Pressure (p/p°)
CAC-1


(b)
Quantity adsorbed (mmmol/g)
Relative Pressure (p/p°)
CAC-2


(c)
Quantity adsorbed (mmmol/g)
Relative Pressure (p/p°)
CAC-3
0
2
4
6
8
10
12
14
16
18
20
0
0.1
0.2
0.3
0.4
0.5
0.6
0.7
0.8
0.9
1


(d)
Quantity adsorbed (mmmol/g)
Relative Pressure (p/p°)
CAC-4
0
2
4
6
8
10
12
14
16
18
20
0
0.1
0.2
0.3
0.4
0.5
0.6
0.7
0.8
0.9
1

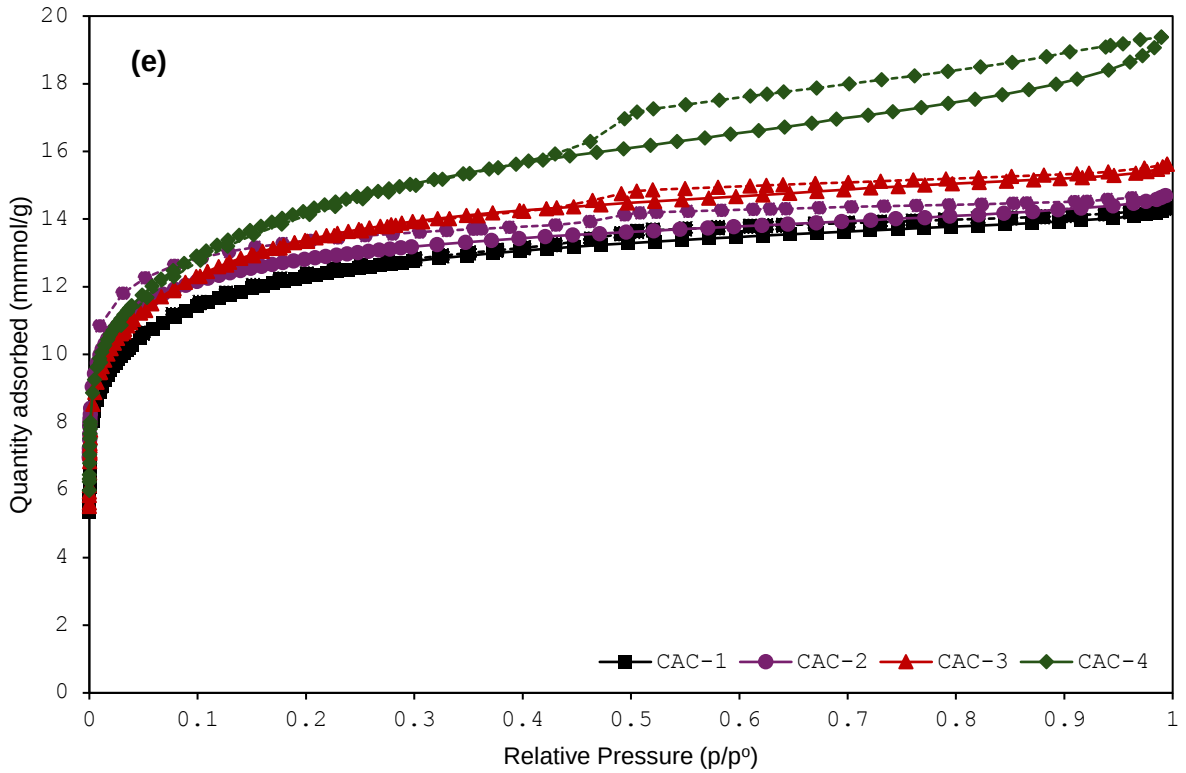


Figure 5.1. N_2 adsorption isotherms obtained at -196 °C for (a) CAC-1, (b) CAC-2, (c) CAC-3 and (d) CAC-4. (e) Overlayed N_2 adsorption isotherms for all ACs.

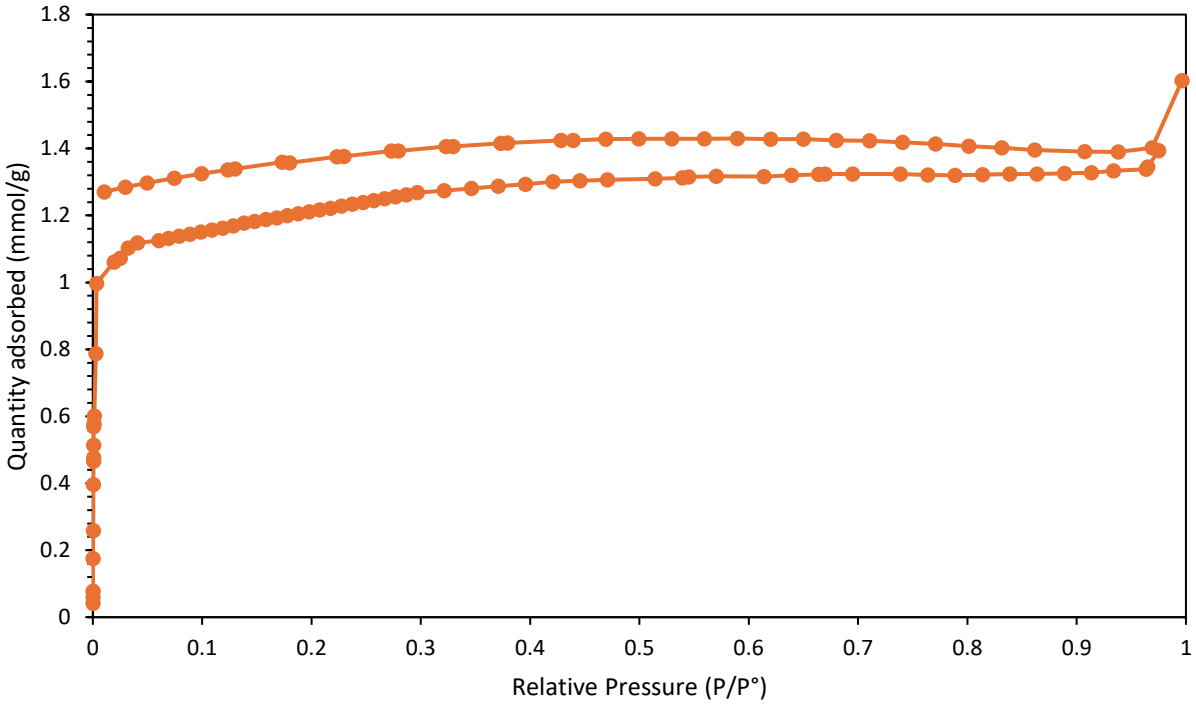


Figure 5.2. N_2 adsorption isotherm obtained at -196 °C for the biochar.

The Brunauer–Emmett–Teller (BET) surface area, pore size distribution, and average pore diameter for the four ACs are summarised in Table 5.1. The high BET surface area values are indicative of extensive pore development resulting from steam activation at elevated temperatures (700 – 1000 °C). This process promotes oxidative reactions between steam and the carbon matrix, leading to the formation and widening of pores.

The BET surface areas are ranked from largest to smallest in the following order: CAC-4 > CAC-3 > CAC-2 > CAC-1. Although the specific conditions of carbonisation and activation are not available, all samples were subjected to physical activation using steam. Notably, CAC-1, CAC-3, and CAC-4 are derived from bituminous coal, yet display significant variation in BET surface area. The superior surface area of CAC-4 may be attributed to more favourable activation parameters, such as an optimal activation temperature around 700 °C.

Table 5.1. Surface textural properties of the four ACs.

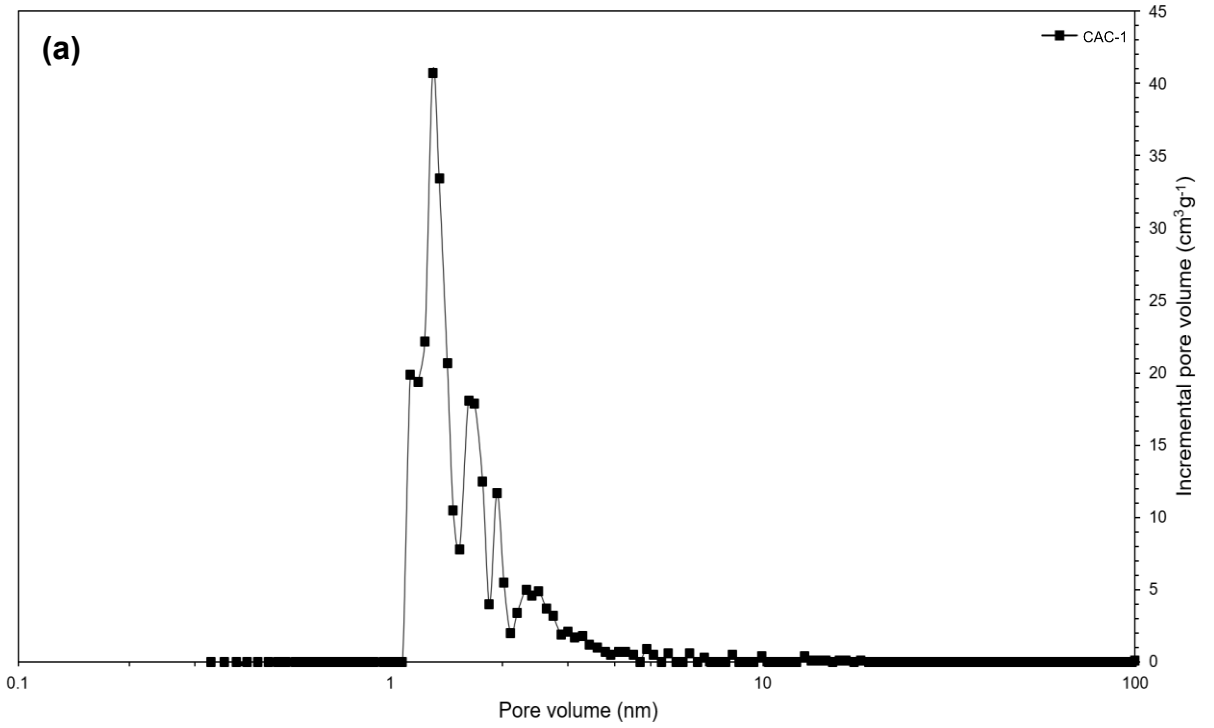
Sample	S_{BET} ($m^2\ g^{-1}$)	V_{total} ($cm^3\ g^{-1}$)	$V_{ultramicro}$ ($cm^3\ g^{-1}$)	V_{micro} ($cm^3\ g^{-1}$)	V_{meso} ($cm^3\ g^{-1}$)	Avg pore diameter (nm)
CAC-1	1021	0.471	0.195	0.361	0.103	1.85
CAC-2	898	0.411	0.162	0.322	0.085	1.83
CAC-3	1051	0.463	0.189	0.384	0.076	1.76
CAC-4	975	0.538	0.166	0.339	0.193	2.21
Biochar	102.6	0.048	0.034	0	0.014	1.89

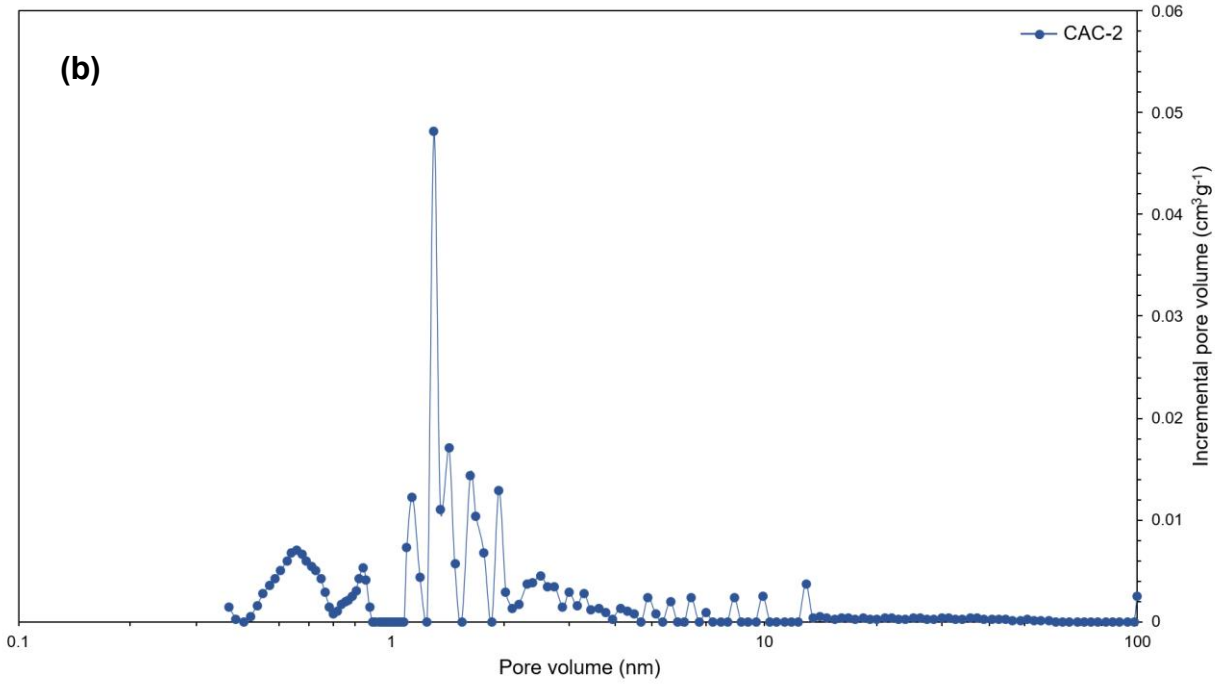
Pore size distribution analysis reveals that CAC-4 possesses the highest total pore volume ($0.538\ cm^3\ g^{-1}$) amongst the four ACs. Additionally, CAC-4 exhibits the

greatest mesopore volume at 0.193 $cm^3 g^{-1}$. Prior studies have shown that mesoporous ACs typically exhibit enhanced adsorption capacities for more hydrophobic PFAS, whilst microporous carbons are generally more effective at adsorbing hydrophilic PFAS. Moreover, mesopores have been reported to reduce pore blocking in microporous materials, thereby improving overall adsorption performance.[19]

Siriwardena *et al.* reported that the molecular lengths of both PFOA and PFOS are approximately 1 nm, with hydrated diameters of around 1.5 nm.[232] Given that micropores are defined as having diameters ≤ 2 nm, these dimensions indicate that long-chain PFAS are more likely to adsorb within mesopores, whereas short-chain PFAS may more readily access and be retained in micropores.

CAC-4 is notable for its nearly 1:1 micropore-to-mesopore volume ratio, with the majority of micropores exceeding 0.7 nm in diameter. Combined with its highest BET surface area, this balanced pore structure suggests that CAC-4 possesses the most favourable textural properties for the adsorption of both short-chain and long-chain PFAS.


(a)
CAC-1
45
40
35
30
25
20
15
10
5
0
Incremental pore volume (cm3g-1)
0.1
1
10
100
Pore volume (nm)


(b)
CAC-2
0.06
0.05
0.04
0.03
0.02
0.01
0
Incremental pore volume (cm3g-1)
0.1
1
10
100
Pore volume (nm)

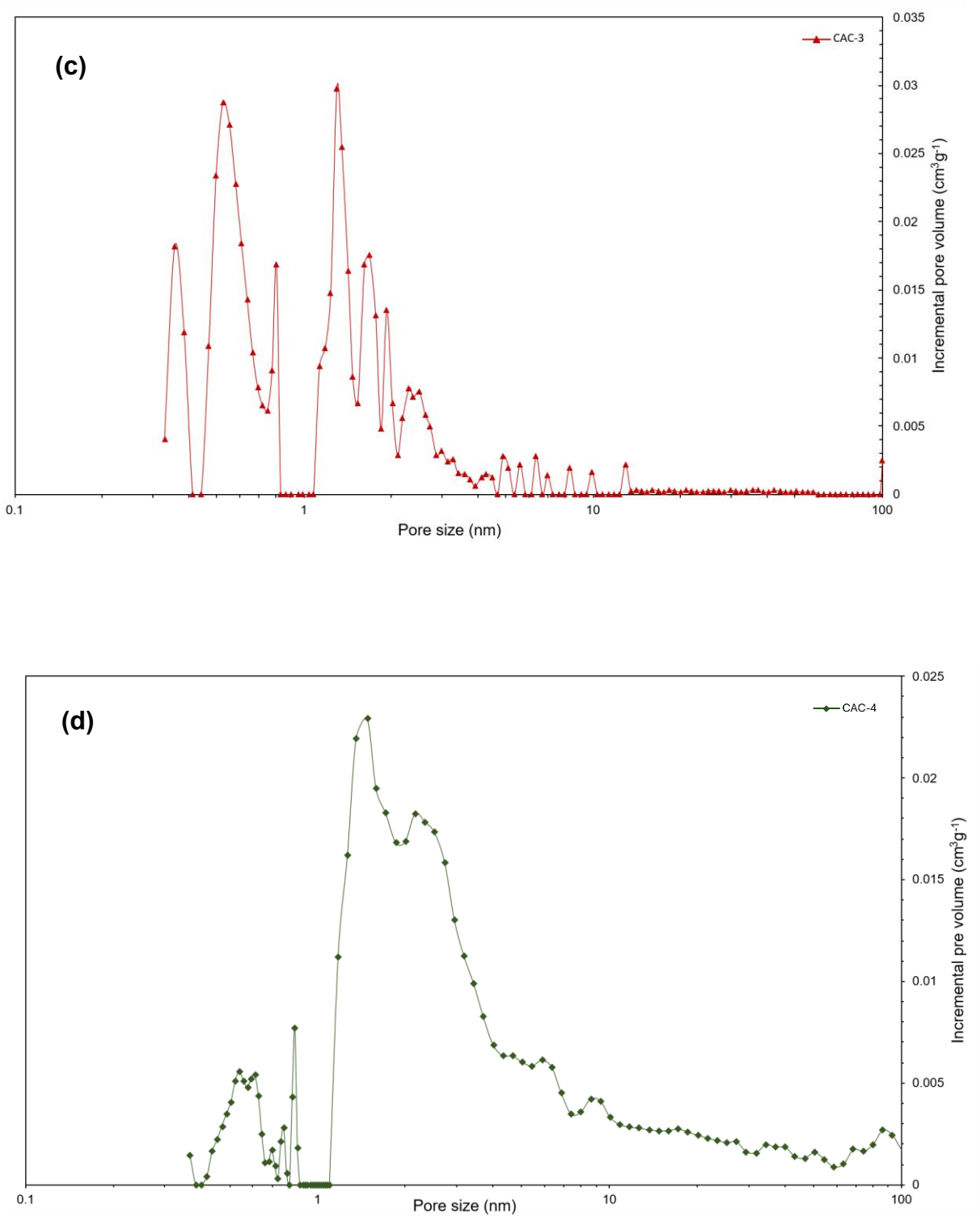


Figure 5.3. Pore size distributions of activated carbons (a) CAC-1, (b) CAC-2, (c) CAC-3 and (d) CAC-4.

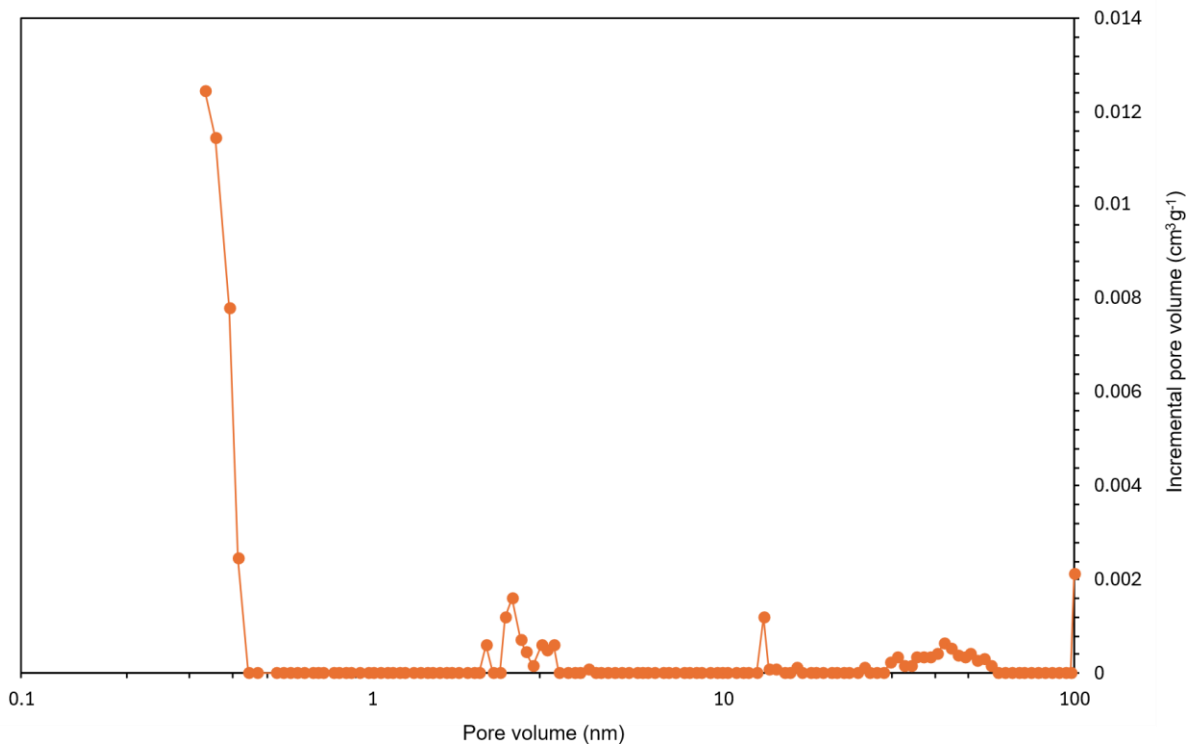


Figure 5.4. Pore size distributions of biochar.

Detailed graphical representations of the pore size distributions for the ACs and Biochar samples are presented in Figure 5.3 and Figure 5.4, respectively, offering visual insight into their porosity profiles. All four ACs exhibit exceptionally high pore volumes below 2 nm, emphasising the dominance of microporosity relative to meso- and macroporosity within these materials.

Of particular note is the near absence of ultramicropores (< 0.7 nm) in CAC-1. This limited ultramicroporosity may be attributed to its relatively low to moderate burn-off level — the mass reduction from the raw feedstock to the final AC. Despite this, the scarcity of ultramicropores in CAC-1 is unlikely to adversely impact its PFAS adsorption capacity, as PFAS predominantly adsorb within micro- and mesopores.

By contrast, CAC-2, CAC-3, and CAC-4 exhibit substantially greater ultramicropore volumes, which is most likely resulting from higher burn-off levels during activation. Amongst the four samples, CAC-4 demonstrates a particularly well-developed mesopore structure whilst maintaining a high micropore volume. Given that PFAS adsorption occurs in both micropores and mesopores, CAC-4 is expected to exhibit superior adsorption performance based on its pore size distribution and surface area characteristics alone.

To complement the N_2 adsorption isotherm analysis presented above and to provide quantitative comparison of accessible microporosity across all materials, butane activity measurements were undertaken for the four ACs and the woodchip-derived biochar. Butane activity is commonly used as a proxy for accessible micropore volume, as butane molecules preferentially adsorb within micropores and small mesopores due to their molecular size and non-polar character. As such, this parameter provides a practical indicator of pore accessibility that is directly relevant to adsorption performance.

In this study, butane activity measurements were particularly valuable because conventional approaches for assessing microporosity were not available for all materials at a certain time. The BET pore analyser was out of operation during the experimental period and carbon tetrachloride activity testing was not permitted due to regulatory restrictions. Consequently, butane activity, determined using the ASTM D5742-16 Standard Test Method for Determination of Butane Activity of AC, was employed to enable consistent comparison of the biochar with the four ACs. The resulting values, summarised in Table 5.2, represent the average of five replicate experiments and therefore provide a robust basis for comparison.

Table 5.2. Butane activity measurements for the four ACs and biochar.

Sample	Butane activity (%)
CAC-1	61.15
CAC-2	51.61
CAC-3	58.82
CAC-4	63.51
biochar	9.79

As shown in Table 5.2, substantial differences in butane activity are observed between the ACs and the biochar, reflecting variations in accessible micropore volume. The ACs exhibit significantly higher butane activity values, consistent with their well-developed microporous structures inferred from the N_2 adsorption isotherms. In contrast, the markedly lower butane activity of the biochar indicates limited accessible microporosity, which is consistent with its lack of post-pyrolysis activation and substantially lower BET surface area.

These results provide important quantitative context for interpreting adsorption behaviour discussed later in this chapter. Higher butane activity suggests a greater availability of micropores capable of supporting strong adsorption at low solute concentrations, while lower values indicate restricted pore accessibility. When considered alongside mesopore development and capillary condensation behaviour, the butane activity data help elucidate the structure–property relationships governing PFAS adsorption across the different materials.

Together with the N_2 adsorption isotherms and pore size distribution analysis, the butane activity measurements reinforce the distinction between the ACs and the biochar and support interpretation of their relative PFAS removal performance presented in subsequent sections.

5.3. Morphology of Activated Carbons

The scanning electron microscopy (SEM) images of the four AC samples are presented in Figure 5.5. The micrographs reveal that the external surfaces of the ACs are characterised by a variety of cracks, crevices, and granular features, differing in both geometry and size. These surface features are likely to have resulted from the release of volatile organic compounds during pyrolysis; a process further intensified during steam activation, contributing to the development of the porous structure.

In particular, the information presented in Figure 5.5(c) highlights irregularly shaped structures consistent with re-agglomerated AC, accompanied by a markedly rougher surface texture compared to the other samples. This roughness further supports the occurrence of re-agglomeration during activation.

Although the resolution and scale of the SEM images are insufficient to visualise micro- and mesopores directly, all samples clearly exhibit macropores (> 50 nm). The fractured and highly textured surfaces observed across the samples are consistent with the high surface area values determined through BET analysis, providing visual confirmation of the extensive porosity within the ACs.

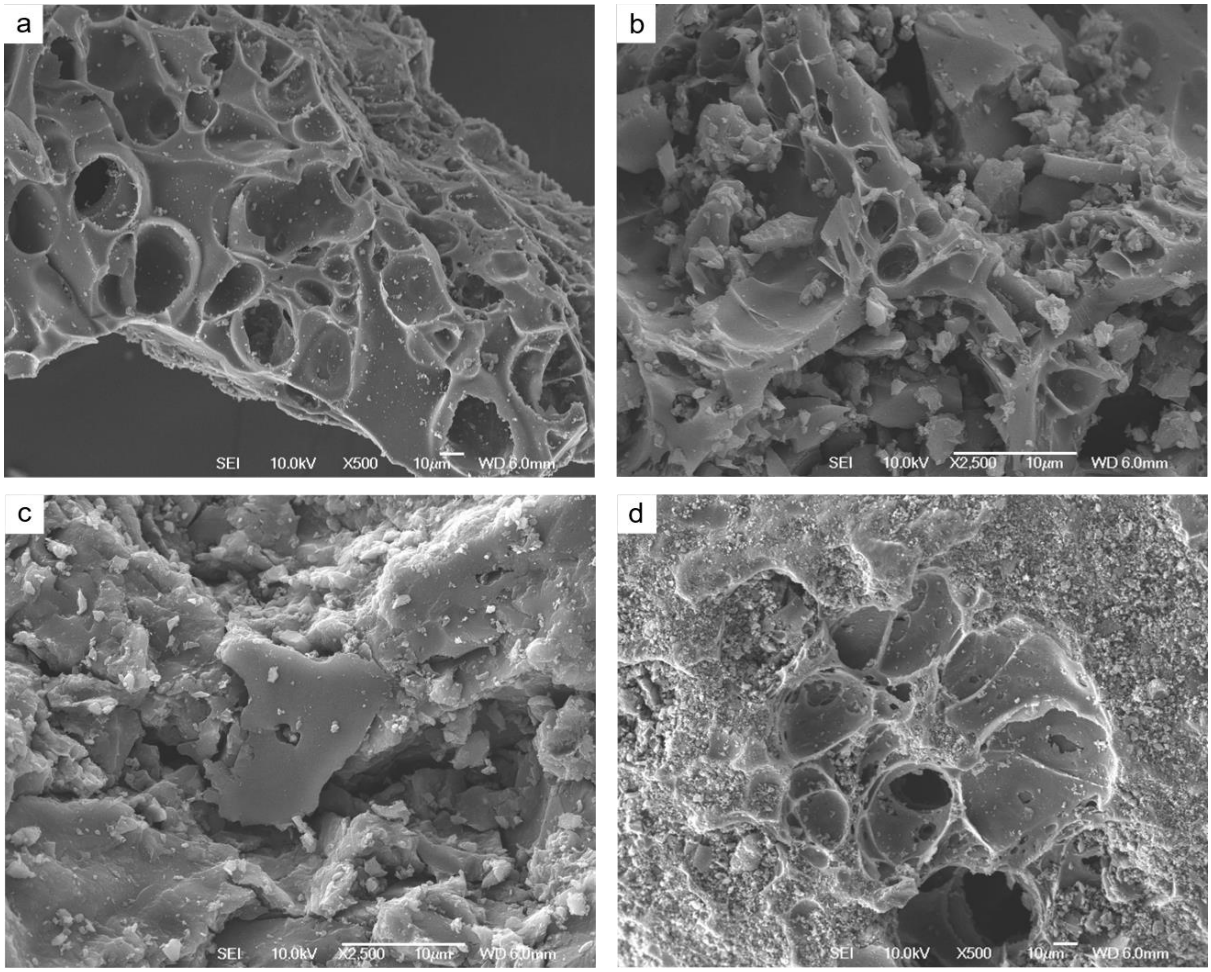


Figure 5.5. SEM images of the four activated carbons; (a) CAC-1, (b) CAC-2, (c) CAC-3 and (d) CAC-4.

Transmission electron microscopy (TEM) images of the four AC samples are presented in Figure 5.6 offering a closer look at their internal structure.

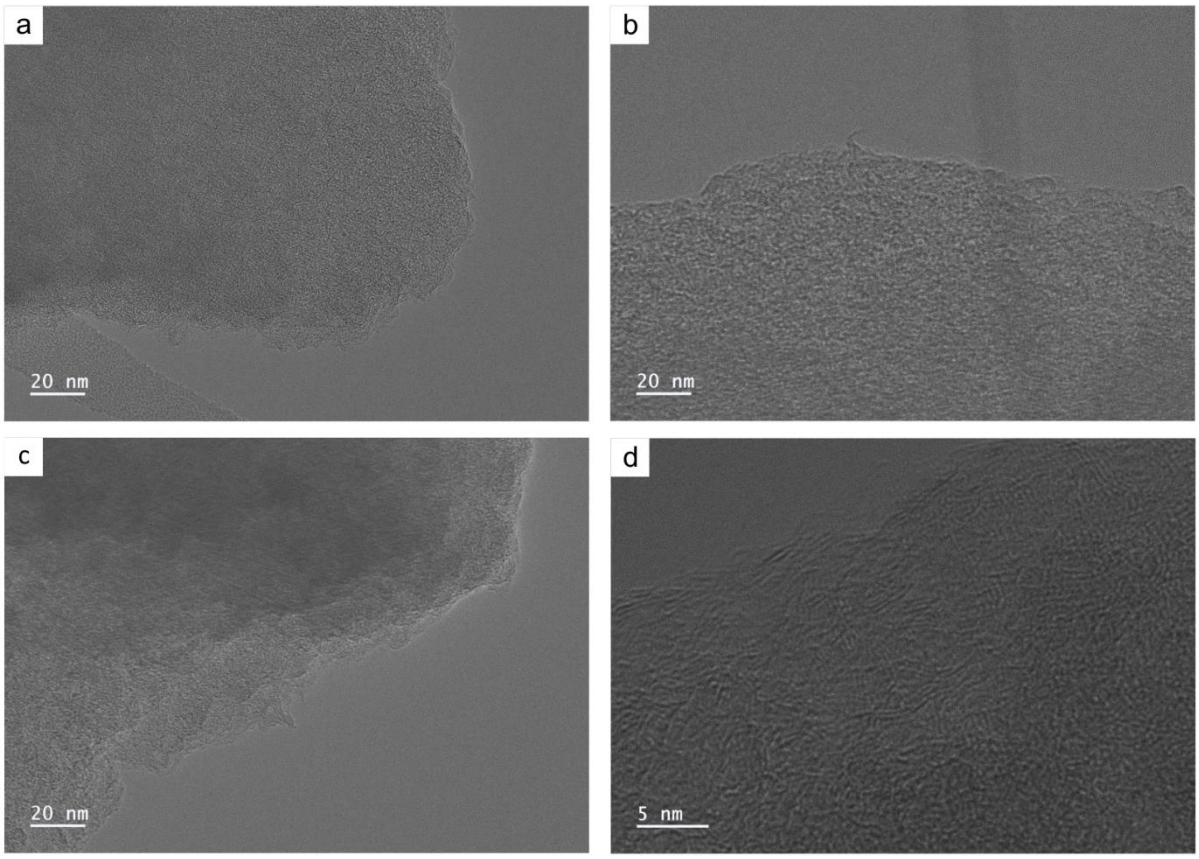


Figure 5.6. TEM images of the four ACs; (a) CAC-1, (b) CAC-2, (c) CAC-3 and (d) CAC-4.

Unlike SEM, TEM offers substantially higher spatial resolution and can provide indirect visual evidence of fine-scale porosity through contrast variations and textural features within the carbon matrix. While individual micropores are not directly resolved, TEM images can reveal regions of higher structural disorder and density variations that are consistent with the presence of nanoscale porosity beyond the resolution of SEM.

Aberration-corrected transmission electron microscopy (ACTEM) would have been a valuable technique for further structural elucidation. ACTEM, which employs magnetic lenses capable of subatomic resolution whilst operating at lower acceleration voltages,[174] could potentially reveal the atomic arrangement of carbon frameworks.

Such detailed imaging might offer insights into the presence of hexagonal and non-hexagonal ring structures within the carbon matrix, thereby deepening understanding of the material's microstructural organisation.

Comprehensive physicochemical characterisation was performed for the ACs in this study to support detailed interpretation of adsorption behaviour. In contrast, characterisation of the woodchip-derived biochar was necessarily more limited. The inclusion of biochar as a comparator material was decided at a late stage of the project, following completion of the primary AC-focused experimental programme. As a result, only selected characterisation techniques were applied to the biochar, specifically BET surface area analysis and butane activity measurements, which were sufficient to establish its relative porosity and adsorption potential.

These measurements provided the key textural parameters required for meaningful comparison with the ACs, particularly with respect to accessible surface area and microporosity. More extensive characterisation techniques were not pursued due to time and instrumentation constraints and because the biochar was not intended to be examined with the same depth as the ACs. Instead, it was included to provide contextual insight into the performance of a low-cost, non-AC material relative to commercially relevant ACs.

The limited characterisation of the biochar is therefore reflective of its role within the study as a comparative benchmark rather than a primary focus. This distinction is taken into account when interpreting adsorption results and drawing conclusions regarding relative performance.

5.4. Physicochemical Properties of the Activated Carbons

5.4.1. Proximate and Ultimate Analyses

The results of the proximate analysis for the four AC samples are summarised in Table 5.3. This analysis provides insight into the proportions of combustible and non-combustible constituents within each sample, serving as a useful indicator for assessing AC quality. The fixed carbon content (wt%) is influenced by the corresponding ash and moisture contents, whilst the volatile matter (wt%) reflects the residual volatiles remaining after the activation process.

Typically, biomass-derived ACs exhibit a higher volatile matter content compared to coal-based ACs due to fundamental differences in the chemical composition of their precursor materials. Biomass feedstocks, such as wood, coconut shells, and agricultural residues, contain substantially higher concentrations of hemicellulose, cellulose, and lignin, which are rich in oxygen-containing functional groups (hydroxyl, methoxy, and carbonyl groups) and aliphatic structures that readily decompose at relatively low temperatures.[233] In contrast, coal is a more thermally mature material with a higher degree of aromatisation and lower oxygen content, having undergone geological coalification processes over millions of years that have already driven off much of the volatile organic matter. Consequently, during pyrolysis and activation, biomass-derived precursors release a greater quantity of volatile organic compounds, including tar, methane, carbon monoxide, and low-molecular-weight oxygenated species, which manifests as a larger fraction of mass loss prior to and during pore development. This higher volatile matter content has important implications for the activation process itself: the greater mass loss means that achieving a given level of burn-off (the percentage of carbon consumed during activation) requires less severe activation conditions for biomass compared to coal, but it also means that controlling

pore structure development can be more challenging due to the complex interplay between volatile release, pore formation, and pore widening. Furthermore, the residual oxygen-containing functional groups that remain on biomass-derived ACs after activation tend to be more abundant and diverse compared to coal-derived carbons, which can significantly influence their adsorption behaviour, particularly for polar adsorbates such as PFAS where electrostatic interactions and hydrogen bonding play important roles.

In line with this, the coconut shell-derived AC sample CAC-2 shows an elevated volatile matter content relative to typical coal-derived ACs. Nevertheless, its measured volatile matter value of 5.12 wt% is relatively low for a biomass-derived precursor, suggesting that the activation and carbonisation history of this material resulted in effective removal of volatiles and a higher degree of carbon consolidation prior to pore development, which is generally associated with more stable, well-AC structures.[234]

Table 5.3. Proximate analysis data for the four activated carbons.

	Proximate analysis (as received, wt%)			
Sample	Moisture	Volatile matter	Fixed carbon	Ash
CAC-1	4.65 ± 1.66	3.36 ± 0.03	77.38 ± 4.93	14.61 ± 3.47
CAC-2	6.77 ± 0.39	5.12 ± 0.12	80.51 ± 0.87	7.60 ± 0.84
CAC-3	13.9 ± 4.78	3.33 ± 0.28	76.83 ± 4.73	5.94 ± 0.23
CAC-4	5.36 ± 0.92	2.19 ± 0.40	81.18 ± 0.64	11.27 ± 0.24

Amongst the four ACs, CAC-1 exhibits the highest ash content, approaching 15 wt%. This value is near the 16 wt% rejection threshold established by CPL Activated Carbons, suggesting that CAC-1 is close to the upper limit of acceptable ash levels.

Elevated ash content may indicate over-activation during the production process, leading to excessive mineral residue formation.[235]

High ash content can negatively impact the performance of AC by contributing to pore blockage and reducing the effective surface area.[236] Additionally, increased ash reduces the relative proportion of fixed carbon, thereby diminishing the number of available adsorption sites and lowering the overall adsorption capacity of the material.

The ultimate analysis results, detailing the elemental composition by weight percentage (wt%) of carbon (C), nitrogen (N), hydrogen (H), sulphur (S), and oxygen (O), are presented in Table 5.4.

Table 5.4. Ultimate analysis data for the four activated carbons.

	Chemical Compositions (as received, wt%)				
Sample	C	N	H	S	O
CAC-1	73.2 ± 0.12	0.8 ± 0.02	0.6 ± 0.10	0.9 ± 0.03	24.5
CAC-2	80.6 ± 0.26	0.8 ± 0.01	1.3 ± 0.01	0.6 ± 0.05	16.7
CAC-3	76.3 ± 0.20	0.5 ± 0.03	2.0 ± 0.02	0.8 ± 0.02	20.4
CAC-4	79.9 ± 0.68	0.5 ± 0.02	0.9 ± 0.03	0.8 ± 0.02	17.9

The ultimate analysis reveals that all four AC samples possess relatively similar carbon contents, with variations within a narrow range of approximately 7 wt%. Nitrogen content remains below 1 wt% across all samples. This low nitrogen presence may be a disadvantage for the adsorption of short-chain PFAS, as positively charged nitrogen-containing surface functional groups have been shown to enhance electrostatic interactions with the negatively charged head groups of PFAS molecules.[237]

The relatively high oxygen content, ranging from 16.7 to 24.5 wt%, suggests that the activation conditions were optimised to promote the formation of oxygen-containing functional groups on the AC surfaces. These groups can influence adsorption behaviour through mechanisms such as hydrogen bonding and dipole–dipole interactions with PFAS head groups and other polar moieties.[238] However, whilst the oxygen content provides a useful quantitative measure, it does not reveal the specific chemical nature of these functional groups. Therefore, complementary surface-sensitive techniques such as X-ray photoelectron spectroscopy (XPS) are necessary for a more comprehensive characterisation of the ACs' surface chemistry.

5.4.2. X-Ray Photoelectron Spectroscopy

The chemical groups and corresponding peak labels are presented in Table 5.5 and the fitted XPS spectra for the four ACs are presented in Figure 5.7.

Table 5.5. The chemical groups and corresponding peak labels.

Chemical group	Synthetic component label
C-C low	Peak I
C-C primary	Peak II
C-C high	Peak III
C-O	Peak IV
C=O	Peak V
COO	Peak VI

To determine the various oxygen-containing functional groups present on the AC surfaces, high-resolution scans of the C1s region were collected for each sample using 0.1 eV step sizes. The C1s spectrum corresponds to the binding energy region of core-

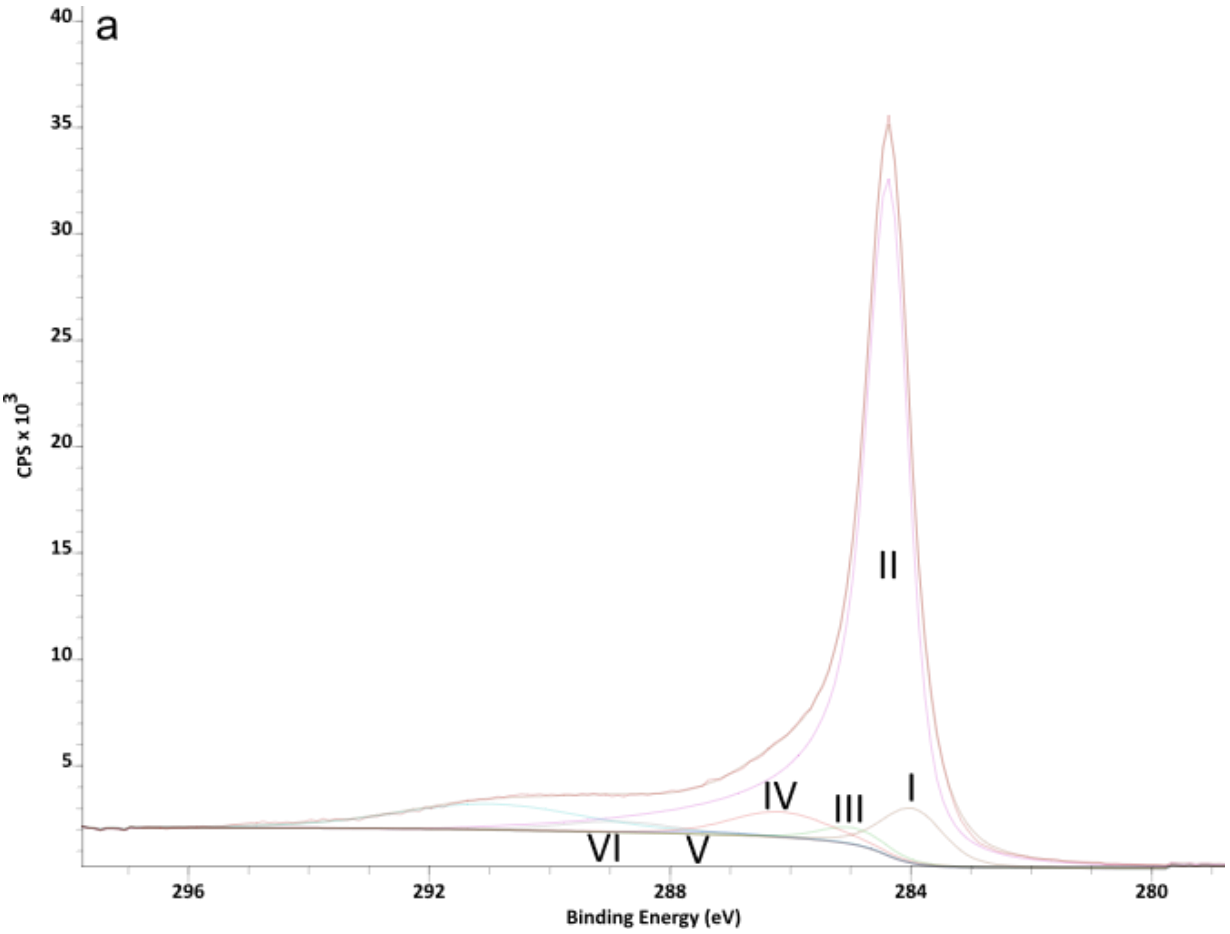
level electrons (1s orbital) in carbon atoms, typically centred around 284-285 eV. This region is particularly informative for ACs because carbon atoms in different structural environments exhibit characteristic shifts in their binding energies due to variations in the local chemical configuration and bonding geometry.

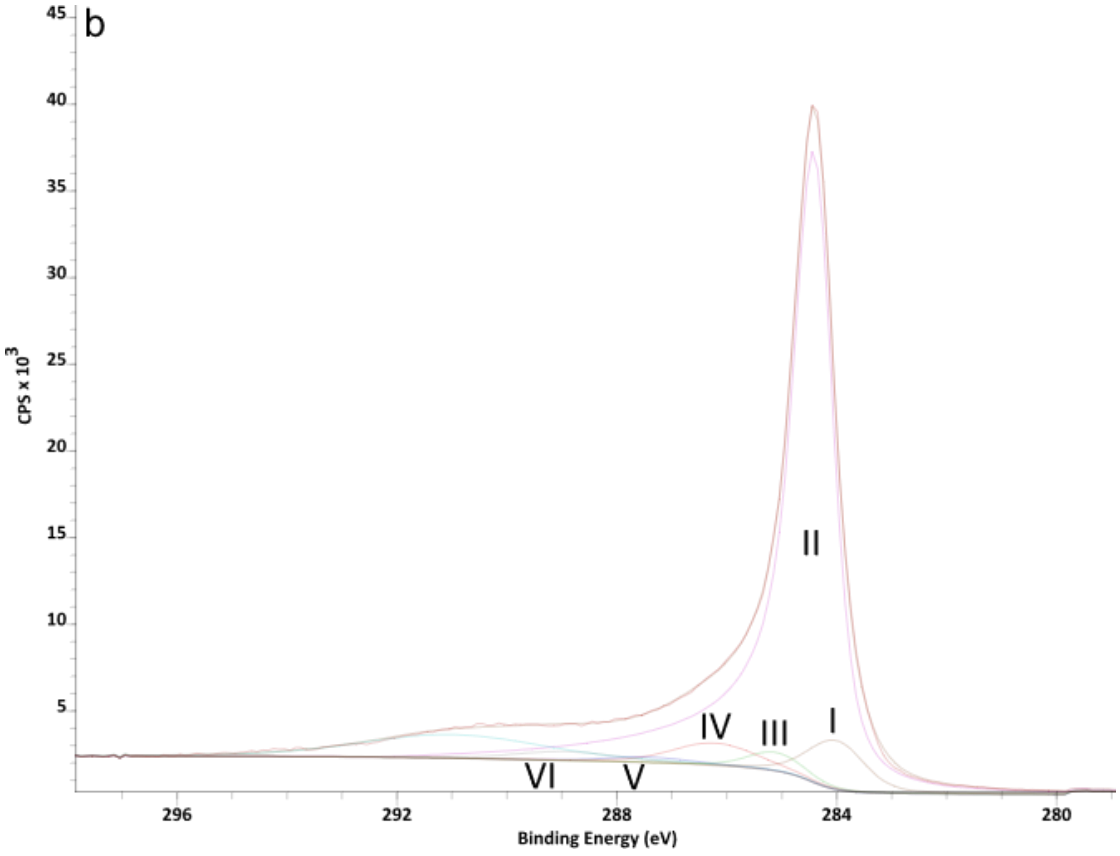
The C1s region of ACs cannot be adequately described by a single peak due to the presence of structural heterogeneity arising from defects, strain, and variations in the sp^2 aromatic network. Consequently, the C-C region was deconvoluted into three distinct peaks to account for these structural variations. The primary C-C peak (C-C primary), positioned at approximately 284.4-284.6 eV, corresponds to sp^2 hybridised carbon atoms in unstrained, six-membered aromatic rings- the dominant structural motif in ACs. This peak represents the graphitic or graphene-like domains within the carbon structure, where carbon atoms exist in energetically favourable, planar hexagonal arrangements.

The C-C low peak, shifted to lower binding energies (approximately 283.4-284.0 eV, a downshift of ~0.4-0.6 eV from the primary peak), arises from carbon atoms in strained five-membered rings (cyclopentane-like defects) embedded within the polyaromatic structure. The formation of five-membered rings induces out-of-plane distortions in adjacent six-membered rings, creating localised strain that reduces the core electron binding energy. Such pentagonal defects are common in non-graphitising carbons like ACs and have been identified in high-resolution transmission electron microscopy studies of AC microstructure. The intensity of the C-C low peak provides an indication of the concentration of small-ring defects, which typically decreases with increasing activation temperature as the carbon structure undergoes thermal annealing and rearrangement toward more stable six-membered ring configurations.

The C-C high peak, shifted to higher binding energies (approximately 284.8-285.4 eV, an upshift of ~0.4-1.0 eV from the primary peak), is attributed to several overlapping contributions: (i) carbon atoms in strained seven-membered or larger rings (cycloheptane and higher) within the aromatic network, which experience increased binding energy due to ring strain and distortion; (ii) sp^3 hybridised carbon atoms at edge sites or in aliphatic linkages, which exhibit higher binding energies than sp^2 carbons; and (iii) carbon atoms in small aromatic clusters adjacent to carbonyl groups, where long-range electronic effects from the electronegative oxygen increase the binding energy of nearby carbons. The presence of the C-C high peak is indicative of structural disorder and incomplete aromatisation, which are characteristic of ACs produced at moderate temperatures (400-600°C). As activation temperature increases and aromatic condensation proceeds, the relative intensity of this peak typically decreases, reflecting the elimination of large-ring defects and sp^3 carbons through thermal restructuring.

By deconvoluting the C-C region into these three peaks, it becomes possible to semi-quantitatively assess the degree of structural order and defect concentration in the AC samples. These structural features are important for understanding PFAS adsorption behaviour, as defect sites can influence the accessibility of micropores, the distribution of surface functional groups, and the overall hydrophobicity of the carbon surface.


a
CPS x 10^3
40
35
30
25
20
15
10
5
II
IV
III
I
VI
V
296
292
288
284
280
Binding Energy (eV)


b
CPS x 10^3
45
40
35
30
25
20
15
10
5
II
IV
III
I
VI
V
296
292
288
284
280
Binding Energy (eV)

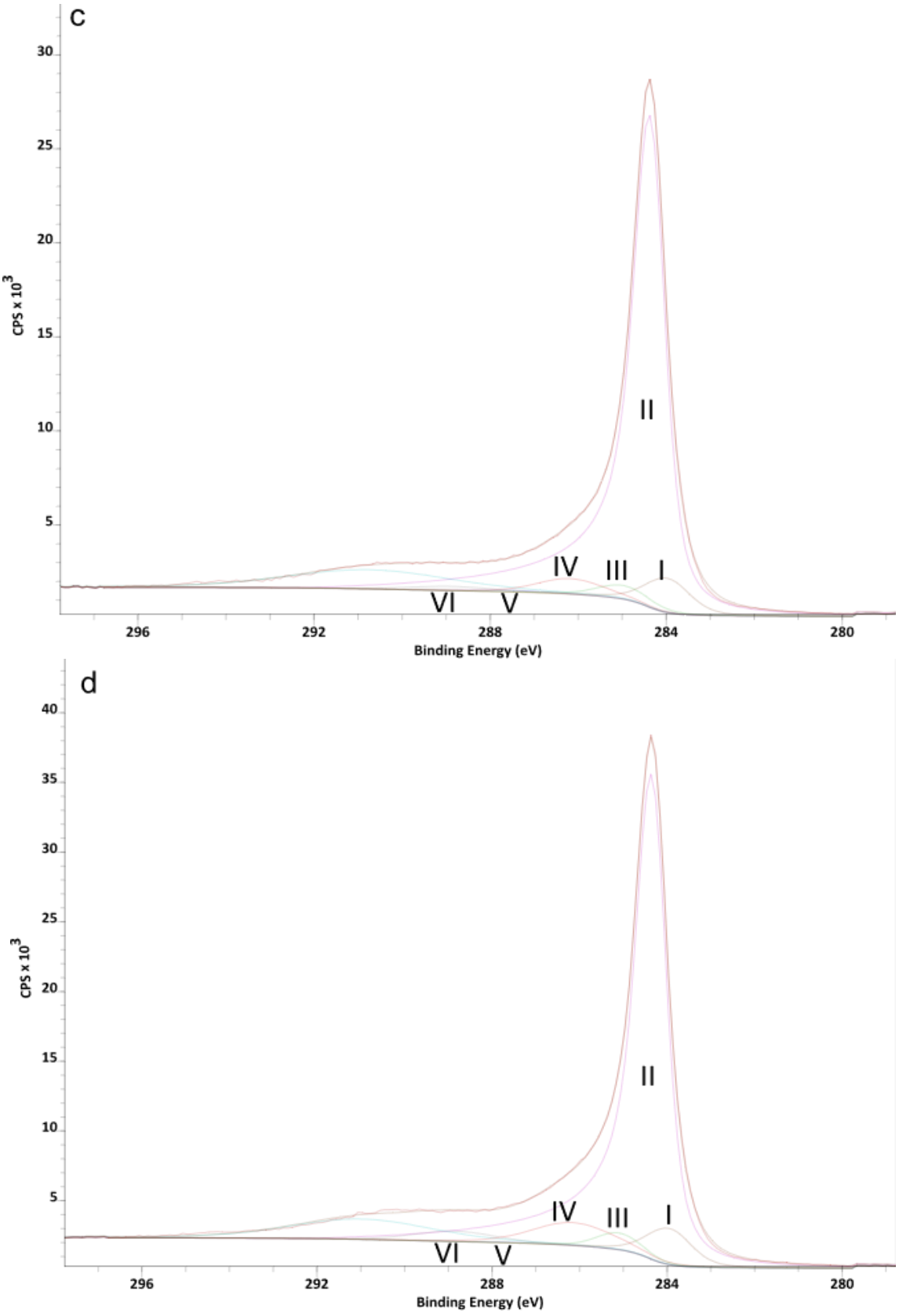


Figure 5.7. The fitted C1s XPS spectra for (a) CAC-1, (b) CAC-2, (c) CAC-3 and (d) CAC-4.

Various peak shapes have been developed for X-ray photoelectron spectroscopy (XPS) peak fitting, with more being introduced in recent years to accommodate increasingly complex materials.[239, 240] Historically, the Doniach–Šunjić (DS) line shape has been widely used for modelling asymmetric peaks; however, a significant limitation of the DS function is that it lacks a convergent integral, as it integrates to infinity.[241]

To address background contributions in XPS spectra, the Shirley background subtraction method is commonly employed. This approach assumes constant background levels on either side of a peak and enables more accurate quantification by isolating peak intensities.[242] For the XPS analysis performed in this study, a more advanced peak-fitting approach was adopted using the recently developed Doniach–Šunjić–Shirley (DSS) line shape. This hybrid model integrates the DS function's treatment of energy loss with a Shirley-style background correction.[243]

The deconvolution of the C 1s spectra for the four ACs was based on the method proposed by Fairley *et al*.[243], who successfully applied the DSS line shape to deconvolute C 1s spectra in graphene oxide — materials with surface chemistry analogous to ACs.

In all four ACs, the asymmetric DSS line shape was applied specifically to the primary C–C peak (Peak II), with each sample analysed in five replicates. A pass energy of 20 eV was selected to minimise instrumental artefacts, but at the expense of a lower count rate. The peak fitting strategy was designed to ensure a consistent and minimised residual standard deviation (STD), aiming for values close to 1 whilst retaining all chemically expected components.

The primary C–C peak (Peak II), corresponding to aromatic carbon structures, was anchored at 248.8 eV and used as the reference for other carbon oxidation states. Notably, assignment of binding energies in graphitic materials can be complicated by π–π* shake-up effects arising from sp^2 hybridised carbon. In the ACs analysed, this shake-up feature overlaps with signals from carbon species possessing multiple oxygen bonds, leading to spectral convolution.

The C 1s envelope was resolved into seven distinct peaks, which are characteristic of chars and ACs. The full width at half maximum (FWHM) for the primary C–C peak was constrained to 1.2–2.0 eV, reflecting a relatively narrow distribution of aromatic carbon environments. Peaks attributed to oxygenated carbon species (C–O, C=O, and O–C=O; Peaks IV–VI) were assigned broader FWHM values of 1.8–2.2 eV, consistent with the more diverse range of chemical states. The π–π* shake-up peak, expected to be broader due to its delocalised electronic nature, was modeled with an FWHM between 2.0 and 3.0 eV.

In total, the deconvolution included:

- **Peak I (C–C low)** and **Peak III (C–C high)** – associated with structural defects and fitted using Lorentzian Asymmetric (LA) line shapes;
- **Peak II (C–C primary)** – modeled with the DSS line shape;
- **Peaks IV–VI (oxygenated carbon species)** – fitted with LA line shapes;
- ***Peak VII (π–π shake-up)**** – also fitted with an LA line shape.

The parameters and constraints used for the line shapes are detailed in Table 5.6.

Table 5.6. Parameters and line shapes employed for the peak model used in Figure 5.7.

Chemical group	Line shape	Position constraint	FWHM constraint	Synthetic component label
C-C low	LA (1,1,400)	PII – 0.4	1.2-2.0	Peak I
C-C primary	DS (0.1, 200, 52)	284.3–284.8	1.2-2.0	Peak II
C-C high	LA (1,1,400)	PII + 0.4-0.8	1.2-2.0	Peak III
C-O	LA (1,1,400)	PII + 1.8	1.8-2.2	Peak IV
C=O	LA (1,1,400)	PII + 3.0	1.8-2.2	Peak V
COO	LA (1,1,400)	PII + 4.5	1.8-2.2	Peak VI

The oxygen to carbon ratio (O:C) was calculated using Equation (5.1).

$$O{:}\,C = \frac{A_{C-OH} + A_{C=O} + \frac{1}{2}A_{C-O} + 2A_{COO}}{A_{Total}} \qquad (5.1)$$

Where A is the area beneath the specified peaks of Table 5.6. The values provided in Table 5.7 are the average of 5 deconvoluted spectra for each sample.

Table 5.7. Peak distribution and O:C ratio calculated from the C1s deconvolution.

Deconvolution peaks	Peak label	CAC-1	CAC-2	CAC-3	CAC-4
C-C low (%)	I	6.8	6.5	6.9	6.4
C-C Primary (%)	II	83.6	83.8	84.1	79.2
C-C High (%)	III	1.7	2.1	1.7	4.2
C-O (%)	IV	5.0	4.5	4.3	6.9
C=O (%)	V	0.8	0.8	0.9	0.4
COO (%)	VI	2.1	2.2	2.0	2.9
Pi-pi*		0	0	0	0
O:C (C1s)		0.10	0.10	0.09	0.13

The O:C atomic ratio derived from XPS analysis is comparable across CAC-1, CAC-2 and CAC-3; however, CAC-4 exhibits the highest O:C ratio among the four ACs. A higher concentration of surface functional groups on carbon surfaces is recognised as an important factor controlling PFAS uptake, as surface chemistry influences the balance of hydrophobic and electrostatic interactions between PFAS molecules and the adsorbent. In particular, positively charged or basic surface sites and surface moieties that can interact with PFAS anions have been correlated with increased adsorption affinity, especially for short-chain PFAS where electrostatic contributions become more significant.[244] Therefore, based on XPS data, CAC-4 is predicted to have greater affinity for short-chain PFAS relative to the other ACs.

Additionally, CAC-4 possesses a large specific surface area (as reported in Table 5.1), which is a critical factor for enhancing hydrophobic interactions, the dominant adsorption mechanism for long-chain PFAS. Both textural properties and surface chemistry are known to jointly govern PFAS adsorption performance, with larger surface area providing more available sites for interaction and functional groups modulating the nature and strength of those interactions, including electrostatic attraction and hydrogen bonding with PFAS head groups.[245] Therefore, from a surface chemistry and textural property standpoint, CAC-4 is expected to outperform the other ACs in the adsorption of both short- and long-chain PFAS.

X-ray photoelectron spectroscopy (XPS) is a powerful surface-sensitive technique that enables the semi-quantitative determination of surface oxygen-containing functional groups on ACs. Through analysis of the relative elemental compositions, XPS facilitates the calculation of the oxygen-to-carbon ratio, providing valuable insights into surface functionality. However, XPS data can be further corroborated by

complementary wet chemical techniques, such as Boehm titrations, which quantify the molar concentrations of acidic oxygen-containing groups.

5.4.3. Boehm Titrations

Boehm titration operates on the principle that different oxygenated functional groups exhibit distinct acid-base reactivities. Specifically:

- **$NaHCO_3$** neutralises **carboxylic acids**;
- **Na_2CO_3** neutralises **carboxylic and lactonic groups**;
- **NaOH** neutralises **carboxylic, lactonic, and phenolic groups**.

Therefore, under ideal conditions, the molar concentrations obtained from titrations are expected to follow this order: [NaOH] > [Na_2CO_3] > [$NaHCO_3$].

However, when Boehm titrations were conducted on the four ACs in this study, an anomalous trend was observed: the titrations using Na_2CO_3 consistently yielded higher molar concentrations than those using NaOH. According to the fundamental principles of Boehm titration, NaOH, being the strongest base typically employed, should neutralise a broader range of acidic surface functional groups, including carboxylic, lactonic and phenolic groups, and therefore yield equal or higher concentrations compared with Na_2CO_3.[246] In practice, however, indirect titration work has shown that Na_2CO_3 can produce higher apparent titration values under certain conditions, and that the precision and quantification derived from different bases can vary depending on reaction kinetics, endpoint determination and the specifics of the titration procedure. These methodological influences can lead to results that deviate from the expected neutralisation order.[247]

The reason for this discrepancy remains unclear, and it is unfortunate that the titration data could not be reliably used to validate the surface oxygen functionalities inferred from XPS. Nevertheless, the XPS analysis alone still offers strong predictive insights into the likely adsorption behaviour of each AC towards different PFAS types.

5.4.4. pH and Point of Zero Charge

The results of the pH drift and point of zero charge (PZC) experiments are presented in **Error! Reference source not found.**. The PZC represents the pH at which the net surface charge of an AC is zero. At solution pH values below the PZC, surface functional groups are predominantly protonated and the AC surface carries a net positive charge, whereas at pH values above the PZC, deprotonation leads to a net negative surface charge. This parameter therefore provides an important framework for assessing electrostatic interactions between AC surfaces and ionic adsorbates.

According to UK drinking water regulations, potable water must maintain a pH between 6.5 and 9.0. For optimal PFAS removal in water treatment applications, it is generally desirable for the AC to possess a PZC that exceeds the pH of the water being treated. Under such conditions, the AC surface acquires a net positive charge, which promotes electrostatic attraction with the negatively charged anionic head groups of PFAS molecules in solution. This effect is particularly relevant for short-chain PFAS, for which hydrophobic interactions are weaker and electrostatic contributions play a more significant role in adsorption.

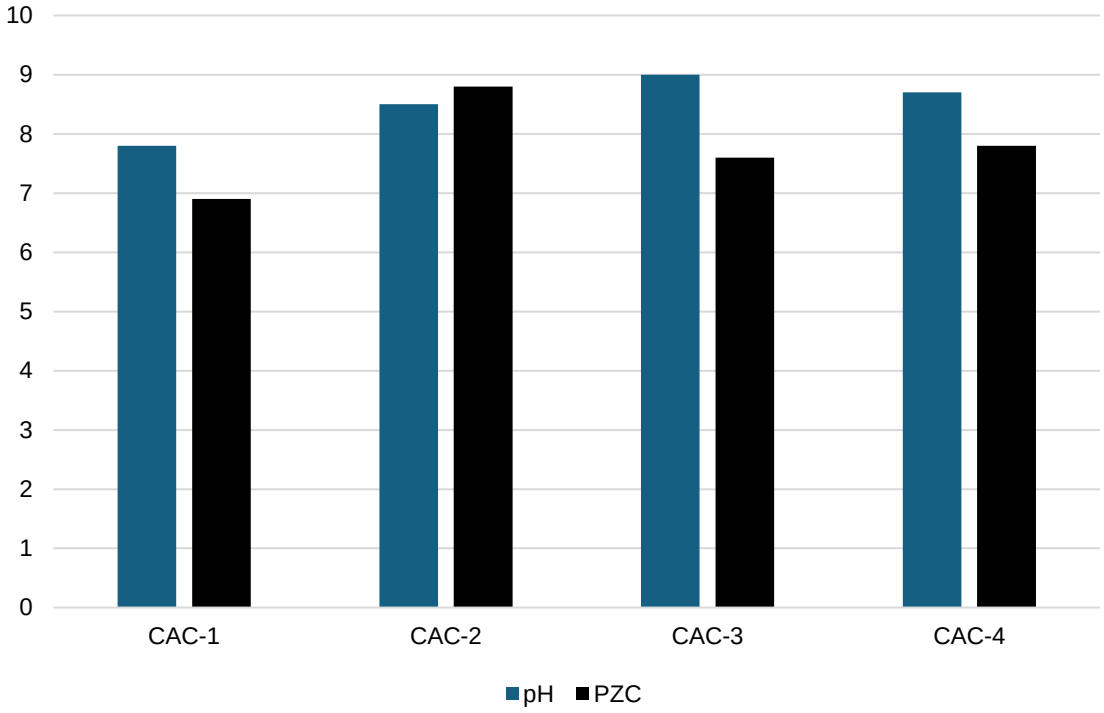


Figure 5.8. pH and point of zero charge of the four ACs.

The PZCs of all four ACs in this study fall within the regulatory pH range of 6.5 to 9.0. Whilst this alignment with drinking water standards is advantageous from an operational perspective, it complicates the prediction of adsorption performance under real-world conditions. When the solution pH lies close to the PZC, relatively small fluctuations in pH may result in changes to the net surface charge, causing the AC surface to alternate between weakly positive and weakly negative states. This dynamic behaviour may influence both the strength and stability of electrostatic interactions with PFAS molecules.

When considered alongside surface chemistry data obtained from XPS and Boehm titration, the similarity in PZC values across the four ACs suggests broadly comparable surface charge behaviour. However, subtle differences in PZC likely reflect variations in the distribution and acidity of surface functional groups. These differences may

contribute to variations in PFAS adsorption behaviour, particularly for short-chain PFAS, even when the overall PZC values fall within a narrow range.

Consequently, although all four ACs appear suitable for use in regulated water treatment environments based on their PZC values, their comparative effectiveness in PFAS removal under fluctuating pH conditions cannot be reliably predicted from PZC measurements alone. Instead, PZC should be interpreted in conjunction with surface chemistry, pore structure and adsorption data. Further empirical testing under representative operational conditions is therefore required to fully assess performance under dynamic pH regimes.

Chapter 6 ^{19}F NMR Method Development for the Rapid Screening of Novel Activated Carbon Adsorbents

6.1. Introduction

The need for non-selective and quantitative analytical methods for detecting per- and polyfluoroalkyl substances (PFAS) is increasingly critical. As the production and use of legacy PFAS such as PFOA and PFOS become more tightly regulated, chemical manufacturers are shifting toward novel PFAS compounds with varied and often less-characterised structures. These newer PFAS may be synthesized from a range of starting materials, resulting in diverse by-products, transformation products, and degradation pathways. Consequently, as regulatory controls expand to encompass more PFAS, the diversity and prevalence of these substances in the environment is also likely to increase.

Currently, the gold standard for detecting PFAS in aqueous samples is liquid chromatography tandem mass spectrometry (LC-MS/MS). However, as discussed in Chapter I, this technique has significant limitations. It generally requires the availability of isotopically labelled standards for accurate quantification, which restricts its effectiveness to under 100 compounds. Moreover, certain PFAS species exhibit poor ionization efficiency and may not appear in chromatograms, leading to underestimation of their presence.[248]

Nuclear magnetic resonance (NMR) spectroscopy is a non-destructive analytical technique capable of identifying and characterising novel compound structures without relying on existing chemical libraries. In particular, ^{19}F NMR offers quantitative capabilities whilst operating under conditions comparable to ^{1}H NMR. As PFAS contamination in drinking water continues to pose a growing threat to human health, the development of novel and more effective adsorbent materials is essential. This study presents the development of a new quantitative method for PFAS detection, aimed at facilitating the rapid screening and evaluation of innovative AC adsorbents.

6.2. PFAS Selection

The PFAS selected for this study were PFOA, PFOS, PFHxA, and PFBS, chosen for the following reasons:

- The most environmentally prevalent PFAS can be categorised into four groups: long-chain, short-chain, carboxylic acids, and sulfonic acids. PFOA and PFOS are representative of long-chain PFAS, whilst PFHxA and PFBS are short-chain variants. Additionally, PFOA and PFHxA are carboxylic acids, whilst PFOS and PFBS are sulfonic acids. These four PFAS were selected to demonstrate how different structural variants behave during the adsorption process.
- Over the years, it has become increasingly challenging to source PFAS from reputable chemical suppliers in the UK, even for research purposes. Whilst a broader range of PFAS would have been ideal for this study, limitations in availability constrained the selection.
- The experimental timeline was further limited by the restricted access to the university's cryoprobe 500 MHz NMR instrument, which was in high demand from other researchers. This constraint became the primary bottleneck in obtaining usable NMR data for the study. Given additional time, more

experiments could have been conducted on the selected PFAS, and contemporary alternatives, such as GenX (HFPO-DA), which replaced PFOA following its international ban, could have been explored.

- All four selected PFAS have commercially available isotopically labelled standards for use in LC-MS/MS. This technique was employed to validate the quantitative data obtained from the ^{19}F NMR experiments.

6.3. ^{19}F NMR Method Considerations

One of the primary objectives of the study was to *rapidly* screen novel AC adsorbents using ^{19}F NMR. To achieve this, the sample preparation process needed to be efficient, particularly when compared to more laborious methods such as solid-phase extraction (SPE), which demands significant resource and time. This meant trying to avoid SPE due to the huge amount of time and resources the processers require. As a consequence of having no SPE, this meant having a maximum of half of the final volume in the NMR tube being made up of the experimental aqueous PFAS solutions. As a result, selected NMR sample composition introduced potential challenges related to lock and shimming during NMR experiments.

High-resolution NMR magnets, whilst powerful, are not immune to imperfections and can exhibit a phenomenon known as ‘drift’. For accurate NMR data, it is critical that the precise frequency of the signals emitted by the sample are measured. As these frequencies are directly related to the strength of the magnetic field, any fluctuation in the field strength causes the signal frequency to drift, which can distort the spectrum. To mitigate this, the NMR system utilises a lock system. This system, which operates independently of the sample spectrometer, monitors deuterium (D) in the sample. Since the frequencies of deuterium signals are well-defined for a given magnet

strength, the lock system ensures the stability of the magnetic field by adjusting it to correct for drift, as illustrated in Figure 6.1 (taken from NMR Spectroscopy Explained[249]). The lock circuit feedback is essential for obtaining reliable, high-quality NMR data.

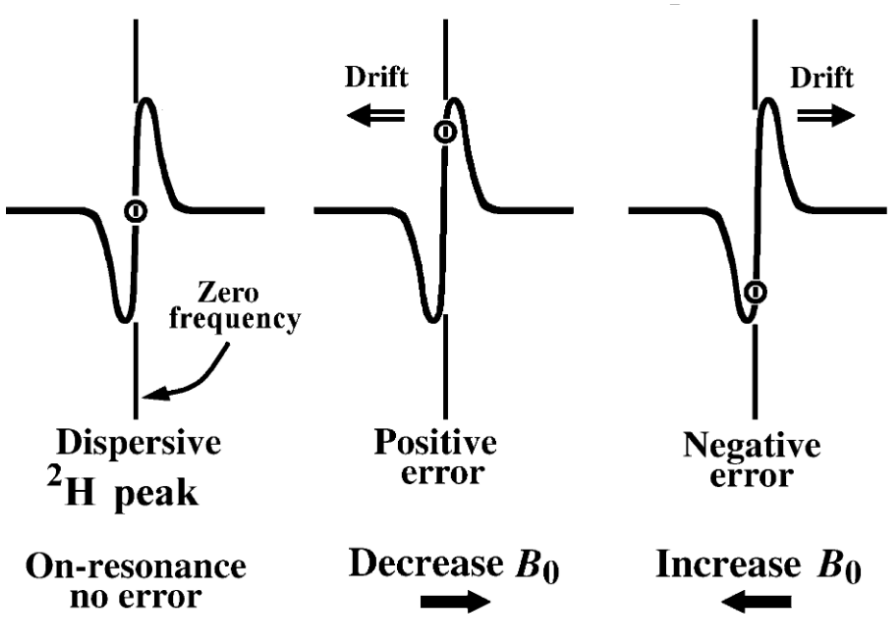


Figure 6.1. Lock circuit feedback loop that adjusts the strength of the magnetic field (B_0).[230]

A shim is a tool used in NMR to adjust the homogeneity of the applied magnetic field by correcting inhomogeneities. These inhomogeneities can arise from two sources: imperfections in the large magnet that cause variations in the magnetic field, and the presence of the sample or probe within the magnetic field, which can introduce deviations. In modern NMR instruments, shimming is typically achieved through small electrical circuits with some inherent resistance. When an electrical current is passed through these circuits, a secondary magnetic field is generated, which can be used to fine-tune the main magnetic field produced by the primary NMR magnet.

Poor shimming can result from a variety of factors including:

- The sample is too concentrated or not homogeneous.
- The presence of paramagnetic ions within the sample.
- Solid particulates in the NMR sample tube.
- Inadequate adjustment of the shim.

Examples of correct and incorrect free induction decay (FID) shapes are presented in Figure 6.2 (image taken from Modern NMR Techniques, A. Derome, 1987). In the context of this study, the primary risk for poor shimming arises if any AC particles are added to the NMR tube along with the analyte. To mitigate this issue, syringe filters with an appropriate mesh size (0.45 µm) were used to filter the treated PFAS solutions before transferring an aliquot into the NMR tube.

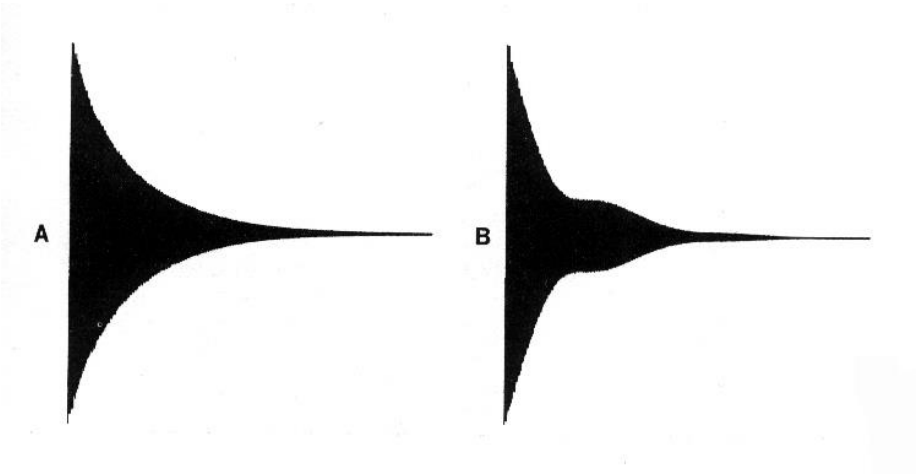


Figure 6.2. (A) correct FID shape produced by proper shimming, and (B) Incorrect FID shape produced by improper shimming.

To obtain a valid and usable NMR spectrum for PFAS samples, the use of a deuterated solvent is essential. Deuterium atoms do not produce signals in standard NMR spectra, thereby providing a “silent” background that enables the accurate detection

of fluorine or proton signals from the analytes of interest. Additionally, a sufficient volume or concentration of deuterium within the final NMR sample is required to maintain spectral stability and ensure precise frequency locking.

Given that approximately half of the final NMR sample volume was to consist of the filtered, treated aqueous PFAS solution, it was necessary to select a deuterated solvent that would be miscible with water and chemically compatible with PFAS compounds. During initial trials, deuterated chloroform ($CDCl_3$) mixed with a PFOA stock solution (100 mg L^{-1}) was used, which yielded a homogeneous mixture and a usable NMR spectrum. However, when the PFOA solution was treated with AC and subsequently mixed with $CDCl_3$, the solutions became immiscible, forming distinct layers. It is likely that this phase separation was due to the formation of micelles or hemi-micelles by PFOA molecules after prolonged residence in the treatment vessel, which may alter their solubility behaviour. Whilst reducing the concentration of the PFOA solution could potentially restore miscibility, this would also reduce the signal-to-noise ratio beyond the sensitivity threshold of the NMR instrument, compromising quantification accuracy.

Furthermore, $CDCl_3$ contains only a single deuterium atom per molecule. In cases where nearly half the sample volume consisted of H_2O, on occasion, this limited deuterium content was found to be insufficient to establish a stable lock, further complicating data acquisition. These issues highlighted the need for an alternative deuterated solvent system with better miscibility and adequate deuterium density for consistent locking.

A viable solution to the miscibility issue was the use of deuterium oxide (D_2O) as the NMR solvent. Given the full miscibility of H_2O and D_2O, and the known solubility of PFOA in both, this approach provided a homogeneous sample matrix. Indeed, high-

quality NMR spectra could be obtained using this solvent system. However, an additional consideration emerged regarding the need to increase the throughput of NMR analyses.

With hundreds of samples to be analysed over the course of the project, coupled with limited access to the NMR instrument, there was a clear imperative to minimise acquisition time. To achieve this, a paramagnetic relaxation agent was introduced to reduce the relaxation time (T_1) of the fluorine nuclei, thereby allowing for shorter repetition delays between scans. Chromium (III) acetylacetonate ($Cr(acac)_3$) was selected for this purpose, as it is known to enhance polarisation and accelerate spin-lattice relaxation rates.[250]

However, $Cr(acac)_3$ was found to be insoluble in the H_2O/D_2O mixture, rendering it unsuitable for use in this solvent system. This necessitated the evaluation of an alternative deuterated solvent that would be miscible with water-based PFAS solutions and compatible with $Cr(acac)_3$, whilst still maintaining the sensitivity and spectral quality required for rapid and reliable quantification.

Ultimately, deuterated methanol (CD_3OD) was selected as the NMR solvent for the study. CD_3OD contains significantly more deuterium atoms than either $CDCl_3$ or D_2O, four times and twice as many, respectively, which ensures a higher deuterium-to-hydrogen ratio in the final NMR sample. This facilitates the establishment of a reliable lock in each experiment. Furthermore, the aqueous PFAS solution exhibited excellent miscibility with CD_3OD at a 1:1 volume ratio, and the paramagnetic relaxation agent chromium(III) acetylacetonate [$Cr(acac)_3$] dissolved readily in this solvent mixture at a final concentration of 4 mg mL^{-1}.

A final consideration in method development was the selection of a suitable internal standard to enable the quantification of PFAS based on the terminal $–CF_3$ signal. The internal standard needed to; (i) contain the nucleus of interest ^{19}F, (ii) be soluble in the CD_3OD/H_2O mixture, (iii) be present at a concentration comparable to the PFAS analytes to achieve an optimal signal-to-noise ratio, and (iv) produce a non-overlapping, well-resolved signal. Additionally, it was preferable that the internal standard's signal fell near the analyte signal to minimise quantification error due to potential chemical shift variation.

Two compounds met these criteria and were subject to initial evaluation: hexafluorobenzene (HFB) and 4,4'-difluorobenzophenone (DFBP). CD_3OD, HFB yields a sharp signal at around –165 ppm, whilst DFBP produces a signal nearer to –107 ppm. The $–CF_3$ group of most PFAS compounds resonates at approximately –82 ppm. Given its closer proximity to the analyte peak, DFBP was adopted as the internal standard for all subsequent NMR experiments, offering improved accuracy in quantification due to reduced chemical shift separation.

A core principle throughout the method was to minimise sample preparation and keep the method compatible with high sample throughput, in contrast with extraction-heavy LC–MS/MS protocols. Therefore, samples were prepared directly in NMR tubes with deuterated methanol and an internal standard, using acquisition parameters optimised for quantitative work (90° flip angle, adequate relaxation delay, and sufficient transients to exceed the minimum S:N ratio). Locking and shimming required extra care because aqueous PFAS solutions were deliberately not put through any SPE apparatus to preserve speed; a stable lock circuit was therefore critical to mitigate field drift and ensure a flat baseline (Figure 6.1). Poor shimming produces both line-shape distortion and phase distortion, which materially affects peak areas; therefore, a standardised

shim routine was implemented before each NMR experiment and the FID shape was always verified against a standard accepted model spectrum.

6.4. ^{19}F NMR Parameter Tuning and Optimisation

The ^{19}F NMR spectra were acquired on a Bruker 500 MHz spectrometer equipped with a broad-band tuneable liquid-nitrogen cooled cryoprobe and room temperature TXI probe. The cooled cryoprobe slows the random motion of electrons within the circuitry of the instrument, which dampens the electronic noise, thus producing a higher quality spectrum. The highest resonance frequency of ^{19}F nuclei is 470 MHz on a 500 MHz NMR instrument, so the frequency was set accordingly.

Each PFAS sample was analysed over a total experimental time of 2 hours and 20 minutes, corresponding to 1024 scans. The acquisition parameters included a 90° pulse width of 14 µs, a spin-lattice relaxation delay sufficient to allow full relaxation of all ^{19}F nuclei, and a spectral window from –145 to –30 ppm to ensure comprehensive capture of all relevant fluorine signals.

The final concentration of the paramagnetic relaxation agent chromium(III) acetylacetonate [$Cr(acac)_3$] was set at 4 mg mL^{-1}. This concentration was chosen based on findings by Gauthier *et al.*, who reported it as the optimal compromise between relaxation enhancement and spectral resolution.[219] Concentrations exceeding 4 mg mL^{-1} resulted in increased line broadening, whilst lower concentrations failed to significantly reduce T_1 relaxation times. Experimental trials with 8 mg mL^{-1} $Cr(acac)_3$ were conducted, but complete dissolving could not be achieved in the 1:1 CD_3OD:H_2O solvent system.

Following optimisation of the acquisition parameters, SNR was assessed to validate the suitability of the method for quantitative analysis. SNR is defined as the ratio of peak height to the standard deviation of the baseline noise. A minimum SNR of 3:1 is

required for reliable quantification in NMR, although higher values are preferred to ensure robustness without extending acquisition time excessively. SNR can be improved through signal averaging, as the fluorine signals align constructively across scans whilst the random noise components partially cancel. However, due to the square-root relationship between SNR and the number of scans, there are diminishing returns with increasing scan count. Preliminary tests using PFOA at 1 mg L^{-1} yielded an SNR of 4:1 with 1024 scans, confirming the method's suitability for use in subsequent adsorption isotherm and kinetics studies (Figure 6.3).

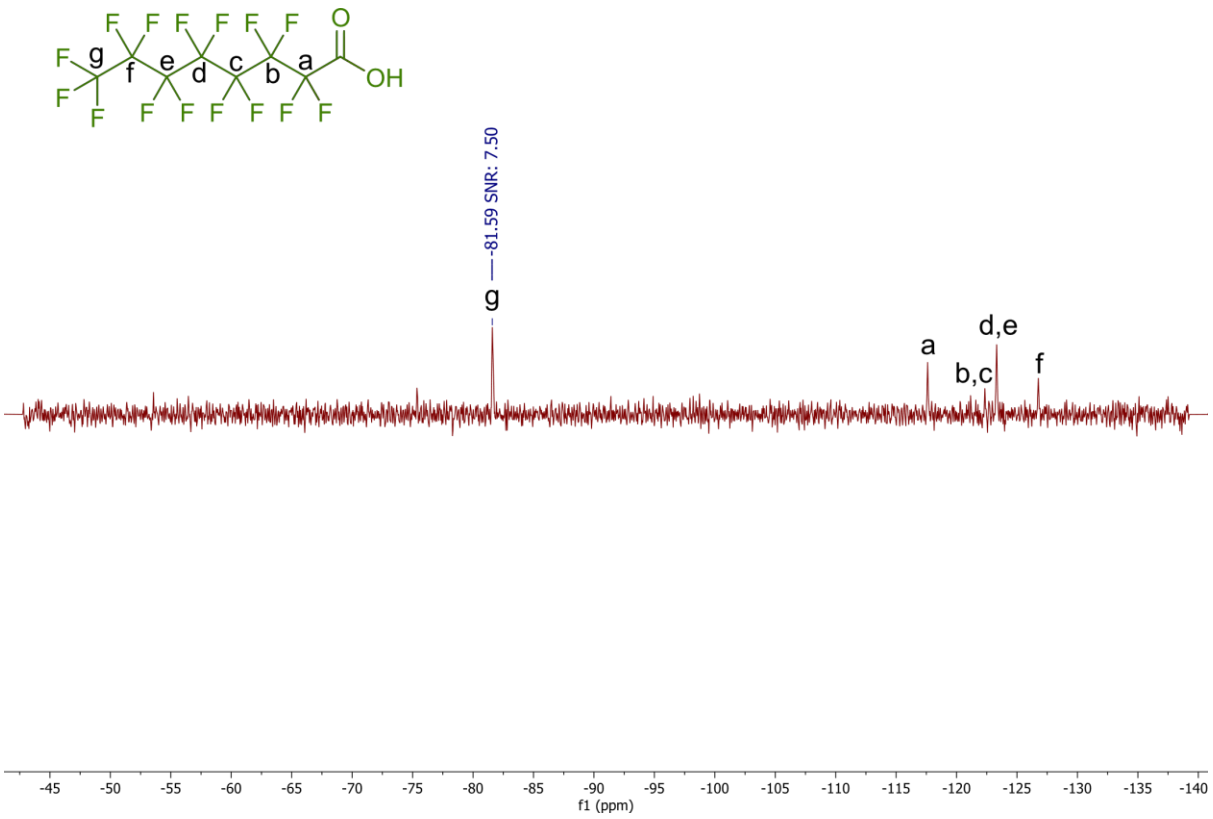


Figure 6.3. ^{19}F NMR spectrum of PFOA at 1 mg L^{-1} in 1:1 ratio H_2O:CD_3OD showing the -CF_3 peak at -81.59 ppm (g) with a signal to noise ratio of > 3.

6.5. ^{19}F NMR spectral processing

Quantification of PFAS concentration in the NMR samples was achieved by integrating the ^{19}F signals of interest to determine the relative concentrations of the internal standard and the analyte. Specifically, the terminal $–CF_3$ resonance of the PFAS molecules was selected for integration and compared against the integrated signal of the internal standard, 4,4′-difluorobenzophenone (DFBP). As the concentration of DFBP was precisely known, the relative integrals could be used to calculate the PFAS concentration using Equation (6.1):

$$C_{PFAS} = \frac{I_{PFAS}}{I_{DFBP}} \cdot \frac{N_{DFBP}}{N_{PFAS}} \cdot C_{DFBP} \qquad (6.1)$$

Where C is the concentration and I is the integral value obtained from the NMR spectrum.

Several critical considerations must be addressed to ensure the reliability of quantification using Equation 6.1. Firstly, the spectral window must include sufficient "empty" space at either end of the frequency range to prevent signal attenuation from the receiver filters. This attenuation typically affects signals located near the spectral edges and can lead to inaccurate integrations. To mitigate this, a spectral margin of at least 10% was included on both ends of the acquisition window, ensuring that both the $–CF_3$ resonance and the internal standard (DFBP) fell well within the unaffected central region of the spectrum.

There must also be adequate digital resolution within the spectrum for accurate integration (digital resolution is the spacing between data points). The digital resolution is expressed in units of Hz/point and is defined by twice the spectral width divided by the number of points, which also happens to be the reciprocal of the acquisition time. For quantitative NMR, a commonly accepted guideline is that the digital resolution should be less than half the full width at half maximum (FWHM) of the peaks being integrated. For instance, if a peak has a FWHM of 0.6 Hz, the digital resolution must be greater than 0.3 Hz/point to yield reliable integration results.

Uniform excitation of resonances across the spectral window is also essential for accurate quantification. This is particularly important in ^{19}F NMR due to the nucleus's high Larmor frequency and wide chemical shift range, which can result in excitation inhomogeneity. To minimise this effect, the transmitter frequency was carefully centred near the $–CF_3$ resonance, which also lies in close proximity to the chemical shift of the internal standard, DFBP. This strategic alignment ensured that both the analyte and standard resonances experienced similar excitation conditions, thereby improving the consistency and reliability of the integration-based quantification.

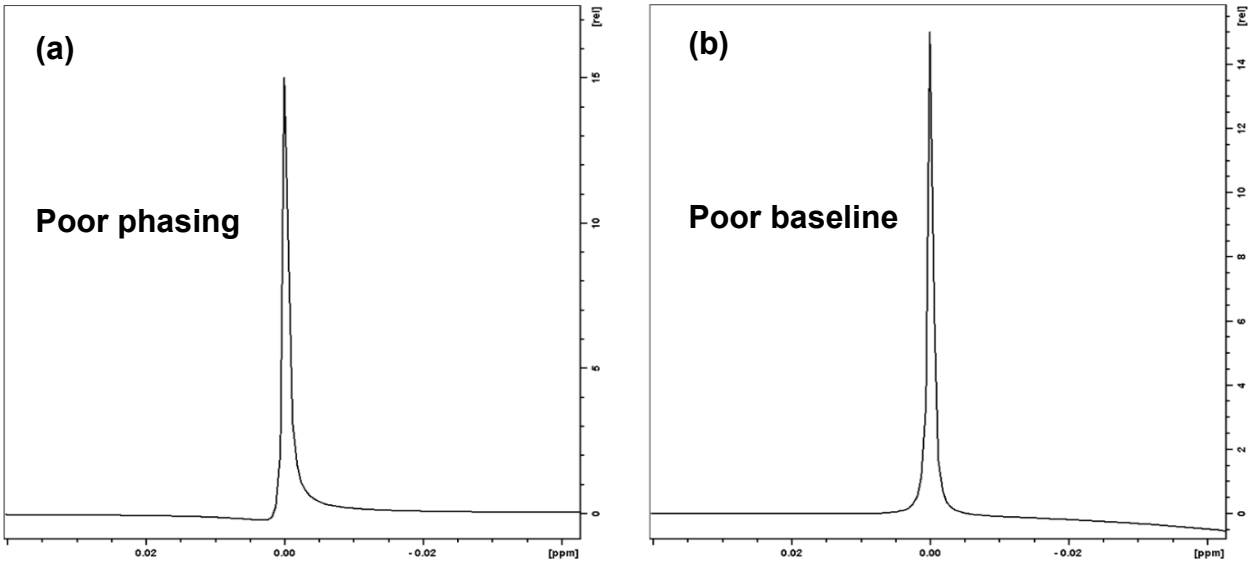


Figure 6.4. NMR spectra exhibiting (a) poor phasing and (b) a poor baseline.

For accurate peak integration, it is essential that the baseline of the spectrum remains flat. An example of a suboptimal NMR spectral baseline is presented in Figure 6.4. To correct this, the Whittaker smoother multipurpose algorithm, available in MNova software, was adopted due to its proven reliability and its application in other published works involving quantitative ^{19}F NMR.[251, 252] Similarly, precise phasing is crucial to achieving consistent results, as demonstrated in Figure 6.4.

In this study, phasing was initially performed automatically, with manual adjustments made only when discrepancies were detected. Additionally, it is critical to apply zero filling during the data processing phase. Zero filling involves appending zero-valued data points to the end of the free induction decay (FID) prior to performing the Fourier

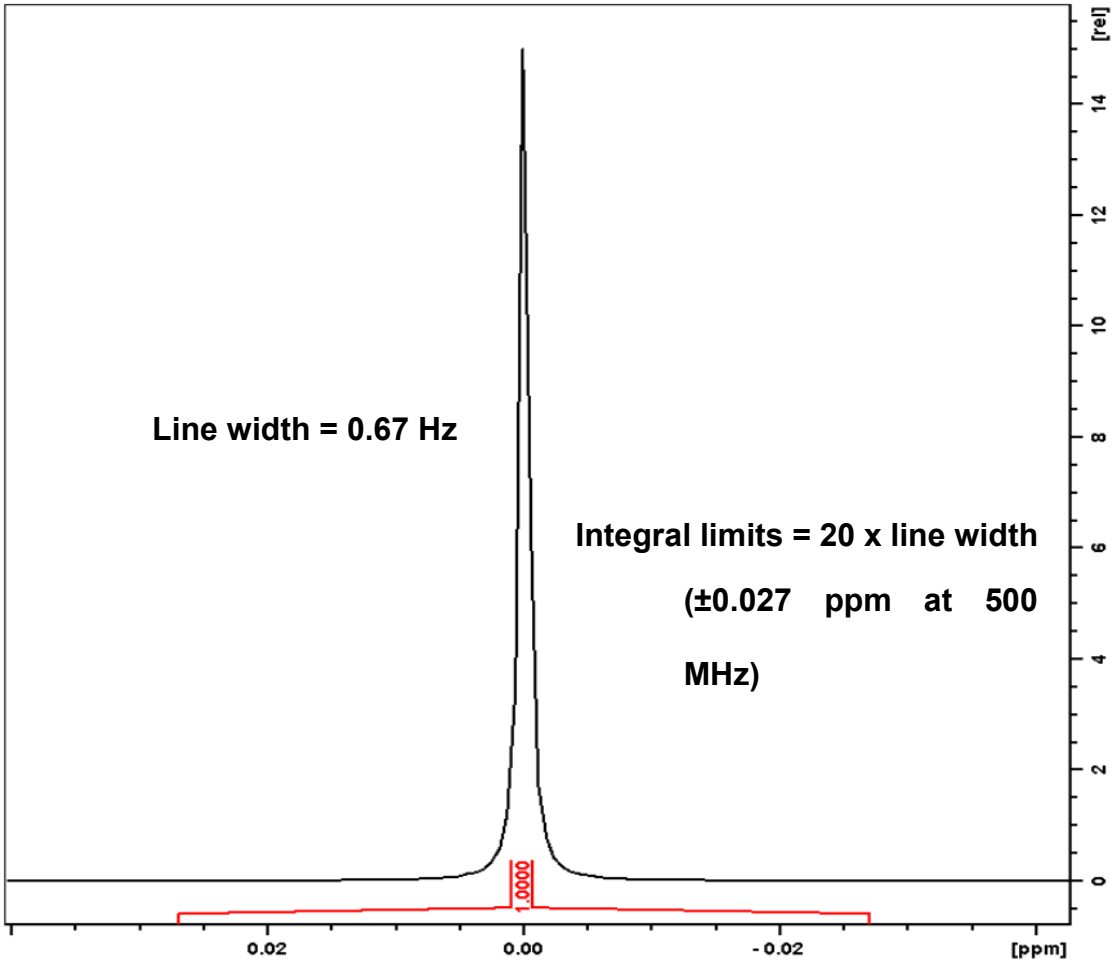


Figure 6.5. Minimum integration region required for accurate peak integration (±20 x peak width at half height).

Transform. To implement zero filling, the size of the real spectrum must be a multiple of the number of data points. In most cases, adjusting the real spectrum size to match the number of data points is sufficient. Furthermore, precise integration regions must be defined to ensure that over 99% of the peak areas are captured. This requires the integration region to extend to at least 20 times the width (Hz) of the peak of interest on both sides (Figure 6.5). For the spectra acquired in this study, the integration region was readily achieved, as the PFAS -CF_3 and DFBP standard signals did not overlap with any other signals within the ideal range.

Processing fidelity is as important as acquisition fidelity in quantitative NMR. Automatic phasing was used initially, with manual phasing only being conducted in particularly noisy spectra. For each spectrum, a quality control procedure was implemented via the assessment of four features: (i) full-width at half-maximum (FWHM) of the -CF_3 peak, (ii) S:N , (iii) baseline slope across the integral region, and (iv) residual spectral artefacts after baseline correction. Runs failing any quality control criterion were repeated.

A key limitation in this study arose from the 500 MHz NMR spectrometer used for all adsorption experiments. The instrument contained PFAS-coated component(s), which in some runs affected the NMR spectral baseline and led to failed measurements (Figure 6.6). The solution to this issue would be to exchange the PFAS-containing parts with PFAS-free components, but this was not possible considering the circumstances under which I was operating.

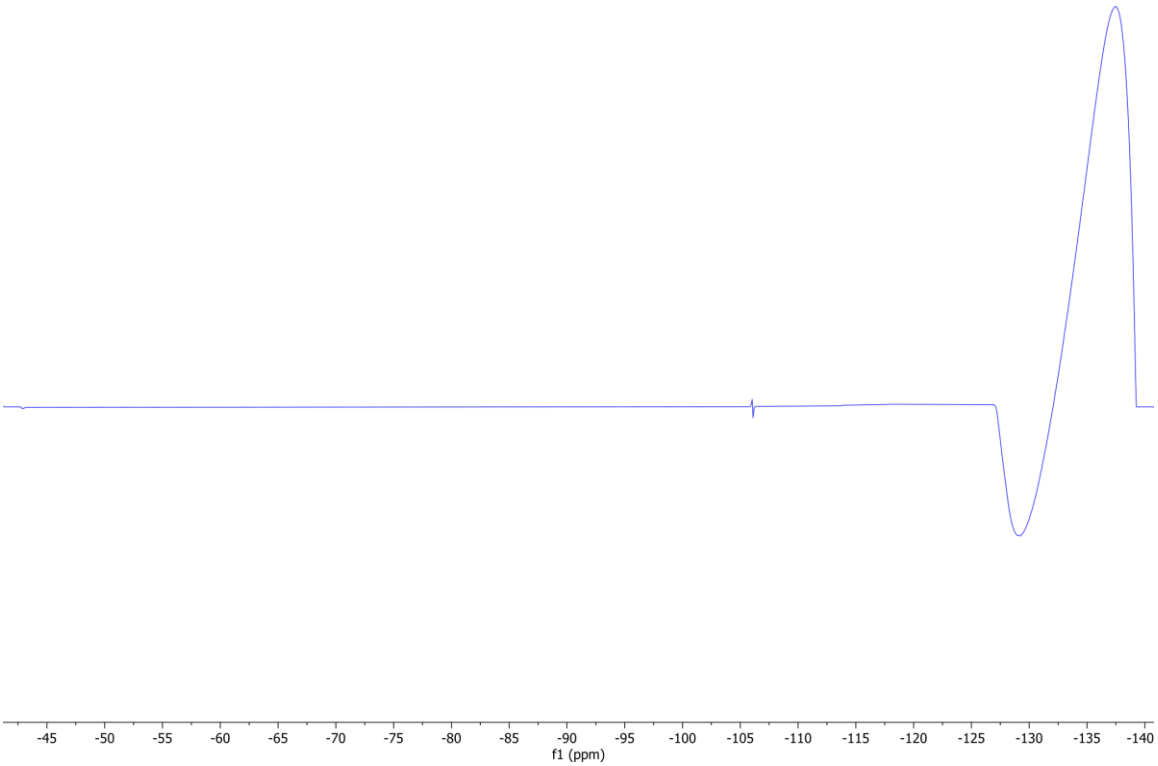


Figure 6.6. NMR spectral baseline distortion that occurred in some spectra.

6.6. Method validation with LC-MS/MS

The quantitative ^{19}F NMR method developed in this study should be validated through comparison with LC-MS/MS to assess its effectiveness in screening novel PFAS removal adsorbents. LC-MS/MS techniques have been successfully used for decades for quantifying PFAS at much lower concentrations than those employed in this study, such as in groundwater and river samples. Given this established precedent, LC-MS/MS was considered to be an appropriate method to verify the efficacy of the NMR approach. To evaluate both techniques, identical adsorption isotherm experiments were conducted and analysed using both ^{19}F NMR and LC-MS/MS. Agreement between the results from both methods would confirm the accuracy of the data obtained by ^{19}F NMR.

Unfortunately, the LC-MS/MS instrumentation owned by my research group was not in service for the majority of the project, and was only back in service for the final six

months of the four-year study period. When finally functional, the LC-MS/MS suffered from significant PFHxA contamination, which meant method validation experiments could not be conducted at environmentally relevant concentrations of PFAS. The source of the PFHxA contamination was not identified until the final month of my doctoral studies, so only a partially complete data set has been obtained for some initial adsorption isotherm experiments. The data is presented in Chapter 7.

6.7. ^{19}F NMR Method Summary

The quantitative ^{19}F NMR method developed in this chapter provides a rapid, non-destructive means of screening PFAS adsorption by novel AC adsorbents, entirely avoiding the solid-phase extraction (SPE) steps and compound-specific isotopically labelled standards required by conventional LC-MS/MS approaches. The following summarises the finalised analytical conditions and performance characteristics of the method so that the analysis can be reproduced independently.

Analytical conditions

All spectra were acquired on a Bruker 500 MHz spectrometer (^{19}F resonance frequency: 470 MHz) equipped with a broad-band tuneable liquid-nitrogen cooled cryoprobe. Samples were prepared by filtering the treated aqueous PFAS solution through a 0.45 µm syringe filter and mixing it with deuterated methanol (CD_3OD) in a 1:1 volume ratio directly in the NMR tube; no SPE or further pre-concentration was applied. The paramagnetic relaxation agent chromium(III) acetylacetonate [$Cr(acac)_3$] was added at a final concentration of 4 mg mL^{-1} to accelerate longitudinal (T_1) relaxation and reduce the required repetition delay. The internal standard 4,4′-difluorobenzophenone (DFBP) was added at a precisely known concentration to every

sample to enable quantification via Equation 6.1. All experiments were conducted at 298 K.

Acquisition parameters were as follows: 90° pulse width, 14 μs; spectral window, −145 to −30 ppm; acquisition time, 2.8 s; relaxation delay, 2 s; number of transients, 1024; total acquisition time per sample, approximately 2 hours and 20 minutes. The transmitter frequency was centred near the $-CF_3$ resonance at approximately −82 ppm, which also lies close to the DFBP signal at −107 ppm, ensuring both resonances experienced uniform excitation conditions. Spectra were processed in MestreNova™ using phase correction (automatic, with manual adjustment where necessary) followed by Whittaker–Smoother baseline correction, and zero-filling to the nearest power of two; apodisation was not applied so as not to alter peak areas. Quantification was performed by integrating the terminal $-CF_3$ resonance of each PFAS and comparing it against the DFBP integral, with the integration region extending to at least 20 times the peak width (Hz) on each side of the resonance to capture greater than 99% of the peak area.

Limits of detection and quantification

The limit of detection (LOD) and limit of quantification (LOQ) of the method were assessed using the signal-to-noise ratio (S:N) criteria of ≥ 3:1 and ≥ 10:1, respectively. Preliminary experiments using PFOA at 1 mg L^{-1} in the optimised sample matrix (1:1 CD_3OD:H_2O, 4 mg mL^{-1} $Cr(acac)_3$, 1024 transients) yielded an S:N of approximately 4:1, confirming that 1 mg L^{-1} represents approximately the LOD of the method under these conditions. The LOQ is therefore estimated to be in the region of 3 mg L^{-1} for PFOA; this will vary modestly between PFAS species depending on the number of fluorine atoms contributing to the $-CF_3$ signal and on individual T_1 relaxation times.

These detection and quantification limits are substantially higher than those routinely achieved by LC-MS/MS, which operates in the sub-nanogram per litre range. However, for the purpose of screening AC adsorbent materials at the mg L^{-1} concentration range used throughout this study, the method is entirely fit for purpose. The primary factors limiting sensitivity are the intrinsically lower sensitivity of NMR spectroscopy relative to mass spectrometry, the deliberate exclusion of pre-concentration steps to preserve analytical speed, and the dilution of the PFAS signal that results from preparing samples in a 1:1 CD_3OD:H_2O matrix. Sensitivity improvements could in principle be achieved by increasing the number of transients, using a higher-field instrument, or incorporating an SPE pre-concentration step, though each of these modifications would reduce the speed advantage that is central to the design of this method.

Reproducibility and quality control

Reproducibility was assessed by acquiring replicate spectra from the blank sample within each experimental set under identical conditions. Inter-run variability in the integrated $-CF_3$ peak area relative to the DFBP internal standard was consistently low, confirming that single-acquisition measurements were sufficient for reliable quantitative comparison between samples. A four-point quality control procedure was applied to every spectrum before data were accepted: (i) FWHM of the $-CF_3$ peak within an acceptable range; (ii) S:N exceeding 3:1; (iii) flat baseline slope across the integral region following Whittaker–Smoother correction; and (iv) absence of residual spectral artefacts. Any spectrum failing one or more of these criteria was discarded and the measurement repeated. Failures attributable to PFAS contamination of NMR instrument components, as described in Section 6.1.5, were recorded and the affected runs excluded from the dataset.

Chapter 7 Rapid Screening of PFAS Targeting Activated Carbon Adsorbents using ^{19}F NMR

7.1. Evaluation of AC for PFAS adsorption

The PFAS adsorption performances of the four CACs were systematically evaluated through a comprehensive experimental programme designed to characterise both equilibrium and kinetic aspects of the adsorption process. This dual approach was essential for developing a complete understanding of how these adsorbents interact with PFAS compounds under controlled laboratory conditions, and for establishing performance rankings that could inform practical water treatment applications. The evaluation strategy encompassed two principal experimental methodologies: adsorption isotherm studies to quantify equilibrium adsorption capacities and elucidate adsorption mechanisms, and adsorption kinetics experiments to determine the time-dependent behaviour of PFAS uptake and establish the rate-controlling steps of the adsorption process.

The adsorption isotherm experiments were conducted to establish the relationship between the equilibrium concentration of PFAS in the aqueous phase (C_e) and the amount of PFAS adsorbed per unit mass of AC at equilibrium (q_e). These isotherms provide critical information about the adsorption capacity of each adsorbent, the strength of adsorbate-adsorbent interactions, and the nature of the adsorption mechanism - whether it proceeds via monolayer or multilayer coverage, and whether the adsorbent surface exhibits homogeneous or heterogeneous binding sites. For this

study, a dose-response experimental design was employed, wherein a fixed initial PFAS concentration (241.5 μM) was contacted with varying doses of AC. This approach allowed the equilibrium PFAS concentration to span a range of values, generating the data points necessary to construct adsorption isotherms. Whilst this methodology differs from the traditional approach of varying initial PFAS concentration whilst maintaining constant adsorbent dose, it offered practical advantages for the ^{19}F NMR analytical method, particularly in terms of sample preparation efficiency and consistency of measurement conditions.

The isotherm data were subsequently fitted to three widely-used adsorption isotherm models: the Langmuir model, which assumes monolayer adsorption on a homogeneous surface with a finite number of identical sites; the Freundlich model, which describes multilayer adsorption on heterogeneous surfaces with an exponential distribution of adsorption energies; and the Sips model (also known as the Langmuir-Freundlich model), which combines features of both Langmuir and Freundlich equations and can describe both homogeneous and heterogeneous adsorption systems. The selection of these three models was deliberate, as they represent the most commonly applied isotherms in the literature for PFAS-AC systems and provide complementary insights into the adsorption mechanism. The Langmuir model serves as a baseline to test whether simple monolayer adsorption can describe the system, the Freundlich model accounts for surface heterogeneity that is characteristic of ACs, and the Sips model offers flexibility to capture behaviour intermediate between these two extremes. By fitting all three models and comparing their performance through regression coefficients and residual analysis, it becomes possible to identify which mechanistic description best represents the experimental observations.

The interpretation of isotherm parameters is particularly valuable for understanding structure-performance relationships. For instance, the Freundlich constant K_F provides a measure of adsorption capacity and can be correlated with adsorbent properties such as surface area, pore volume and surface chemistry. The Freundlich exponent n_F reflects the degree of surface heterogeneity and the favourability of adsorption, with values greater than unity indicating favourable adsorption and increasingly heterogeneous binding sites. In the context of PFAS adsorption on AC, surface heterogeneity arises from several sources: the distribution of pore sizes (ranging from micropores to mesopores), the presence of different oxygen-containing functional groups (carboxyl, hydroxyl, carbonyl), and variations in the graphitic character of different regions of the carbon structure. The Langmuir maximum adsorption capacity $q_{max,}$ even when the model does not provide the best fit, offers a theoretical estimate of the saturation capacity that can be compared across different adsorbents and PFAS compounds. The Langmuir constant K_L relates to the binding energy and can provide insight into the relative strength of adsorbate-adsorbent interactions. These parameters, when considered alongside the physical and chemical characterisation data presented in earlier chapters, enable correlations to be drawn between adsorbent properties and adsorption performance.

Complementing the equilibrium adsorption capacity data, the kinetics experiments were designed to investigate the time-dependent behaviour of PFAS adsorption and to identify the rate-limiting steps controlling the overall adsorption process. Understanding adsorption kinetics is crucial for several reasons. From a fundamental perspective, kinetic data provide insight into the mechanism by which PFAS molecules are transported from the bulk solution to the interior adsorption sites within the AC particles, which typically involves multiple steps: bulk diffusion through the solution,

diffusion through the liquid film surrounding the particle (external mass transfer), diffusion through the pore network (intraparticle diffusion) and finally adsorption onto the pore surface. From a practical engineering perspective, kinetic parameters are essential for designing water treatment systems, as they determine the required contact time to achieve a specified removal efficiency and influence decisions about reactor configuration, bed depth, and flow rates in fixed-bed adsorption columns.

The kinetic experiments were conducted by contacting a fixed dose of AC with a fixed initial PFAS concentration and monitoring the aqueous-phase PFAS concentration as a function of time until equilibrium was reached. The resulting time-series data were fitted to two commonly employed kinetic models: the pseudo-first-order model, which assumes that the rate of adsorption is proportional to the difference between the equilibrium and instantaneous adsorption capacities, and the pseudo-second-order model, which assumes that the rate is proportional to the square of this difference. These models are termed ‘pseudo’ because they are not derived from first principles of chemical kinetics, but rather represent empirical equations that have been found to describe adsorption kinetics in many systems. The pseudo-first-order model is often appropriate when the adsorption process is controlled by external mass transfer or when adsorption sites are far from saturation. The pseudo-second-order model typically provides better fits when the adsorption is controlled by chemisorption mechanisms or when adsorbent surface sites are approaching saturation. By comparing the quality of fit for these two models, it is possible to gain insight into the nature of the rate-limiting step and the underlying adsorption mechanism.

The kinetic parameters derived from model fitting, particularly the rate constants, can be compared across the four ACs to assess how differences in their physical and chemical properties influence the speed of PFAS uptake. For instance, ACs with larger

mesopore volumes might be expected to exhibit faster adsorption kinetics due to reduced intraparticle diffusion resistance, whilst carbons with higher concentrations of surface functional groups might show different kinetic behaviour if specific chemical interactions (such as hydrogen bonding or electrostatic attraction) play an important role in the adsorption mechanism. By examining both equilibrium and kinetic data, a comprehensive picture emerges of how each AC performs across the full spectrum of adsorption behaviour – from initial uptake rates through to ultimate adsorption capacity at equilibrium. This holistic evaluation approach is useful for ranking the adsorbents and for understanding the fundamental relationships between adsorbent structure, surface chemistry, and PFAS removal performance.

Furthermore, the evaluation was conducted for four distinct PFAS compounds – perfluorobutane sulfonic acid (PFBS), perfluorohexanoic acid (PFHxA), perfluorooctanoic acid (PFOA) and perfluorooctane sulfonic acid (PFOS) – which represent both short-chain and long-chain PFAS, as well as both perfluoroalkyl carboxylates and perfluoroalkyl sulfonates. This selection was strategic, as these compounds exhibit different physicochemical properties that are known to influence adsorption behaviour. The longer-chain PFAS (PFOA and PFOS, with C8 chains) possess more extensive hydrophobic fluorocarbon tails compared to the shorter-chain compounds (PFBS with C4 and PFHxA with C6), which affects their interaction with the hydrophobic graphitic regions of AC. The sulfonate-containing compounds (PFBS and PFOS) have different acid dissociation constants (pK_a values) compared to the carboxylate-containing compounds (PFHxA and PFOA), which influences their degree of ionisation at the experimental pH and consequently their electrostatic interactions with charged surface groups on the AC.[253] By evaluating all four AC against all four PFAS compounds, a comprehensive dataset was generated that enables both

adsorbent ranking and mechanistic interpretation of how molecular structure and adsorbent properties jointly determine removal performance.

7.1.1. PFAS Adsorption Isotherms Tests

The non-linear Langmuir, Freundlich, and Sips PFAS adsorption equilibrium data gathered by ^{19}F NMR for each of the four ACs in ultrapure water are shown in Figure 7.1 - Figure 7.8. The corresponding fitting parameters (adsorption constants, capacity terms, and heterogeneity indices) derived from non-linear regression analysis are presented in

Adsorbents	Freundlich			Langmuir			Sips			
	K_F	n_F	R^2	K_L	q_{max}	R^2	K_s	q_{max}	n_S	R^2
	PFOA									
CAC-1	3.34	0.93	0.996	8×10^{-4}	5560	0.951	0.0173	543.3	2.09	0.977
CAC-2	4.07	0.88	0.989	5×10^{-4}	14400	0.987	6.45×10^{-7}	4.40×10^{7}	1.14	0.909
CAC-3	37.96	1.84	0.994	0.023	622	0.992	1.81×10^{-8}	6.29×10^{5}	0.54	0.925
CAC-4	40.02	1.66	0.992	0.018	923	0.991	2.69×10^{-8}	1.48×10^{6}	0.60	0.927
	PFBS									
CAC-1	0.02	0.41	0.997	2×10^{-4}	29300	0.938	1.27×10^{-4}	5.32×10^{7}	2.46	0.943
CAC-2	0.001	0.31	0.990	2×10^{-4}	35000	0.903	5.12×10^{-4}	1.25×10^{8}	3.67	0.136
CAC-3	4×10^{-4}	0.29	0.952	3×10^{-4}	30200	0.864	3.77×10^{-3}	1.04×10^{8}	8.30	0.638
CAC-4	0.003	0.34	0.957	2×10^{-4}	34400	0.908	4.50×10^{-4}	4.37×10^{7}	3.19	0.776
	PFHxA									
CAC-1	2×10^{-4}	0.29	0.969	3×10^{-6}	1.83×10^{6}	0.900	0.00161	8.95×10^{7}	5.49	0.867
CAC-2	0.32	0.32	0.944	5×10^{-6}	1.41×10^{6}	0.892	0.00043	4.11×10^{7}	3.12	0.950
CAC-3	0.41	0.41	0.977	3×10^{-5}	2.08×10^{5}	0.938	0.00013	5.32×10^{7}	2.46	0.832
CAC-4	0.34	0.34	0.976	4×10^{-5}	1.93×10^{3}	0.933	0.00048	9.71×10^{7}	3.50	0.796
	PFOS									
CAC-1	66.86	2.50	0.990	0.05	475	0.988	5.41×10^{-4}	2.02×10^{3}	0.46	0.884
CAC-2	157.03	12.34	0.923	0.62	230	0.928	0.328	224.2	6.97	0.751
CAC-3	90.18	3.52	0.978	0.15	324	0.972	7.60×10^{-9}	1.94×10^{4}	0.29	0.867
CAC-4	87.20	2.43	0.976	0.05	649	0.965	8.04×10^{-9}	1.87×10^{5}	0.41	0.875

Table 7.1, along with the coefficient of determination (R^2) values that indicate the quality of fit for each model.

Comparison of the R^2 values across the three isotherm models reveals that the Freundlich and Sips models consistently provided superior fits to the experimental data compared to the Langmuir model for all four PFAS compounds on all four ACs. This outcome is both expected and mechanistically informative, as it reflects fundamental characteristics of the AC adsorbent surfaces and the nature of PFAS adsorption in these systems. The superior performance of the Freundlich and Sips models can be attributed to several interrelated factors that are inherent to the structure and chemistry of ACs and the adsorption behaviour of PFAS molecules.

Firstly, ACs are characteristically heterogeneous materials with respect to their surface chemistry and pore structure. The surface heterogeneity arises from multiple sources: a broad distribution of pore sizes spanning from micropores (<2 nm) through

mesopores (2-50 nm), variations in the local graphitic character and degree of aromatisation across different regions of the carbon matrix, and a diverse population of oxygen-containing functional groups (carboxyl, hydroxyl, carbonyl, lactone, and phenolic groups) that are distributed non-uniformly across the surface. The XPS and presented in Chapter 4 confirm the presence of such surface heterogeneity in all four ACs studied here. The Freundlich exponent n_F provides a quantitative measure of this surface heterogeneity and adsorption favourability. Values of n_F greater than unity, as observed for PFOA adsorption on CAC-3 and CAC-4, indicate favourable adsorption with increasingly heterogeneous binding site energies, whilst values less than unity suggest less favourable adsorption conditions or weaker adsorbate-adsorbent interactions. The Langmuir model, by contrast, assumes a homogeneous surface with identical, non-interacting adsorption sites-an assumption that is fundamentally incompatible with the physical reality of AC surfaces.

Secondly, the Freundlich and Sips models can accommodate multilayer adsorption and pore-filling mechanisms that are likely operative in these systems. PFAS molecules, particularly the longer-chain compounds PFOA and PFOS, possess both hydrophobic fluorocarbon tails and polar ionic head groups, enabling them to undergo both surface adsorption via hydrophobic interactions with the graphitic carbon surface and pore-filling through cooperative interactions between adsorbed molecules. The micropore volumes of the ACs (ranging from 0.32 to 0.58 $cm^3\ g^{-1}$) provide ample opportunity for PFAS molecules to adsorb in multiple layers within pores, particularly in pores that are sufficiently large to accommodate more than a monolayer of PFAS. The Freundlich model, being an empirical equation originally derived for systems exhibiting an exponential distribution of adsorption energies, naturally accounts for

such multilayer and pore-filling phenomena, whereas the Langmuir model is strictly limited to monolayer coverage at saturation.

Thirdly, the experimental concentration employed in this study (PFAS concentration at 241.5 μM, well above environmental levels) circumvents one of the principal theoretical limitations of the Freundlich model. The Freundlich isotherm lacks a rigorous thermodynamic foundation at vanishing concentrations (as C_e approaches zero) because it predicts infinite adsorption capacity rather than approaching Henry's law behaviour. However, this limitation is inconsequential for the present study because the lowest equilibrium concentrations achieved in the experiments remained sufficiently high that the system behaviour was firmly within the intermediate concentration regime where the Freundlich model provides an accurate empirical description. Had the experiments been conducted at trace concentrations approaching ng L^{-1} levels (as would be encountered in environmental waters), the Freundlich model's behaviour at very low concentrations might have proven problematic, but this was not the case here.

Fourthly, the Sips model (also known as the Langmuir-Freundlich model) combines desirable features of both the Langmuir and Freundlich equations, providing flexibility to describe adsorption behaviour across a wide concentration range. At low adsorbate concentrations, the Sips model reduces mathematically to Freundlich-like behaviour, accommodating surface heterogeneity and favourable adsorption, whilst at high concentrations it approaches Langmuir-like behaviour, predicting a finite saturation capacity. The heterogeneity parameter n_S in the Sips model serves as an adjustable exponent that controls this transition: n_S, the model collapses to the Langmuir equation (indicating homogeneous adsorption), whilst $n_S \neq 1$ reflects heterogeneous adsorption with the degree of deviation from unity indicating the extent of heterogeneity. The n_S

values obtained for the PFAS-AC systems (Table 7.1) generally deviated significantly from unity, confirming the heterogeneous nature of the adsorption process and justifying the use of the Sips model. The Sips model is particularly valuable when one wishes to estimate a maximum adsorption capacity n_S whilst still accounting for surface heterogeneity - a capability that the Freundlich model lacks, as it predicts unlimited adsorption capacity at sufficiently high concentrations.

It should be noted that whilst the Freundlich and Sips models provided superior statistical fits compared to Langmuir based on R^2 values, even these models did not achieve perfect fits to the experimental data in all cases. This imperfect agreement can be attributed to the experimental design employed, wherein a single initial PFAS concentration was contacted with varying adsorbent doses rather than varying the initial PFAS concentration at constant adsorbent dose. This dose-response approach generates equilibrium data points that span a more limited range of C_e values compared to a traditional isotherm experiment, which can reduce the statistical robustness of the fitted isotherm parameters. Nevertheless, the Freundlich and Sips models captured the essential features of the adsorption behaviour and provided sufficiently accurate descriptions to enable meaningful comparisons of adsorbent performance across the four ACs.

Adsorbents	Freundlich			Langmuir			Sips			
	K_F	n_F	R^2	K_L	q_{max}	R^2	K_s	q_{max}	n_S	R^2
	PFOA									
CAC-1	3.34	0.93	0.996	8×10^{-4}	5560	0.951	0.0173	543.3	2.09	0.977
CAC-2	4.07	0.88	0.989	5×10^{-4}	14400	0.987	6.45×10^{-7}	4.40×10^{7}	1.14	0.909
CAC-3	37.96	1.84	0.994	0.023	622	0.992	1.81×10^{-8}	6.29×10^{5}	0.54	0.925
CAC-4	40.02	1.66	0.992	0.018	923	0.991	2.69×10^{-8}	1.48×10^{6}	0.60	0.927
	PFBS									
CAC-1	0.02	0.41	0.997	2×10^{-4}	29300	0.938	1.27×10^{-4}	5.32×10^{7}	2.46	0.943
CAC-2	0.001	0.31	0.990	2×10^{-4}	35000	0.903	5.12×10^{-4}	1.25×10^{8}	3.67	0.136
CAC-3	4×10^{-4}	0.29	0.952	3×10^{-4}	30200	0.864	3.77×10^{-3}	1.04×10^{8}	8.30	0.638
CAC-4	0.003	0.34	0.957	2×10^{-4}	34400	0.908	4.50×10^{-4}	4.37×10^{7}	3.19	0.776
	PFHxA									
CAC-1	2×10^{-4}	0.29	0.969	3×10^{-6}	1.83×10^{6}	0.900	0.00161	8.95×10^{7}	5.49	0.867
CAC-2	0.32	0.32	0.944	5×10^{-6}	1.41×10^{6}	0.892	0.00043	4.11×10^{7}	3.12	0.950
CAC-3	0.41	0.41	0.977	3×10^{-5}	2.08×10^{5}	0.938	0.00013	5.32×10^{7}	2.46	0.832
CAC-4	0.34	0.34	0.976	4×10^{-5}	1.93×10^{3}	0.933	0.00048	9.71×10^{7}	3.50	0.796
	PFOS									
CAC-1	66.86	2.50	0.990	0.05	475	0.988	5.41×10^{-4}	2.02×10^{3}	0.46	0.884
CAC-2	157.03	12.34	0.923	0.62	230	0.928	0.328	224.2	6.97	0.751
CAC-3	90.18	3.52	0.978	0.15	324	0.972	7.60×10^{-9}	1.94×10^{4}	0.29	0.867
CAC-4	87.20	2.43	0.976	0.05	649	0.965	8.04×10^{-9}	1.87×10^{5}	0.41	0.875

Table 7.1. Non-linear Freundlich, Langmuir and Sips adsorption isotherm constants for PFAS in ultrapure water at 25 °C.

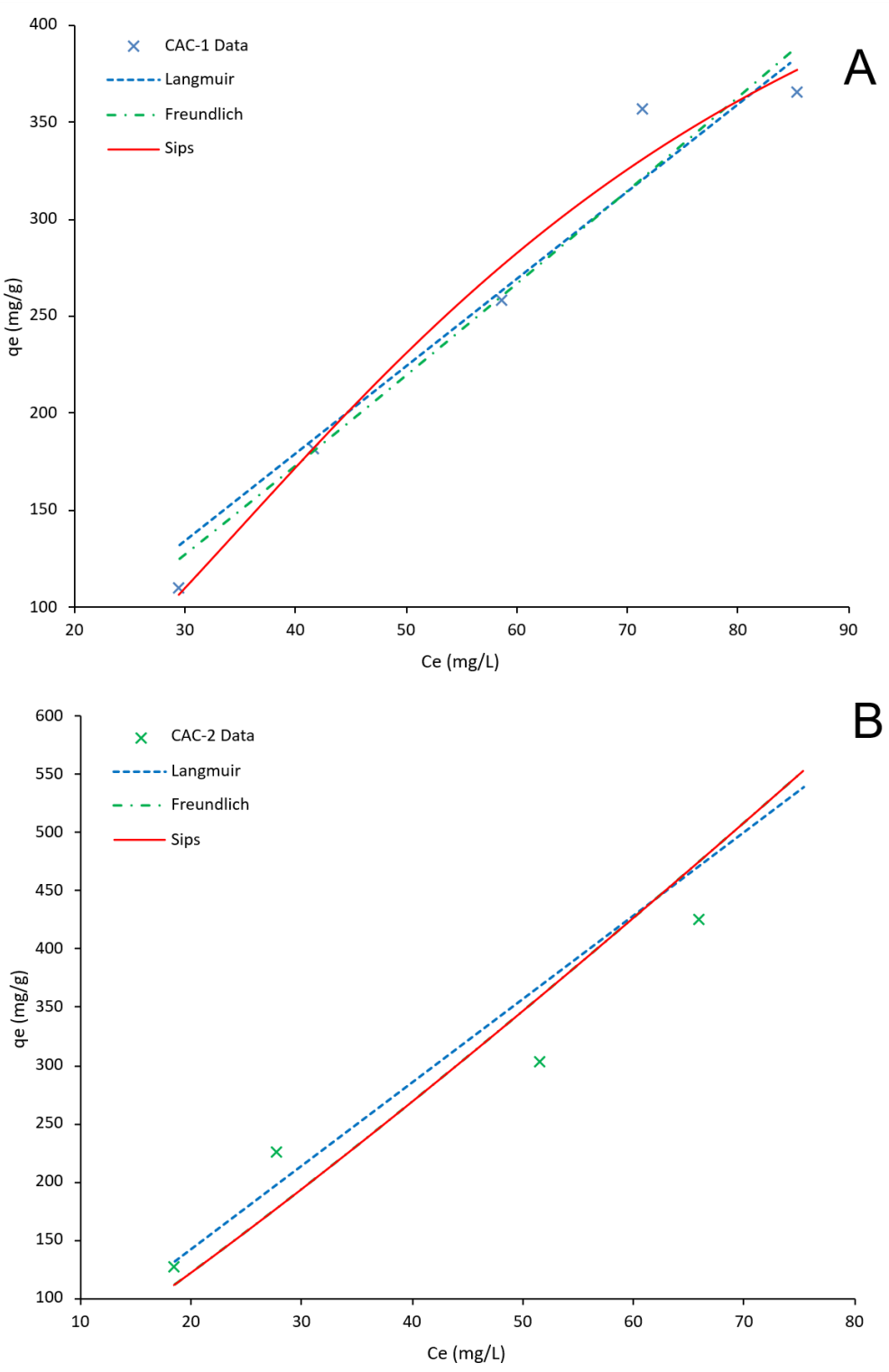


Figure 7.1. Langmuir, Freundlich and Sips adsorption isotherm models for the adsorption of PFOA on (A) CAC-1 and (B) CAC-2.

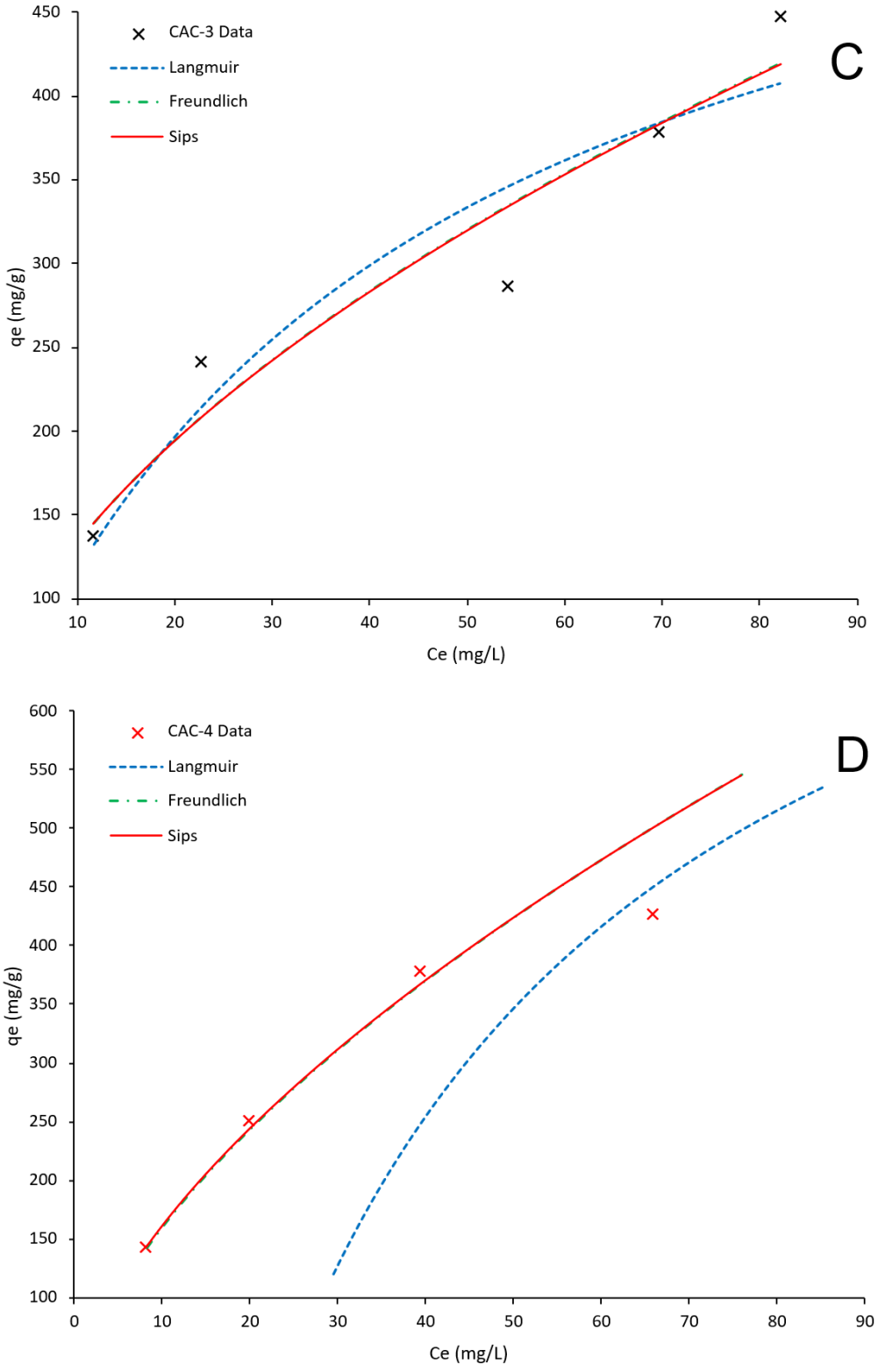


Figure 7.2. Langmuir, Freundlich and Sips adsorption isotherm models for the adsorption of PFOA on (C) CAC-3 and (D) CAC-4.

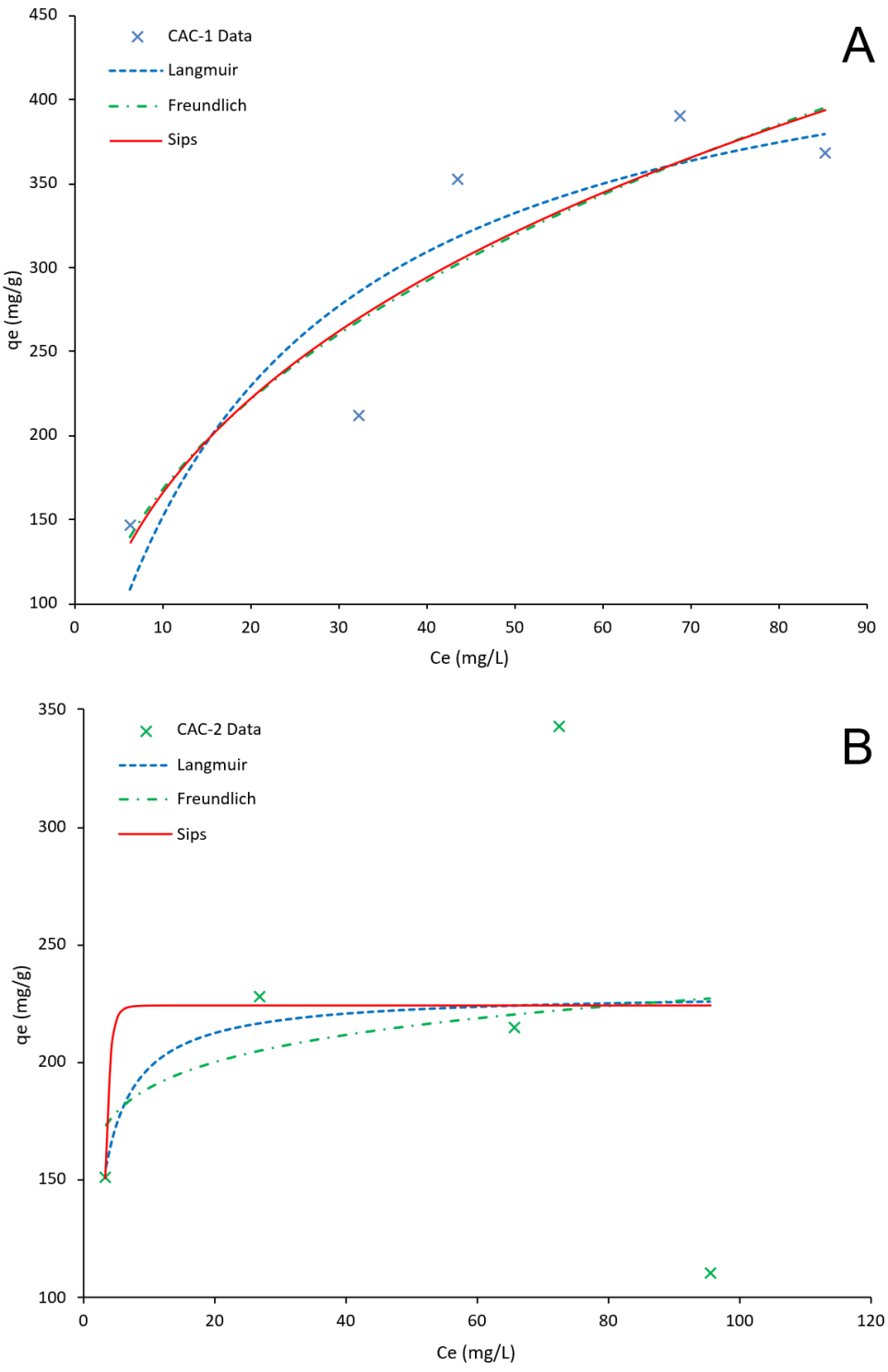


Figure 7.3. Langmuir, Freundlich and Sips adsorption isotherm models for the adsorption of PFOS on (A) CAC-1 and (B) CAC-2.

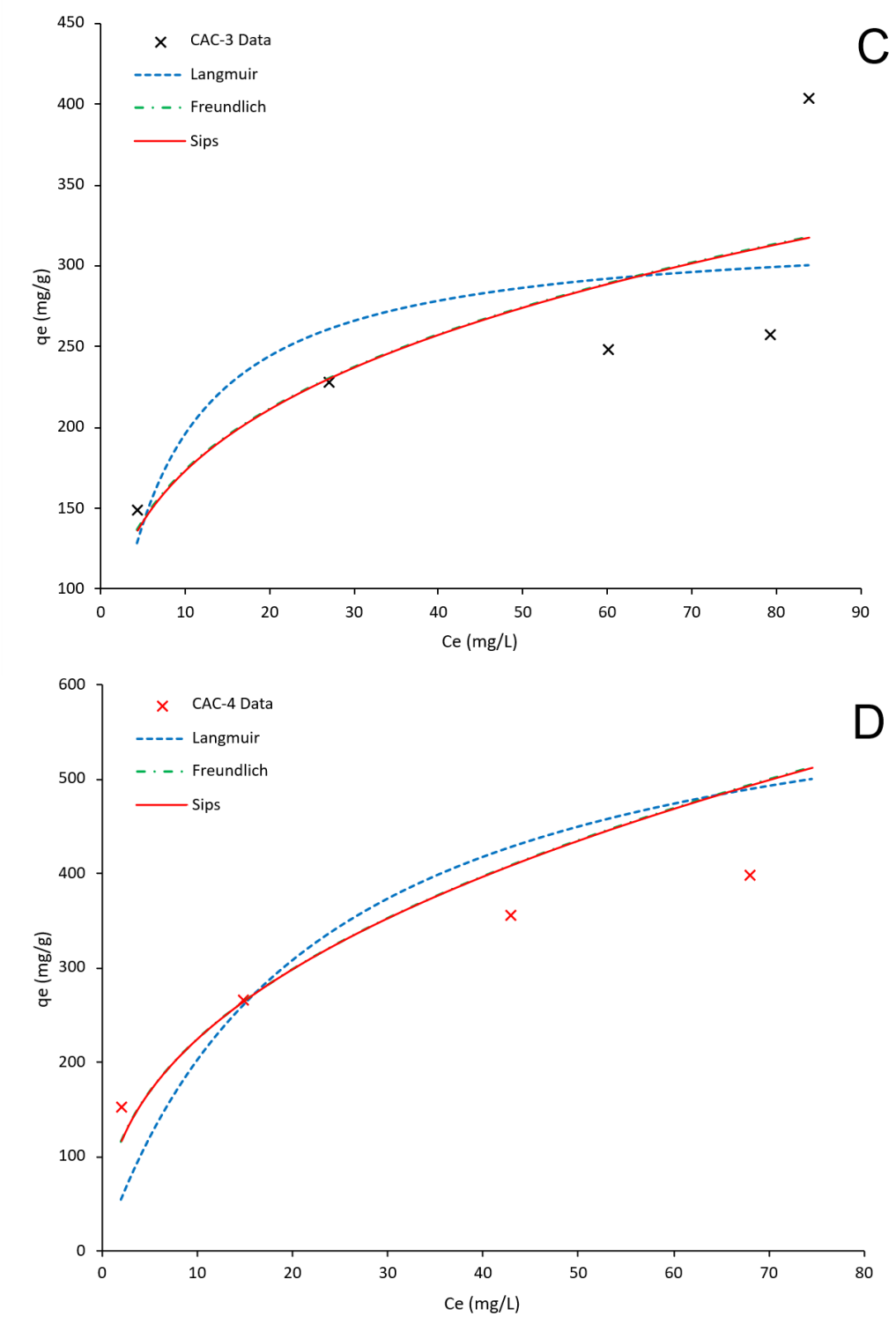


Figure 7.4. Langmuir, Freundlich and Sips adsorption isotherm models for the adsorption of PFOS on (C) CAC-3 and (D) CAC-4.

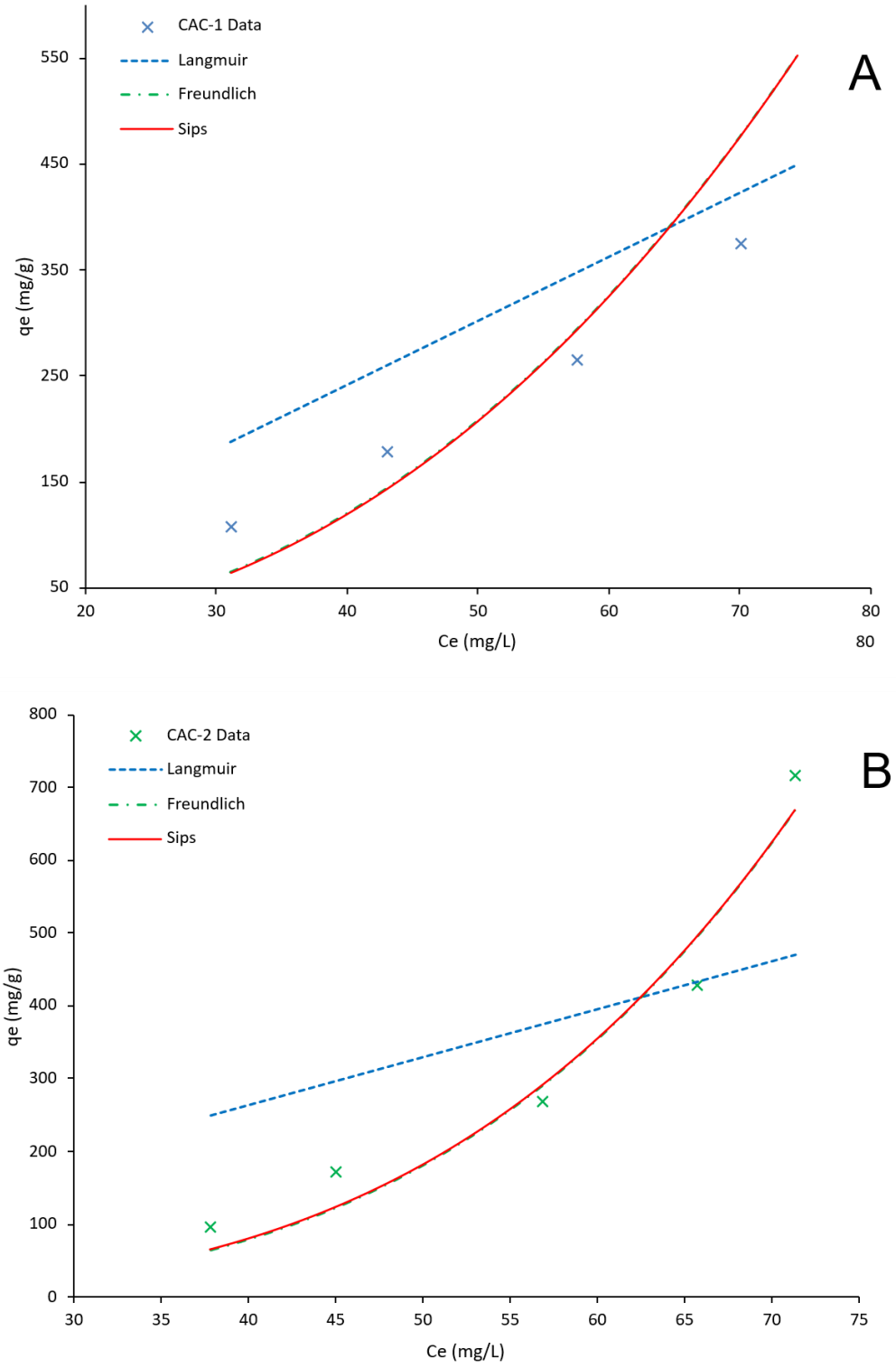


Figure 7.5. Langmuir, Freundlich and Sips adsorption isotherm models for the adsorption of PFBS on (A) CAC-1 and (B) CAC-2.

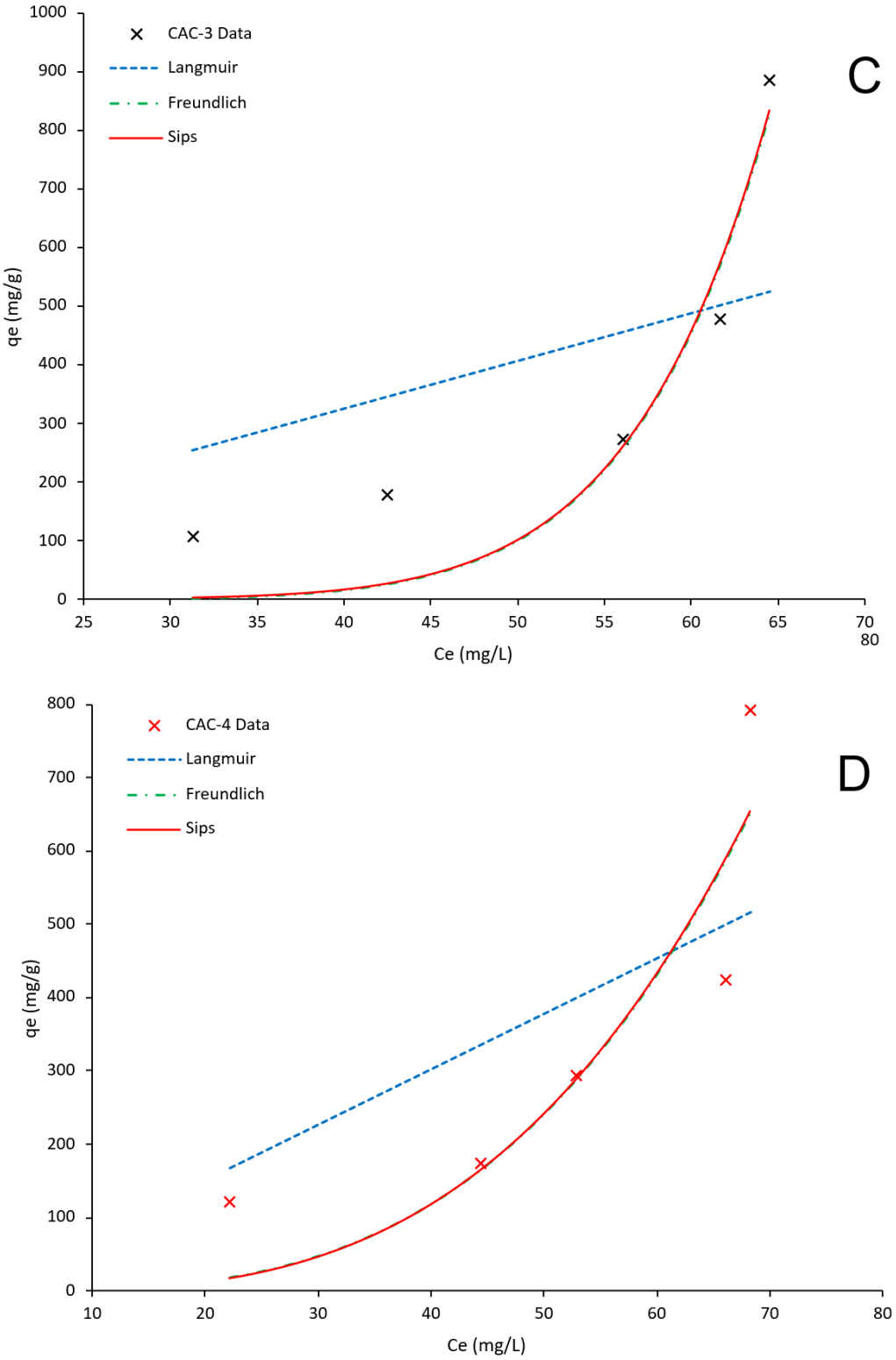


Figure 7.6. Langmuir, Freundlich and Sips adsorption isotherm models for the adsorption of PFBS on (C) CAC-3 and (D) CAC-4.

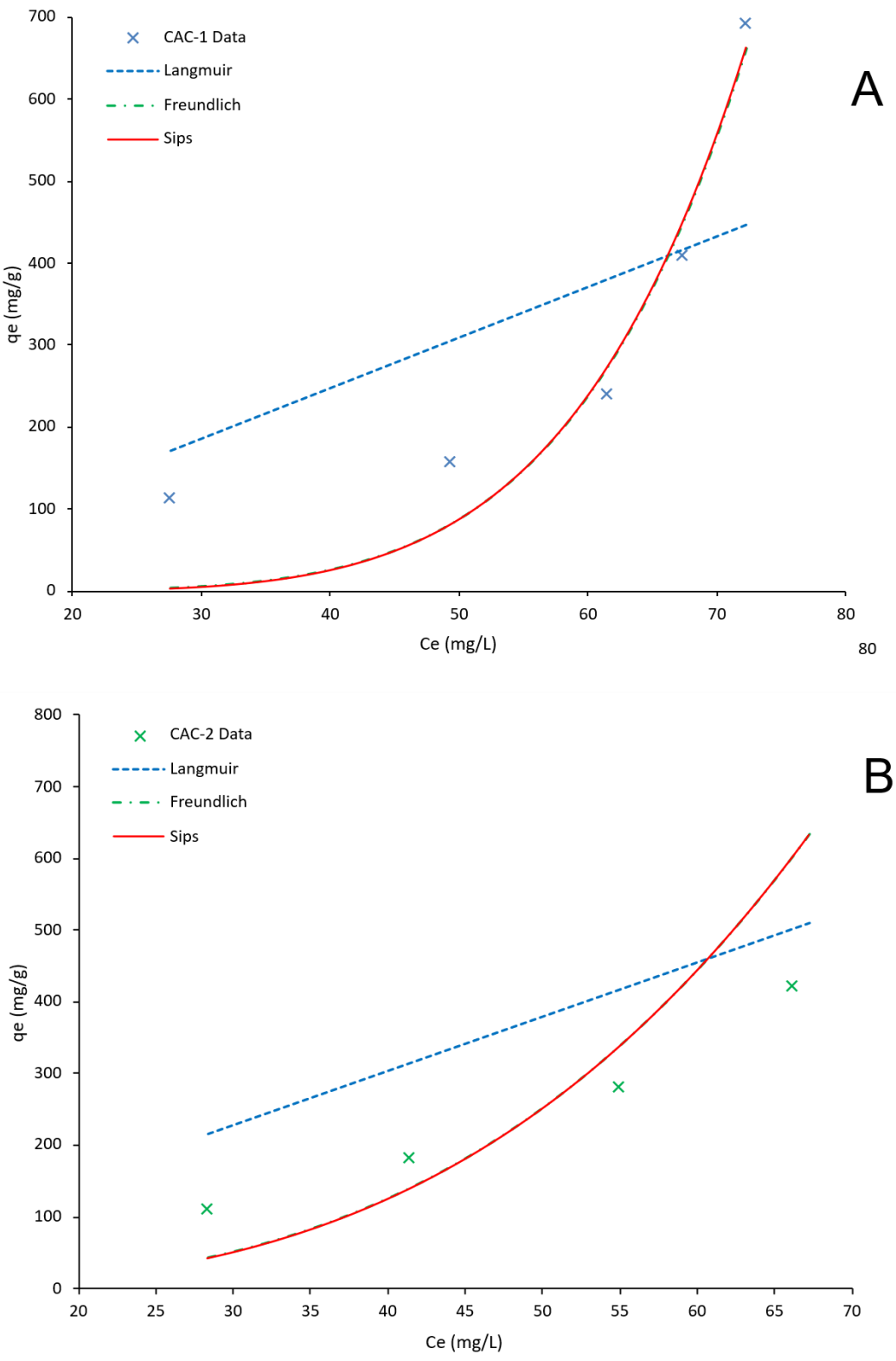


Figure 7.7. Langmuir, Freundlich and Sips adsorption isotherm models for the adsorption of PFHxA on (A) CAC-1 and (B) CAC-2.

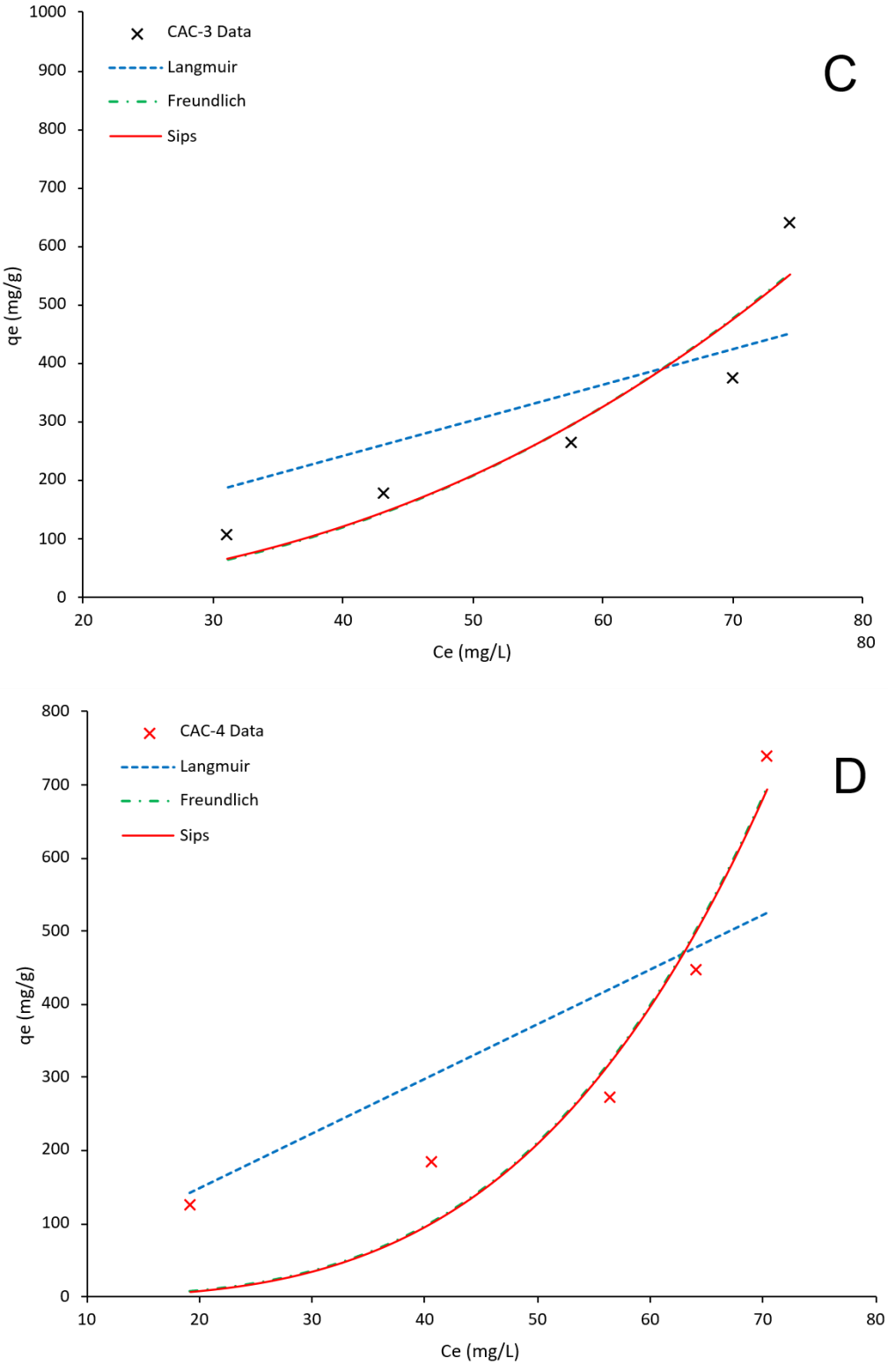


Figure 7.8. Langmuir, Freundlich and Sips adsorption isotherm models for the adsorption of PFHxA on (C) CAC-3 and (D) CAC-4.

The non-linear Freundlich and Sips adsorption isotherm models provided better fits than Langmuir, which indicated the predominant adsorption mechanism of the four PFAS on the four ACS was multi-molecular physical adsorption. The majority of the fits for Freundlich and Sips are identical, which could be explained by the Sips isotherm mathematically reducing to the Freundlich model under the experimental conditions used in this study. The value of K_F in the Freundlich equation is related to the strength of the interaction between adsorbate and adsorbent. Increasingly large values of K_F indicates a stronger adsorbent-adsorbate interaction. The values in

Adsorbents	Freundlich			Langmuir			Sips			
	K_F	n_F	R^2	K_L	q_{max}	R^2	K_s	q_{max}	n_S	R^2
	PFOA									
CAC-1	3.34	0.93	0.996	8×10^{-4}	5560	0.951	0.0173	543.3	2.09	0.977
CAC-2	4.07	0.88	0.989	5×10^{-4}	14400	0.987	6.45×10^{-7}	4.40×10^{7}	1.14	0.909
CAC-3	37.96	1.84	0.994	0.023	622	0.992	1.81×10^{-8}	6.29×10^{5}	0.54	0.925
CAC-4	40.02	1.66	0.992	0.018	923	0.991	2.69×10^{-8}	1.48×10^{6}	0.60	0.927
	PFBS									
CAC-1	0.02	0.41	0.997	2×10^{-4}	29300	0.938	1.27×10^{-4}	5.32×10^{7}	2.46	0.943
CAC-2	0.001	0.31	0.990	2×10^{-4}	35000	0.903	5.12×10^{-4}	1.25×10^{8}	3.67	0.136
CAC-3	4×10^{-4}	0.29	0.952	3×10^{-4}	30200	0.864	3.77×10^{-3}	1.04×10^{8}	8.30	0.638
CAC-4	0.003	0.34	0.957	2×10^{-4}	34400	0.908	4.50×10^{-4}	4.37×10^{7}	3.19	0.776
	PFHxA									
CAC-1	2×10^{-4}	0.29	0.969	3×10^{-6}	1.83×10^{6}	0.900	0.00161	8.95×10^{7}	5.49	0.867
CAC-2	0.32	0.32	0.944	5×10^{-6}	1.41×10^{6}	0.892	0.00043	4.11×10^{7}	3.12	0.950
CAC-3	0.41	0.41	0.977	3×10^{-5}	2.08×10^{5}	0.938	0.00013	5.32×10^{7}	2.46	0.832
CAC-4	0.34	0.34	0.976	4×10^{-5}	1.93×10^{3}	0.933	0.00048	9.71×10^{7}	3.50	0.796
	PFOS									
CAC-1	66.86	2.50	0.990	0.05	475	0.988	5.41×10^{-4}	2.02×10^{3}	0.46	0.884
CAC-2	157.03	12.34	0.923	0.62	230	0.928	0.328	224.2	6.97	0.751
CAC-3	90.18	3.52	0.978	0.15	324	0.972	7.60×10^{-9}	1.94×10^{4}	0.29	0.867
CAC-4	87.20	2.43	0.976	0.05	649	0.965	8.04×10^{-9}	1.87×10^{5}	0.41	0.875

Table 7.1 reveal the strengths of the interactions between the four PFAS and the four ACs as follows:

1) PFOA $\rightarrow$ CAC-4 > CAC-3 > CAC-2 > CAC-1
2) PFBS $\rightarrow$ CAC-1 > CAC-4 > CAC-2 > CAC-3
3) PFHxA $\rightarrow$ CAC-4 > CAC-3 > CAC-2 > CAC-1
4) PFOS $\rightarrow$ CAC-2 > CAC-4 > CAC-3 > CAC-1

Although the maximum adsorption capacity cannot be estimated from the Freundlich model, the values of K_F can be used as a comparative measure of the adsorption capacity for the ACs. Therefore, the ACs can ranked in the descending order regarding their affinity towards the four PFAS; PFOS > PFOA > PFHxA > PFBS.

The Langmuir model provided the worst fit, which was expected since the Langmuir model assumes monolayer adsorption on homogenous sites, and it is already well

known that AC does not contain homogeneous sites.[97, 254] The Langmuir model assumes the presence of a homogeneous surface, monolayer formation during adsorption, equivalent adsorption sites and no interactions between adsorbed molecules.[255] This is clearly not applicable to PFAS adsorption in AC due to the randomness and variety of oxygen-containing functional groups on the adsorbent surfaces, as evidenced by XPS, and the physicochemical properties of the PFAS molecules, which contain a polar head group and hydrophobic tails which enable intermolecular interactions.

The Freundlich isotherm model providing the best fit in this study is comparable to the literature where high PFAS concentrations are used. When you have high PFAS concentrations or you have more heterogeneous surfaces/pores, the Freundlich model is more appropriately applied since it allows for non-ideal, multilayer adsorption. Abulikemu *et al.*[256] and Pranić *et al.*[257] both worked at the lab-scale, using PFAS levels that are several orders of magnitude above environmental concentrations and found that a heterogeneous description with Freundlich parameters described the equilibrium data well. Yu *et al.*[258] showed the same thing but added effluent organic matter, which makes the carbon surface effectively more heterogeneous, again favouring Freundlich.

The removal efficiencies of the four AC were analysed using the same concentration of each PFAS (241.5 μM), the comparison of the AC performances are presented in Figure 7.9 and Figure 7.10. Some patterns can be discerned, with the most prevalent being that CAC-4 outperforms all other AC at the majority of the dose rates used, especially at the highest dose rate used. This could be explained by CAC-4 having the largest specific surface area (1165 m^2 g^{-1}) which enables a larger surface for the attractive hydrophobic interactions between the PFAS tails, especially in the long-

chain PFAS. Moreover, the XPS data revealed CAC-4 had the greatest quantity of oxygen-containing functional groups, which could have contributed to the greater removal efficiencies via hydrogen bonding between the carboxylic and sulfonic acid head groups of the PFAS with the functional groups on the AC surfaces.

The inferior performances of CAC-1, CAC-2 and CAC-3 could be explained by several physicochemical features. All three AC have a similar O:C ratio, which was 0.09-0.10 as defined by the XPS data (CAC-4 has a ratio of 0.13). The BET surface area values are less than the value for CAC-4, which indicates fewer sites of adsorption and less area for hydrophobic interactions. Additionally, CAC-4 has a mesopore volume that is over double that of the next highest (CAC-3), which suggests there is significant adsorption in the mesopores themselves; PFOS has a projection diameter of 1.8 nm which would struggle to adsorb in micropores smaller than this, yet there was significant removal therefore the mesopores must be involved in PFOS adsorption. All AC had similar removal efficiencies of PFOS and it appeared that it was the most easily removed out of the four PFAS, even more easily than PFOA which has the same chain length. This can be attributed to PFOS having an additional C-F bond compared to PFOA, which will increase the strength of the hydrophobic reaction between the graphitic surface and the hydrophobic tail of the PFOS. Notice the lower removal rates of the short-chain PFAS; PFHxA and PFBS. The shorter C-F backbone will reduce hydrophobic interaction strength and allows the molecule to be more mobile. CAC-4 still comes out on top for removal due to having the highest surface area and having the most oxygen-containing functional groups which will support it in its adsorptive removal of the smaller PFAS.

Similar PFOS and PFOA loadings on ACs at a PFAS dose rate of 100 mg L^{-1} have been reported elsewhere. Chen *et al.*[259] obtained sorption capacities of ≈760 mg g^{-1}

for PFOS and ≈302 mg g^{-1} for PFOA on PANF-derived AC fibres, with commercial PAC and GAC still reaching ≈535 and ≈390 mg g^{-1} for PFOS respectively. For PFOA on coconut-shell ACs, Kanchanapiya et al.[60] reported Langmuir capacities of ≈331 mg g^{-1} (PAC-325) and ≈54 mg g^{-1} (GAC-20×50), after testing PFOA at 100 mg L^{-1}, with the GAC-20x50 having a comparable BET surface area to CAC-2.

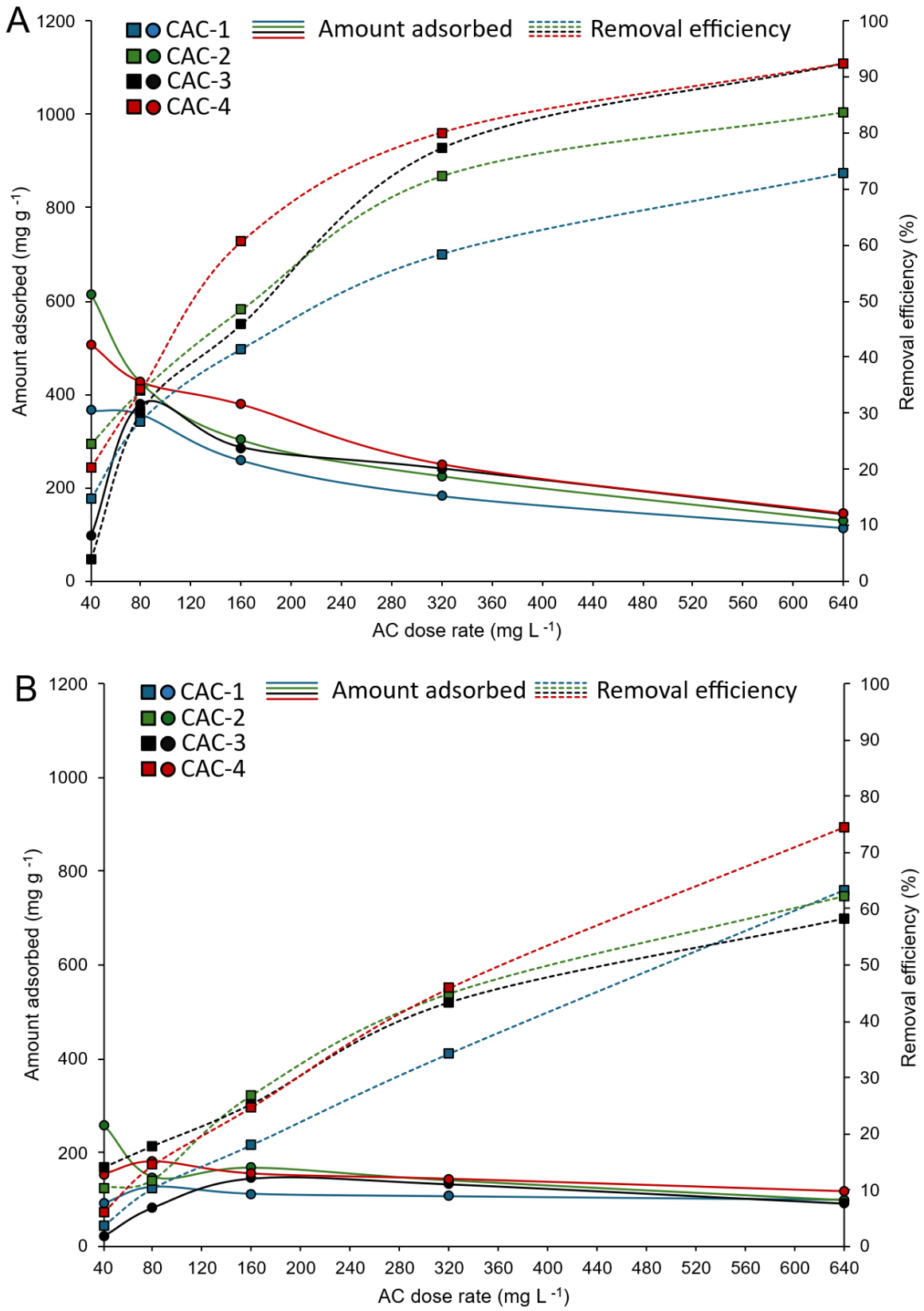


Figure 7.9. Adsorption capacities and removal efficiencies of (A) PFOA and (B) PFHxA, using the four ACs at varying dose rates.

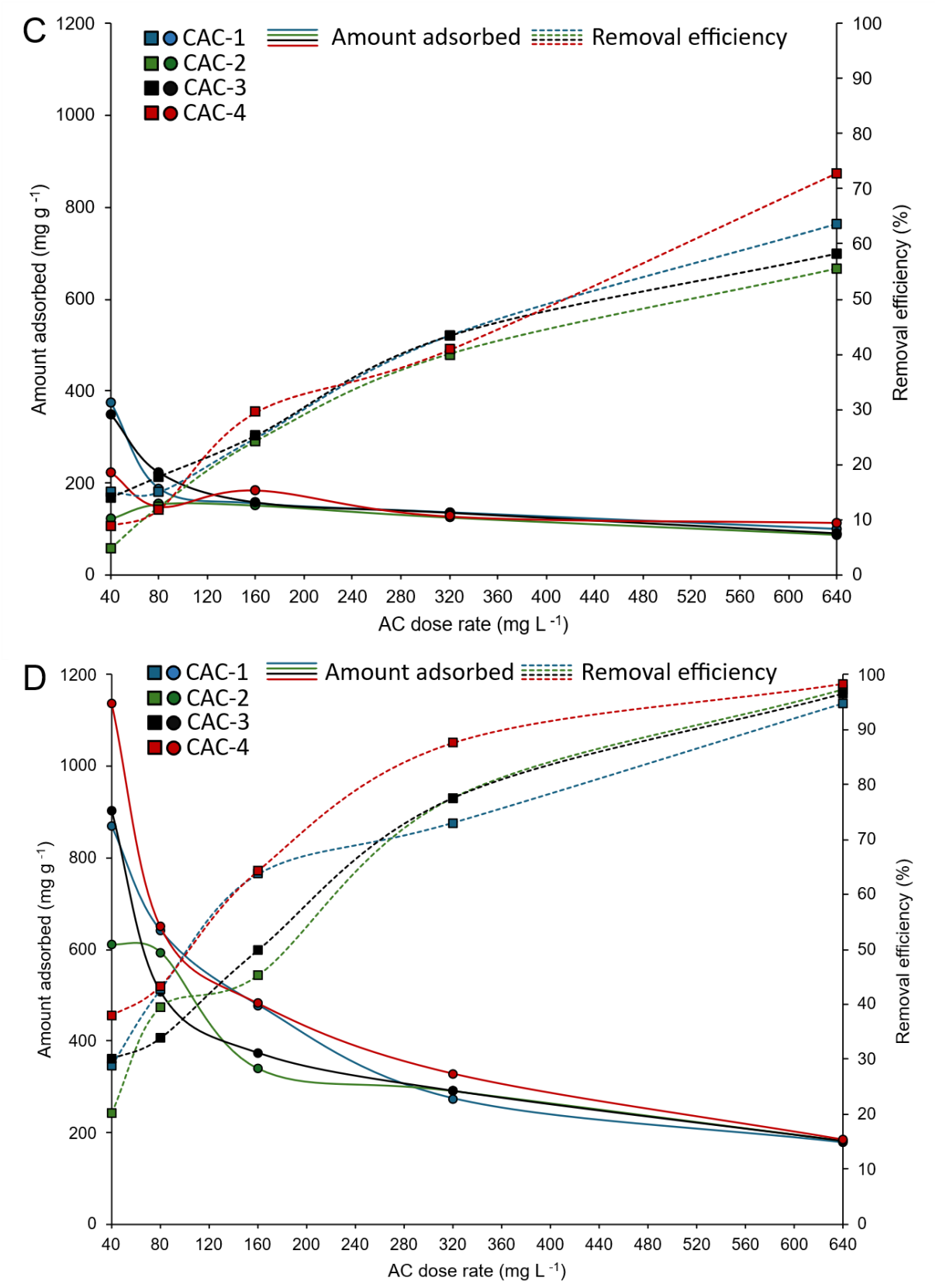


Figure 7.10. Adsorption capacities and removal efficiencies of (C) PFBS and (D) PFOS, using the four ACs at varying dose rates.

Because the PZCs of the four ACs sit within the UK potable-water pH window, small pH fluctuations in plant operation can flip surface charge sign or magnitude, changing the balance between electrostatic attraction and hydrophobic partitioning, particularly for short chain PFAS. Therefore, ranking of adsorbents in ultrapure water should be validated under realistic matrices with DOC, hardness, and competing anions to quantify any capacity loss from pore blocking. The screening here nonetheless provides a robust first pass to narrow candidates before pilot evaluation.

7.1.2. PFAS Adsorption Kinetics Tests

The kinetics data were fitted with the pseudo-first order and pseudo-second order rate equations to examine the PFAS adsorption kinetics. It was found that the adsorption data was best suited to being fitted with the pseudo-second order rate equation, as presented in Figure 7.11 and Figure 7.12. The superior fit of the pseudo-second order model suggests that the rate-limiting step in PFOA adsorption is not solely controlled by external mass transfer or film diffusion but rather involves a combination of mechanisms including intraparticle diffusion and surface adsorption processes. The pseudo-second order kinetics are characteristic of systems where chemisorption or specific interactions between adsorbate and adsorbent play a significant role, which is consistent with the presence of electrostatic interactions and hydrogen bonding between the carboxylic acid head group of PFOA and the oxygen-containing functional groups on the AC surfaces. The applicability of this model also indicates that the adsorption capacity is proportional to the number of active sites occupied on the adsorbent surface, and that the adsorption process may involve valency forces through sharing or exchange of electrons between PFOA molecules and the carbon surface.

All AC adsorbents exhibited similar pseudo-second order adsorption behaviour, indicating that despite differences in their physical and chemical properties, the fundamental mechanism controlling the rate of PFOA uptake remains consistent across the four carbons. This similarity in kinetic behaviour suggests that the rate-limiting step is primarily governed by intraparticle diffusion through the pore network rather than external mass transfer, as the latter would be more sensitive to differences in particle size and external surface area. The pseudo-second order rate constants (k_2) derived from the model fitting can be used to compare the relative adsorption rates, with higher k_2 values indicating faster approach to equilibrium.

Notably, CAC-1 and CAC-3 exhibited the most similar adsorption rates, which can be explained by both carbons having comparable textural properties, such as similar micro- and mesopore volumes, as well as nearly identical O:C ratios. The micropore volumes of CAC-1 and CAC-3 were 0.195 and 0.189 $cm^3\ g^{-1}$ and their mesopore volumes were 0.361 and .384 $cm^3\ g^{-1}$, respectively, whilst their O:C ratios determined by XPS were both approximately 0.09-0.10. This structural similarity results in comparable diffusion path lengths and similar distributions of adsorption sites, which manifests as similar kinetic behaviour. The near-identical oxygen content suggests that both carbons present similar concentrations of polar functional groups that can interact with the PFOA head group, contributing to the similarity in their adsorption mechanisms.

In contrast, whilst CAC-4 also followed pseudo-second order kinetics, its rate constant may differ due to its substantially higher mesopore volume (0.192 $cm^3\ g^{-1}$ compared to 0.076-.103 $cm^3\ g^{-1}$ for the other carbons) and elevated O:C ratio of 0.13. The larger mesopore volume in CAC-4 potentially facilitates faster intraparticle diffusion by reducing mass transfer resistance, particularly for the relatively large PFOA molecules

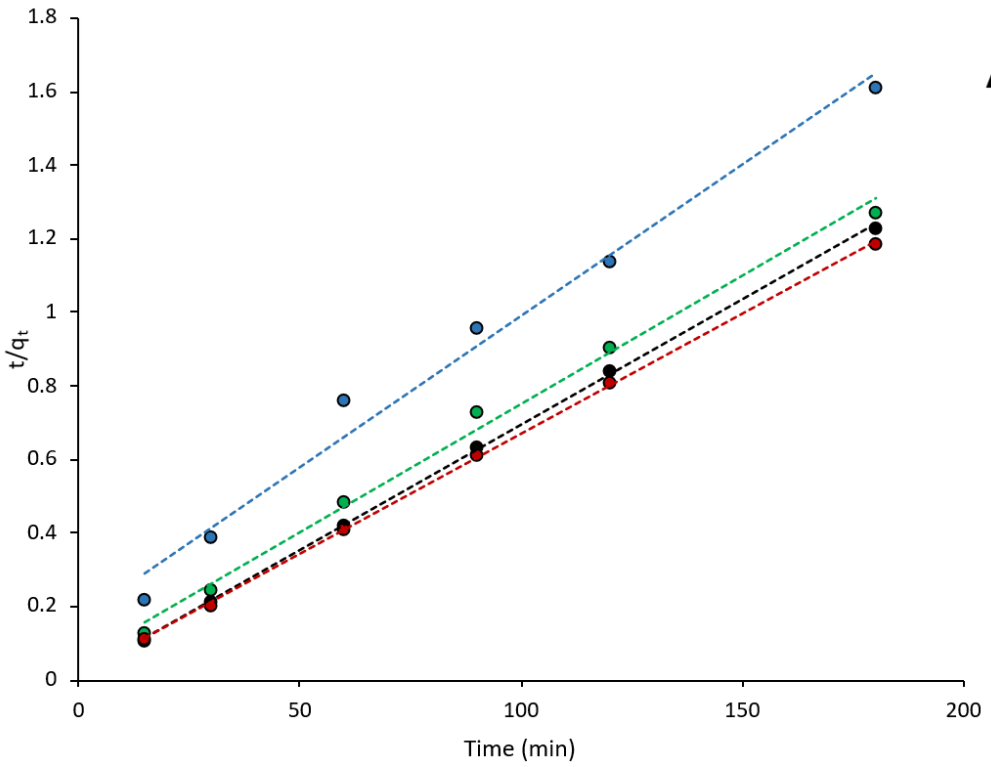
(molecular length ~1.5 nm). However, the increased surface oxygen content may simultaneously introduce stronger adsorbate-adsorbent interactions that could slow the kinetics if the adsorption step itself becomes rate-limiting. The balance between these competing factors determines the overall rate constant observed for CAC-4.

Comparison of the kinetic behaviour across the four PFAS reveals interesting structure-activity relationships. The longer-chain PFAS (PFOA and PFOS with C8 chains) would be expected to exhibit slower adsorption kinetics than the shorter-chain compounds (PFHxA with C6 and PFBS with C4) due to greater molecular size and consequently higher intraparticle diffusion resistance through the micropore network. Conversely, the stronger hydrophobic interactions between the longer fluorocarbon chains and the graphitic carbon surface may result in higher pseudo-second order rate constants if the adsorption step (rather than diffusion) dominates the overall kinetics. The relative magnitudes of the k_2 values for the four PFAS can therefore provide insight into whether diffusion limitations or surface adsorption kinetics control the overall uptake rate. Additionally, differences in adsorption rates between the sulfonate-containing compounds (PFBS and PFOS) and the carboxylate-containing compounds (PFHxA and PFOA) may reflect variations in their electrostatic interactions with the charged surface groups on the ACs, as the pK_a values of these two classes of PFAS differ significantly.

It is important to note that these kinetic experiments were conducted at a single initial concentration for each PFAS and at a single adsorbent dose, which represents a limitation of the current study. In real water treatment scenarios, PFAS concentrations are typically much lower (in the ng L^{-1} to µg L^{-1} range), and the kinetic behaviour may differ at these trace concentrations due to changes in the rate-limiting step or the involvement of different types of adsorption sites. For example, at very low

concentrations, adsorption may be dominated by the highest-energy sites (likely located in the smallest micropores), which could result in different kinetic behaviour than observed at the higher concentrations used in this study. Additionally, the presence of natural organic matter, competing anions (such as sulfate, nitrate, and bicarbonate), and varying water chemistry parameters (pH, ionic strength, hardness) in real water matrices could significantly influence the adsorption kinetics by blocking pores, competing for adsorption sites, or altering the surface charge of the AC. The effect of these matrix components may differ among the four PFAS depending on their molecular size and charge characteristics. Future work should examine kinetic behaviour across a range of PFAS concentrations, in multi-solute systems containing all four PFAS simultaneously, and in the presence of water matrix components to more fully characterise the temporal aspects of PFAS removal under realistic treatment conditions.

The stacked ^{19}F-NMR spectra for all kinetics experiments are presented in Appendix Figure 11 - Appendix Figure 18, which demonstrate the progressive disappearance of the characteristic PFAS peaks (the -CF_3 peak for each compound) as adsorption proceeds, providing visual confirmation of the kinetic data and illustrating the capability of the ^{19}F NMR method to monitor multi-PFAS removal in real-time without extensive sample preparation. The ability to simultaneously track multiple PFAS compounds in a single spectrum represents a significant advantage over LC-MS/MS methods, which require separate chromatographic separation and individual calibration curves for each analyte.



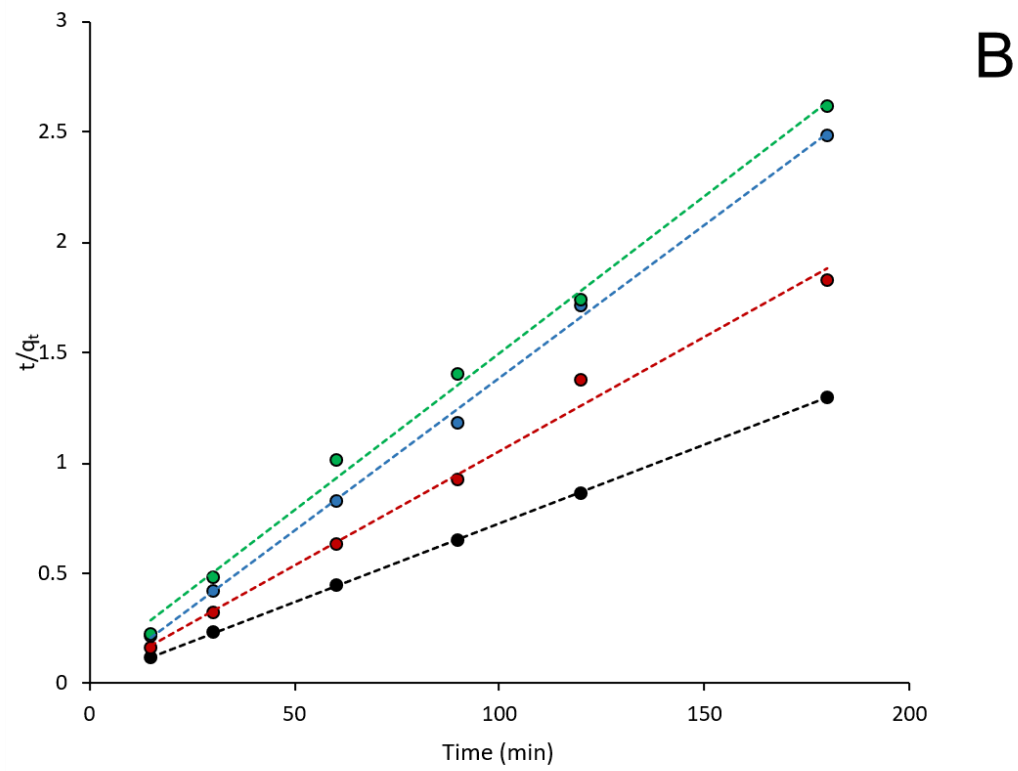


Figure 7.11. The pseudo-second order adsorption model provides the best fit for the adsorption of (A) PFOA and (B) PFHxA.

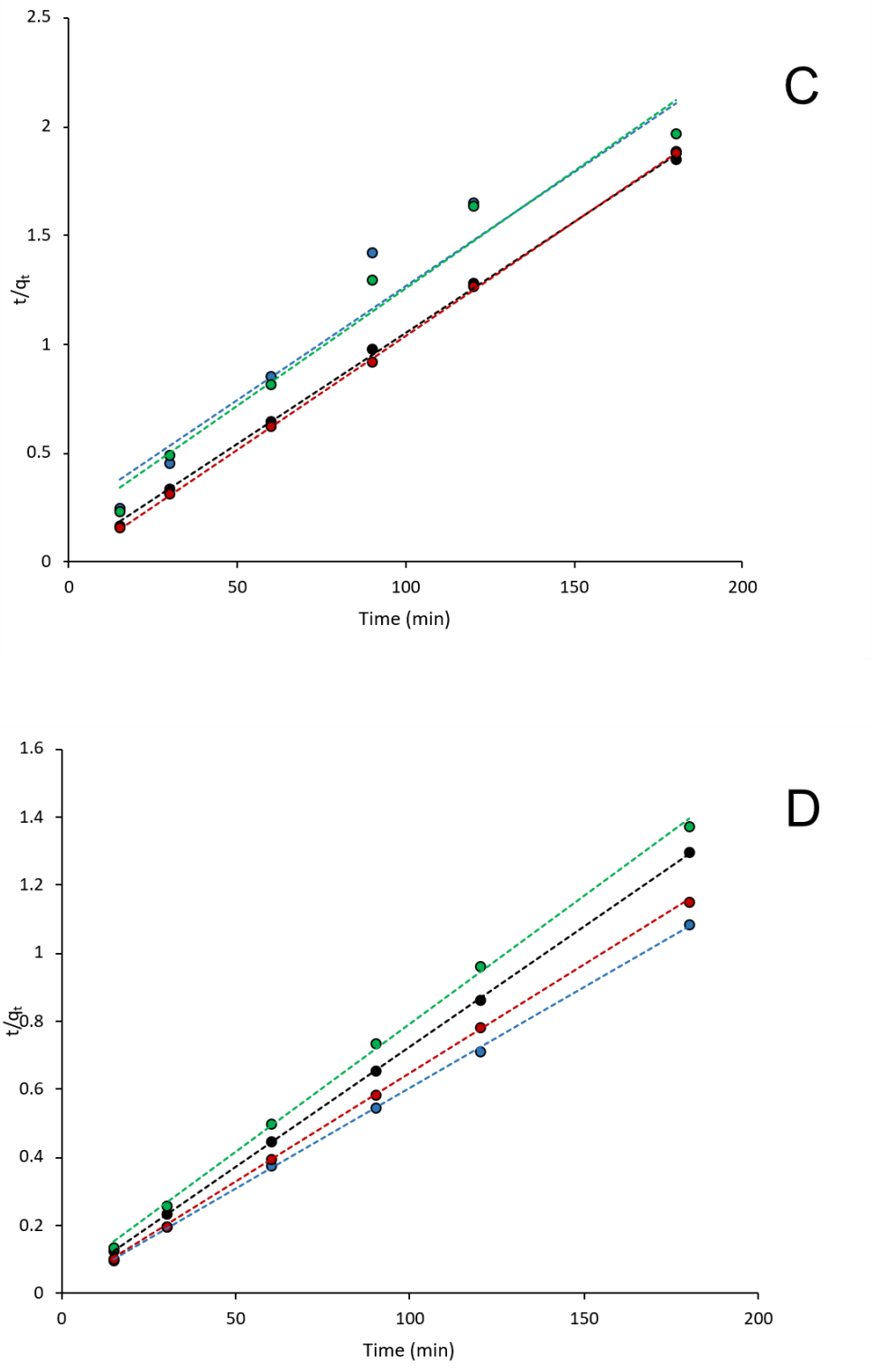


Figure 7.12. The pseudo-second order adsorption model provides the best fit for the adsorption of (C) PFBS and (D) PFOS.

7.2. Biochar Adsorption Performance

The removal adsorption capacities and removal efficiencies of biochar when adsorbing all four PFAS are presented in Figure 7.13 (data gathered with NMR).

The initial experiments were conducted with the exact same conditions as that of the four ACs, but the biochar did not remove a detectable amount of PFAS using a biochar with the ^{19}F NMR method. Therefore, the biochar dose rate was increased by an order of magnitude. This did not have profound affect on PFAS uptake, as removal efficiency for PFOS was < 25% and the removal efficiencies for PFBS, PFHxA and PFOA were all < 12%. This poor performance compared to the ACs can be attributed to the inferior surface area of biochar (~ 102 $m^2 g^{-1}$), which is an order of magnitude lower than all the ACs. Additionally, the biochar did not contain any micropores, which play a key role in PFAS adsorption. The heightened adsorption of PFOS can be explained by the

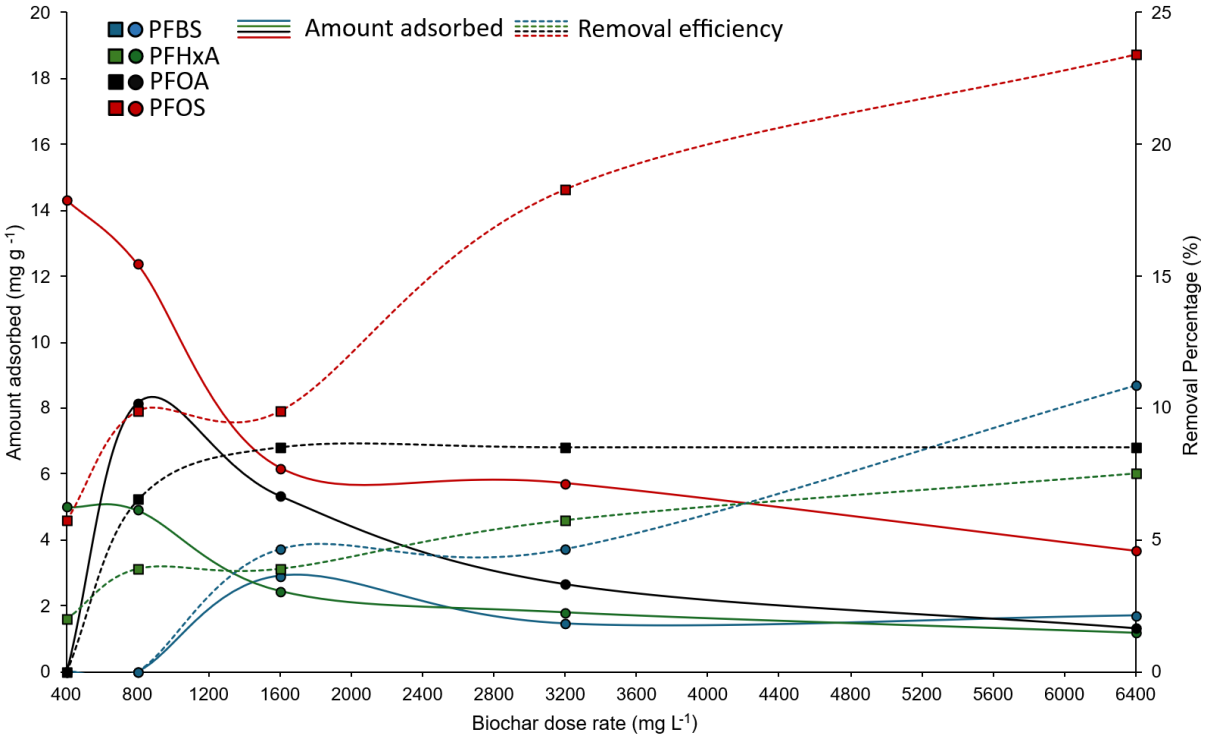


Figure 7.13. Adsorption capacities and removal efficiencies of Biochar when removing PFBS, PFHxA, PFOA and PFOS.

greater hydrophobic interaction taking place due to PFOS exhibiting the greatest number of $-CF_2$ moieties compared to the other PFAS types. Overall, this biochar is not a competitive adsorbent and does not outclass any of the other commercial ACs in anyway. Potential modification with iron nanoparticles or chitosan may enhance adsorptive performance, but its pore size distribution and surface area are the main pitfalls for this adsorbent.

7.3. LC-MS/MS analysis

The original plan was to validate the ^{19}F NMR adsorption data with replicate, proportional experiments at much lower concentrations of AC and PFAS. Unfortunately, significant PFHxA contamination was affecting the outputs of the LC-MS/MS for several months and the contamination issues were only rectified in the final month of the doctoral study period. As a result, the partially complete LC-MS/MS data sets presented in this section is only from initial adsorption isotherm experiments where the LC-MS/MS method was still being designed.

The removal adsorption capacities and removal efficiencies of biochar when adsorbing all four PFAS are presented in Figure 7.14 and Figure 7.15. Even though the dataset is incomplete, some assumptions on AC performance can be drawn. Based on the incomplete data below, the ACs general removal performances analysed with LC-MS/MS can be ranked in exactly the same order as the AC removal performances analysed by the ^{19}F NMR method developed in this study: CAC-4 > CAC-3 > CAC-2 > CAC-1.

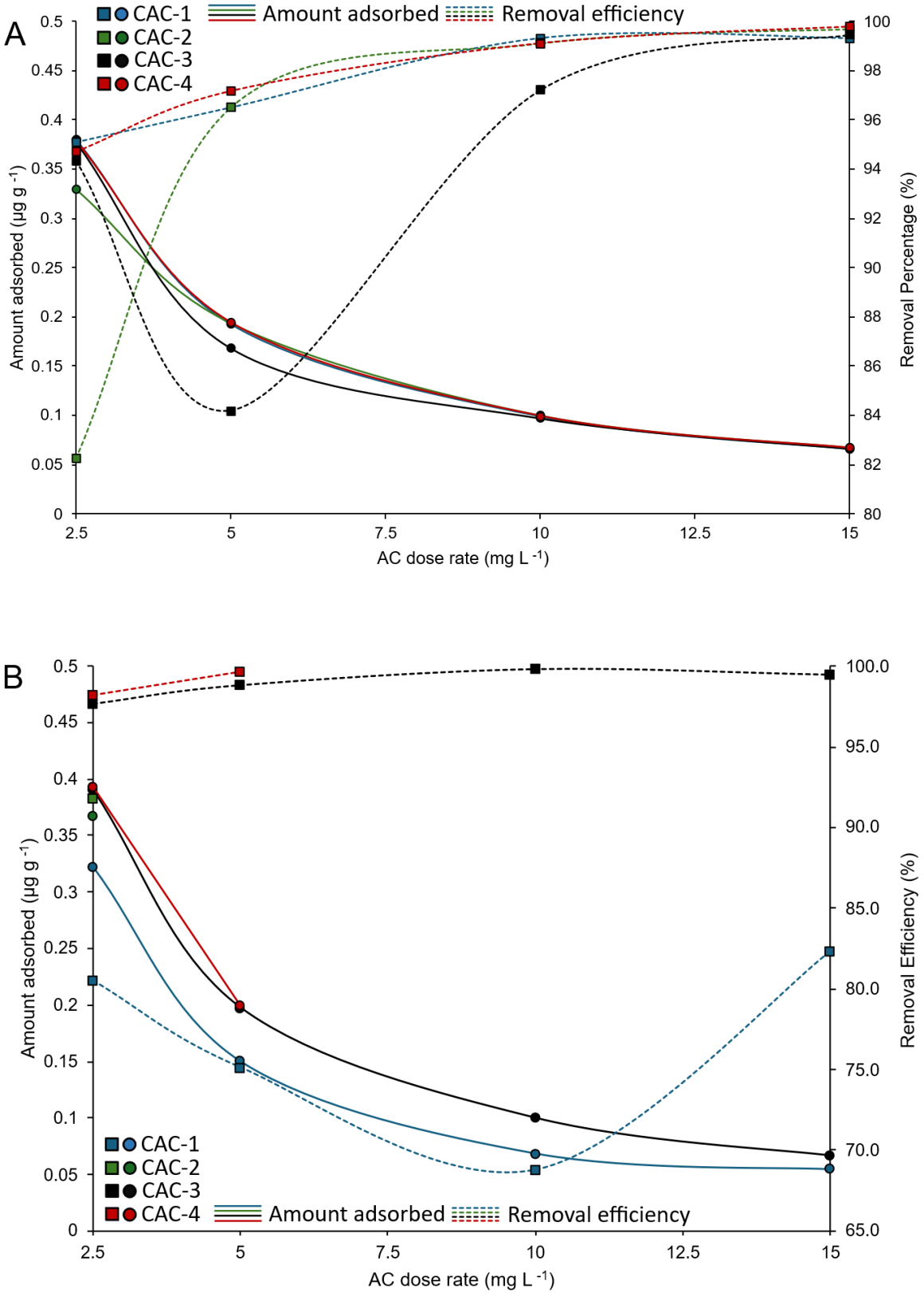


Figure 7.14. Adsorption capacities and removal efficiencies of (A) PFOA and (B) PFHxA, using the four ACs at varying dose rates (LC-MS/MS).

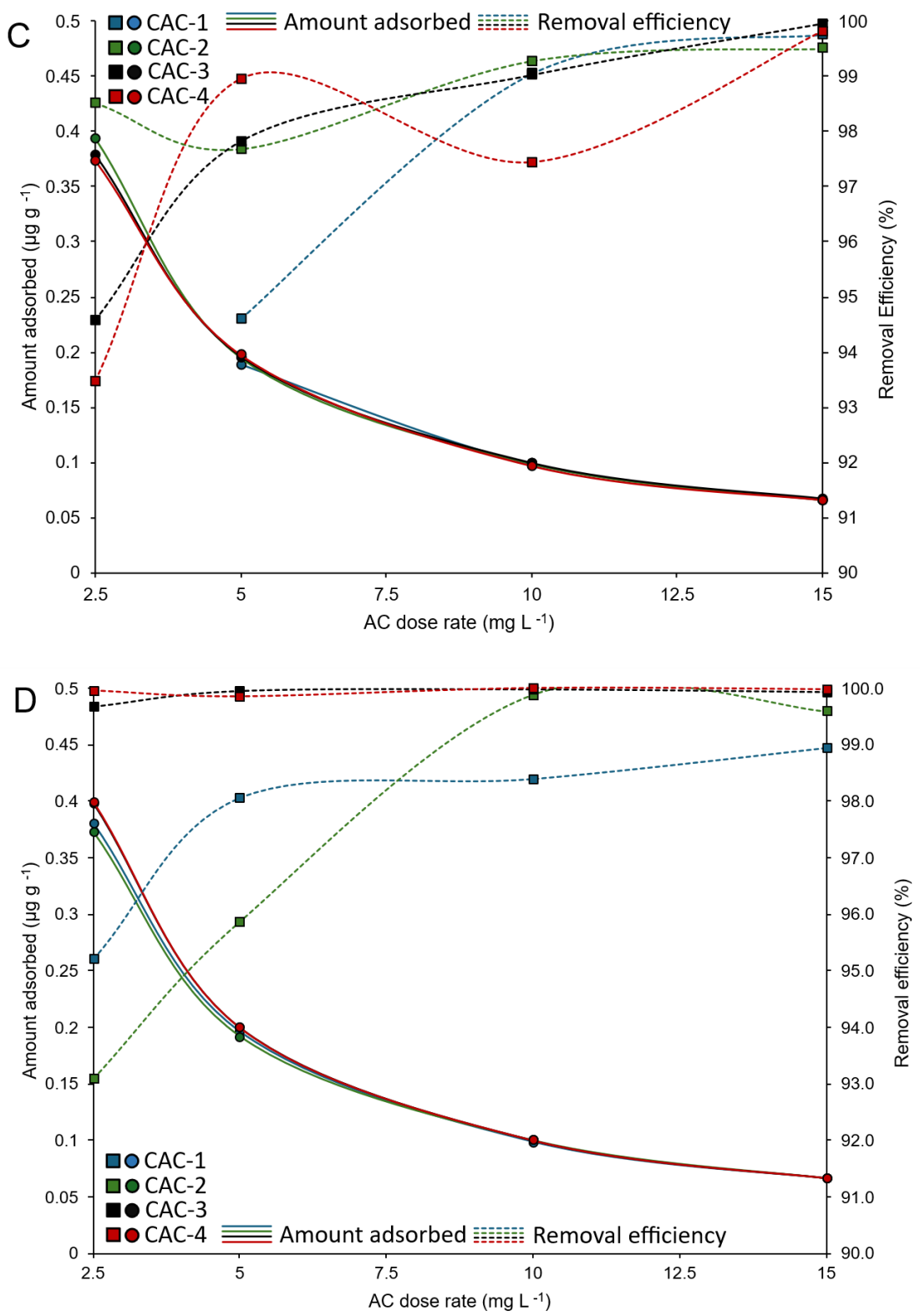


Figure 7.15. Adsorption capacities and removal efficiencies of (C) PFBS and (D) PFOS, using the four ACs at varying dose rates (LC-MS/MS).

Chapter 8 Conclusions and Future Work

8.1. Key Conclusions

1. Thorough physical and chemical characterisation of the adsorbents proved vital for the elucidation of the modes of PFAS adsorption. The chemical composition, surface chemistry, surface area and pore size distribution information enabled the PFAS adsorption data to be fully understood and for the adsorbent performance to be ranked.
2. A novel application of ^{19}F NMR for the rapid screening of PFAS targeting adsorbents was developed with sufficient sensitivity for initial adsorbent screening processes. The lack of sample clean-up demonstrated in the method is a desirable feature of adsorbent testing, especially when compared to the standard sample-preparation-heavy analytical technique of LC-MS/MS. The sensitivity of the NMR instrument used in the study is not suitable for environmental concentrations of PFAS due to the magnet strength being too weak, and even then, the samples may need to be pre-concentrated. However, each sample can be analysed in under one hour counting both sample preparation and NMR experimental time, and can also quantify all PFAS types with a terminal -CF_3 group (LC-MS/MS cannot detect the majority of PFAS types due to the lack of internal standards).
3. The initial data obtained by the ^{19}F NMR spectroscopy in this study indicated that CAC-4 was the best performing adsorbent for the removal of all the PFAS types used, which was expected due to the varied physical and chemical properties data obtained through the full characterisation of the ACs. CAC-4, exhibited the highest surface area and the most favourable pore size

distribution for PFAS adsorption, presenting the highest mesopore volume. Additionally, the CAC-1 had the highest oxygen to carbon ratio, further enhancing adsorption of short-chain PFAS compared to the other ACs.

4. A boreal woodchip biochar was also analysed and was found to be inferior in its adsorption performance for all PFAS types when compared to the four ACs. BET and XPS analysis revealed a far lower surface area and oxygen to carbon ratio, respectively. The biochar was not in granular form and so cannot be commercially regenerated either, and so was deemed not suitable for industrial PFAS treatment in water.

8.2. Future Work

Lab-scale future work: It would be useful to investigate environmental water samples with the proposed ^{19}F NMR method in this study. Although the PFAS levels may be at ppt levels when samples are taken initially, and would not be able to be detected by the NMR method, if enough sample volume was taken, the samples could be pre-concentrated to a high enough concentration for detection/quantification. This could be carried out using solid-phase extraction (SPE), or even the more modern micro-SPE (μSPE) method, which employs smaller sorbent particles and higher pressures, enabling smaller sample volumes to be used whilst also improving efficiency in some cases. The concentrations used in this study were on the ppm scale, but SPE could enable analysis of PFAS on ppb/ppt scale.

Pilot-scale: The investigation of adsorbent performance in PFAS treatment using a packed bed AC column with analysis using the ^{19}F NMR method outlined in this study would provide insight into the PFAS adsorption in a more realistic treatment setup. This process would enable quantification of samples from a process more

similar to a real water treatment plant and could potentially be conducted with real environmental water samples which contain other contaminants as well as PFAS, like DOM, which could compete with or slow down PFAS adsorption.

NMR Instrumentation: A major drawback in this study was to do with the specific 500 MHz NMR spectrometer used for all adsorption experimental data collection – the instrument contained part(s) coated with PFAS. This did have an impact on the NMR spectral baseline in some experiments, which caused them to fail (Figure 6.6).

For future work, the quantitative ^{19}F-NMR method outlined in this study should be carried out with an NMR spectrometer with PFAS-free coatings to ensure a stable baseline that cannot impact quantification accuracy. Moreover, lower limits of detection and quantification could be reached using an NMR spectrometer with an ultra-high magnetic field, such as the Bruker AVANCE NEO 1.2 GHz NMR instrument. A stronger magnetic field would enable a higher signal-to-noise ratio for the same number of scans when compared to an NMR instrument with a lower magnetic field, enabling more accurate quantification or allowing for shorter experimental time by achieving the same signal-to-noise ratio but with fewer scans.

^{19}F-NMR Method: The method presented in this study could be further enhanced with both reductions in experimental time and increases in sensitivity through modification of the method and the fine-tuning of the experimental parameters. A recent study by Gauthier *et al.*[260] demonstrated the use of Steady State Free Precession NMR combined with non-Fourier based time-domain analysis, which enabled a ~50 fold increase in the detection limit for PFOA-spiked human blood samples when compared to standard NMR methods. A similar NMR method could

be used alongside the sample preparation outlined in this project to enable much lower limits of detection and the progression towards quantifying environmental PFAS samples without arduous sample extraction steps.

References

(1) Smalling, K. L.; Romanok, K. M.; Bradley, P. M.; Morriss, M. C.; Gray, J. L.; Kanagy, L. K.; Gordon, S. E.; Williams, B. M.; Breitmeyer, S. E.; Jones, D. K.; et al. Per- and polyfluoroalkyl substances (PFAS) in United States tapwater: Comparison of underserved private-well and public-supply exposures and associated health implications. *Environment International* **2023**, *178*, 108033.
(2) Panieri, E.; Baralic, K.; Djukic-Cosic, D.; Buha Djordjevic, A.; Saso, L. PFAS Molecules: A Major Concern for the Human Health and the Environment. *Toxics* **2022**, *10* (2), 44.
(3) van der Veen, I.; Fiedler, H.; de Boer, J. Assessment of the per-and polyfluoroalkyl substances analysis under the Stockholm Convention–2018/2019. *Chemosphere* **2023**, *313*, 137549.
(4) Sunderland, E. M.; Hu, X. C.; Dassuncao, C.; Tokranov, A. K.; Wagner, C. C.; Allen, J. G. A review of the pathways of human exposure to poly- and perfluoroalkyl substances (PFASs) and present understanding of health effects. *Journal of Exposure Science & Environmental Epidemiology* **2019**, *29* (2), 131-147.
(5) Gaines, L. G. T. Historical and current usage of per- and polyfluoroalkyl substances (PFAS): A literature review. *American Journal of Industrial Medicine* **2023**, *66* (5), 353-378.
(6) Buck, R. C.; Franklin, J.; Berger, U.; Conder, J. M.; Cousins, I. T.; De Voogt, P.; Jensen, A. A.; Kannan, K.; Mabury, S. A.; van Leeuwen, S. P. Perfluoroalkyl and polyfluoroalkyl substances in the environment: terminology, classification, and origins. *Integrated environmental assessment and management* **2011**, *7* (4), 513-541.
(7) Tian, Q.; Sun, M. Chapter 14 - Analysis of GenX and Other Per- and Polyfluoroalkyl Substances in Environmental Water Samples. In *Separation Science and Technology*, Ahuja, S. Ed.; Vol. 11; Academic Press, 2019; pp 355-370.
(8) Li, J.; Sun, J.; Li, P. Exposure routes, bioaccumulation and toxic effects of per- and polyfluoroalkyl substances (PFASs) on plants: A critical review. *Environment International* **2022**, *158*, 106891.
(9) O'Hagan, D. Understanding organofluorine chemistry. An introduction to the C–F bond. *Chemical Society Reviews* **2008**, *37* (2), 308-319, 10.1039/B711844A.
(10) Kucharzyk, K. H.; Darlington, R.; Benotti, M.; Deeb, R.; Hawley, E. Novel treatment technologies for PFAS compounds: A critical review. *Journal of Environmental Management* **2017**, *204*, 757-764.
(11) Risk assessments under regulation 27 and associated reports under regulation 28 of the Water Supply (Water Quality) Regulations 2016 (2018 in Wales) for Poly and Perfluorinated Alkyl Substances (PFAS). Inspectorate, D. W., Ed.; DEFRA: 2022.
(12) ECHA. PFAS Restriction Proposal. ECHA, Ed.; 2023; Vol. ECHA/NR/23/04.
(13) Rigby, H.; Dowding, A.; Fernandes, A.; Humphries, D.; Jones, N. R.; Lake, I.; Petch, R. G.; Reynolds, C. K.; Rose, M.; Smith, S. R. Concentrations of organic contaminants in industrial and municipal bioresources recycled in agriculture in the UK. *Science of The Total Environment* **2021**, *765*, 142787.
(14) Ateia, M.; Maroli, A.; Tharayil, N.; Karanfil, T. The overlooked short- and ultrashort-chain poly- and perfluorinated substances: A review. *Chemosphere* **2019**, *220*, 866-882.
(15) Fenton, S. E.; Ducatman, A.; Boobis, A.; DeWitt, J. C.; Lau, C.; Ng, C.; Smith, J. S.; Roberts, S. M. Per- and Polyfluoroalkyl Substance Toxicity and Human Health Review: Current State of

Knowledge and Strategies for Informing Future Research. *Environmental Toxicology and Chemistry* **2021**, *40* (3), 606-630.
(16) Chain, E. Panel o. C. i. t. F.; Schrenk, D.; Bignami, M.; Bodin, L.; Chipman, J. K.; del Mazo, J.; Grasl-Kraupp, B.; Hogstrand, C.; Hoogenboom, L.; Leblanc, J.-C.; et al. Risk to human health related to the presence of perfluoroalkyl substances in food. *EFSA Journal* **2020**, *18* (9), e06223.
(17) Rao, U.; Su, Y.; Khor, C. M.; Jung, B.; Ma, S.; Cwiertny, D. M.; Wong, B. M.; Jassby, D. Structural Dependence of Reductive Defluorination of Linear PFAS Compounds in a UV/Electrochemical System. *Environmental Science & Technology* **2020**, *54* (17), 10668-10677.
(18) Moneta, B. G.; Feo, M. L.; Torre, M.; Tratzi, P.; Aita, S. E.; Montone, C. M.; Taglioni, E.; Mosca, S.; Balducci, C.; Cerasa, M.; et al. Occurrence of per- and polyfluorinated alkyl substances in wastewater treatment plants in Northern Italy. *Science of The Total Environment* **2023**, *894*, 165089.
(19) Cantoni, B.; Turolla, A.; Wellmitz, J.; Ruhl, A. S.; Antonelli, M. Perfluoroalkyl substances (PFAS) adsorption in drinking water by granular activated carbon: Influence of activated carbon and PFAS characteristics. *Science of The Total Environment* **2021**, *795*, 148821.
(20) Liu, C.; Zhao, X.; Faria, A. F.; Quiñones, K. Y. D.; Zhang, C.; He, Q.; Ma, J.; Shen, Y.; Zhi, Y. Evaluating the efficiency of nanofiltration and reverse osmosis membrane processes for the removal of per-and polyfluoroalkyl substances from water: A critical review. *Separation and Purification Technology* **2022**, 122161.
(21) Boyer, T. H.; Fang, Y.; Ellis, A.; Dietz, R.; Choi, Y. J.; Schaefer, C. E.; Higgins, C. P.; Strathmann, T. J. Anion exchange resin removal of per-and polyfluoroalkyl substances (PFAS) from impacted water: A critical review. *Water research* **2021**, *200*, 117244.
(22) Lee, T.; Speth, T. F.; Nadagouda, M. N. High-pressure membrane filtration processes for separation of Per-and polyfluoroalkyl substances (PFAS). *Chemical Engineering Journal* **2022**, *431*, 134023.
(23) Baudequin, C.; Mai, Z.; Rakib, M.; Deguerry, I.; Severac, R.; Pabon, M.; Couallier, E. Removal of fluorinated surfactants by reverse osmosis – Role of surfactants in membrane fouling. *Journal of Membrane Science* **2014**, *458*, 111–119.
(24) Dixit, F.; Dutta, R.; Barbeau, B.; Berube, P.; Mohseni, M. PFAS removal by ion exchange resins: A review. *Chemosphere* **2021**, *272*, 129777.
(25) Riegel, M.; Haist-Gulde, B.; Sacher, F. Sorptive removal of short-chain perfluoroalkyl substances (PFAS) during drinking water treatment using activated carbon and anion exchanger. *Environmental Sciences Europe* **2023**, *35* (1), 12.
(26) Dixit, F.; Barbeau, B.; Mostafavi, S. G.; Mohseni, M. PFAS and DOM removal using an organic scavenger and PFAS-specific resin: Trade-off between regeneration and faster kinetics. *Science of the Total Environment* **2021**, *754*, 142107.
(27) Dixit, F.; Barbeau, B.; Mostafavi, S. G.; Mohseni, M. Efficient removal of GenX (HFPO-DA) and other perfluorinated ether acids from drinking and recycled waters using anion exchange resins. *Journal of hazardous materials* **2020**, *384*, 121261.
(28) Chularueangaksorn, P.; Tanaka, S.; Fujii, S.; Kunacheva, C. Adsorption of perfluorooctanoic acid (PFOA) onto anion exchange resin, non-ion exchange resin, and granular-activated carbon by batch and column. *Desalination and Water Treatment* **2014**, *52* (34-36), 6542-6548.
(29) Woodard, S.; Berry, J.; Newman, B. Ion exchange resin for PFAS removal and pilot test comparison to GAC. *Remediation Journal* **2017**, *27* (3), 19-27.
(30) Gagliano, E.; Sgroi, M.; Falciglia, P. P.; Vagliasindi, F. G. A.; Roccaro, P. Removal of poly- and perfluoroalkyl substances (PFAS) from water by adsorption: Role of PFAS chain length, effect

of organic matter and challenges in adsorbent regeneration. *Water Research* **2020**, *171*, 115381.
(31) Kitagawa, S. Metal–organic frameworks (MOFs). *Chemical Society Reviews* **2014**, *43* (16), 5415-5418.
(32) Azmi, L. H. M.; Williams, D. R.; Ladewig, B. P. Polymer-assisted modification of metal-organic framework MIL-96 (Al): influence of HPAM concentration on particle size, crystal morphology and removal of harmful environmental pollutant PFOA. *Chemosphere* **2021**, *262*, 128072.
(33) An, Y.; Lv, X.; Jiang, W.; Wang, L.; Shi, Y.; Hang, X.; Pang, H. The stability of MOFs in aqueous solutions—research progress and prospects. *Green Chemical Engineering* **2023**.
(34) Liu, K.; Zhang, S.; Hu, X.; Zhang, K.; Roy, A.; Yu, G. Understanding the Adsorption of PFOA on MIL-101(Cr)-Based Anionic-Exchange Metal–Organic Frameworks: Comparing DFT Calculations with Aqueous Sorption Experiments. *Environmental Science & Technology* **2015**, *49* (14), 8657-8665.
(35) Sini, K.; Bourgeois, D.; Idouhar, M.; Carboni, M.; Meyer, D. Metal-organic frameworks cavity size effect on the extraction of organic pollutants. *Materials Letters* **2019**, *250*, 92-95.
(36) Rojas, S.; Horcajada, P. Metal–Organic Frameworks for the Removal of Emerging Organic Contaminants in Water. *Chemical Reviews* **2020**, *120* (16), 8378-8415.
(37) Wang, R.; Lin, Z.-W.; Klemes, M. J.; Ateia, M.; Trang, B.; Wang, J.; Ching, C.; Helbling, D. E.; Dichtel, W. R. A Tunable Porous β-Cyclodextrin Polymer Platform to Understand and Improve Anionic PFAS Removal. *ACS Central Science* **2022**, *8* (5), 663-669.
(38) Ateia, M.; Arifuzzaman, M.; Pellizzeri, S.; Attia, M. F.; Tharayil, N.; Anker, J. N.; Karanfil, T. Cationic polymer for selective removal of GenX and short-chain PFAS from surface waters and wastewaters at ng/L levels. *Water Research* **2019**, *163*, 114874.
(39) Parvin, S.; Hara-Yamamura, H.; Kanai, Y.; Yamasaki, A.; Adachi, T.; Sorn, S.; Honda, R.; Yamamura, H. Important properties of anion exchange resins for efficient removal of PFOS and PFOA from groundwater. *Chemosphere* **2023**, *341*, 139983.
(40) Xie, R.; Zhou, L.; Smith, A. E.; Almquist, C. B.; Berberich, J. A.; Danielson, N. D. A dual grafted fluorinated hydrocarbon amine weak anion exchange resin polymer for adsorption of perfluorooctanoic acid from water. *Journal of Hazardous Materials* **2022**, *431*, 128521.
(41) Kong, Z.; Lu, L.; Zhu, C.; Xu, J.; Fang, Q.; Liu, R.; Shen, Y. Enhanced adsorption and photocatalytic removal of PFOA from water by F-functionalized MOF with in-situ-growth TiO2: Regulation of electron density and bandgap. *Separation and Purification Technology* **2022**, *297*, 121449.
(42) Maimaiti, A.; Deng, S.; Meng, P.; Wang, W.; Wang, B.; Huang, J.; Wang, Y.; Yu, G. Competitive adsorption of perfluoroalkyl substances on anion exchange resins in simulated AFFF-impacted groundwater. *Chemical Engineering Journal* **2018**, *348*, 494-502.
(43) Deng, S.; Yu, Q.; Huang, J.; Yu, G. Removal of perfluorooctane sulfonate from wastewater by anion exchange resins: Effects of resin properties and solution chemistry. *Water Research* **2010**, *44* (18), 5188-5195.
(44) Zhao, C.; Xu, Y.; Xiao, F.; Ma, J.; Zou, Y.; Tang, W. Perfluorooctane sulfonate removal by metal-organic frameworks (MOFs): Insights into the effect and mechanism of metal nodes and organic ligands. *Chemical Engineering Journal* **2021**, *406*, 126852.
(45) Wang, W.; Maimaiti, A.; Shi, H.; Wu, R.; Wang, R.; Li, Z.; Qi, D.; Yu, G.; Deng, S. Adsorption behavior and mechanism of emerging perfluoro-2-propoxypropanoic acid (GenX) on activated carbons and resins. *Chemical Engineering Journal* **2019**, *364*, 132-138.

(46) Guo, H.; Hu, T.; Yang, X.; Liu, Z.; Cui, Q.; Qu, C.; Guo, F.; Liu, S.; Sweetman, A. J.; Hou, J.; et al. Roles of varying carbon chains and functional groups of legacy and emerging per-/polyfluoroalkyl substances in adsorption on metal-organic framework: Insights into mechanism and adsorption prediction. *Environmental Research* **2024**, *251*, 118679.
(47) Wang, Y.; Ji, Y.; Tishchenko, V.; Huang, Q. Removing per- and polyfluoroalkyl substances (PFAS) in water by foam fractionation. *Chemosphere* **2023**, *311*, 137004.
(48) Smith, S. J.; Wiberg, K.; McCleaf, P.; Ahrens, L. Pilot-scale continuous foam fractionation for the removal of per-and polyfluoroalkyl substances (PFAS) from landfill leachate. *ACS Es&t Water* **2022**, *2* (5), 841-851.
(49) Buckley, T.; Karanam, K.; Xu, X.; Shukla, P.; Firouzi, M.; Rudolph, V. Effect of mono-and di-valent cations on PFAS removal from water using foam fractionation–A modelling and experimental study. *Separation and Purification Technology* **2022**, *286*, 120508.
(50) Li, Y.-F.; Ho, C.-Y.; Liu, Y.-J.; Lee, Y.-C.; Hu, C.-Y.; Lo, S.-L. Enhance electrocoagulation-flotation (ECF) removal efficiency perfluorohexanoic acid (PFHxA) by adding surfactants. *Journal of Environmental Chemical Engineering* **2024**, *12* (1), 111773.
(51) Sivagami, K.; Sharma, P.; Karim, A. V.; Mohanakrishna, G.; Karthika, S.; Divyapriya, G.; Saravanathamizhan, R.; Kumar, A. N. Electrochemical-based approaches for the treatment of forever chemicals: removal of perfluoroalkyl and polyfluoroalkyl substances (PFAS) from wastewater. *Science of the Total Environment* **2023**, *861*, 160440.
(52) Shi, H.; Chiang, S.-Y. D.; Wang, Y.; Wang, Y.; Liang, S.; Zhou, J.; Fontanez, R.; Gao, S.; Huang, Q. An electrocoagulation and electrooxidation treatment train to remove and degrade per- and polyfluoroalkyl substances in aqueous solution. *Science of the Total Environment* **2021**, *788*, 147723.
(53) Mudumbi, J.; Ntwampe, S.; Muganza, M.; Okonkwo, J. Susceptibility of riparian wetland plants to perfluorooctanoic acid (PFOA) accumulation. *International journal of phytoremediation* **2014**, *16* (9), 926-936.
(54) Mayakaduwage, S.; Ekanayake, A.; Kurwadkar, S.; Rajapaksha, A. U.; Vithanage, M. Phytoremediation prospects of per-and polyfluoroalkyl substances: a review. *Environmental Research* **2022**, *212*, 113311.
(55) Rivera-Utrilla, J.; Sánchez-Polo, M.; Gómez-Serrano, V.; Álvarez, P.; Alvim-Ferraz, M.; Dias, J. Activated carbon modifications to enhance its water treatment applications. An overview. *Journal of hazardous materials* **2011**, *187* (1-3), 1-23.
(56) Bhatnagar, A.; Hogland, W.; Marques, M.; Sillanpää, M. An overview of the modification methods of activated carbon for its water treatment applications. *Chemical Engineering Journal* **2013**, *219*, 499-511.
(57) Allen, S.; Whitten, L.; McKay, G. The production and characterisation of activated carbons: a review. *Developments in Chemical Engineering and Mineral Processing* **1998**, *6* (5), 231-261.
(58) Viswanathan, B.; Neel, P. I.; Varadarajan, T. Methods of activation and specific applications of carbon materials. *India, Chennai* **2009**, *600* (36), 1-160.
(59) Leng, C.-C.; Pinto, N. G. An Investigation of the Mechanisms of Chemical Regeneration of Activated Carbon. *Industrial & Engineering Chemistry Research* **1996**, *35* (6), 2024-2031.
(60) Kanchanapiya, P.; Songngam, S.; Tantisattayakul, T. The Adsorption of Perfluorooctanoic Acid on Coconut Shell Activated Carbons. *AIMS Environmental Science* **2022**, *9* (2).
(61) Omo-Okoro, P. N.; Curtis, C. J.; Marco, A. M.; Melymuk, L.; Okonkwo, J. O. Removal of per- and polyfluoroalkyl substances from aqueous media using synthesized silver nanocomposite-activated carbons. *Journal of Environmental Health Science and Engineering* **2021**, *19* (1), 217-236.

(62) Liu, W.; Lin, T.; Zhang, X.; Jiang, F.; Yan, X.; Chen, H. Adsorption of perfluoroalkyl acids on granular activated carbon supported chitosan: Role of nanobubbles. *Chemosphere* **2022**, *309*, 136733.
(63) Arana Juve, J.-M.; Baami González, X.; Bai, L.; Xie, Z.; Shang, Y.; Saad, A.; Gonzalez-Olmos, R.; Wong, M. S.; Ateia, M.; Wei, Z. Size-selective trapping and photocatalytic degradation of PFOA in Fe-modified zeolite frameworks. *Applied Catalysis B: Environment and Energy* **2024**, *349*, 123885.
(64) Shin, J.; An, B. Effect of ligand interactions within modified granular activated carbon (GAC) on mixed perfluorooctanoic acid (PFOA) and perfluorooctanesulfonic acid (PFOS) adsorption. *Chemosphere* **2024**, *357*, 142025.
(65) Medha, S.; Romisher, Z.; Van Bramer, S.; Weyrich, J.; Khan, S.; Saha, D. Enhanced adsorption of perfluorooctanesulfonic acid (PFOS) in fluorine doped mesoporous carbon: Experiment and simulation. *Carbon* **2024**, *218*, 118745.
(66) Fagbayigbo, B. O.; Opeolu, B. O.; Fatoki, O. S. Adsorption of perfluorooctanoic acid (PFOA) and perfluorooctane sulfonate (PFOS) from water using leaf biomass (Vitis vinifera) in a fixed-bed column study. *Journal of Environmental Health Science and Engineering* **2020**, *18* (1), 221-233.
(67) Steigerwald, J. M.; Ray, J. R. Adsorption behavior of perfluorooctanesulfonate (PFOS) onto activated spent coffee grounds biochar in synthetic wastewater effluent. *Journal of Hazardous Materials Letters* **2021**, *2*, 100025.
(68) Kang, J.-K.; Kim, M.-G.; Kim, S.-B.; Jeong, S.; Oh, J.-E. Comparative study on Perfluoro(2-methyl-3-oxahexanoic) acid removal by quaternary ammonium functionalized silica gel and granular activated carbon from batch and column experiments and molecular simulation-based interpretation. *Science of The Total Environment* **2024**, *926*, 171753.
(69) Krahn, K. M.; Cornelissen, G.; Castro, G.; Arp, H. P. H.; Asimakopoulos, A. G.; Wolf, R.; Holmstad, R.; Zimmerman, A. R.; Sørmo, E. Sewage sludge biochars as effective PFAS-sorbents. *Journal of Hazardous Materials* **2023**, *445*, 130449.
(70) Wang, H.; Zhang, H.; He, L.; Wang, J.; Wang, S.; Shi, X.; Zhang, X.; Wang, H.; He, F. Environmental behavior of per- and polyfluoroalkyl substances (PFASs) and the potential role of biochar for its remediation: a review. *Biochar* **2025**, *7* (1), 14.
(71) Zhang, Y.; Tan, X.; Lu, R.; Tang, Y.; Qie, H.; Huang, Z.; Zhao, J.; Cui, J.; Yang, W.; Lin, A. Enhanced Removal of Polyfluoroalkyl Substances by Simple Modified Biochar: Adsorption Performance and Theoretical Calculation. *ACS ES&T Water* **2023**, *3* (3), 817-826.
(72) Afrooz, M.; Zeynali, R.; Soltan, J.; McPhedran, K. N. A novel biochar adsorbent for treatment of perfluorooctanoic acid (PFOA) contaminated water: Exploring batch and dynamic adsorption behavior. *Journal of Water Process Engineering* **2025**, *69*, 106586.
(73) Nguyen, M. D.; Sivaram, A. K.; Megharaj, M.; Webb, L.; Adhikari, S.; Thomas, M.; Surapaneni, A.; Moon, E. M.; Milne, N. A. Investigation on removal of perfluorooctanoic acid (PFOA), perfluorooctane sulfonate (PFOS), perfluorohexane sulfonate (PFHxS) using water treatment sludge and biochar. *Chemosphere* **2023**, *338*, 139412.
(74) Sahu, O. Remediation of perfluorooctanoic acid (PFOA) with nano ceramic clay: Synthesis, characterization, scale-up and regenerations. *Environmental Pollution* **2023**, *322*, 121241.
(75) Inyang, M.; Dickenson, E. R. V. The use of carbon adsorbents for the removal of perfluoroalkyl acids from potable reuse systems. *Chemosphere* **2017**, *184*, 168-175.
(76) Niaz, W.; Zhang, D.; Ahmad, Z.; Shen, N.; Haider, W.; Ali, I.; Usman, M.; Majid, A.; Javaid, S. F.; Amjed, M. A.; et al. Efficient removal of perfluorooctanoic acid (PFOA) and perfluorooctane sulfonic acid (PFOS) from aqueous solution using modified biochar:

Preparation, performance, and mechanistic insights. *Journal of Environmental Chemical Engineering* **2024**, *12* (6), 114894.
(77) Liang, D.; Li, C.; Chen, H.; Sørmo, E.; Cornelissen, G.; Gao, Y.; Reguyal, F.; Sarmah, A.; Ippolito, J.; Kammann, C.; et al. A critical review of biochar for the remediation of PFAS-contaminated soil and water. *Science of The Total Environment* **2024**, *951*, 174962.
(78) Zhao, L.; Bian, J.; Zhang, Y.; Zhu, L.; Liu, Z. Comparison of the sorption behaviors and mechanisms of perfluorosulfonates and perfluorocarboxylic acids on three kinds of clay minerals. *Chemosphere* **2014**, *114*, 51-58.
(79) Mukhopadhyay, R.; Sarkar, B.; Palansooriya, K. N.; Dar, J. Y.; Bolan, N. S.; Parikh, S. J.; Sonne, C.; Ok, Y. S. Natural and engineered clays and clay minerals for the removal of poly- and perfluoroalkyl substances from water: State-of-the-art and future perspectives. *Advances in Colloid and Interface Science* **2021**, *297*, 102537.
(80) Deng, J.; Han, J.; Hou, C.; Zhang, Y.; Fang, Y.; Du, W.; Li, M.; Yuan, Y.; Tang, C.; Hu, X. Efficient removal of per- and polyfluoroalkyl substances from biochar composites: Cyclic adsorption and spent regenerant degradation. *Chemosphere* **2023**, *341*, 140051.
(81) Jiang, T.; Pervez, M. N.; Ilango, A. K.; Ravi, Y. K.; Zhang, W.; Feldblyum, J. I.; Yigit, M. V.; Efstathiadis, H.; Liang, Y. Magnetic surfactant-modified clay for enhanced adsorption of mixtures of per- and polyfluoroalkyl substances (PFAS) in snowmelt: Improving practical applicability and efficiency. *Journal of Hazardous Materials* **2024**, *471*, 134390.
(82) Luft, C. M.; Schutt, T. C.; Shukla, M. K. Properties and mechanisms for PFAS adsorption to aqueous clay and humic soil components. *Environmental Science & Technology* **2022**, *56* (14), 10053-10061.
(83) Wang, M.; Orr, A. A.; Jakubowski, J. M.; Bird, K. E.; Casey, C. M.; Hearon, S. E.; Tamamis, P.; Phillips, T. D. Enhanced adsorption of per-and polyfluoroalkyl substances (PFAS) by edible, nutrient-amended montmorillonite clays. *Water research* **2021**, *188*, 116534.
(84) Sarkar, B.; Rusmin, R.; Ugochukwu, U. C.; Mukhopadhyay, R.; Manjaiah, K. M. Modified clay minerals for environmental applications. In *Modified clay and zeolite nanocomposite materials*, Elsevier, 2019; pp 113-127.
(85) Gong, Y.; Wang, L.; Liu, J.; Tang, J.; Zhao, D. Removal of aqueous perfluorooctanoic acid (PFOA) using starch-stabilized magnetite nanoparticles. *Science of the Total Environment* **2016**, *562*, 191-200.
(86) Arvaniti, O. S.; Hwang, Y.; Andersen, H. R.; Stasinakis, A. S.; Thomaidis, N. S.; Aloupi, M. Reductive degradation of perfluorinated compounds in water using Mg-aminoclay coated nanoscale zero valent iron. *Chemical Engineering Journal* **2015**, *262*, 133-139.
(87) Hassan, M.; Liu, Y.; Naidu, R.; Du, J.; Qi, F. Adsorption of Perfluorooctane sulfonate (PFOS) onto metal oxides modified biochar. *Environmental Technology & Innovation* **2020**, *19*, 100816.
(88) Sonmez Baghirzade, B.; Zhang, Y.; Reuther, J. F.; Saleh, N. B.; Venkatesan, A. K.; Apul, O. G. Thermal Regeneration of Spent Granular Activated Carbon Presents an Opportunity to Break the Forever PFAS Cycle. *Environmental Science & Technology* **2021**, *55* (9), 5608-5619.
(89) Li, F.; Duan, J.; Tian, S.; Ji, H.; Zhu, Y.; Wei, Z.; Zhao, D. Short-chain per- and polyfluoroalkyl substances in aquatic systems: Occurrence, impacts and treatment. *Chemical Engineering Journal* **2020**, *380*, 122506.
(90) Veciana, M.; Bräunig, J.; Farhat, A.; Pype, M.-L.; Freguia, S.; Carvalho, G.; Keller, J.; Ledezma, P. Electrochemical oxidation processes for PFAS removal from contaminated water and wastewater: fundamentals, gaps and opportunities towards practical implementation. *Journal of Hazardous Materials* **2022**, *434*, 128886.

(91) Pierpaoli, M.; Szopińska, M.; Wilk, B. K.; Sobaszek, M.; Łuczkiewicz, A.; Bogdanowicz, R.; Fudala-Książek, S. Electrochemical oxidation of PFOA and PFOS in landfill leachates at low and highly boron-doped diamond electrodes. *Journal of Hazardous Materials* **2021**, *403*, 123606.
(92) Fang, Y.; Meng, P.; Schaefer, C.; Knappe, D. R. Removal and destruction of perfluoroalkyl ether carboxylic acids (PFECAs) in an anion exchange resin and electrochemical oxidation treatment train. *Water Research* **2023**, *230*, 119522.
(93) Yang, S.; Fernando, S.; Holsen, T. M.; Yang, Y. Inhibition of perchlorate formation during the electrochemical oxidation of perfluoroalkyl acid in groundwater. *Environmental Science & Technology Letters* **2019**, *6* (12), 775-780.
(94) Shi, L.; Leng, C.; Zhou, Y.; Yuan, Y.; Liu, L.; Li, F.; Wang, H. A review of electrooxidation systems treatment of poly-fluoroalkyl substances (PFAS): electrooxidation degradation mechanisms and electrode materials. *Environmental Science and Pollution Research* **2024**, *31* (30), 42593-42613.
(95) Burkhardt, J. B.; Burns, N.; Mobley, D.; Pressman, J. G.; Magnuson, M. L.; Speth, T. F. Modeling PFAS Removal Using Granular Activated Carbon for Full-Scale System Design. *J Environ Eng (New York)* **2022**, *148* (3), 1-11. From NLM.
(96) Singh, M.; Hakimabadi, S. G.; Van Geel, P. J.; Carey, G. R.; Pham, A. L.-T. Modified competitive Langmuir model for prediction of multispecies PFAS competitive adsorption equilibria on colloidal activated carbon. *Separation and Purification Technology* **2024**, *345*, 127368.
(97) Reid, E.; Ma, Q.; Gan, L.; He, J.; Igou, T.; Huang, C.-H.; Chen, Y. Improving the Hydrophobicity of Powder Activated Carbon to Enhance the Adsorption Kinetics of Per- and Polyfluoroalkyl Substances. *ACS ES&T Water* **2025**, *5* (5), 2322-2332.
(98) Krause Max, J.; Thoma, E.; Sahle-Damesessie, E.; Crone, B.; Whitehill, A.; Shields, E.; Gullett, B. Supercritical Water Oxidation as an Innovative Technology for PFAS Destruction. *Journal of Environmental Engineering* **2022**, *148* (2), 05021006.
(99) Li, J.; Austin, C.; Moore, S.; Pinkard, B. R.; Novosselov, I. V. PFOS destruction in a continuous supercritical water oxidation reactor. *Chemical Engineering Journal* **2023**, *451*, 139063.
(100) Singh, R. K.; Fernando, S.; Baygi, S. F.; Multari, N.; Thagard, S. M.; Holsen, T. M. Breakdown Products from Perfluorinated Alkyl Substances (PFAS) Degradation in a Plasma-Based Water Treatment Process. *Environmental Science & Technology* **2019**, *53* (5), 2731-2738.
(101) Nau-Hix, C.; Multari, N.; Singh, R. K.; Richardson, S.; Kulkarni, P.; Anderson, R. H.; Holsen, T. M.; Mededovic Thagard, S. Field demonstration of a pilot-scale plasma reactor for the rapid removal of poly-and perfluoroalkyl substances in groundwater. *ACS ES&T Water* **2021**, *1* (3), 680-687.
(102) Chowdhury, P.; Viraraghavan, T. Sonochemical degradation of chlorinated organic compounds, phenolic compounds and organic dyes–a review. *Science of the total environment* **2009**, *407* (8), 2474-2492.
(103) Gole, V. L.; Sierra-Alvarez, R.; Peng, H.; Giesy, J. P.; Deymier, P.; Keswani, M. Sono-chemical treatment of per-and poly-fluoroalkyl compounds in aqueous film-forming foams by use of a large-scale multi-transducer dual-frequency based acoustic reactor. *Ultrasonics Sonochemistry* **2018**, *45*, 213-222.
(104) Fuller, M. E.; Zhao, Y.; Hedman, P. C.; Koster van Groos, P. G.; Soto, A.; Boodoo, F.; Yniguez, J.; McKenzie, E. R. Sonochemical degradation of PFAS in ion exchange regeneration wastes. *Journal of Hazardous Materials* **2024**, *471*, 134291.

(105) Jing, C.; Zhang, P.-Y.; Jian, L. Photodegradation of perfluorooctanoic acid by 185 nm vacuum ultraviolet light. *Journal of Environmental Sciences* **2007**, *19* (4), 387-390.
(106) Xin, X.; Kim, J.; Ashley, D. C.; Huang, C.-H. Degradation and Defluorination of Per- and Polyfluoroalkyl Substances by Direct Photolysis at 222 nm. *ACS ES&T Water* **2023**, *3* (8), 2776-2785.
(107) Hori, H.; Yamamoto, A.; Hayakawa, E.; Taniyasu, S.; Yamashita, N.; Kutsuna, S.; Kiatagawa, H.; Arakawa, R. Efficient Decomposition of Environmentally Persistent Perfluorocarboxylic Acids by Use of Persulfate as a Photochemical Oxidant. *Environmental Science & Technology* **2005**, *39* (7), 2383-2388.
(108) Chen, Y.-C.; Lo, S.-L.; Kuo, J. Effects of titanate nanotubes synthesized by a microwave hydrothermal method on photocatalytic decomposition of perfluorooctanoic acid. *Water Research* **2011**, *45* (14), 4131-4140.
(109) Wackett, L. P.; Robinson, S. L. The ever-expanding limits of enzyme catalysis and biodegradation: polyaromatic, polychlorinated, polyfluorinated, and polymeric compounds. *Biochemical Journal* **2020**, *477* (15), 2875-2891.
(110) Huang, S.; Jaffé, P. R. Defluorination of Perfluorooctanoic Acid (PFOA) and Perfluorooctane Sulfonate (PFOS) by Acidimicrobium sp. Strain A6. *Environmental Science & Technology* **2019**, *53* (19), 11410-11419.
(111) Ruiz-Urigüen, M.; Shuai, W.; Huang, S.; Jaffé, P. R. Biodegradation of PFOA in microbial electrolysis cells by Acidimicrobiaceae sp. strain A6. *Chemosphere* **2022**, *292*, 133506.
(112) Yu, Y.; Che, S.; Ren, C.; Jin, B.; Tian, Z.; Liu, J.; Men, Y. Microbial Defluorination of Unsaturated Per- and Polyfluorinated Carboxylic Acids under Anaerobic and Aerobic Conditions: A Structure Specificity Study. *Environmental Science & Technology* **2022**, *56* (8), 4894-4904.
(113) Rayne, S.; Forest, K. Perfluoroalkyl sulfonic and carboxylic acids: A critical review of physicochemical properties, levels and patterns in waters and wastewaters, and treatment methods. *Journal of Environmental Science and Health, Part A* **2009**, *44* (12), 1145-1199.
(114) Du, Z.; Deng, S.; Bei, Y.; Huang, Q.; Wang, B.; Huang, J.; Yu, G. Adsorption behavior and mechanism of perfluorinated compounds on various adsorbents—A review. *Journal of Hazardous Materials* **2014**, *274*, 443-454.
(115) Harif, T.; Khai, M.; Adin, A. Electrocoagulation versus chemical coagulation: Coagulation/flocculation mechanisms and resulting floc characteristics. *Water Research* **2012**, *46* (10), 3177-3188.
(116) Xiao, F.; Zhang, X.; Penn, L.; Gulliver, J. S.; Simcik, M. F. Effects of Monovalent Cations on the Competitive Adsorption of Perfluoroalkyl Acids by Kaolinite: Experimental Studies and Modeling. *Environmental Science & Technology* **2011**, *45* (23), 10028-10035.
(117) Cai, W.; Navarro, D. A.; Du, J.; Ying, G.; Yang, B.; McLaughlin, M. J.; Kookana, R. S. Increasing ionic strength and valency of cations enhance sorption through hydrophobic interactions of PFAS with soil surfaces. *Science of the Total Environment* **2022**, *817*, 152975.
(118) Li, H.; Junker, A. L.; Wen, J.; Ahrens, L.; Sillanpää, M.; Tian, J.; Cui, F.; Vergeynst, L.; Wei, Z. A recent overview of per- and polyfluoroalkyl substances (PFAS) removal by functional framework materials. *Chemical Engineering Journal* **2023**, *452*, 139202.
(119) Kabiri, S.; Monaghan, C. L.; Navarro, D.; McLaughlin, M. J. Hydrophobic interaction is the dominant mechanism of zwitterionic PFAS adsorption to carbon-based sorptive materials in water and soil. *Environmental Science: Water Research & Technology* **2024**.

(120) Park, M.; Wu, S.; Lopez, I. J.; Chang, J. Y.; Karanfil, T.; Snyder, S. A. Adsorption of perfluoroalkyl substances (PFAS) in groundwater by granular activated carbons: Roles of hydrophobicity of PFAS and carbon characteristics. *Water research* **2020**, *170*, 115364.
(121) Kancharla, S.; Alexandridis, P.; Tsianou, M. Sequestration of per- and polyfluoroalkyl substances (PFAS) by adsorption: Surfactant and surface aspects. *Current Opinion in Colloid & Interface Science* **2022**, *58*, 101571.
(122) Wang, F.; Lu, X.; Shih, K. M.; Wang, P.; Li, X. Removal of perfluoroalkyl sulfonates (PFAS) from aqueous solution using permanently confined micelle arrays (PCMAs). *Separation and Purification Technology* **2014**, *138*, 7-12.
(123) Lei, X.; Yao, L.; Lian, Q.; Zhang, X.; Wang, T.; Holmes, W.; Ding, G.; Gang, D. D.; Zappi, M. E. Enhanced adsorption of perfluorooctanoate (PFOA) onto low oxygen content ordered mesoporous carbon (OMC): Adsorption behaviors and mechanisms. *Journal of Hazardous Materials* **2022**, *421*, 126810.
(124) Zhang, Y.; Thomas, A.; Apul, O.; Venkatesan, A. K. Coexisting ions and long-chain per- and polyfluoroalkyl substances (PFAS) inhibit the adsorption of short-chain PFAS by granular activated carbon. *Journal of Hazardous Materials* **2023**, *460*, 132378.
(125) Missagia, B.; Guerrero, C.; Narra, S.; Sun, Y.; Ay, P.; Krautz, H. J. Physicomechanical properties of rice husk pellets for energy generation. *Energy & fuels* **2011**, *25* (12), 5786-5790.
(126) Iftikhar, M.; Asghar, A.; Ramzan, N.; Sajjadi, B.; Chen, W.-y. Biomass densification: Effect of cow dung on the physicochemical properties of wheat straw and rice husk based biomass pellets. *Biomass and Bioenergy* **2019**, *122*, 1-16.
(127) Jindo, K.; Mizumoto, H.; Sawada, Y.; Sanchez-Monedero, M. A.; Sonoki, T. Physical and chemical characterization of biochars derived from different agricultural residues. *Biogeosciences* **2014**, *11* (23), 6613-6621.
(128) Mukherjee, A.; Zimmerman, A.; Harris, W. Surface chemistry variations among a series of laboratory-produced biochars. *Geoderma* **2011**, *163* (3-4), 247-255.
(129) Weber, K.; Quicker, P. Properties of biochar. *Fuel* **2018**, *217*, 240-261.
(130) Jain, A.; Balasubramanian, R.; Srinivasan, M. P. Hydrothermal conversion of biomass waste to activated carbon with high porosity: A review. *Chemical Engineering Journal* **2016**, *283*, 789-805.
(131) Molina-Sabio, M.; Gonzalez, M. T.; Rodriguez-Reinoso, F.; Sepúlveda-Escribano, A. Effect of steam and carbon dioxide activation in the micropore size distribution of activated carbon. *Carbon* **1996**, *34* (4), 505-509.
(132) Hayashi, J. i.; Kazehaya, A.; Muroyama, K.; Watkinson, A. P. Preparation of activated carbon from lignin by chemical activation. *Carbon* **2000**, *38* (13), 1873-1878.
(133) Min, H. S.; Abbas, M.; Kanthasamy, R.; Aziz, H. A.; Chay, T. C. Activated carbon: prepared from various precursors. *Ideal international E-publication Pvt. Ltd* **2017**, 1-20.
(134) Kong, K. K.; Yek, P. N. Y.; Sii, H. S.; Lee, M. D.; Liew, R. K.; Lam, S. S. Microwave physicochemical activation: an advanced approach to produce activated biochar for palm oil mill effluent treatment. *Waste Disposal & Sustainable Energy* **2022**, *4* (4), 323-333.
(135) Pallarés, J.; González-Cencerrado, A.; Arauzo, I. Production and characterization of activated carbon from barley straw by physical activation with carbon dioxide and steam. *Biomass and Bioenergy* **2018**, *115*, 64-73.
(136) Bouchelta, C.; Medjram, M. S.; Bertrand, O.; Bellat, J.-P. Preparation and characterization of activated carbon from date stones by physical activation with steam. *Journal of Analytical and Applied Pyrolysis* **2008**, *82* (1), 70-77.

(137) Aworn, A.; Thiravetyan, P.; Nakbanpote, W. Preparation and characteristics of agricultural waste activated carbon by physical activation having micro- and mesopores. *Journal of Analytical and Applied Pyrolysis* **2008**, *82* (2), 279-285.
(138) Maciá-Agulló, J. A.; Moore, B. C.; Cazorla-Amorós, D.; Linares-Solano, A. Activation of coal tar pitch carbon fibres: Physical activation vs. chemical activation. *Carbon* **2004**, *42* (7), 1367-1370.
(139) Juan, Y.; Ke-Qiang, Q. Preparation of activated carbon by chemical activation under vacuum. *Environmental science & technology* **2009**, *43* (9), 3385-3390.
(140) Ahmadpour, A.; Do, D. D. The preparation of activated carbon from macadamia nutshell by chemical activation. *Carbon* **1997**, *35* (12), 1723-1732.
(141) Garba, Z. N.; Abdul Rahim, A.; Hamza, S. A. Potential of Borassus aethiopum shells as precursor for activated carbon preparation by physico-chemical activation; optimization, equilibrium and kinetic studies. *Journal of Environmental Chemical Engineering* **2014**, *2* (3), 1423-1433.
(142) Tongpoothorn, W.; Sriuttha, M.; Homchan, P.; Chanthai, S.; Ruangviriyachai, C. Preparation of activated carbon derived from Jatropha curcas fruit shell by simple thermo-chemical activation and characterization of their physico-chemical properties. *Chemical Engineering Research and Design* **2011**, *89* (3), 335-340.
(143) Patel, H.; Weldekidan, H.; Mohanty, A.; Misra, M. Effect of physicochemical activation on CO2 adsorption of activated porous carbon derived from pine sawdust. *Carbon Capture Science & Technology* **2023**, *8*, 100128.
(144) Georgin, J.; Dotto, G. L.; Mazutti, M. A.; Foletto, E. L. Preparation of activated carbon from peanut shell by conventional pyrolysis and microwave irradiation-pyrolysis to remove organic dyes from aqueous solutions. *Journal of Environmental Chemical Engineering* **2016**, *4* (1), 266-275.
(145) Liu, Q.-S.; Zheng, T.; Wang, P.; Guo, L. Preparation and characterization of activated carbon from bamboo by microwave-induced phosphoric acid activation. *Industrial Crops and Products* **2010**, *31* (2), 233-238.
(146) Yang, K.; Peng, J.; Srinivasakannan, C.; Zhang, L.; Xia, H.; Duan, X. Preparation of high surface area activated carbon from coconut shells using microwave heating. *Bioresource Technology* **2010**, *101* (15), 6163-6169.
(147) Guo, J.; Lua, A. C. Preparation of activated carbons from oil-palm-stone chars by microwave-induced carbon dioxide activation. *Carbon* **2000**, *38* (14), 1985-1993.
(148) Ao, W.; Fu, J.; Mao, X.; Kang, Q.; Ran, C.; Liu, Y.; Zhang, H.; Gao, Z.; Li, J.; Liu, G.; et al. Microwave assisted preparation of activated carbon from biomass: A review. *Renewable and Sustainable Energy Reviews* **2018**, *92*, 958-979.
(149) Liu, C. J.; Werner, D.; Bellona, C. Removal of per- and polyfluoroalkyl substances (PFASs) from contaminated groundwater using granular activated carbon: a pilot-scale study with breakthrough modeling. *Environmental Science: Water Research & Technology* **2019**, *5* (11), 1844-1853, 10.1039/C9EW00349E.
(150) Herkert, N. J.; Merrill, J.; Peters, C.; Bollinger, D.; Zhang, S.; Hoffman, K.; Ferguson, P. L.; Knappe, D. R. U.; Stapleton, H. M. Assessing the Effectiveness of Point-of-Use Residential Drinking Water Filters for Perfluoroalkyl Substances (PFASs). *Environmental Science & Technology Letters* **2020**, *7* (3), 178-184.
(151) Xiao, F.; Sasi, P. C.; Yao, B.; Kubátová, A.; Golovko, S. A.; Golovko, M. Y.; Soli, D. Thermal Stability and Decomposition of Perfluoroalkyl Substances on Spent Granular Activated Carbon. *Environmental Science & Technology Letters* **2020**, *7* (5), 343-350.

(152) Wibowo, N.; Setyadhi, L.; Wibowo, D.; Setiawan, J.; Ismadji, S. Adsorption of benzene and toluene from aqueous solutions onto activated carbon and its acid and heat treated forms: Influence of surface chemistry on adsorption. *Journal of Hazardous Materials* **2007**, *146* (1), 237-242.
(153) Li, Q.; Qi, Y.; Gao, C. Chemical regeneration of spent powdered activated carbon used in decolorization of sodium salicylate for the pharmaceutical industry. *Journal of cleaner production* **2015**, *86*, 424-431.
(154) Cazetta, A. L.; Vargas, A. M.; Nogami, E. M.; Kunita, M. H.; Guilherme, M. R.; Martins, A. C.; Silva, T. L.; Moraes, J. C.; Almeida, V. C. NaOH-activated carbon of high surface area produced from coconut shell: Kinetics and equilibrium studies from the methylene blue adsorption. *Chemical Engineering Journal* **2011**, *174* (1), 117-125.
(155) Lu, P.-J.; Lin, H.-C.; Yu, W.-T.; Chern, J.-M. Chemical regeneration of activated carbon used for dye adsorption. *Journal of the Taiwan institute of chemical engineers* **2011**, *42* (2), 305-311.
(156) Larasati, A.; Fowler, G. D.; Graham, N. J. D. Insights into chemical regeneration of activated carbon for water treatment. *Journal of Environmental Chemical Engineering* **2021**, *9* (4), 105555.
(157) Argaman, Y.; Sassu, G. M. Treatment of chlorinated hydrocarbons waste water by activated carbon adsorption with steam regeneration. *Progress in water technology* **1977**, *9* (1), 65-73.
(158) Shah, I. K.; Pre, P.; Alappat, B. J. Steam regeneration of adsorbents: an experimental and technical review. *Chemical Science Transactions* **2013**, *2* (4).
(159) Ying, X.; Kim, G.; Han, I.; Sheng, J.; Mei, Q.; Kim, Y. High Efficiency Regeneration Performance of Exhausted Activated Carbon by Superheated Steam and Comparison with Conventional Chemical Regeneration Method. *KSCE Journal of Civil Engineering* **2022**, *26* (5), 2058-2067.
(160) Ledesma, B.; Román, S.; Sabio, E.; Álvarez-Murillo, A. Improvement of spent activated carbon regeneration by wet oxidation processes. *The Journal of Supercritical Fluids* **2015**, *104*, 94-103.
(161) Ania, C.; Menéndez, J.; Parra, J.; Pis, J. Microwave-induced regeneration of activated carbons polluted with phenol. A comparison with conventional thermal regeneration. *Carbon* **2004**, *42* (7), 1383-1387.
(162) Ania, C.; Parra, J.; Menéndez, J.; Pis, J. Microwave-assisted regeneration of activated carbons loaded with pharmaceuticals. *Water research* **2007**, *41* (15), 3299-3306.
(163) Ania, C.; Parra, J.; Menéndez, J.; Pis, J. Effect of microwave and conventional regeneration on the microporous and mesoporous network and on the adsorptive capacity of activated carbons. *Microporous and Mesoporous Materials* **2005**, *85* (1-2), 7-15.
(164) Gagliano, E.; Falciglia, P. P.; Zaker, Y.; Karanfil, T.; Roccaro, P. Microwave regeneration of granular activated carbon saturated with PFAS. *Water Research* **2021**, *198*, 117121.
(165) Ban, A.; Schafer, A.; Wendt, H. Fundamentals of electrosorption on activated carbon for wastewater treatment of industrial effluents. *Journal of Applied Electrochemistry* **1998**, *28*, 227-236.
(166) Kim, J.-S.; Jung, C.-H.; Oh, W.-Z.; Ryu, S.-K. Electrosorption and separation of $ Co^{2+} $ and $ Sr^{2+} $ ions from decontaminated liquid wastes. *Carbon letters* **2002**, *3* (1), 6-12.
(167) Cheng, H.; Scott, K.; Christensen, P. Electrochemical Hydrodehalogenation of Chlorinated Phenols in Aqueous Solutions: I. Material Aspects. *Journal of the Electrochemical Society* **2002**, *150* (2), D17.

(168) Chiang, L.-C.; Chang, J.-E.; Wen, T.-C. Indirect oxidation effect in electrochemical oxidation treatment of landfill leachate. *Water research* **1995**, *29* (2), 671-678.
(169) Ersan, G.; Ersan, M. S.; Perreault, F.; Garcia-Segura, S. Enabling in situ electro-regeneration systems for PFOA-laden spent activated carbon adsorbents reuse. *Journal of Environmental Chemical Engineering* **2023**, *11* (6), 111369.
(170) Shende, R.; Mahajani, V. Wet oxidative regeneration of activated carbon loaded with reactive dye. *Waste Management* **2002**, *22* (1), 73-83.
(171) Okawa, K.; Suzuki, K.; Takeshita, T.; Nakano, K. Regeneration of granular activated carbon with adsorbed trichloroethylene using wet peroxide oxidation. *Water Research* **2007**, *41* (5), 1045-1051.
(172) El Gamal, M.; Mousa, H. A.; El-Naas, M. H.; Zacharia, R.; Judd, S. Bio-regeneration of activated carbon: A comprehensive review. *Separation and Purification Technology* **2018**, *197*, 345-359.
(173) Ameh, C.; Jimoh, A.; Abdulkareem, A.; Otaru, A. Experimental studies on bioregeneration of activated carbon contaminated with hydrocarbon. *IOSR J. Appl. Chem* **2013**, *4*, 50-66.
(174) Harris, P. J.; Liu, Z.; Suenaga, K. Imaging the structure of activated carbon using aberration corrected TEM. In *Journal of Physics: Conference Series*, 2010; IOP Publishing: Vol. 241, p 012050.
(175) Scimeca, M.; Bischetti, S.; Lamsira, H. K.; Bonfiglio, R.; Bonanno, E. Energy Dispersive X-ray (EDX) microanalysis: A powerful tool in biomedical research and diagnosis. *European journal of histochemistry: EJH* **2018**, *62* (1).
(176) Ozdemir, I.; Şahin, M.; Orhan, R.; Erdem, M. Preparation and characterization of activated carbon from grape stalk by zinc chloride activation. *Fuel Processing Technology* **2014**, *125*, 200-206.
(177) Sricharoenchaikul, V.; Pechyen, C.; Aht-ong, D.; Atong, D. Preparation and characterization of activated carbon from the pyrolysis of physic nut (Jatropha curcas L.) waste. *Energy & Fuels* **2008**, *22* (1), 31-37.
(178) Chen, X.; Wang, X.; Fang, D. A review on C1s XPS-spectra for some kinds of carbon materials. *Fullerenes, Nanotubes and Carbon Nanostructures* **2020**, *28* (12), 1048-1058.
(179) Seah, M. The quantitative analysis of surfaces by XPS: A review. *Surface and Interface Analysis* **1980**, *2* (6), 222-239.
(180) Boehm, H. P.; Diehl, E.; Heck, W.; Sappok, R. Surface oxides of carbon. *Angewandte Chemie International Edition in English* **1964**, *3* (10), 669-677.
(181) Goertzen, S. L.; Thériault, K. D.; Oickle, A. M.; Tarasuk, A. C.; Andreas, H. A. Standardization of the Boehm titration. Part I. CO2 expulsion and endpoint determination. *Carbon* **2010**, *48* (4), 1252-1261.
(182) Armaroli, T.; Bécue, T.; Gautier, S. Diffuse Reflection Infrared Spectroscopy (Drifts): Application to the in Situ Analysis of Catalysts. *Oil & Gas Science and Technology-revue De L Institut Francais Du Petrole* **2004**, *59*, 215-237.
(183) Dittmann, D.; Saal, L.; Zietzschmann, F.; Mai, M.; Altmann, K.; Al-Sabbagh, D.; Schumann, P.; Ruhl, A. S.; Jekel, M.; Braun, U. Characterization of activated carbons for water treatment using TGA-FTIR for analysis of oxygen-containing functional groups. *Applied Water Science* **2022**, *12* (8), 203.
(184) Ali, R.; Aslam, Z.; Shawabkeh, R. A.; Asghar, A.; Hussein, I. A. BET, FTIR, and RAMAN characterizations of activated carbon from waste oil fly ash. *Turk J Chem* **2020**, *44* (2), 279-295. From NLM.

(185) Brunauer, S.; Emmett, P. H.; Teller, E. Adsorption of gases in multimolecular layers. *Journal of the American chemical society* **1938**, *60* (2), 309-319.
(186) Nimmo, J. R. Porosity and pore size distribution. *Encyclopedia of Soils in the Environment* **2004**, *3* (1), 295-303.
(187) Beda, A.; Vaulot, C.; Matei Ghimbeu, C. Hard carbon porosity revealed by the adsorption of multiple gas probe molecules (N2, Ar, CO2, O2 and H2). *Journal of Materials Chemistry A* **2021**, *9* (2), 937-943, 10.1039/D0TA10088A.
(188) Freundlich, H. Über die adsorption in lösungen. *Zeitschrift für physikalische Chemie* **1907**, *57* (1), 385-470.
(189) Azizian, S.; Eris, S.; Wilson, L. D. Re-evaluation of the century-old Langmuir isotherm for modeling adsorption phenomena in solution. *Chemical physics* **2018**, *513*, 99-104.
(190) de Vargas Brião, G.; Hashim, M. A.; Chu, K. H. The Sips isotherm equation: Often used and sometimes misused. *Separation Science and Technology* **2023**, *58* (5), 884-892.
(191) Chu, K. H. Revisiting the Temkin isotherm: dimensional inconsistency and approximate forms. *Industrial & Engineering Chemistry Research* **2021**, *60* (35), 13140-13147.
(192) Hu, Q.; Zhang, Z. Application of Dubinin–Radushkevich isotherm model at the solid/solution interface: A theoretical analysis. *Journal of Molecular Liquids* **2019**, *277*, 646-648.
(193) Wu, F.-C.; Liu, B.-L.; Wu, K.-T.; Tseng, R.-L. A new linear form analysis of Redlich–Peterson isotherm equation for the adsorptions of dyes. *Chemical Engineering Journal* **2010**, *162* (1), 21-27.
(194) Foo, K. Y.; Hameed, B. H. Insights into the modeling of adsorption isotherm systems. *Chemical engineering journal* **2010**, *156* (1), 2-10.
(195) Dodds, J. N.; Hopkins, Z. R.; Knappe, D. R.; Baker, E. S. Rapid characterization of per-and polyfluoroalkyl substances (PFAS) by ion mobility spectrometry–mass spectrometry (IMS-MS). *Analytical chemistry* **2020**, *92* (6), 4427-4435.
(196) Strynar, M.; McCord, J.; Newton, S.; Washington, J.; Barzen-Hanson, K.; Trier, X.; Liu, Y.; Dimzon, I. K.; Bugsel, B.; Zwiener, C. Practical application guide for the discovery of novel PFAS in environmental samples using high resolution mass spectrometry. *Journal of Exposure Science & Environmental Epidemiology* **2023**, *33* (4), 575-588.
(197) Tanim-Al Hassan, M.; Chen, X.; Fnu, P. I. J.; Osonga, F. J.; Sadik, O. A.; Li, M.; Chen, H. Rapid detection of per-and polyfluoroalkyl substances (PFAS) using paper spray-based mass spectrometry. *Journal of Hazardous Materials* **2024**, *465*, 133366.
(198) Vera, P.; Canellas, E.; Dreolin, N.; Goshawk, J.; Nerín, C. The analysis of the migration of per and poly fluoroalkyl substances (PFAS) from food contact materials using ultrahigh performance liquid chromatography coupled to ion-mobility quadrupole time-of-flight mass spectrometry (UPLC-IMS-QTOF). *Talanta* **2024**, *266*, 124999.
(199) Whitaker, J. S.; Hrabak, R. B.; Ramos, M.; Neslund, C.; Li, Y. An interlaboratory study on EPA methods 537.1 and 533 for per-and polyfluoroalkyl substance analyses. *AWWA Water Science* **2021**, *3* (4), e1234.
(200) Enders, J. R.; O'Neill, G. M.; Whitten, J. L.; Muddiman, D. C. Understanding the electrospray ionization response factors of per-and poly-fluoroalkyl substances (PFAS). *Analytical and bioanalytical chemistry* **2022**, *414*, 1227-1234.
(201) Jia, S.; Marques Dos Santos, M.; Li, C.; Snyder, S. A. Recent advances in mass spectrometry analytical techniques for per- and polyfluoroalkyl substances (PFAS). *Analytical and Bioanalytical Chemistry* **2022**, *414* (9), 2795-2807.

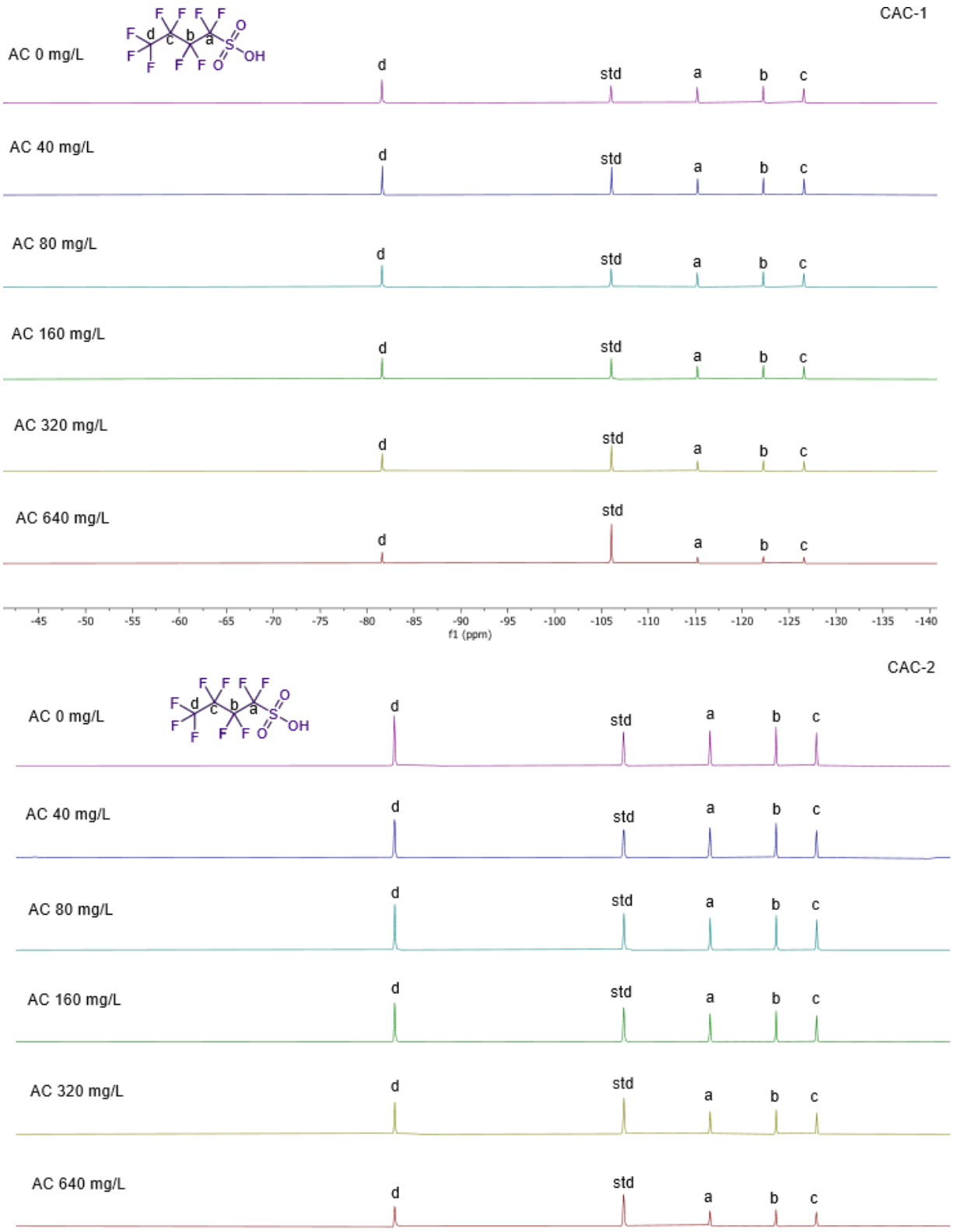
(202) Brase, R. A.; Spink, D. C. Enhanced Sensitivity for the Analysis of Perfluoroethercarboxylic Acids Using LC–ESI–MS/MS: Effects of Probe Position, Mobile Phase Additive, and Capillary Voltage. *Journal of the American Society for Mass Spectrometry* **2020**, *31* (10), 2124-2132.
(203) Borrull, J.; Colom, A.; Fabregas, J.; Pocurull, E.; Borrull, F. A liquid chromatography tandem mass spectrometry method for determining 18 per- and polyfluoroalkyl substances in source and treated drinking water. *Journal of Chromatography A* **2020**, *1629*, 461485.
(204) Phomsopha, T., Roberts, S.; Butt, C. M.; Oetjen, K.; Noestheden, M.; Lodge, S. Achieving Low Parts-per-Quadrillion Detection Limits for PFAS Analysis in Drinking Water. *Sciex Application Note* **2022**.
(205) Point, A. D.; Holsen, T. M.; Fernando, S.; Hopke, P. K.; Crimmins, B. S. Towards the development of a standardized method for extraction and analysis of PFAS in biological tissues. *Environmental Science: Water Research & Technology* **2019**, *5* (11), 1876-1886, 10.1039/C9EW00765B.
(206) Huang, P.-J.; Hwangbo, M.; Chen, Z.; Liu, Y.; Kameoka, J.; Chu, K.-H. Reusable Functionalized Hydrogel Sorbents for Removing Long- and Short-Chain Perfluoroalkyl Acids (PFAAs) and GenX from Aqueous Solution. *ACS Omega* **2018**, *3* (12), 17447-17455.
(207) Peng, H.; Hu, K.; Zhao, F.; Hu, J. Derivatization method for sensitive determination of fluorotelomer alcohols in sediment by liquid chromatography–electrospray tandem mass spectrometry. *Journal of Chromatography A* **2013**, *1288*, 48-53.
(208) Xian, F.; Hendrickson, C. L.; Marshall, A. G. High Resolution Mass Spectrometry. *Analytical Chemistry* **2012**, *84* (2), 708-719.
(209) Nikolaev, E.; Lioznov, A. How to Increase Further the Resolving Power of the Ultrahigh Magnetic Field FT ICR Instruments? The New Concept of the FT ICR Cell–the Open Dynamically Harmonized Cell as a Part of the Vacuum System Wall. *Analytical Chemistry* **2021**, *93* (3), 1249-1253.
(210) Liu, Y.; Pereira Ados, S.; Martin, J. W. Discovery of C5-C17 poly- and perfluoroalkyl substances in water by in-line SPE-HPLC-Orbitrap with in-source fragmentation flagging. *Anal Chem* **2015**, *87* (8), 4260-4268. From NLM.
(211) Idjaton, B. I. T.; Togola, A.; Ghestem, J. P.; Kastler, L.; Bristeau, S.; Ronteltap, M.; Colombano, S.; Devau, N.; Lions, J.; van Hullebusch, E. D. Determination of organic fluorinated compounds content in complex samples through combustion ion chromatography methods: a way to define a "Total Per- and Polyfluoroalkyl Substances (PFAS)" parameter? *Science of The Total Environment* **2024**, *932*, 172589.
(212) Forster, A. L.; Zhang, Y.; Westerman, D. C.; Richardson, S. D. Improved total organic fluorine methods for more comprehensive measurement of PFAS in industrial wastewater, river water, and air. *Water research* **2023**, *235*, 119859.
(213) Aro, R.; Eriksson, U.; Kärrman, A.; Reber, I.; Yeung, L. W. Combustion ion chromatography for extractable organofluorine analysis. *Iscience* **2021**, *24* (9).
(214) Simpson, A. J.; McNally, D. J.; Simpson, M. J. NMR spectroscopy in environmental research: From molecular interactions to global processes. *Progress in Nuclear Magnetic Resonance Spectroscopy* **2011**, *58* (3-4), 97-175.
(215) Bastawrous, M.; Jenne, A.; Tabatabaei Anaraki, M.; Simpson, A. J. In-vivo NMR spectroscopy: A powerful and complimentary tool for understanding environmental toxicity. *Metabolites* **2018**, *8* (2), 35.
(216) Alves Filho, E. G.; Alexandre e Silva, L. M.; Ferreira, A. G. Advancements in waste water characterization through NMR spectroscopy. *Magnetic Resonance in Chemistry* **2015**, *53* (9), 648-657.

(217) Freedberg, D. I.; Selenko, P. Live cell NMR. *Annual Review of Biophysics* **2014**, *43* (1), 171-192.
(218) Soong, R.; Liaghati Mobarhan, Y.; Tabatabaei, M.; Bastawrous, M.; Biswas, R. G.; Simpson, M.; Simpson, A. Flow-based in vivo NMR spectroscopy of small aquatic organisms. *Magnetic Resonance in Chemistry* **2020**, *58* (5), 411-426.
(219) Gauthier, J. R.; Mabury, S. A. Noise-reduced quantitative fluorine NMR spectroscopy reveals the presence of additional per-and polyfluorinated alkyl substances in environmental and biological samples when compared with routine mass spectrometry methods. *Analytical Chemistry* **2022**, *94* (7), 3278-3286.
(220) Heerah, K.; Waclawek, S.; Konzuk, J.; Longstaffe, J. G. Benchtop 19F NMR spectroscopy as a practical tool for testing of remedial technologies for the degradation of perfluorooctanoic acid, a persistent organic pollutant. *Magnetic Resonance in Chemistry* **2020**, *58* (12), 1160-1167.
(221) Chen, P.; Zhuang, S.; Chen, W.; Chen, Z.; Li, R.; Chen, F.; Jiang, T.; Fu, X. Facile identification of fluorosurfactant category in aqueous film-forming foam concentrates via optimized 19F NMR. *Magnetic Resonance Letters* **2024**, 100097.
(222) Gerig, J. Fluorine NMR. **2001**.
(223) Petkowski, J. J.; Seager, S.; Bains, W. Reasons why life on Earth rarely makes fluorine-containing compounds and their implications for the search for life beyond Earth. *Scientific Reports* **2024**, *14* (1), 15575.
(224) Kovacs, H.; Moskau, D.; Spraul, M. Cryogenically Cooled Probes — A Leap in NMR Technology. *Progress in Nuclear Magnetic Resonance Spectroscopy - PROG NUCL MAGN RESON SPECTROS* **2005**, *46*, 131-155.
(225) Rosenau, C. P.; Jelier, B. J.; Gossert, A. D.; Togni, A. Exposing the Origins of Irreproducibility in Fluorine NMR Spectroscopy. *Angewandte Chemie International Edition* **2018**, *57* (30), 9528-9533.
(226) Lewis, R. E.; Huang, C.-H.; White, J. C.; Haynes, C. L. Using 19F NMR to Investigate Cationic Carbon Dot Association with Per- and Polyfluoroalkyl Substances (PFAS). *ACS Nanoscience Au* **2023**, *3* (5), 408-417.
(227) Miglio, V.; Begni, F.; Cassino, C.; Paul, G.; Bortoli, A.; Marchese, L.; Bisio, C. Removal of Forever Chemicals from Aqueous Solutions through Adsorption on Swellable Organically Modified Silicas. *The Journal of Physical Chemistry C* **2024**, *128* (5), 2179-2189.
(228) Tan, X.; Sawczyk, M.; Chang, Y.; Wang, Y.; Usman, A.; Fu, C.; Král, P.; Peng, H.; Zhang, C.; Whittaker, A. K. Revealing the Molecular-Level Interactions between Cationic Fluorinated Polymer Sorbents and the Major PFAS Pollutant PFOA. *Macromolecules* **2022**, *55* (3), 1077-1087.
(229) Jagiello, J.; Olivier, J. P. 2D-NLDFT adsorption models for carbon slit-shaped pores with surface energetical heterogeneity and geometrical corrugation. *Carbon* **2013**, *55*, 70-80.
(230) Thommes, M.; Kaneko, K.; Neimark, A. V.; Olivier, J. P.; Rodriguez-Reinoso, F.; Rouquerol, J.; Sing, K. S. W. Physisorption of gases, with special reference to the evaluation of surface area and pore size distribution (IUPAC Technical Report). *Pure and Applied Chemistry* **2015**, *87* (9-10), 1051-1069.
(231) Donohue, M. D.; Aranovich, G. L. Classification of Gibbs adsorption isotherms. *Advances in Colloid and Interface Science* **1998**, *76-77*, 137-152.
(232) Siriwardena, D. P.; Crimi, M.; Holsen, T. M.; Bellona, C.; Divine, C.; Dickenson, E. Influence of groundwater conditions and co-contaminants on sorption of perfluoroalkyl compounds on granular activated carbon. *Remediation Journal* **2019**, *29* (3), 5-15.

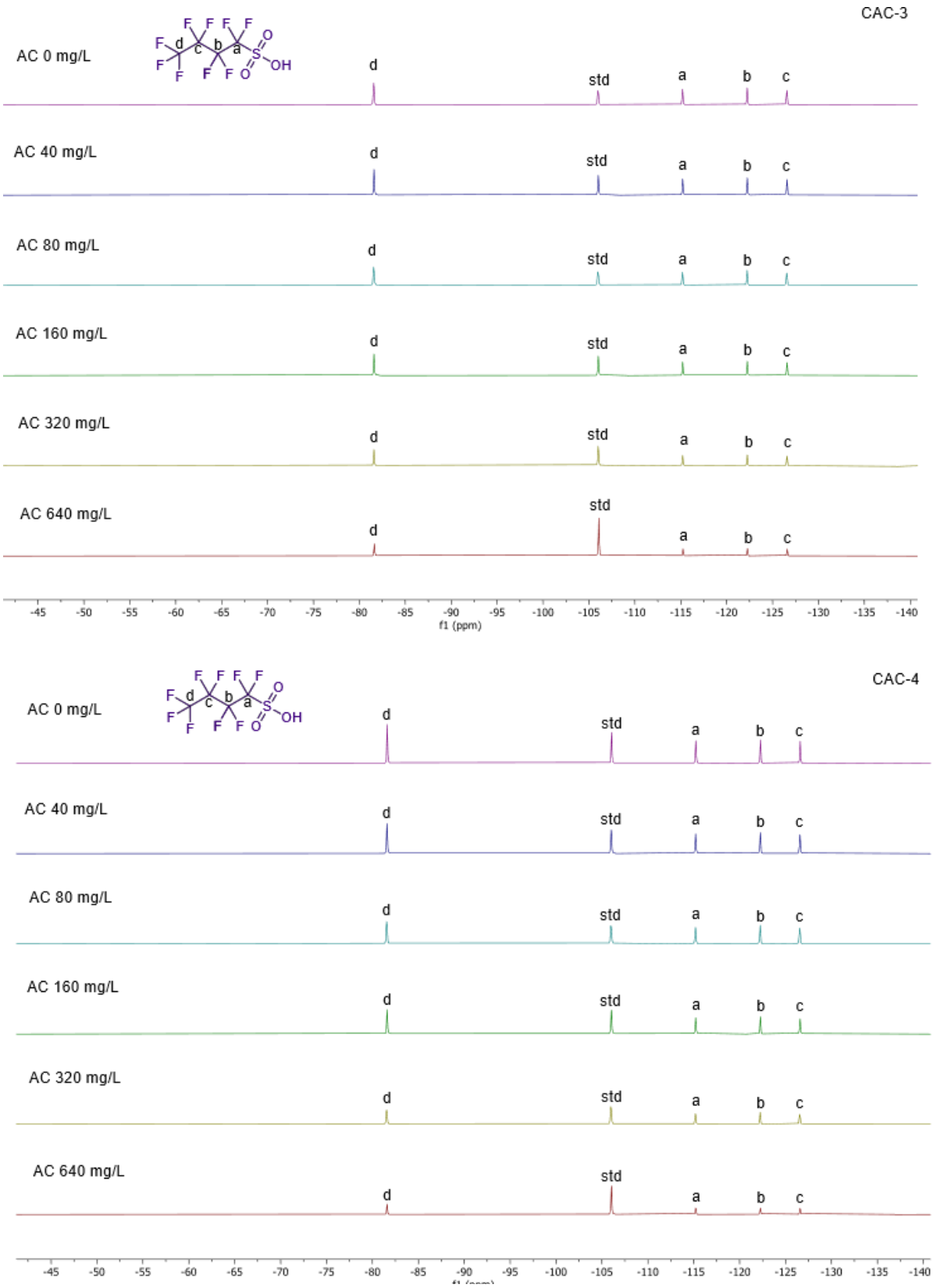
(233) Hai, A.; Daud, W. M. A. W.; Patah, M. F. A.; Bharath, G.; AlMohamadi, H.; Tang, D. Y. Y.; Show, P. L.; Banat, F. A comprehensive insight on activated carbon production from agricultural biomass: Parametric analysis, challenges, future recommendations & machine learning modelling. *Resources, Conservation & Recycling Advances* **2025**, *27*, 200284.
(234) de Lima, T. A. d. M.; Arantes, M. S. T.; Araújo, J. A.; de Lima, G. G.; Andrade, D. R. M.; Murphy, E. J.; Magalhães, W. L. E.; Nugent, M. J. D. Valorisation of invasive plant (Rhododendron ponticum) biomass into activated biochar as a sustainable adsorbent for emerging pharmaceutical contaminant removal from water. *RSC Sustainability* **2025**, *3* (12), 5507-5517, 10.1039/D5SU00589B.
(235) Chin, K. L.; Lee, C. L.; H'ng, P. S.; Rashid, U.; Paridah, T.; Khoo, P. S.; Mamiński, M. Ł. Refining micropore capacity of activated carbon derived from coconut shell via deashing post-treatment. *Bioresources* **2020**, *15*, 7749-7769.
(236) Wiśniewska, M.; Sadłowska, A.; Herda, K.; Urban, T.; Nowicki, P. Production of Mineral-Carbon Composites and Activated Carbons as a Method of Used Gear Oil, Ashes, and Low-Quality Brown Coals Management. *Molecules* **2023**, *28* (19). From NLM.
(237) Saeidi, N.; Kopinke, F.-D.; Georgi, A. Understanding the effect of carbon surface chemistry on adsorption of perfluorinated alkyl substances. *Chemical Engineering Journal* **2020**, *381*, 122689.
(238) Yang, X.; Wan, Y.; Zheng, Y.; He, F.; Yu, Z.; Huang, J.; Wang, H.; Ok, Y. S.; Jiang, Y.; Gao, B. Surface functional groups of carbon-based adsorbents and their roles in the removal of heavy metals from aqueous solutions: A critical review. *Chem Eng J* **2019**, *366*, 608-621. From NLM.
(239) Jain, V.; Biesinger, M. C.; Linford, M. R. The Gaussian-Lorentzian Sum, Product, and Convolution (Voigt) functions in the context of peak fitting X-ray photoelectron spectroscopy (XPS) narrow scans. *Applied Surface Science* **2018**, *447*, 548-553.
(240) Sherwood, P. M. A. Rapid evaluation of the Voigt function and its use for interpreting X-ray photoelectron spectroscopic data. *Surface and Interface Analysis* **2019**, *51* (2), 254-274.
(241) Doniach, S.; Sunjic, M. Many-electron singularity in X-ray photoemission and X-ray line spectra from metals. *Journal of Physics C: Solid State Physics* **1970**, *3* (2), 285.
(242) Végh, J. The Shirley background revised. *Journal of Electron Spectroscopy and Related Phenomena* **2006**, *151* (3), 159-164.
(243) Moeini, B.; Linford, M. R.; Fairley, N.; Barlow, A.; Cumpson, P.; Morgan, D.; Fernandez, V.; Baltrusaitis, J. Definition of a new (Doniach-Sunjic-Shirley) peak shape for fitting asymmetric signals applied to reduced graphene oxide/graphene oxide XPS spectra. *Surface and Interface Analysis* **2022**, *54* (1), 67-77.
(244) Kim, G.; Mengesha, D. N.; Choi, Y. Adsorption dynamics of per- and polyfluoroalkyl substances (PFAS) on activated carbon: Interplay of surface chemistry and PFAS structural properties. *Separation and Purification Technology* **2024**, *349*, 127851.
(245) Zhang, B.; Moriyama, D.; Herath, T. M.; Zhao, H.; Bai, Y.; Dang, Y.; Liu, W.; Kato, H.; Yamamoto, K.; Mochizuki, Y.; et al. Pore structure modulation and surface functionalization boosted adsorption of PFAS on porous carbon: Experimental and theoretical investigations. *Journal of Hazardous Materials* **2025**, *499*, 140063.
(246) Oickle, A. M.; Goertzen, S. L.; Hopper, K. R.; Abdalla, Y. O.; Andreas, H. A. Standardization of the Boehm titration: Part II. Method of agitation, effect of filtering and dilute titrant. *Carbon* **2010**, *48* (12), 3313-3322.
(247) Schönherr, J.; Buchheim, J. R.; Scholz, P.; Adelhelm, P. Boehm Titration Revisited (Part I): Practical Aspects for Achieving a High Precision in Quantifying Oxygen-Containing Surface Groups on Carbon Materials. *C* **2018**, *4* (2), 21.

(248) Wang, X.; Yu, N.; Qian, Y.; Shi, W.; Zhang, X.; Geng, J.; Yu, H.; Wei, S. Non-target and suspect screening of per-and polyfluoroalkyl substances in Chinese municipal wastewater treatment plants. *Water research* **2020**, *183*, 115989.
(249) Fundamentals of NMR Spectroscopy in Liquids. In *NMR Spectroscopy Explained*, 2007; pp 1-38.
(250) Ellis, D. A.; Martin, J. W.; Muir, D. C.; Mabury, S. A. Development of an 19F NMR method for the analysis of fluorinated acids in environmental water samples. *Anal Chem* **2000**, *72* (4), 726-731. From NLM.
(251) Carlos Cobas, J.; Bernstein, M. A.; Martín-Pastor, M.; Tahoces, P. G. A new general-purpose fully automatic baseline-correction procedure for 1D and 2D NMR data. *Journal of Magnetic Resonance* **2006**, *183* (1), 145-151.
(252) Liu, C.-m.; Song, C.-h.; Jia, W.; Hua, Z.-d.; Liao, Q. The application of 19F NMR spectroscopy for the analysis of fluorinated new psychoactive substances (NPS). *Forensic Science International* **2022**, *340*, 111450.
(253) Balasuryia, D.; Queral-Beltran, A.; Vick, T.; Simpson, S.; Lacorte, S.; Aga, D. S.; Hoepker, A. C. Experimental Determination of pK (a) for 10 PFAS, Mono-, Di-, and Trifluoroacetic Acid by (19)F-NMR. *Environ Sci Technol Lett* **2025**, *12* (9), 1238-1246. From NLM.
(254) Kebede, M. M.; Masud, M. A. A.; Ortbal, S.; Shin, W. S.; Mekonnen, M. M.; Clement, T. P.; Terry, L. G. Adsorptive Removal of PFAS from Aqueous Solutions Using GAC, PAC and Ball-Milled Colloidal Activated Carbon: Characterizing Efficiency, Kinetics, and Mechanisms. *ACS ES T Water* **2025**, *5* (11), 6554-6566. From NLM.
(255) Swenson, H.; Stadie, N. P. Langmuir's Theory of Adsorption: A Centennial Review. *Langmuir* **2019**, *35* (16), 5409-5426.
(256) Abulikemu, G.; Pressman, J. G.; Sorial, G. A.; Sanan, T. T.; Haupert, L. M.; Burkhardt, J. B.; Smith, S. J.; Kleiner, E. J.; Stebel, E. K.; Gray, B. N.; et al. Perfluoroalkyl chemical adsorption by granular activated carbon: Assessment of particle size impact on equilibrium parameters and associated rapid small-scale column test scaling assumptions. *Water Research* **2025**, *271*, 122977.
(257) Pranić, M.; Zhou, K.; Biesheuvel, P. M.; van der Wal, A.; Dykstra, J. E. Temperature impacts PFAS Adsorption on Activated Carbon. *ACS ES&T Water* **2025**, *5* (9), 5233-5242.
(258) Yu, J.; Lv, L.; Lan, P.; Zhang, S.; Pan, B.; Zhang, W. Effect of effluent organic matter on the adsorption of perfluorinated compounds onto activated carbon. *Journal of Hazardous Materials* **2012**, *225-226*, 99-106.
(259) Chen, W.; Zhang, X.; Mamadiev, M.; Wang, Z. Sorption of perfluorooctane sulfonate and perfluorooctanoate on polyacrylonitrile fiber-derived activated carbon fibers: in comparison with activated carbon. *RSC Advances* **2017**, *7* (2), 927-938, 10.1039/C6RA25230C.
(260) Gauthier, J. R.; Kock, F.; Downey, K.; Moraes, T.; Almeida, L. S.; Muir, D. C. G.; Letcher, R. J.; Colnago, L.; Krishnamurthy, K.; Mabury, S.; et al. Steady State Free Precession NMR without Fourier Transform: Redefining the Capabilities of 19F NMR as a Discovery Tool. *Angewandte Chemie International Edition* **2025**, *64* (15), e202422971.

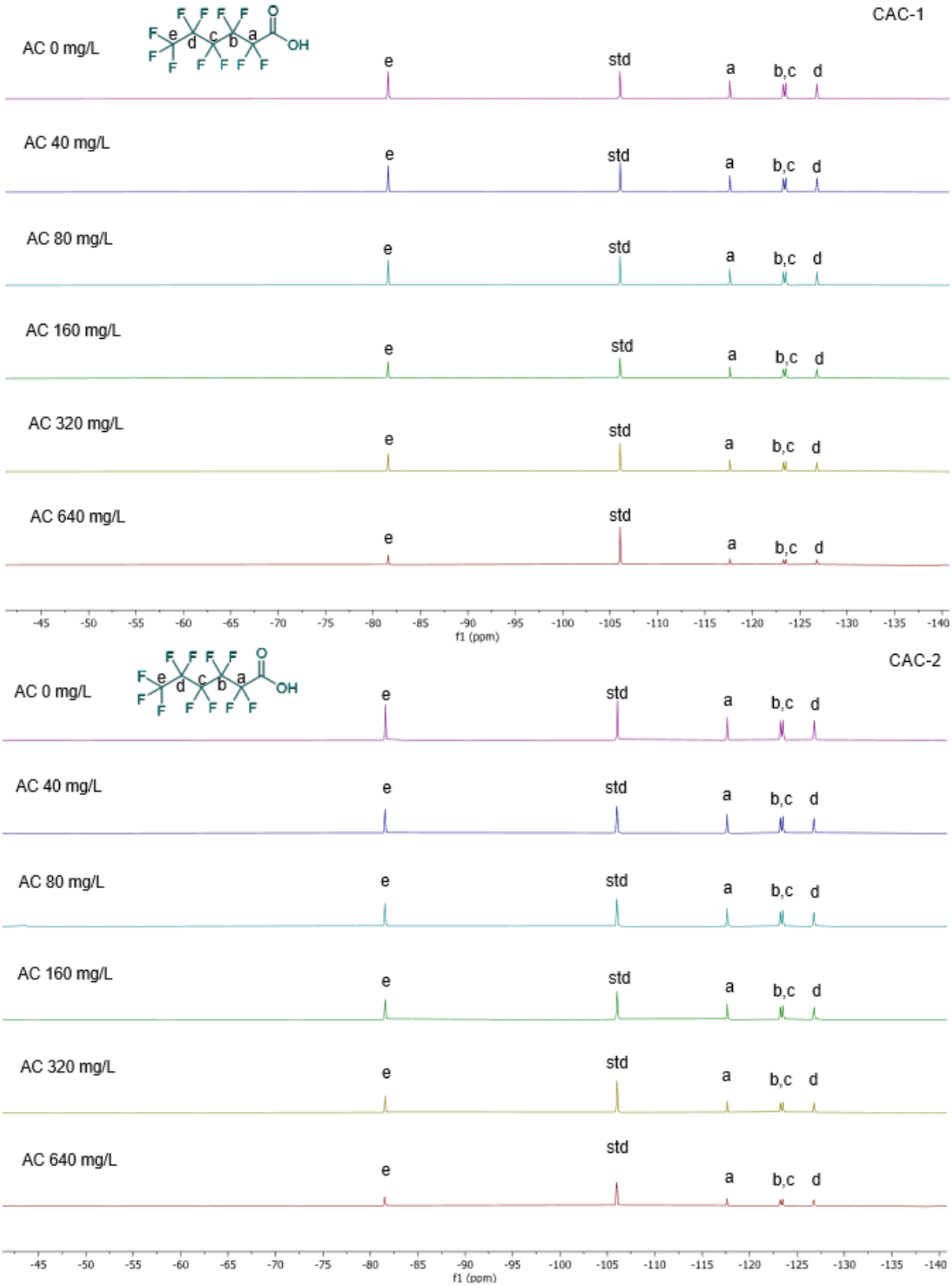
Appendix



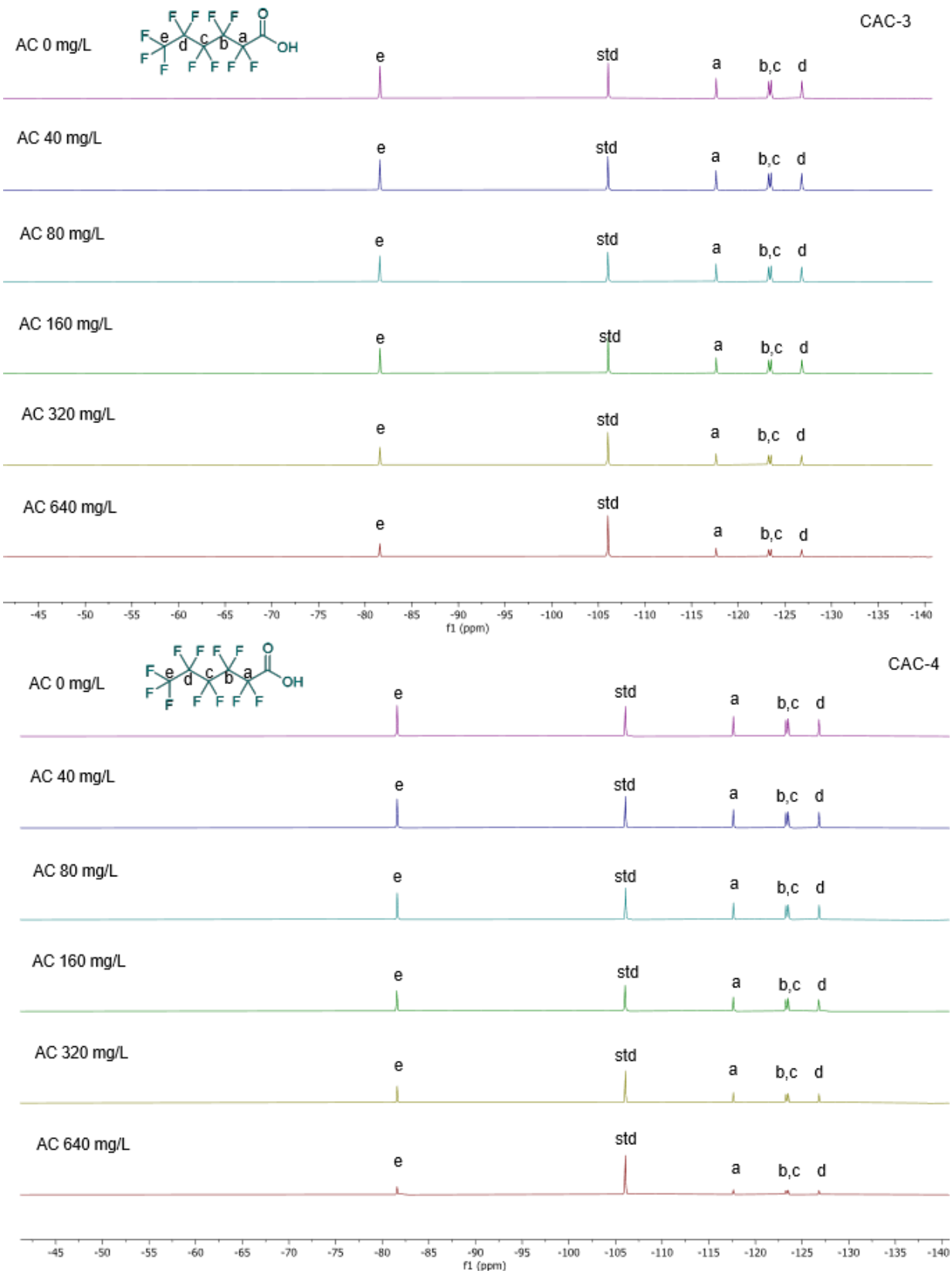
Appendix Figure 1. Stacked NMR spectra obtained for the adsorption isotherms of PFBS with CAC-1 and CAC-2.



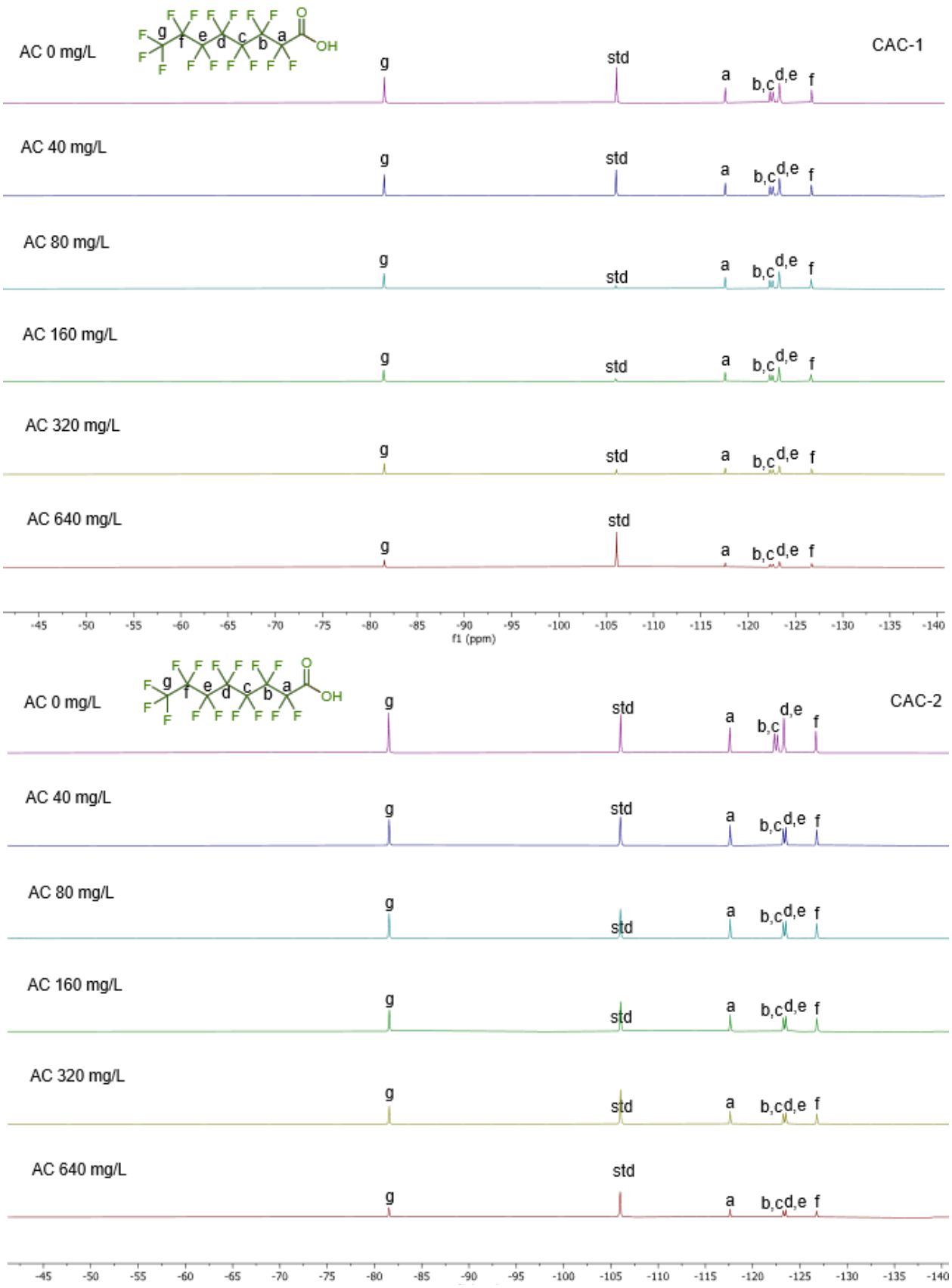
Appendix Figure 2. Stacked NMR spectra obtained for the adsorption isotherms of PFBS with CAC-3 and CAC-4.



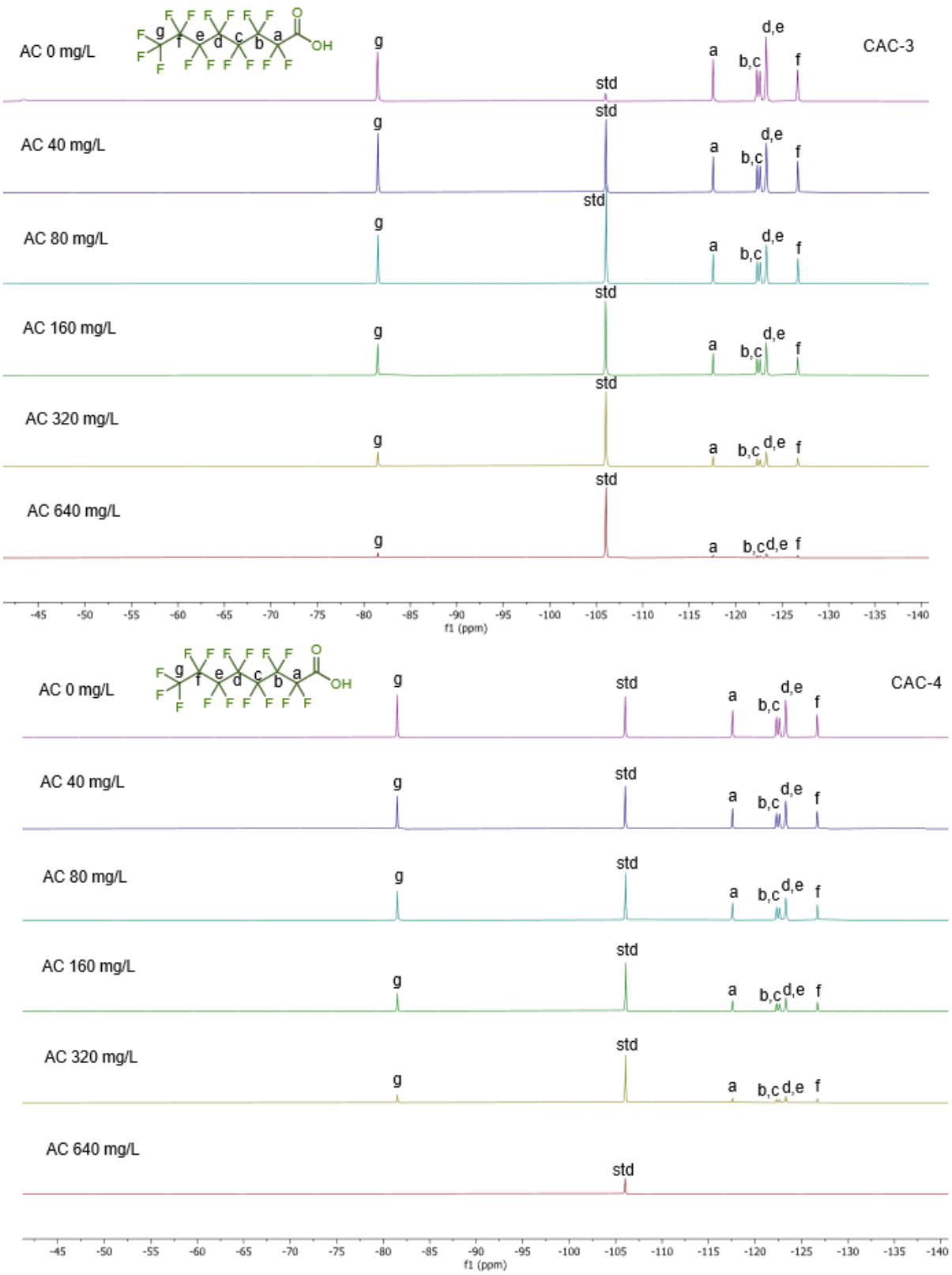
Appendix Figure 3. Stacked NMR spectra obtained for the adsorption isotherms of PFHxA with CAC-1 and CAC-2.



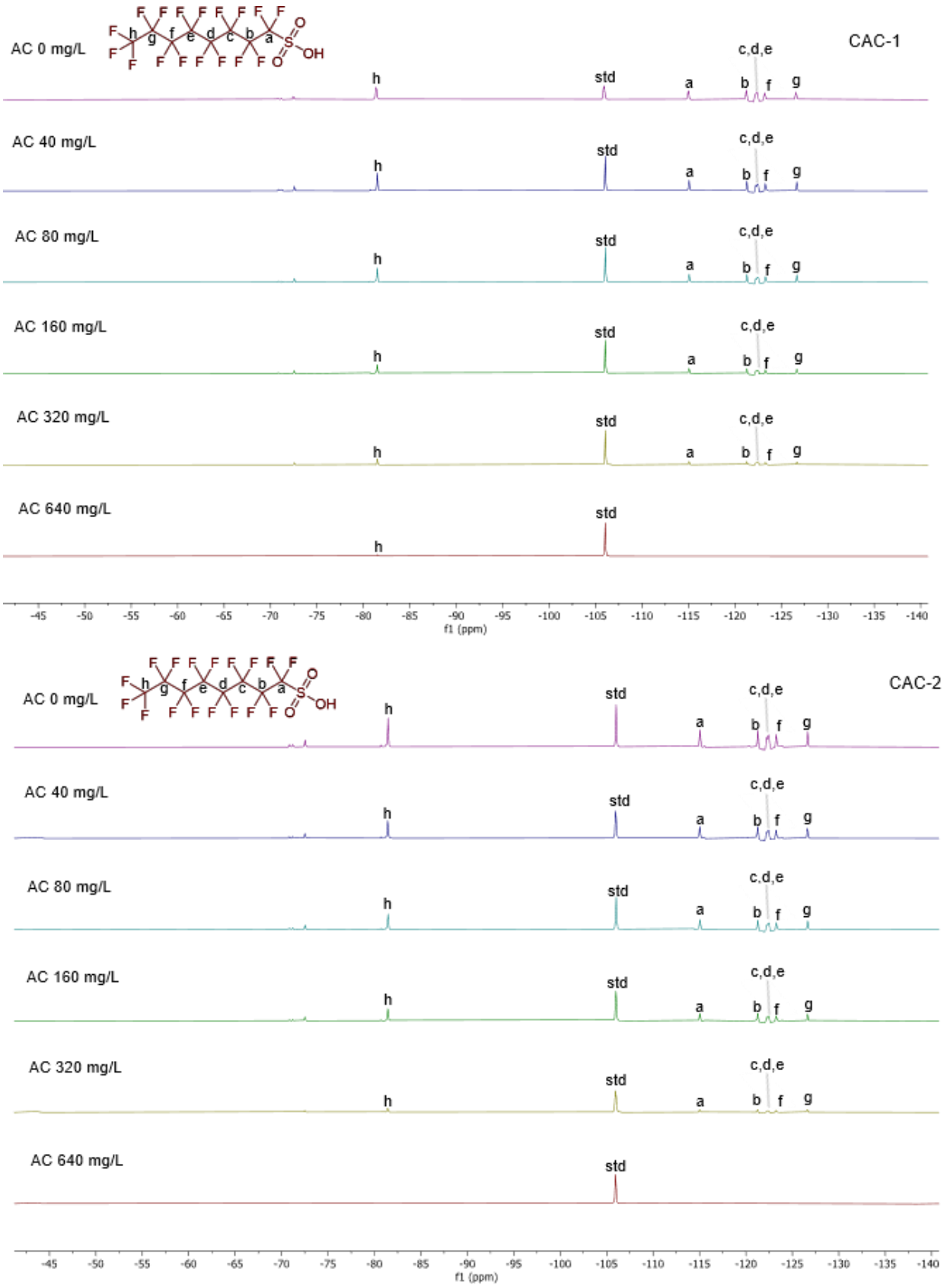
Appendix Figure 4. Stacked NMR spectra obtained for the adsorption isotherms of PFHxA with CAC-3 and CAC-4.



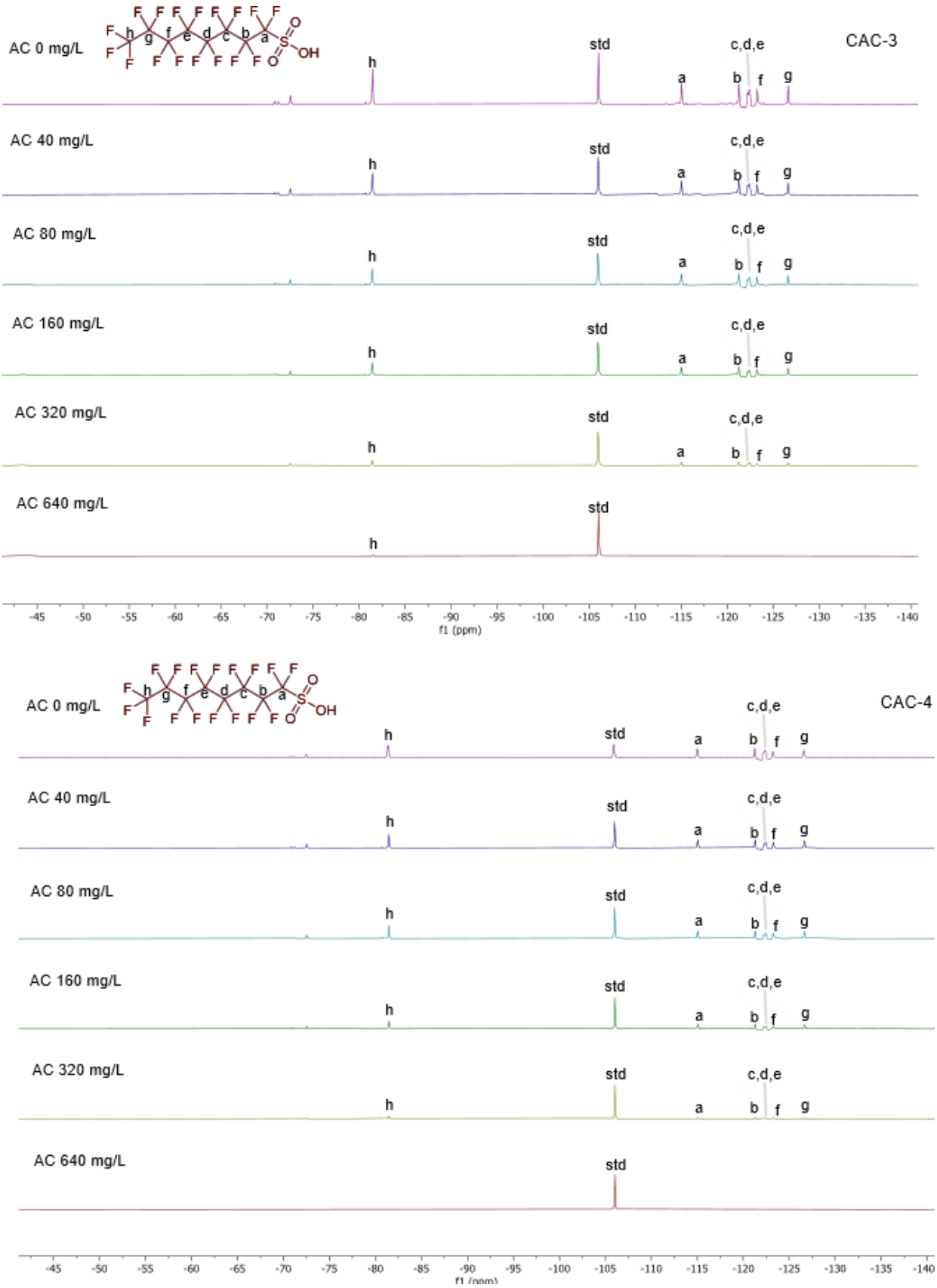
Appendix Figure 5. Stacked NMR spectra obtained for the adsorption isotherms of PFOA with CAC-1 and CAC-2.



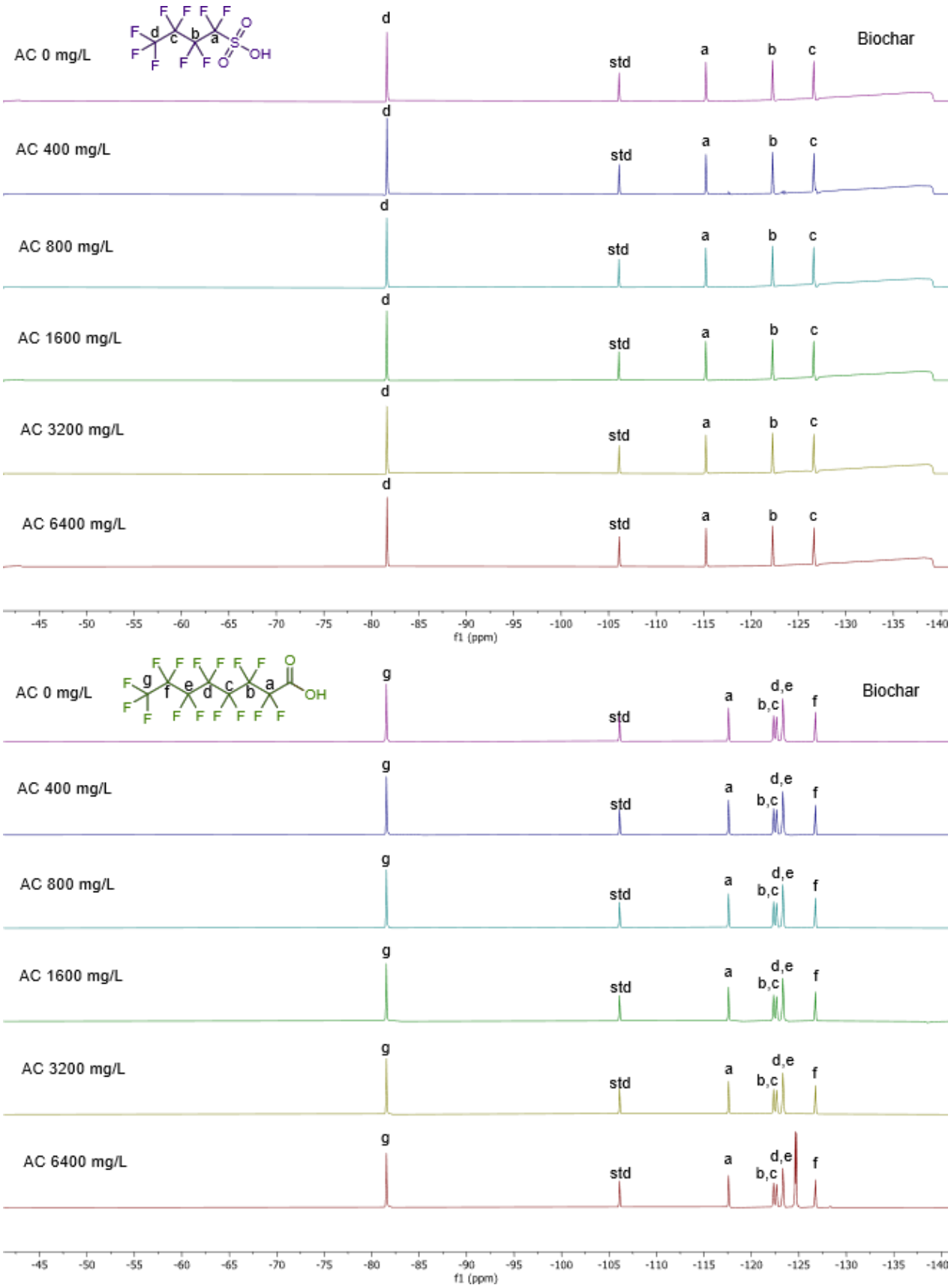
Appendix Figure 6. Stacked NMR spectra obtained for the adsorption isotherms of PFOA with CAC-3 and CAC-4.



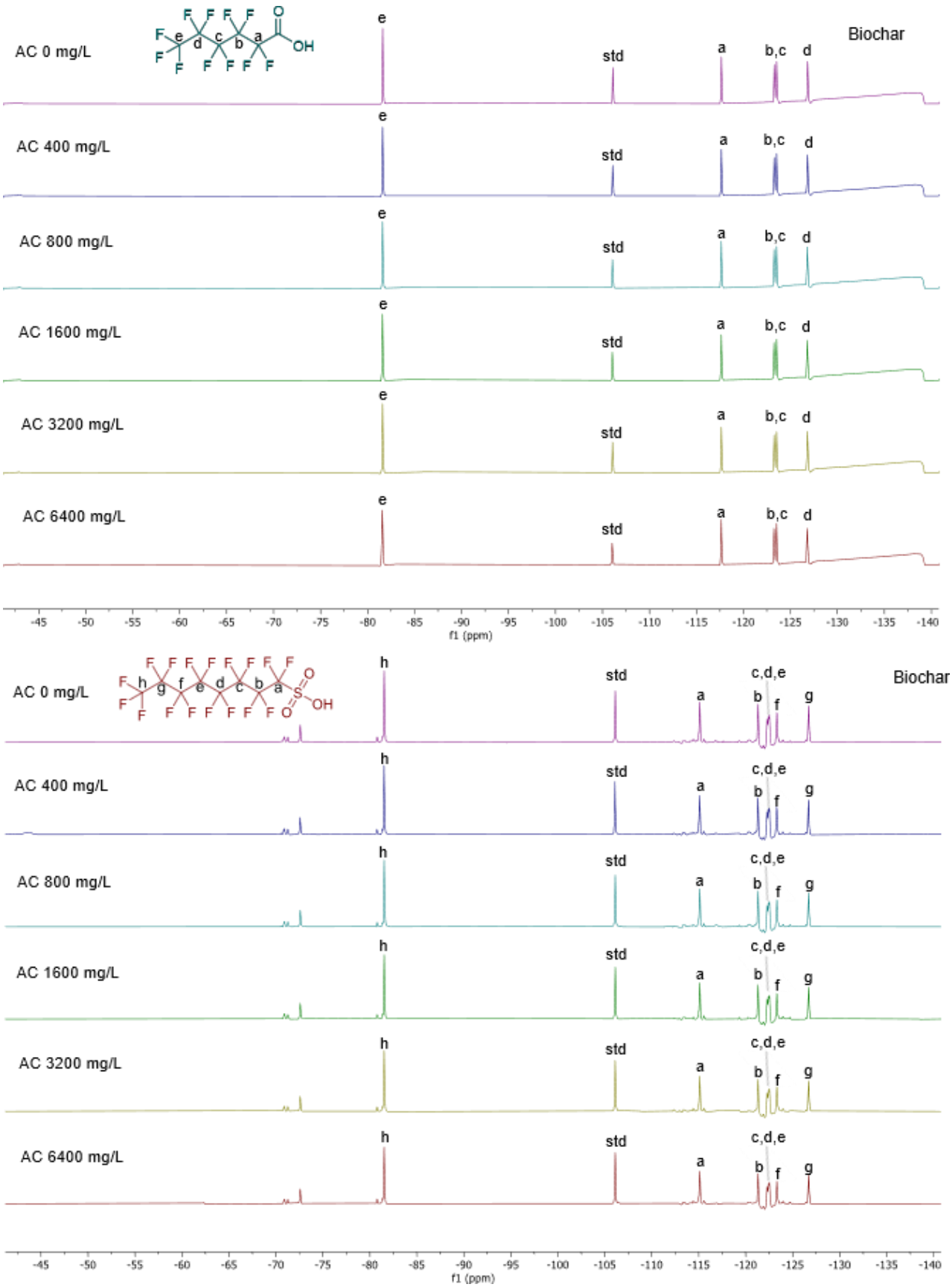
Appendix Figure 7. Stacked NMR spectra obtained for the adsorption isotherms of PFOS with CAC-1 and CAC-2.



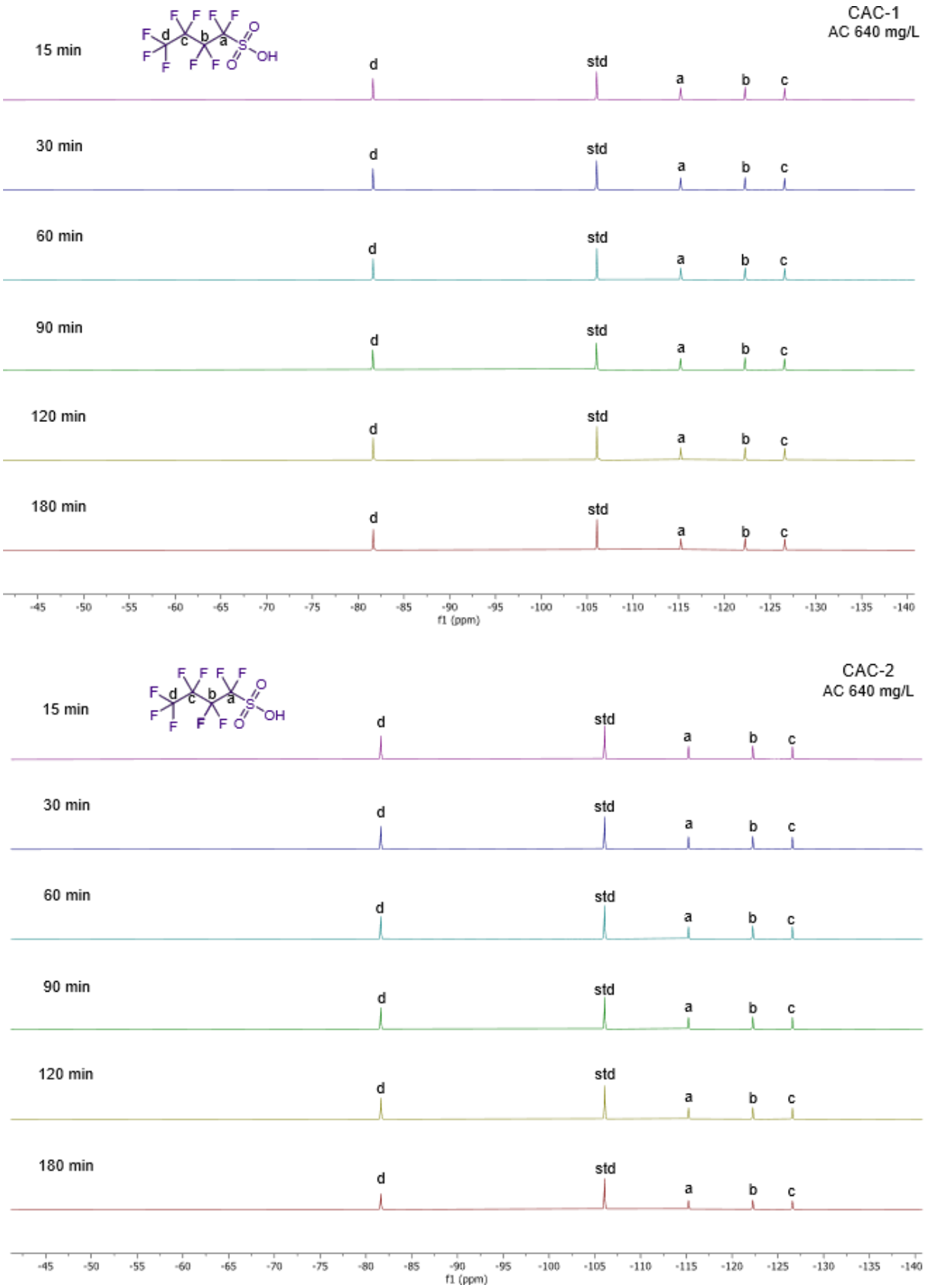
Appendix Figure 8.Stacked NMR spectra obtained for the adsorption isotherms of PFOS with CAC-3 and CAC-4.



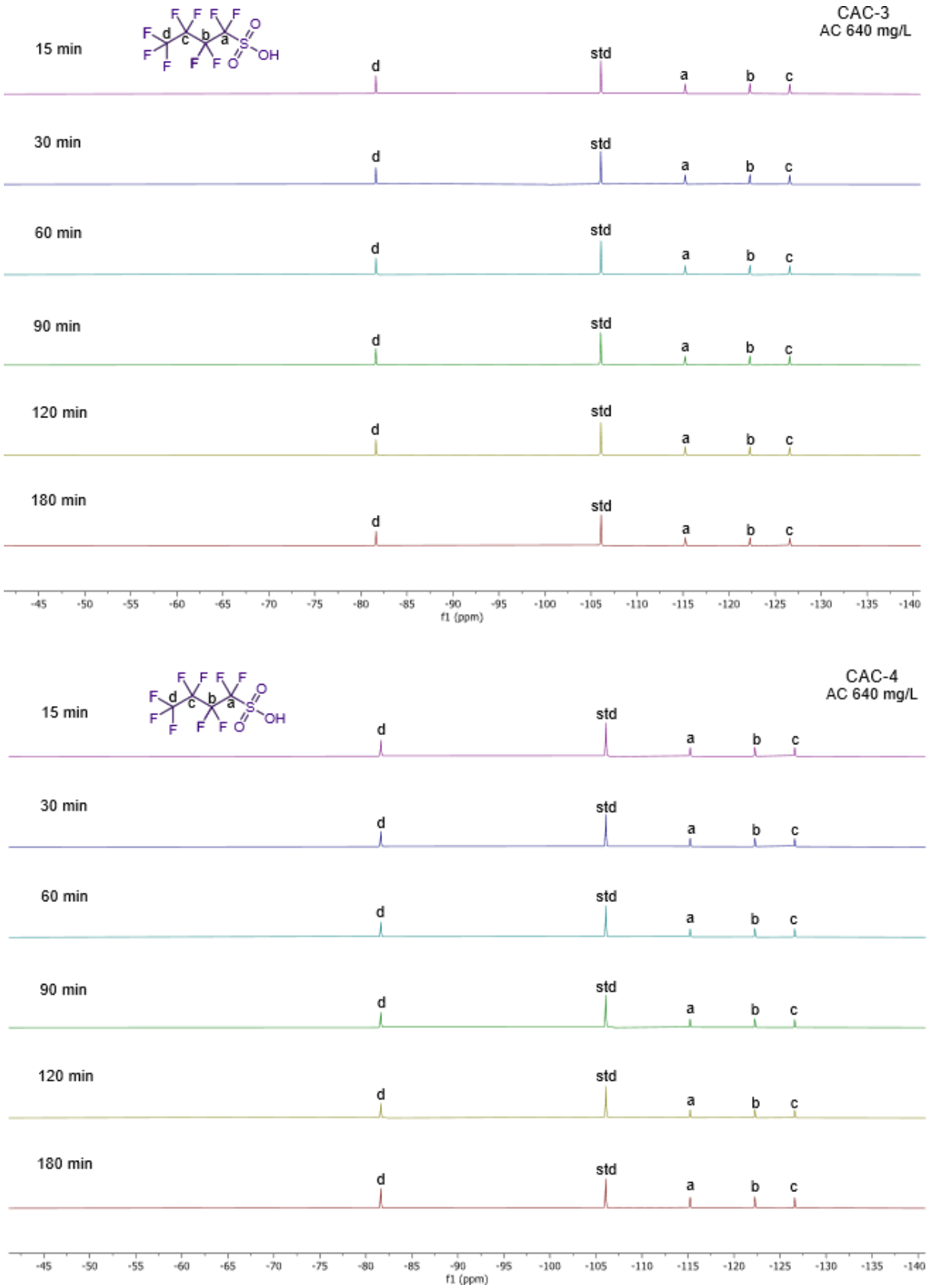
Appendix Figure 9. Stacked NMR spectra obtained for the adsorption isotherms of PFBS and PFOA with Biochar.



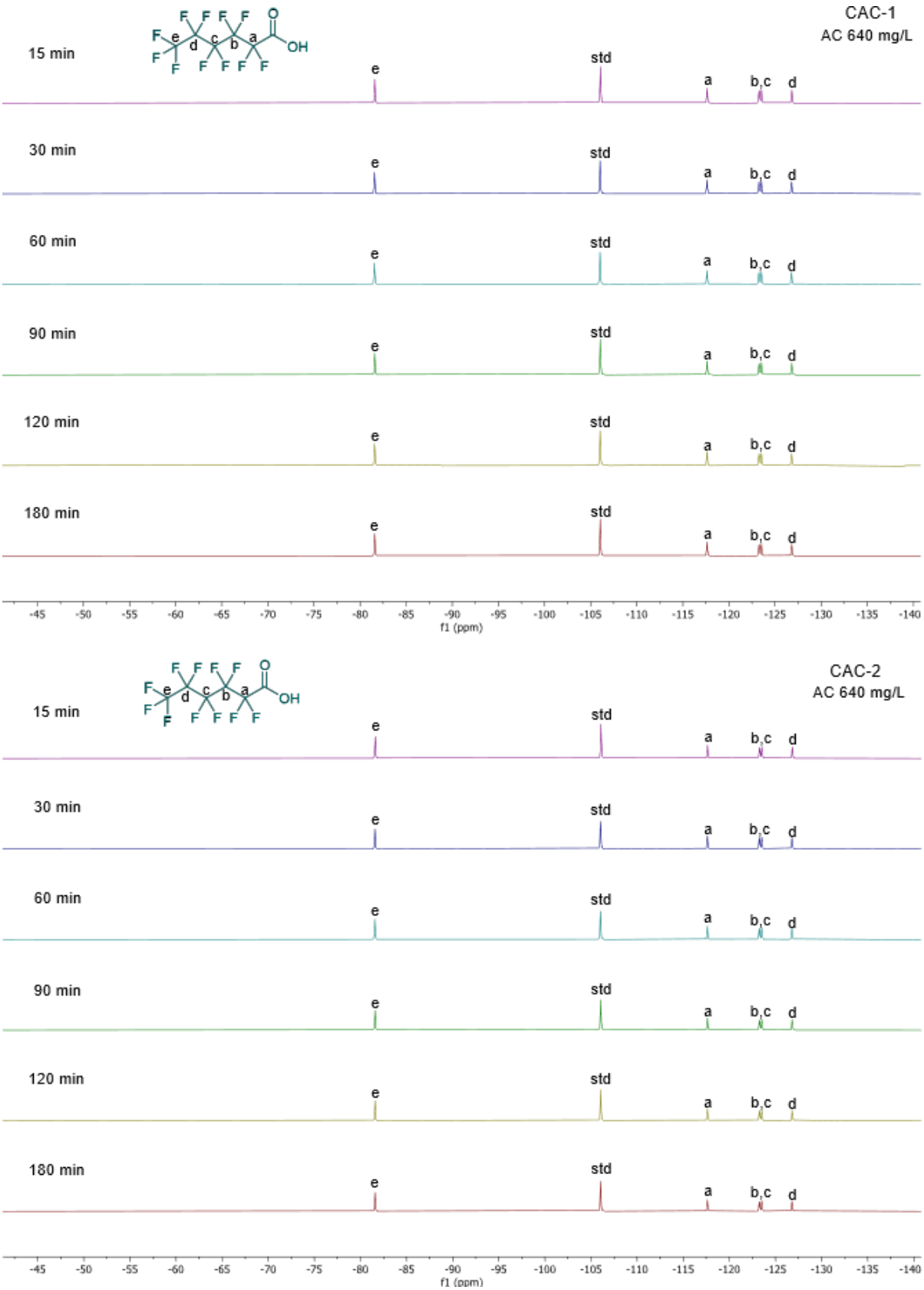
Appendix Figure 10. Stacked NMR spectra obtained for the adsorption isotherms of PFHxA and PFOS with Biochar.



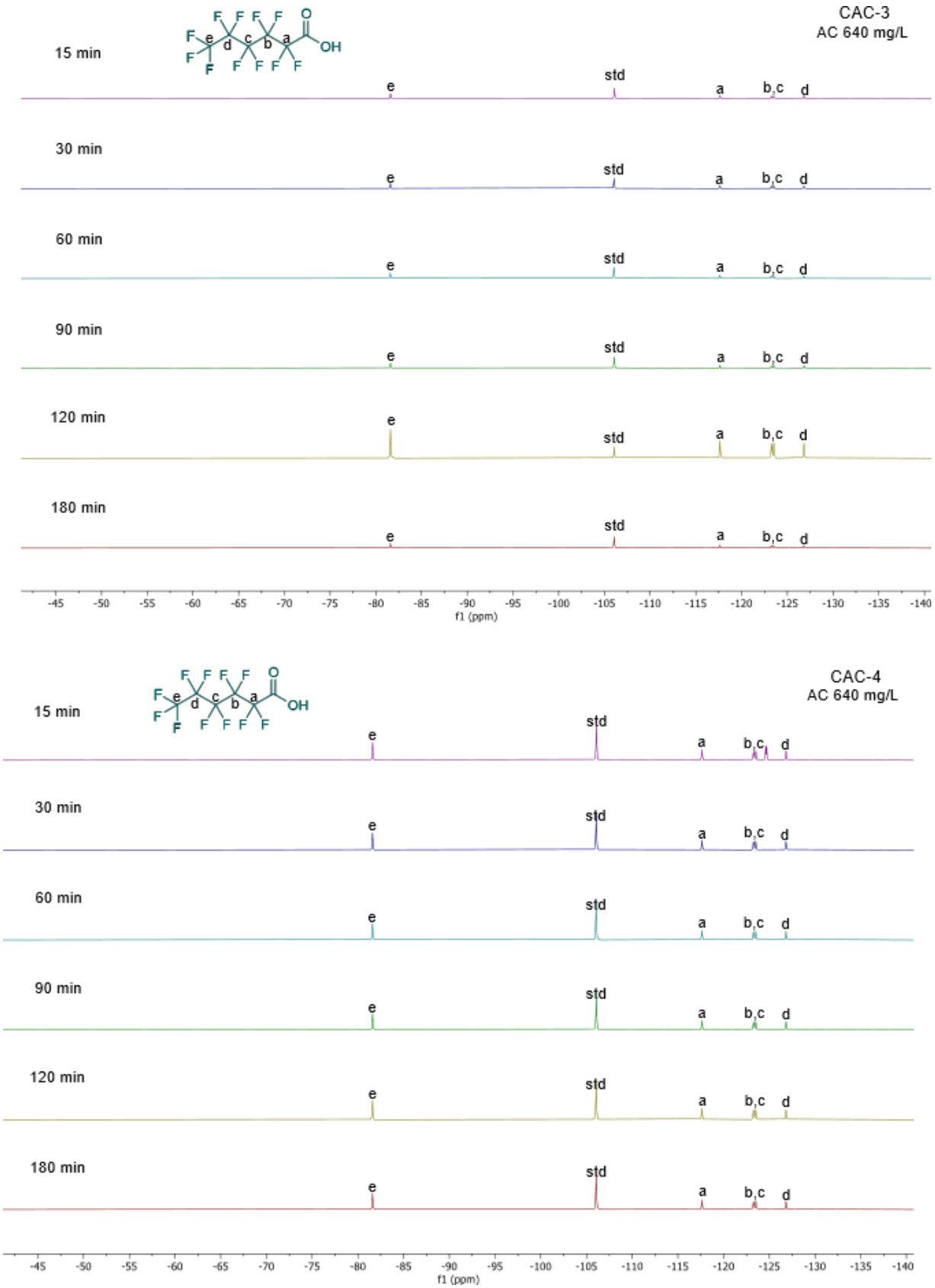
Appendix Figure 11. Stacked NMR spectra obtained for the adsorption kinetics experiments for PFBS with CAC-1 and CAC-2.



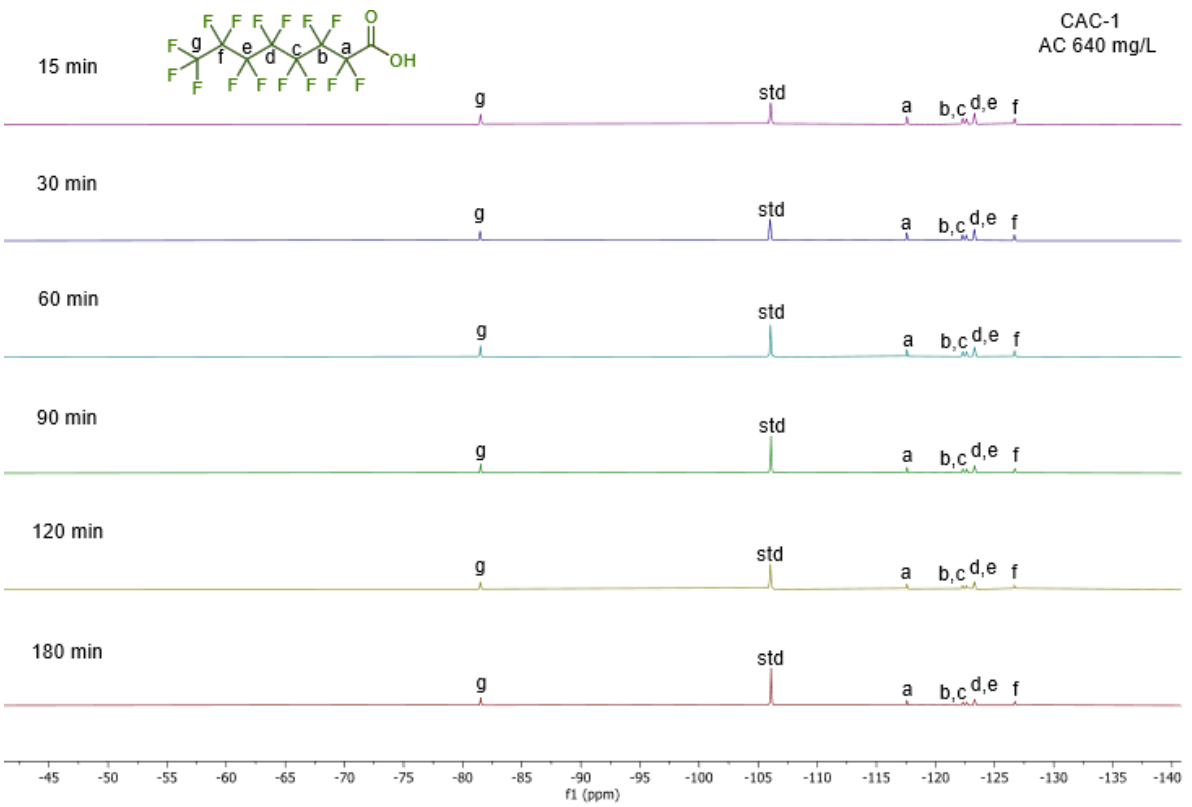
Appendix Figure 12. Stacked NMR spectra obtained for the adsorption kinetics experiments for PFBS with CAC-3 and CAC-4.



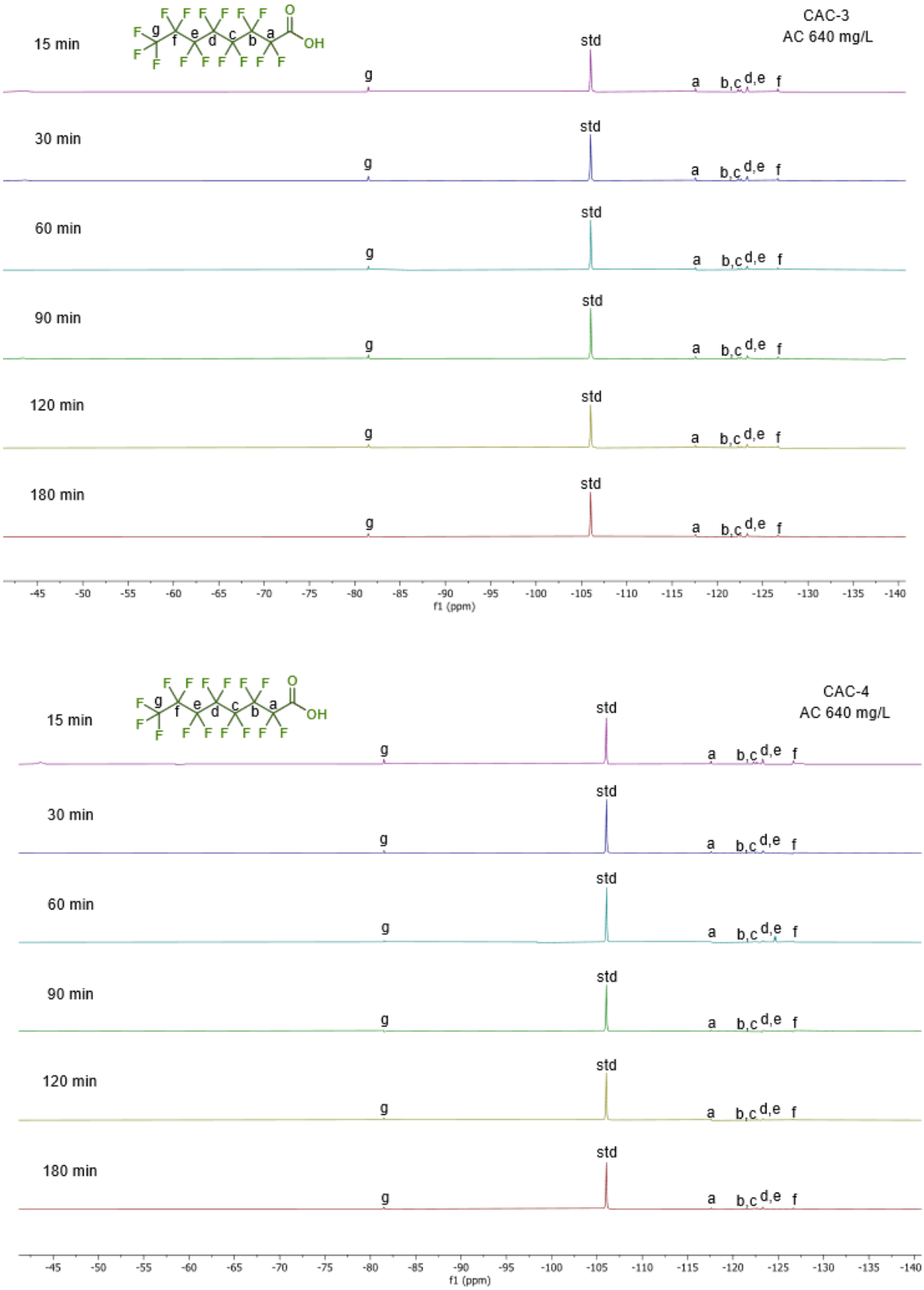
Appendix Figure 13. Stacked NMR spectra obtained for the adsorption kinetics experiments for PFHxA with CAC-1 and CAC-2.



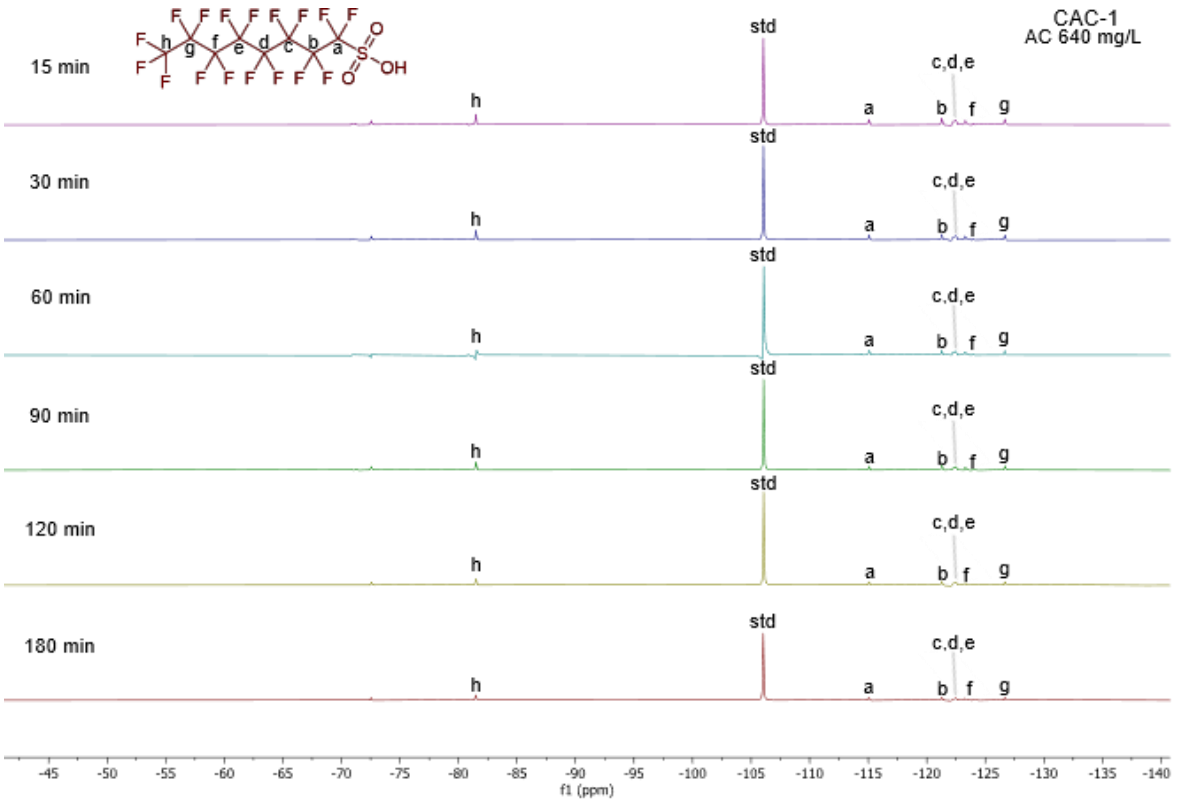
Appendix Figure 14. Stacked NMR spectra obtained for the adsorption kinetics experiments for PFHxA with CAC-3 and CAC-4.

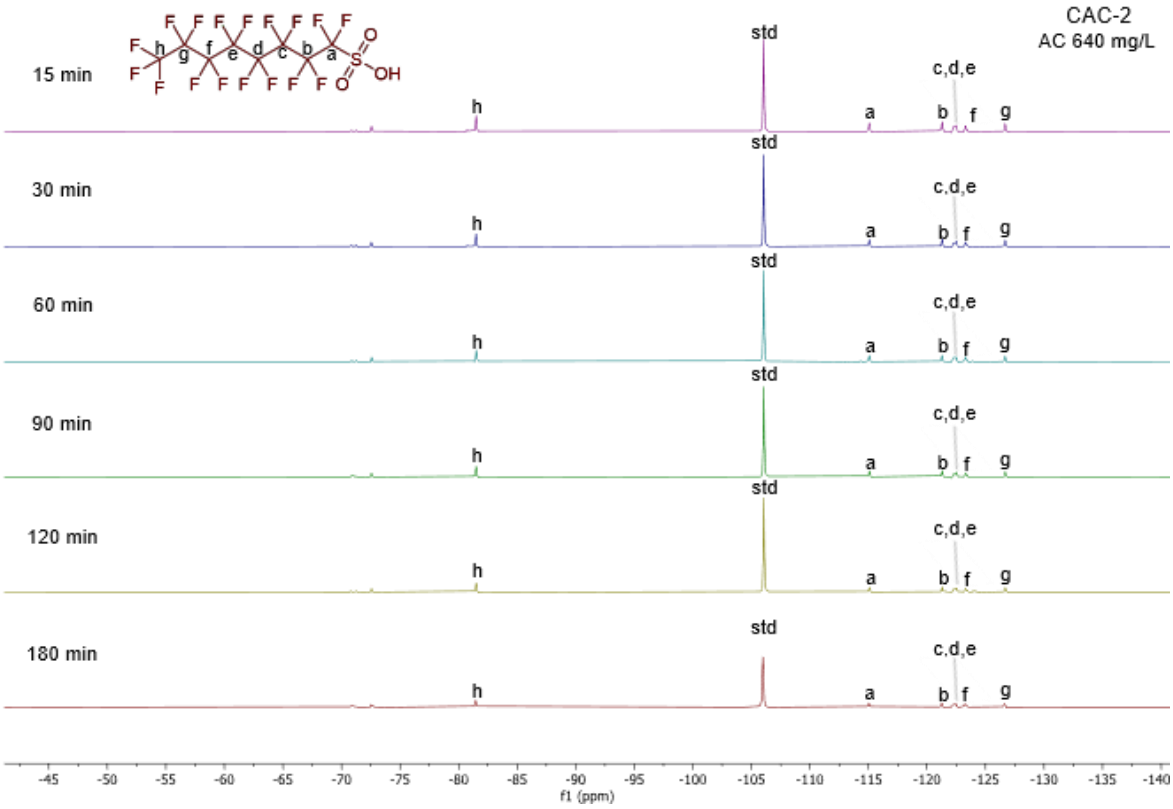


Appendix Figure 15. Stacked NMR spectra obtained for the adsorption kinetics experiments for PFOA with CAC-1 and CAC-2.

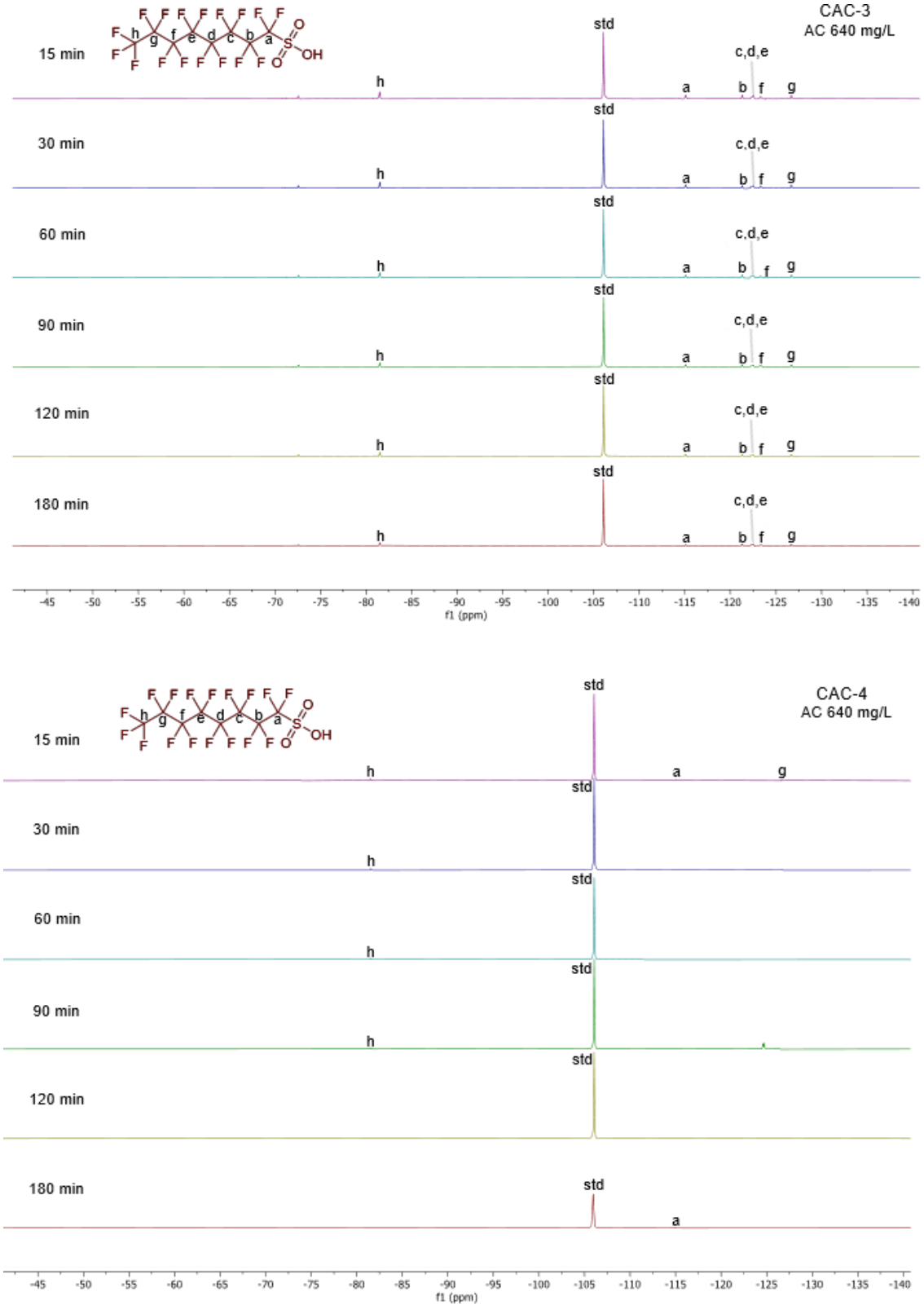


Appendix Figure 16. Stacked NMR spectra obtained for the adsorption kinetics experiments for PFOA with CAC-3 and CAC-4.





Appendix Figure 17. Stacked NMR spectra obtained for the adsorption kinetics experiments for PFOS with CAC-1 and CAC-2.



Appendix Figure 18. Stacked NMR spectra obtained for the adsorption kinetics experiments for PFOS with CAC-1 and CAC-2.